

ÉCOLE DOCTORALE DES SCEINCES CHIMIQUES
UMR 7006 - Institut de Science et d'Ingénierie Supramoléculaires

THÈSE

présentée par :

Luca CUSIN

soutenue le : **30 Juin 2023**

pour obtenir le grade de : **Docteur de l'université de Strasbourg**

Discipline/ Spécialité : Chimie

**2D COF films: advanced synthetic methods
toward new functional materials**

THÈSE dirigée par :

M. SAMORÌ Paolo

Professeur, Université de Strasbourg, France

RAPPORTEURS :

M. HECHT Stefan

Professeur, Humboldt-Universität zu Berlin, Allemagne

Mme. DE LUCA Giovanna

Professeure, Università degli Studi di Messina, Italie

AUTRES MEMBRES DU JURY :

M. STADLER Adrian-Mihail

Chargé de recherches HDR, CNRS-ISIS, Strasbourg, France

Résumé de thèse

Les polymères synthétiques font partie de notre vie depuis les 100 dernières années. Leurs innombrables applications ont rendu ces matériaux indispensables à la société moderne. Ces macromolécules sont composées d'unités de construction répétitives reliées selon des topologies définies. Alors qu'au départ, les recherches sur les polymères étaient principalement axées sur des chaînes linéaires unidimensionnelles (1D) et des réseaux tridimensionnels (3D) réticulés, d'autres topologies ont rapidement attiré l'attention des chercheurs.^[1] Les dendrimères, les polymères en étoile, les polymères peigne, les polymères échelle, les polymères cycliques et les polymères en brosse présentent des topologies fascinantes qui confèrent aux matériaux correspondants de nouvelles propriétés. Cependant, malgré le contrôle de la polymérisation en 1D et en 3D, la réalisation de macromolécules présentant des topologies bidimensionnelles (2D) a été très difficile pendant longtemps.^[2] Seulement récemment, les progrès réalisés dans les méthodes de synthèse ont permis la préparation de macromolécules dont la connectivité covalente est entièrement confinée dans un espace 2D. Une avancée révolutionnaire dans cette direction a été réalisée en 2005 lorsque le groupe d'Omar Yaghi a préparé le premier cadre organique covalent en 2D (COF 2D).^[3]

Les COF 2D sont une classe de solides en couches, cristallins et à porosité permanente, et ils sont actuellement la classe de polymères en 2D la plus étudiée.^[4] Leur préparation a été rendue possible en assemblant des unités de construction organiques planes et rigides (conjugaison π) par le biais de la liaison ester boronate hautement réversible, selon les principes de conception de la chimie réticulaire.^[5] Dans les bonnes conditions, les unités de construction réagissent et forment des cristaux en couches de type graphite, dont les défauts structuraux sont éliminés lors de la formation du matériau. Alors que la macromolécule individuelle se compose d'une feuille entièrement liée de manière covalente, la structure en vrac globale de ces structures en couches comprend une alternance régulière de réseaux π en colonnes d'unités de construction et de canaux poreux 1D. Grâce à leurs caractéristiques structurales innovantes et à leur flexibilité en termes de type de liaison et d'unités de construction, ces matériaux suscitent un intérêt croissant depuis 18 ans. Ils ont été proposés pour des applications dans divers domaines, notamment la catalyse, la détection, l'optoélectronique, le stockage et la conversion de l'énergie électrochimique, la séparation moléculaire et gazeuse, ainsi que le stockage de gaz. Plusieurs questions ouvertes et défis se posent dans la conception et la synthèse des COF 2D, notamment le développement de nouveaux types de liaisons recherchant le bon équilibre entre réversibilité, stabilité et fonctionnalité,^[6] l'assemblage de COF 2D en films minces cristallins et orientés,^[7] et l'obtention d'un contrôle précis

de la relation entre structure et propriétés pour l'application réussie de ces matériaux en optoélectronique et en stockage de l'énergie.^[8]

L'objectif principal de cette thèse est de développer des matériaux à base de COF 2D avec des propriétés physico-chimiques personnalisées et orientées vers des applications, qui sont étudiées à plusieurs échelles. Cette thèse est divisée en cinq chapitres, comprenant deux chapitres introductifs et trois chapitres expérimentaux. Le premier chapitre présente aux lecteurs les polymères synthétiques en mettant l'accent sur les COF 2D, leur synthèse et leurs applications. Le deuxième chapitre décrit les techniques analytiques les plus pertinentes pour la caractérisation des matériaux. Les trois chapitres restants sont consacrés aux recherches originales réalisées pour cette thèse. Dans chaque chapitre, un ou plusieurs matériaux à base de COF 2D sont conçus pour une application spécifique, puis synthétisés, traités et caractérisés. En particulier, les trois chapitres expérimentaux se concentrent sur les défis suivants : 1. développement d'une nouvelle technique de traitement en solution pour obtenir une morphologie et une orientation spécifiques ; 2. conception d'un COF 2D conjugué avec des propriétés semi-conductrices ; 3. préparation de matériaux composites rGO-COF pour l'électronique flexible.

Indépendamment de la structure chimique spécifique des unités de construction et de la liaison qui les maintient ensemble, les COF 2D sont complètement inertes aux solvants organiques conventionnels, ce qui signifie que, une fois synthétisés, ils sont insolubles et non transformables, se comportant ainsi comme des polymères thermodurcissables. Le contrôle de la morphologie lors de la synthèse est donc fondamental.^[9] La méthode de préparation la plus courante, c'est-à-dire la synthèse solvothermale, conduit intrinsèquement à la cristallisation de petites particules, souvent de forme sphérique, qui s'agrègent pour former un précipité solide en poudre. Pour de nombreuses applications, telles que le stockage de gaz ou la catalyse, la poudre polycristalline présente une morphologie appropriée, mais pour des applications telles que les membranes, l'électronique ou le stockage de l'énergie, une morphologie de film mince ordonné serait fortement préférable. Jusqu'à présent, seules quelques méthodes ont été développées pour la préparation de films de COF 2D. Par exemple, la polymérisation interfaciale permet la synthèse ascendante de films d'une épaisseur souhaitée, mais les protocoles établis sont laborieux et prennent beaucoup de temps.^[7]

Dans le **chapitre 3**, nous rapportons une nouvelle stratégie de synthèse pour la préparation de COF 2D liés par des imines, en ciblant une morphologie de film continue et orientée, et proposant un mécanisme pour la formation du matériau. Des rapports récents ont révélé que l'acide trifluoroacétique (TFA), présent en tant que composant principal ou additif, est

un solvant et un catalyseur prometteur pour la réaction de Schiff, à la base de la formation de COF en 2D liés par des imines.^[10,11] Nous avons initialement étudié la réaction entre le 1,3,5-tris(4-aminophényl)benzène (TPB) et le 2,5-diméthoxytéréphtalaldéhyde (MeOTP). En utilisant des mélanges d'eau et de TFA comme solvant de réaction, une polyimine soluble a pu être synthétisée à température ambiante. L'acidité forte du TFA empêche les interactions intercouches et évite la précipitation du solide, même à des concentrations élevées. Par conséquent, la solution polymère a pu être traitée par coulée, et remarquablement, lors de l'évaporation rapide du solvant, un film de polyimine (PI_m) continu s'est formé sur le substrat cible. Le film, d'une épaisseur d'environ 50 µm, pouvait être facilement décollé du substrat et était suffisamment robuste pour se maintenir debout et être manipulé sans être endommagé. L'ordre structural des films a été caractérisé par diffraction des rayons X à grand angle en incidence rasante (GIWAXS). Remarquablement, le motif de diffraction en 2D a révélé une structure hautement orientée mais faiblement cristalline. L'analyse en microscopie électronique à balayage (MEB) en coupe transversale a confirmé les résultats en révélant une structure fortement stratifiée, tandis que les mesures d'adsorption d'azote ont indiqué que le film de PI_m présente une structure non poreuse. Les caractéristiques observées ont été attribuées à la formation d'un réseau covalent fortement défectueux, dont les brins polymères sont partiellement alignés parallèlement à la surface du substrat utilisé pour le dépôt. Étonnamment, grâce à un traitement par recuit du film, un mécanisme de correction d'erreur à l'état solide a pu être introduit et a permis de réparer les défauts dans la structure du polymère covalent. Par conséquent, lors du traitement thermique, le polymère a cristallisé pour former un COF 2D hautement poreux, tout en préservant l'alignement des feuillets polymères 2D parallèlement au plan du film. Ces découvertes revêtent une grande importance, car elles présentent une approche simple et novatrice pour la synthèse de films robustes et autoportants, avec un contrôle précis de l'orientation des structures polycristallines. Ce chapitre dévoile également les détails mécanistiques liés à la transition de la solution vers l'état solide, qui est caractérisée par la formation d'un gel amorphe 3D intermédiaire. De plus, la portée a été étendue à d'autres COF en 2D liés par des imines, contenant des blocs de construction à base de pyrène en tant que nœuds amine, ce qui démontre une applicabilité générale de la méthode.

Dans le **chapitre 2**, nous présentons la conception, la synthèse et l'étude des propriétés (opto)électroniques d'un COF en 2D lié par des imines contenant les composants riches en électrons triphénylamine et thiénothiophène. L'intégration de blocs de construction (photo)électroactifs dans le squelette des COFs 2D, associée à une conjugaison étendue dans le

plan et à un empilement colonnaire hors du plan des fragments organiques, confère à ces matériaux un attrait pour les applications en (opto)électronique telles que les dispositifs électroluminescents, les dispositifs photoconducteurs, les cellules solaires et les transistors organiques à effet de champ (OFETs).^[8] La triphénylamine est une unité de construction en forme d'hélice thermiquement stable qui présente des comportements photoactifs et électroactifs intéressants. Ces caractéristiques sont liées à la stabilité du radical cation correspondant, facilement généré par oxydation monoélectronique.^[12] Pour ces raisons, les polymères en 2D à base de triphénylamine sont prometteurs pour les applications (opto)électroniques. Ici, pour la préparation du matériau, nous avons utilisé une approche solvothermique : la tétramine N,N,N',N'-tétrakis(4-aminophényl)-1,4-phénylène diamine (BTA) et le dialdéhyde linéaire thién[3,2-b]thiophène-2,5-dicarboxaldéhyde (TT) ont été dispersés dans un mélange de solvants contenant de l'alcool benzylique et du mésitylène, et la réaction a été catalysée par l'acide acétique. Après trois jours de réaction à 120 °C, nous avons obtenu un matériau en poudre rouge foncé, et la réussite de la polymérisation a été confirmée par spectroscopie infrarouge à transformée de Fourier (FTIR) et par spectroscopie photoélectronique des rayons X (XPS). Le COF 2D a montré un bon degré de cristallinité lorsqu'il a été mesuré par diffraction des rayons X sur poudre (PXRD). De plus, la correspondance du schéma de diffraction avec ceux rapportés dans la littérature pour d'autres COFs 2D basés sur la moitié BTA et avec le modèle simulé nous a permis de conclure que ce matériau présente une topologie de type Kagome à double pore avec un agencement en couches éclipsées.^[13] La microscopie électronique en transmission à haute résolution (HR TEM) a clairement indiqué la nature polycristalline du COF en 2D avec une taille de domaine d'environ 30 nm. En mesurant et en analysant l'isotherme d'adsorption-désorption d'azote, nous avons pu calculer la surface spécifique ($720 \text{ m}^2 \text{ g}^{-1}$) du matériau et estimer la taille des pores (2,3 et 3,8 nm). Afin de caractériser pleinement les propriétés (opto)électroniques du polymère conjugué en 2D, le matériau en poudre n'est pas adapté, des films minces du matériau ont donc été fabriqués. La synthèse a été réalisée dans des conditions analogues à la réaction en vrac, en immergeant le substrat à revêtir dans une suspension de monomères, avec une approche appelée "croissance solvothermale sur substrat". Les films ont été caractérisés par spectroscopie XPS et Raman, obtenant des spectres correspondant à ceux du matériau en vrac, confirmant ainsi la réussite de la synthèse. La microscopie à force atomique (AFM) et la MEB ont été utilisées pour analyser la nanomorphologie des films minces. Un film typique est caractérisé par une épaisseur d'environ 90 nm et une faible rugosité de surface. Des dispositifs à deux électrodes ont été fabriqués en faisant croître le film sur des substrats

en verre avec des électrodes interdigitées en or pré-patinées. Le film présentait un comportement de semi-conducteur de type p avec un niveau de bande de valence situé à -5,1 eV, un niveau de bande de conduction à -3,0 eV et une bande interdite optique de 2,1 eV. Le film présentait une conductivité électrique de $\sigma = 4 \times 10^{-11} \text{ S m}^{-1}$ sous vide et de $\sigma = 3 \times 10^{-6} \text{ S m}^{-1}$ après 20 heures à l'air libre. La conductivité pourrait être encore augmentée jusqu'à $\sigma = 2 \times 10^{-4} \text{ S m}^{-1}$ par infiltration de petites molécules présentant de fortes propriétés accepteurs d'électrons, telles que le 2,3,5,6-tétrafluoro-tétracyanoquinodiméthane (F_4TCNQ).^[14] La différence de conductivité entre le vide et l'air était liée à la tendance du matériau à interagir avec l' O_2 , ce qui provoquait une augmentation initiale de la conductivité par dopage de type p, suivie de la perte des propriétés de transport de charge après une exposition prolongée, probablement due à des réactions d'oxydation (photo)irréversibles qui perturbent la conjugaison π dans le polymère en 2D et le chevauchement π hors du plan des unités conjuguées. Ces résultats revêtent une importance capitale, car ils démontrent que, en règle générale, le COF 2D riche en électrons doit être manipulé avec précaution lorsqu'on tente de caractériser ses conductivités intrinsèques, car les valeurs peuvent varier énormément en fonction du temps d'exposition à l'atmosphère.

Enfin, à titre de démonstration, le film et le matériau en poudre ont été intégrés dans un dispositif électronique et un dispositif de stockage d'énergie, et leurs performances ont été évaluées. En particulier, le film a été utilisé comme canal actif dans un transistor à effet de champ organique (OFET) où la modulation du courant était réalisée par une goutte d'eau déionisée (transistor à grille d'eau). Le diélectrique liquide a permis de commuter le dispositif de manière volumétrique, ce qui a conduit à de bonnes performances du dispositif, avec une modulation du courant de trois ordres de grandeur et une tension de seuil de $V_{\text{th}} = -0,4 \text{ V}$. Le matériau en poudre a été testé comme matériau électrode actif dans un pseudo-condensateur symétrique, en utilisant une solution de NBu_4PF_6 à 1 M dans de l'acétonitrile comme électrolyte de soutien, qui a montré une bonne capacitance spécifique de 108 F g^{-1} à $0,1 \text{ A g}^{-1}$, mais une faible stabilité à des densités de courant plus élevées.

La grande surface spécifique et l'arrangement périodique des canaux poreux 1D et des empilements π des unités constitutives confèrent aux COF 2D un grand potentiel pour plusieurs applications, allant de la détection au stockage d'énergie.^[15] Cependant, comme nous l'avons montré dans les chapitres précédents, la préparation de matériaux purs présentant une conductivité électrique élevée n'est pas une tâche facile. Plus généralement, une approche possible pour conférer de nouvelles propriétés aux COF 2D consiste à les combiner avec d'autres nanomatériaux tels que des nanoparticules métalliques, de la silice, des oxydes

métalliques, des polymères ou des matériaux carbonés.^[16] Alors que la préparation et les propriétés de plusieurs COF 2D purs sont bien établies, leur utilisation en tant que matrice pour disperser d'autres nanomatériaux est encore peu étudiée. Dans le chapitre 5, nous présentons la synthèse, la caractérisation et l'étude d'une application potentielle d'un nouveau matériau composite conducteur à morphologie de film, composé d'oxyde de graphène réduit (rGO) conducteur et d'un COF 2D non conducteur. Pour la synthèse et la fabrication du film de ce matériau, nous avons appliqué une version modifiée de la méthode utilisée dans le premier projet, c'est-à-dire la méthode de coulée de solution polymère. L'oxyde de graphène (GO) a été utilisé comme précurseur du rGO pour la préparation du composite. Grâce à ses groupes fonctionnels polaires, le GO est généralement facilement dispersible dans les solvants organiques, nous l'avons donc utilisé comme additif à 4 % en masse dans la solution de polyimine. La suspension des matériaux mélangés a été déposée par coulée et, après séchage, un film d'une épaisseur d'environ 50 μm a été obtenu. La combinaison d'un GO fonctionnalisé à l'amine et d'une polyimine fonctionnalisée à l'octyloxy comme précurseurs s'est avérée conduire à une compatibilisation optimale des deux matériaux nanostructurés. Ensuite, une recristallisation et un recuit thermique ont été réalisés pour produire un film composite conducteur. Remarquablement, les films manifestaient une asymétrie dans leurs propriétés conductrices, avec un côté du film présentant une résistance de surface de $R_s = 1,3 \times 10^5 \Omega \text{sq}^{-1}$, tandis que l'autre était électriquement isolant. Cette caractéristique, associée à la flexibilité et à la durabilité mécanique, rendait le matériau adapté aux applications électroniques flexibles. Plus précisément, nous avons montré que les films pouvaient servir de capteurs de contrainte piézo-résistifs, leur résistivité inhérente variant en fonction du type et de l'intensité de la contrainte appliquée (compressive ou de traction).

En conclusion, dans cette thèse, nous avons tenté de relever certains défis ouverts dans le développement de matériaux COF 2D aux propriétés sur mesure. Les résultats que nous rapportons ont le potentiel d'offrir une nouvelle perspective sur la conception et la synthèse des COF 2D. En particulier, nous nous sommes concentrés sur le contrôle de la morphologie en développant une nouvelle méthode pour préparer des films orientés à grande surface, ce qui est fortement souhaité pour améliorer les performances de ces matériaux dans des applications telles que les membranes de filtration, le stockage d'énergie et les semi-conducteurs. De plus, nous avons présenté deux méthodes différentes pour améliorer les performances électriques des COF 2D, soit en modifiant les groupes fonctionnels dans l'ossature du polymère 2D, soit en mélangeant le matériau avec du rGO conducteur. Nos résultats représentent une référence solide pour la communauté scientifique qui, selon nous, favori-

sera le développement de nouvelles méthodes de synthèse et de nouveaux designs dans le domaine des COF 2D fonctionnels.

Summary of the thesis

Synthetic polymers have been part of our life for the past 100 years. Their countless applications have made these materials vital to modern society. These macromolecules consist of repetitive building units connected according to defined topologies. While initially, mainly one-dimensional (1D) linear strands and three-dimensional (3D) cross-linked networks dominated polymer research, soon enough other topologies attracted the researchers' attention.^[1] Dendrimers, star polymers, comb polymers, ladder polymers, cyclic polymers, and polymer brushes exhibit fascinating topologies that endow the corresponding materials with new properties. However, despite having controlled the polymerization in 1D and 3D, macromolecules with two-dimensional (2D) topologies have been for long time very hard to achieve.^[2] Only recently, the advances in the synthetic methods have allowed the preparation of macromolecules whose covalent connectivity is fully confined in a 2D space. A disruptive step in this direction was taken in 2005 when the group of Omar Yaghi prepared the first 2D covalent organic framework (COF).^[3]

2D COFs are a class of layered, crystalline, and permanently porous solids and they are currently the most studied class of 2D polymers.^[4] Their preparation was made possible by stitching together flat and rigid (π conjugated) organic building blocks through the highly reversible boronate ester bond according to the design principles of reticular chemistry.^[5] In the right conditions the building blocks react and form graphite-like layered crystals, whose structural defects are annealed during the material formation. While the single macromolecule consists of a fully covalently linked sheet, the overall bulk structure of these layered frameworks comprises a regular alternation of columnar π arrays of building units and 1D pore channels. Owing to their innovative structural features and the flexibility in terms of type of linkage and building blocks, these materials have received ever growing attention for the past 18 years. They have been proposed for applications in various fields, including catalysis, sensing, (opto)electronics, electrochemical energy storage and conversion, molecular and gas separation, and gas storage. Several are the open questions and challenges in the design and synthesis of 2D COFs, including the development of new types of linkages seeking for the right balance between reversibility, stability, and functionality;^[6] the assembly of 2D COFs into crystalline and oriented thin films;^[7] and achieving a fine control over the structure-properties relationship for the successful application of these materials in (opto)electronics and energy storage.^[8]

The main goal of this thesis is to develop 2D COFs-based materials with customized, application-oriented physicochemical properties that are studied at multiple length scales. This

thesis is divided into five chapters, including two introductory and three experimental chapters. The first chapter introduces the reader to synthetic polymers with a focus on 2D COFs, their synthesis, and their applications. The second chapter outlines the most relevant analytical techniques for the characterization of the materials. The remaining three chapters are dedicated to the original research conducted for this thesis. In each chapter, a single, or a family of 2D COF-based materials are designed for a specific application, then synthesized, processed, and characterized. In particular, the three experimental chapters focus on the following challenges: 1. development of a new technique for solution processing to achieve specific morphology and orientation; 2. design of a conjugated 2D COF with semiconductor properties; 3. preparation of a composite rGO-COF materials for flexible electronics.

Regardless the specific chemical structure of the building blocks and the linkage holding them together, 2D COFs are completely inert to conventional organic solvents, with the result that once synthesized they are insoluble and unprocessable, thus behaving like thermosetting polymers. Controlling the morphology during the synthesis is therefore fundamental.^[9] The most common preparation method, *i.e.* solvothermal synthesis, inherently leads to the crystallization of small particles, often of spherical shape, that aggregate to form a solid powder precipitate. For many applications, such as gas storage or catalysis, the polycrystalline powder is a suitable morphology, but for applications such as membranes, electronics, or energy storage, an ordered thin film morphology would be strongly preferred. Thus far, only a few methods have been developed for the preparation of 2D COF films. For example, interfacial polymerization allows the bottom-up synthesis of films with a desired thickness, but the established protocols are laborious and time-consuming.^[7]

In **Chapter 3** we report a new synthetic strategy for the preparation of imine-linked 2D COFs, targeting a continuous and oriented film morphology and proposing a mechanism for the material formation. Recent reports revealed that trifluoroacetic acid (TFA) present as main component or additive, is a promising solvent and catalyst for the Schiff-base reaction, at the base of the formation of imine-linked 2D COFs.^[10,11] We initially investigated the reaction between 1,3,5-tris(4-aminophenyl)benzene (TPB) and 2,5-dimethoxy terephthalaldehyde (MeOTP). By exploiting water-TFA mixtures as reaction solvent, a soluble polyimine could be synthesized at room temperature. The strong acidity of TFA prevents interlayer interactions and avoids the precipitation of the solid, up to high concentrations. Therefore, the polymer solution could be processed by drop-casting, and remarkably, upon fast solvent evaporation, a continuous polyimine (PI_m) film formed on the target substrate. The film, with a thickness of approximately 50 μm, could be easily peeled off the substrate and was

robust enough to self-stand and be manipulated without being damaged. The structural order of the films was characterized by grazing-incidence wide-angle X-ray diffraction (GIWAXS). Remarkably, the 2D diffraction pattern revealed a highly oriented, but poorly crystalline structure. The cross-sectional scanning electron microscopy (SEM) analysis supported the results by unveiling a highly layered structure, while nitrogen sorption measurements indicated that the PIm film exhibits a non-porous structure. The observed features were attributed to the formation of a highly defective covalent network, whose polymeric strands are partially aligned parallel to the surface of the substrate used for the drop-casting. Surprisingly enough, by means of a post-synthesis solvent annealing treatment an error-correction mechanism at the solid state could be introduced and could heal the defects in the structure of the covalent polymer. Therefore, upon thermal treatment the polymer crystallized to form a highly porous 2D COF, while preserving the alignment of the polymeric 2D sheets parallel to the plane of the film. These findings carry significant relevance, as they present a simple and innovative approach, for the synthesis of robust and self-standing films, with a precise control over the orientation of the polycrystalline structures. This chapter also unveils the mechanistic details related to the solution-to-solid transition, which is characterized by the formation of an intermediate 3D amorphous gel. Furthermore, the scope was extended to other imine-linked 2D COFs, containing pyrene-based building blocks as amine nodes, which demonstrates a general applicability of the method.

In **Chapter 4** we report the design, the synthesis, and the study of the (opto)electronic properties of an imine-linked 2D COF containing the electron-rich triphenyl amine and thienothiophene components. The integration of (photo)electroactive building-blocks into the skeleton of 2D COFs, along with the extended in-plane conjugation and the out-of-plane columnar stacking of the organic moieties, render these materials appealing for the application as active materials in (opto)electronics such as light-emitting devices, photoconductive devices, solar cells, organic field-effect transistors (OFETs).^[8] Triphenylamine is a thermally stable, propeller-shaped building unit which exhibits interesting photoactive and electroactive behaviors. These features are related to the stability of corresponding radical cation, easily generated by mono-electron oxidation.^[12] For these reasons triphenylamine-based 2D polymers are promising for (opto)electronic applications. Here, for the preparation of the material, we used a solvothermal approach: the tetramine *N,N,N',N'*-tetrakis(4-aminophenyl)-1,4-phenylene diamine (BTA) and the linear dialdehyde thieno[3,2-*b*]thiophene-2,5-dicarboxaldehyde (TT) were dispersed in a solvent mixture containing benzyl alcohol and mesitylene, and the reaction was catalyzed by acetic acid. After running for

three days at 120 °C we obtained a dark red powder material, and the successful polymerization was confirmed by Fourier-transform infrared spectroscopy (FTIR) and X-ray photoelectron spectroscopy (XPS). The 2D COF showed a good degree of crystallinity when measured by powder X-ray diffraction (PXRD). Moreover, the match of the diffraction pattern with those reported in the literature for other 2D COFs based on the BTA moiety and with the simulated model, allowed us to conclude that this material presents a dual-pore, Kagome-type topology with a eclipsed layers arrangement.^[13] High-resolution transmission electron microscopy (TEM) clearly indicated the polycrystalline nature of the 2D COF with a domain size of about 30 nm. By measuring and analyzing the nitrogen adsorption-desorption isotherm, we could calculate the surface area ($720 \text{ m}^2 \text{ g}^{-1}$) of the material and estimate the pore size (2.3 and 3.8 nm). In order to fully characterize the (opto)electronic properties of the conjugated 2D polymer the powder material is not suitable, so thin films of the material were fabricated. The synthesis was carried out in conditions analogue to the bulk reaction, by immersing the substrate to coat in a suspension of the monomers, with an approach called "solvothermal growth on substrate". The films were characterized by XPS and Raman spectroscopy obtaining spectra that matched with those of the bulk material, thereby confirming the successful synthesis. Atomic force microscopy (AFM) and SEM were used to analyze the nanomorphology of the thin films. A typical film is characterized by a thickness of about 90 nm and low surface roughness. Two-terminal device were fabricated by growing the film on glass substrates with pre-patterned gold interdigitated electrodes. The film exhibited a p-type semiconductor behavior with a valence band edge located at -5.1 eV, a conduction band edge at -3.0 eV, and an optical band gap of 2.1 eV. The film displayed an electrical conductivity of $\sigma = 4 \times 10^{-11} \text{ S m}^{-1}$ in vacuum and of $\sigma = 3 \times 10^{-6} \text{ S m}^{-1}$ after 20 hours in air. The conductivity could be further increased up to $\sigma = 2 \times 10^{-4} \text{ S m}^{-1}$ upon infiltration of small molecule with strong electron-acceptor properties such as 2,3,5,6-tetrafluoro-tetracyanoquinodimethane (F_4TCNQ).^[14] The difference between the conductivity in vacuum and in air was related to the tendency of the material to interact with O_2 , which caused an initial increase of the conductivity by p-doping followed by the loss of the charge transport properties upon longer exposure, likely due to irreversible (photo)oxidation reactions that disrupt the π -conjugation in the 2D polymer and the out-of-plane π overlap of the conjugated units. These results are of paramount importance, as they demonstrate that as a general rule the electron rich 2D COF must be handled with care when attempting to characterize their intrinsic conductivities as the values can vary enormously depending on the time of exposure to the atmosphere.

Finally, as proof-of-concept, the film and the powder materials were integrated in an electronic and in an energy storage device and their performances were evaluated. In particular, film was used as active channel in an OFET where the current modulation was performed by a drop of de-ionized water (water-gated transistor). The liquid dielectric switched the device volumetrically leading to a good device performance, with a modulation of the current of three orders of magnitude and a threshold voltage of $V_{th} = -0.4$ V. The powder material was tested as active electrodic material in a symmetric pseudocapacitor, using a 1 M NBu_4PF_6 solution in acetonitrile as supporting electrolyte, which exhibited a good specific capacitance of 108 F g^{-1} at 0.1 A g^{-1} , but poor stability at higher current densities.

The high surface area and the periodic arrangement of 1D pore channels and π stacks of the building units, endow 2D COFs with great potential for several applications in from sensing to energy storage.^[15] However, as we showed in the previous chapter, preparing pristine materials that display high electrical conductivities is not a trivial task. More in general, a possible approach to impart 2D COFs new properties is to combine them with other nanomaterials such as metal nanoparticles, silica, metal oxides, polymers, or carbon materials.^[16] While the preparation and the properties of several pristine 2D COF materials are well established, their use as matrix to disperse other nanomaterials is still poorly investigated. In **Chapter 5**, we show the synthesis, characterization, and investigation of a potential application of a novel conductive composite material in the film morphology consisting of conductive reduced graphene oxide (rGO) and a non-conductive 2D COF. For the synthesis and processing of the material in the film morphology, we applied a modified version of the method used in the first project, *i.e.* the polymer solution casting method. Graphene oxide (GO) was used as precursor of rGO for the preparation of the composite. Thanks to its polar functional groups, GO is typically easily dispersible in organic solvents, so we used it as additive at the 4 % in mass in the solution of the polyimine. The suspension of the mixed materials was drop-casted and upon drying a film with a thickness of approximately $50 \mu\text{m}$ was obtained. The combination of an amine-functionalized GO and octyloxy-functionalized polyimine as precursors was found to lead to an optimal compatibilization of the two nanostructured materials. Subsequently, recrystallization and thermal annealing were carried out to produce a conductive composite film. Remarkably, the films manifested an asymmetry in their conductive properties, with one side of the film exhibiting a sheet resistance of $R_s = 1.3 \times 10^5 \Omega \text{ sq}^{-1}$, and the other being electrically insulating. This feature, coupled with the mechanical flexibility and durability, made the material suitable for flexible electronics. Specifically, we showed that the films could serve as piezo-resistive strain sensors, as their inherent resistivity varies

depending on the type and intensity of the stress applied (compressive or tensile).

In conclusion, in this thesis we attempted to tackle some open challenges in the development of 2D COF materials with tailored properties. The results that we report have the potential to offer a new perspective on the design and synthesis of 2D COFs. In particular, we focused on the control of morphology developing a new method to prepare large-area oriented films, which are strongly desired for improving the performances of these materials in applications such as filtration membrane, energy storage, and semiconductors. Moreover, we showcased two different methods to boost the electrical performance of 2D COFs namely, by engineering the functional moieties in the backbone of the 2D polymer or by blending the material with conductive rGO. Our findings represent a solid reference for the scientific community that, in our view, will promote the development of new synthetic methods and new designs into the world of functional 2D COFs.

Symbols and abbreviations

Symbols

A: absorbance
C: capacitance
 C_0 : functional group concentration
d: channel depth
E: potential
 E_g : band gap
f: functionality
 g_m : transconductance
H: enthalpy
 H_0 : Hammett acidity function
i: current
k: kinetic constant
 K_{eq} : equilibrium constant
K: equilibrium constant
L: channel length
r: radius
p: pressure, extent of reaction
 p_0 : saturation pressure
R: resistance
r: radius
 R_s : sheet resistance
S: entropy
t: time
t: thickness
T: temperature
t: thickness
 $t_{1/2}$: half-life
V: voltage
W: channel width
[X]: concentration
% v: volumetric percentage
% wt: weight percentage
 δ : chemical shift
 Φ : work function
 ϵ : strain
 σ : conductivity
 λ : wavelength
 μ : mobility
 ν : frequency
 ρ : conductivity
 τ : time constant
 θ : angle of incidence
 \bar{X}_n : number average degree of polymerization

Abbreviations:

AC: alternating current
AFM: atomic force microscopy

An: aniline
ATR: attenuated total reflection
BDBA: 1,4-benzenediboronic acid
BE: binding energy
BET: Brunauer-Emmett-Teller
BFBAPy: 1,6-bis(4-formylphenyl)-3,8-bis(4-aminophenyl)pyrene
COF: covalent organic framework
CT: charge transfer
CV: cyclic voltammetry
CMP: conjugated microporous polymer
DC: direct current
DCM: dichloromethane
DMF: dimethylformamide
DRS: diffuse reflectance spectroscopy
EDA: ethylene diamine
BnOH: benzyl alcohol
BTA: N,N,N',N'-tetraphenyl-1,4phenylenediamine
BJH: Barrett-Joyner-Halenda
EDX: energy-dispersive X-ray spectroscopy
EES: electrochemical energy storage
EIS: electrochemical impedance spectroscopy
EtOH: ethanol
FET: field-effect transistors
FFT: fast Fourier transform
FID: free-induction decay
FPP: four-point probe
FTIR: Fourier-transform infrared spectroscopy
FWHM: full-width at half-maximum
F₄TCNQ: 2,3,5,6-tetrafluoro-tetracyanoquinodimethane
GCD: galvanostatic charge-discharge
GF: gauge factor
GISAXS: grazing-incidence small-angle X-ray scattering
GIWAXS: grazing-incidence wide-angle X-ray scattering
GO: Graphene Oxide
HOAc: acetic acid
HOMO: highest occupied molecular orbital
HOPG: highly oriented pyrolytic graphite
HTTP: 2,3,6,7,10,11-hexahydroxytriphenylene
KE: kinetic energy
IE: Ionization Energy
IR: infrared spectroscopy
ITO: Indium-Tin Oxide
LB: Langmuir-Blodgett
LED: light-emitting diode
LUMO: lowest unoccupied molecular orbital
MeCN: acetonitrile
MeOH: methanol
MeOTP: 2,5-dimethoxy terephthalaldehyde
MOF: metal-organic frameworks
NIR: near infrared
NLDFT: non-local density functional theory

NMP: N-methyl-2-pyrrolidone
NMR: nuclear magnetic resonance
OctOTP: 2,5-dioctyloxyterephthalaldehyde
o-DCB: ortho dichlorobenzene
OER: oxygen evolution reaction
OFET: organic field-effect transistor
OPR: one-pot reaction
ORR: oxygen reduction reaction
OSC: organic semiconductor
PI_m: polyimine
PSM: post-synthesis modification
PTSA: *p*-toluene sulfonic acid
PXRD: powder X-ray diffraction
PVDF: polyvinylidene fluoride
P3HT: poly(3-hexyl-thiophene-2,5-diyl
QSDFT: quenched-solid density functional theory
rGO: reduced graphene oxide
SEM: scanning electron microscopy
SMAIS: surfactant monolayer assisted interfacial synthesis
SMU: source measure unit
STP: standard pressure and temperature
TBPM: tetra(4-dihydroxyborylphenyl)methane
TBPS: tetra(4-dihydroxyborylphenyl)silane
TEA: triethylamine
TEM: transmission electron microscopy
TFA: trifluoroacetic acid
TGA: thermogravimetric analysis
THF: tetrahydrofuran
TMDC: transition-metal dichalcogenides
TMS: tetramethylsilane
Tp: 1,3,5-triformylphloroglucinol
TP: terephthalaldehyde
TPB: tris(4-aminophenyl)benzene
TPPy: 1,3,6,8-Tetrakis (4-aminophenyl) pyrene
TSMCN: trimethylsilyl cyanide
TT: thieno[3,2-*b*]thiophene
UV-Vis: ultraviolet-visible
XPS: X-ray photoelectron spectroscopy
1D: one-dimensional
2D: two-dimensional
3D: three-dimensional

Table of contents

1.	Introduction to the thesis.....	1
1.1.	Motivations and aims of the thesis	1
1.2.	Synthetic polymers: from the origin to 3D porous architectures	2
1.3.	Covalent Organic Frameworks	3
1.4.	Chemistry of the Linkages	5
1.5.	Conversion and locking of the imine linkage.....	8
1.6.	Structural and chemical diversity in 2D COFs.....	13
1.7.	Synthesis and morphology control.....	18
1.7.1.	Synthesis of COF powders	19
1.7.2.	Synthesis of COF films	21
1.8.	2D COF composites.....	25
1.9.	Properties and Applications of 2D COFs.....	26
1.9.1.	Gas storage and separation.....	27
1.9.2.	Liquid-phase molecular and ionic separation	28
1.9.3.	Chemical sensing	28
1.9.4.	Catalysis.....	28
1.9.5.	Optoelectronics	29
1.9.6.	Electrochemical energy storage	30
2.	Experimental tools for the characterization of 2D COFs.....	32
2.1.	Chemical characterization	32
2.1.1.	Fourier-Transform Infrared Spectroscopy (FTIR)	32
2.1.2.	Nuclear Magnetic Resonance (NMR)	33
2.1.3.	X-ray Photoelectron Spectroscopy (XPS).....	34
2.1.4.	Thermogravimetric analysis (TGA)	35
2.1.5.	Raman Spectroscopy	36
2.2.	Structural Characterization	36
2.2.1.	Powder X-ray Diffraction (PXRD).....	36
2.2.2.	Structural simulations and refinements.....	38
2.2.3.	Grazing-Incidence Wide-Angle X-ray Scattering (GIWAXS).....	39
2.2.4.	Gas sorption measurements	39

2.3.	Morphological Characterization	41
2.3.1.	Scanning Electron Microscopy (SEM)	41
2.3.2.	Transmission Electron Microscopy (TEM)	42
2.3.3.	Atomic Force Microscopy (AFM)	42
2.4.	Optoelectronic and Electrochemical characterization	43
2.4.1.	UV-vis absorption spectroscopy.....	43
2.4.2.	Charge transport measurements	44
2.4.3.	Electrochemical impedance spectroscopy (EIS)	45
2.4.4.	Cyclic voltammetry	46
3.	Kinetic suppression of nucleation enabling strain crystallization of oriented self-standing 2D COF films	48
3.1.	Oriented and self-standing 2D COF films	48
3.2.	Synthesis by polymer solution casting	50
3.2.1.	Synthesis of an oriented PIm film.....	51
3.2.2.	Morphological and structural characterization.....	53
3.2.3.	Chemical characterization	56
3.3.	Non-porous PIm to oriented COF.....	58
3.3.1.	Solvent annealing (recrystallization)	58
3.3.2.	Morphological and structural characterization.....	59
3.3.3.	Chemical characterization	63
3.4.	Mechanism of the reaction in solution	65
3.4.1.	The sol-gel transition.....	66
3.4.2.	Characterization of the gel	67
3.4.3.	Step-growth polymerization of PIm	68
3.4.4.	Thermodynamic parameters.....	73
3.4.5.	The role of the solvent	75
3.4.6.	Kinetic considerations	76
3.5.	Structural evolution during gel consolidation	82
3.5.1.	A plausible mechanism: evaporation-dependent strain crystallization.....	82
3.5.2.	Microfluidic flows in a drying sessile polymer droplet.....	83
3.5.3.	Morphological evolution of the drying polymer	84

3.5.4.	Structural evolution of the drying polymer	88
3.5.5.	The effect of the evaporation rate	90
3.6.	Scope of the method	95
3.7.	Conclusions and perspectives	99
3.8.	Materials and methods	101
4.	Design of an electron-rich imine-based 2D COF for optoelectronics and energy storage.....	105
4.1.	Introduction.....	105
4.2.	Results and discussion	108
4.2.1.	Solvothermal synthesis of BTA-TT-COF	108
4.2.2.	Structural and morphological characterization of BTA-TT-COF	109
4.2.3.	Chemical characterization of BTA-TT-COF.....	113
4.2.4.	Direct growth of BTA-TT-film in solvothermal conditions.....	117
4.3.	Optoelectronic properties of BTA-TT-COF and film	122
4.3.1.	Energy levels.....	122
4.3.2.	(Photo)conductivity and molecular doping.....	124
4.4.	Proposed applications for BTA-TT-COF and film	129
4.4.1.	Active material in organic field effect transistor	129
4.4.2.	Symmetric pseudocapacitor	130
4.5.	Conclusions and perspectives	134
4.6.	Materials and methods	135
5.	Functionalized reduced graphene oxide as nanofiller for an asymmetrically conductive COF composite film.....	138
5.1.	Introduction on COF composite materials and applications.....	138
5.2.	Synthesis and characterization of the GO-COF composite	140
5.2.1.	Synthesis of the GO-PIIm composite	140
5.2.2.	Functionalization of GO with ethylene diamine (EDA).....	142
5.2.3.	Synthesis of the GO _{EDA} -PIIm composites	144
5.2.4.	Characterization of the GO _{EDA} -PIIm _{Oct} composite and recrystallization to GO _{EDA} -COF _{Oct}	146
5.3.	Thermal Reduction and Conductivity Measurements.....	151

5.4.	Strain sensing.....	155
5.5.	Conclusion and Perspectives	157
5.6.	Experimental section	159
6.	Conclusion and outlook.....	162
7.	References.....	167

1. Introduction to the thesis

1.1. Motivations and aims of the thesis

Two-dimensional covalent organic frameworks (2D COFs) are layered, crystalline, and permanently porous solids which can be regarded as being currently the most studied class of 2D polymers.^[4] While the single macromolecular unit consists of a fully covalently linked sheet (which is often π -conjugated), the overall bulk structure of these materials comprises a regular alternation of columnar π -arrays of building units and 1D pore channels. Due to the innovative structural features and the flexibility in terms of type of linkage and building blocks, these materials have received ever growing attention in the past 18 years. They have been proposed for applications in various fields, including catalysis, sensing, (opto)electronics, electrochemical energy storage, molecular and gas separation, and gas storage.^[17] Despite the advancements, the design and synthesis of 2D COFs continue to present a range of significant challenges and unresolved questions. Among these obstacles some are particularly noteworthy, including the development of new types of linkages seeking for the right balance between reversibility, stability, and functionality,^[6] the production of single-crystalline samples,^[18] the simultaneous tuning of the morphology and the crystallinity of the solid materials,^[7] and the manipulation of their optoelectronic properties.^[8]

In this context, the general objective of this thesis is to develop functional 2D COFs-based materials with tailored physico-chemical properties and characterize them at multiple length scales, toward their integration as active materials in sensing, electronic, and energy storage devices. The main focus is on the preparation of materials in the film morphology, which is ideal for the investigation of the properties. Moreover, the development of large-area oriented films, is strongly desired for improving integration and the performances of 2D COFs in applications such as filtration membrane, energy storage, and optoelectronics. The first experimental chapter (**Chapter 3**) describes an innovative method for preparing large-area, self-standing, mechanically robust, and structurally oriented films. In the following two chapters (**Chapter 4** and **Chapter 5**) the focus on the application-oriented design of conductive materials. In particular, in **Chapter 4** a 2D COF was designed to include known electroactive building blocks in its polymeric backbone and its optoelectronic properties were investigated toward the application as active material in field-effect transistors (FETs) and electrochemical energy storage (EES) devices. In **Chapter 5** an innovative composite-material approach is

used to transform a non-conductive, but self-standing and mechanically robust 2D COF film into an asymmetrically conductive material that could be implemented in a strain sensor device. In conclusion, the reported results hold the potential to become a solid reference for the scientific community working of new synthetic methods and new designs in functional 2D COFs.

1.2. Synthetic polymers: from the origin to 3D porous architectures

The discovery of synthetic polymers constitute one of the most significant breakthroughs in chemistry of the past 100 years.^[19] Their development has revolutionized almost every aspect of modern life, enabling the preparation of materials with a wide range of applications and effectively driving the human civilization into a new era, known as “age of plastic”.^[20] Modern synthetic polymer science was born in the early 19th century, when Baekeland reacted formaldehyde with phenol at controlled pressure and temperature, obtaining the first completely synthetic polymer, poly-phenol-formaldehyde, commercially known as Bakelite.^[21] However, despite the progress in polymer synthesis, the molecular structure of polymers remained poorly understood until the 1920s when Staudinger proposed the concept of polymers consisting of long sequences of atoms linked by covalent bonds.^[22] Carothers further advanced the field of polymer chemistry with his work on polycondensation, which led to the development of numerous polyamides and polyesters.^[23] Carothers also showed that the rational selection of the component monomers can be used to modify the properties of polymers, fact that paved the way to the rapid advancements in the field of functional materials. Thanks to the discovery of catalysts based on transition metals, Natta and Ziegler enabled the efficient synthesis of various polyolefins, which represent today the most common class of commodity chemicals in the world.^[24] Although one-dimensional (1D) polymers have been very successful, researchers developed also more complex three-dimensional (3D) macromolecular architectures such as star-branched, comb-branched hyper-branched, cross-linked, dendritic polymers.^[19] A special class of polymers with a 3D architecture is constituted by conjugated microporous polymers (CMPs).^[25] CMPs are characterized by an amorphous hyper-branched architecture that results from random interconnection of conjugated building blocks. In reason of their rigid skeletons, CMPs possess unique permanent microporosity due to voids within their structure that can be accessed by guest molecules and vary in size and shape. They typically exhibit high surface areas with many poten-

tial applications, including gas storage and separation, as well as heterogeneous catalysis.^[26]

1.3. Covalent Organic Frameworks

A novel class of porous polymeric materials was introduced in 2005 by Coté, Yaghi and coworkers.^[3] In contrast with CMPs, the new materials consisted of crystalline, covalently linked 2D or 3D extended organic solids and were named “covalent organic frameworks” (COFs). COFs can be considered as fully organic equivalents of metal organic frameworks (MOFs),^[5] as they are composed only of organic building blocks. As a result, they are light-weight materials mostly constituted by carbon and hydrogen, but also containing heteroatoms such as nitrogen, oxygen, boron, and sulfur.^[5] COFs are porous materials that exhibit a modular construction, leading to an almost infinite range structural and chemical configurations, making them ideal candidates for a diverse range of applications, such as gas adsorption and separation, liquid-phase membranes, catalysis, ionic conduction, sensing, optoelectronic, energy storage.^[17]

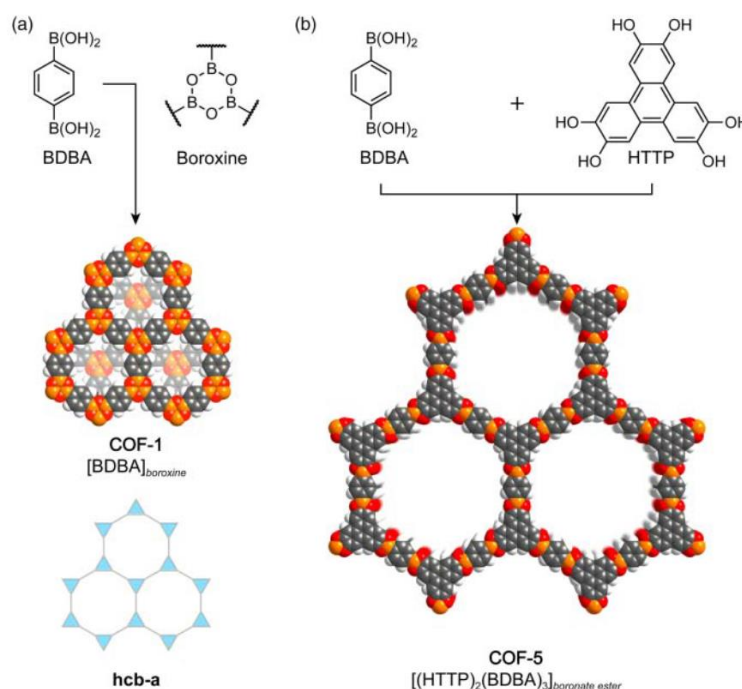


Figure 1.1 Reaction scheme for the preparation of the first two COFs. **(a)** Boroxine-linked COF-1 prepared by self-condensation of BDBA. **(b)** Catechol boronate ester-linked COF-5 prepared by polymerization of BDBA with HHTP. Both materials exhibit a honeycomb hcb topology. Reproduced with permission from ref.^[5]

COFs are synthesized through the covalent bonding of polyfunctional organic monomers, resulting in a crystalline polymer. COF-1 and COF-5 were the first two examples of COFs and were synthesized using boronic acid-based polycondensation.^[3] Namely, COF-1 was prepared by self-condensation reaction of BDBA (1,4-benzenediboronic acid) to form a boroxine ring linkage while COF-5 was obtained from a combination of BDBA and HHTP (2,3,6,7,10,11-hexahydroxytriphenylene) through the formation of catechol boronate ester bond (**Figure 1.1**).

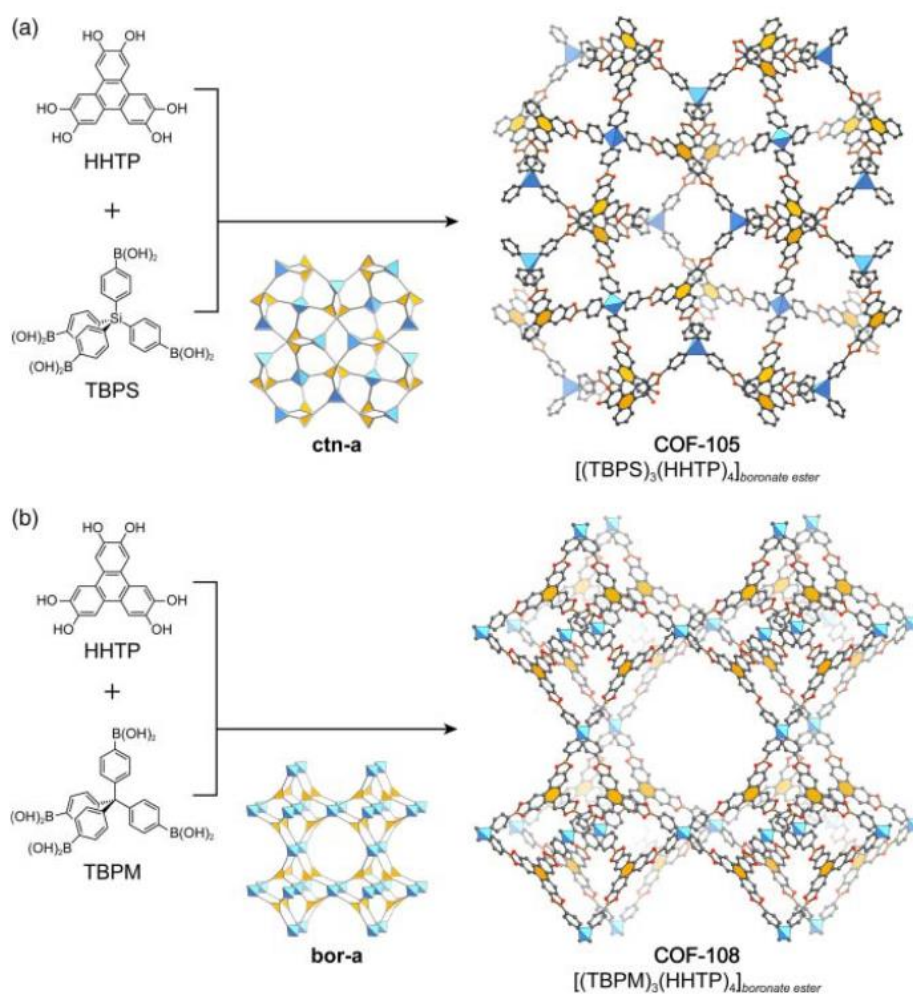


Figure 1.2 Reaction scheme for the preparation of the first 3D COFs. **(a)** Boronate ester-linked COF-105 prepared by polymerization of TBPS with HHTP (cnt topology) **(b)** Boronate ester-linked COF-108 prepared by polymerization of TBPM with HHTP (bor topology). Reproduced with permission from ref.^[5]

COF-1 and COF-5 exhibit high thermal stability and permanent porosity and crystallinity. They are described as 2D COFs as their extended covalent structure is entirely confined with-

in molecular-thick layers, stacked in the third dimension by out-of-plane π - π interactions and van der Waals forces. In both cases, the defined and rigid geometry of the building blocks and the connecting linkage induces the formation of a 2D polymer with a honeycomb hcb topology.

Soon after the first reports on 2D COFs, Yaghi, El-Kaderi, and colleagues demonstrated that through the same chemistry it is possible to expand the ordered covalent network in the third dimension.^[27] While, 2D COFs commonly feature rigid aromatic building blocks that promote the formation of stacked layers, for 3D frameworks, polyhedral monomers must be employed. By introducing tetrahedral tetratopic building blocks, such as TBPM (tetra(4-dihydroxyborylphenyl)methane) and TBPS (tetra(4-dihydroxyborylphenyl)silane) the authors were able to synthesize the first crystalline 3D COFs by cross-condensation with HHTP, obtaining COF-108 and COF-105, respectively (**Figure 1.2**). Moreover, it was shown that by self-condensation (boroxine ring formation) of TBPM or TBPS could also afford crystalline the single-component COF-102 or COF-103, respectively.

The crystallization of such ordered structures is made possible by the accurate choice of the building blocks, linkage chemistry, and reaction conditions. In contrast to kinetically controlled polymer synthesis, where irreversible covalent bond formation occurs, COFs are synthesized through partially reversible reactions that enable a self-correction mechanism of the structural defects. Indeed, the condensation reactions leading to the formation of boroxine and catechol boronate esters are known to exhibit high reversibility under thermodynamic conditions, which involve maintaining the reaction system at elevated temperatures and retaining the condensation by-product (H_2O).^[28]

1.4. Chemistry of the Linkages

In the 18 years of research since the discovery of the first COFs, the field has witnessed an impressive growth in the diversity of chemistry used for the polymerization and crystallization of these structures (**Figure 1.3**). Due to the tendency of most covalent bonds to form irreversibly under mild conditions, their use as linkages for the construction of crystalline frameworks presents a particular challenge known as the “crystallization problem”. As a general rule, the synthesis of COFs can be achieved through polycondensation reactions that involve the elimination of a small by-product, often water, which must be retained in the reaction mixture. Moreover, the linkages between the individual building blocks must be reversible and formed at a sufficient rate to enable an error self-correction mechanism and

obtain extended crystalline solids. This is typically achieved through the help of a catalyst and by increasing the temperature and the pressure of the reaction mixture. However, the organic molecular building blocks must maintain their structural integrity throughout the polymerization process. As a result, specific reaction conditions must be established for each new linkage and each new building-block, simultaneously allowing for reversible bond formation without relying on extreme temperatures or pressures, which might degrade the organic monomers.

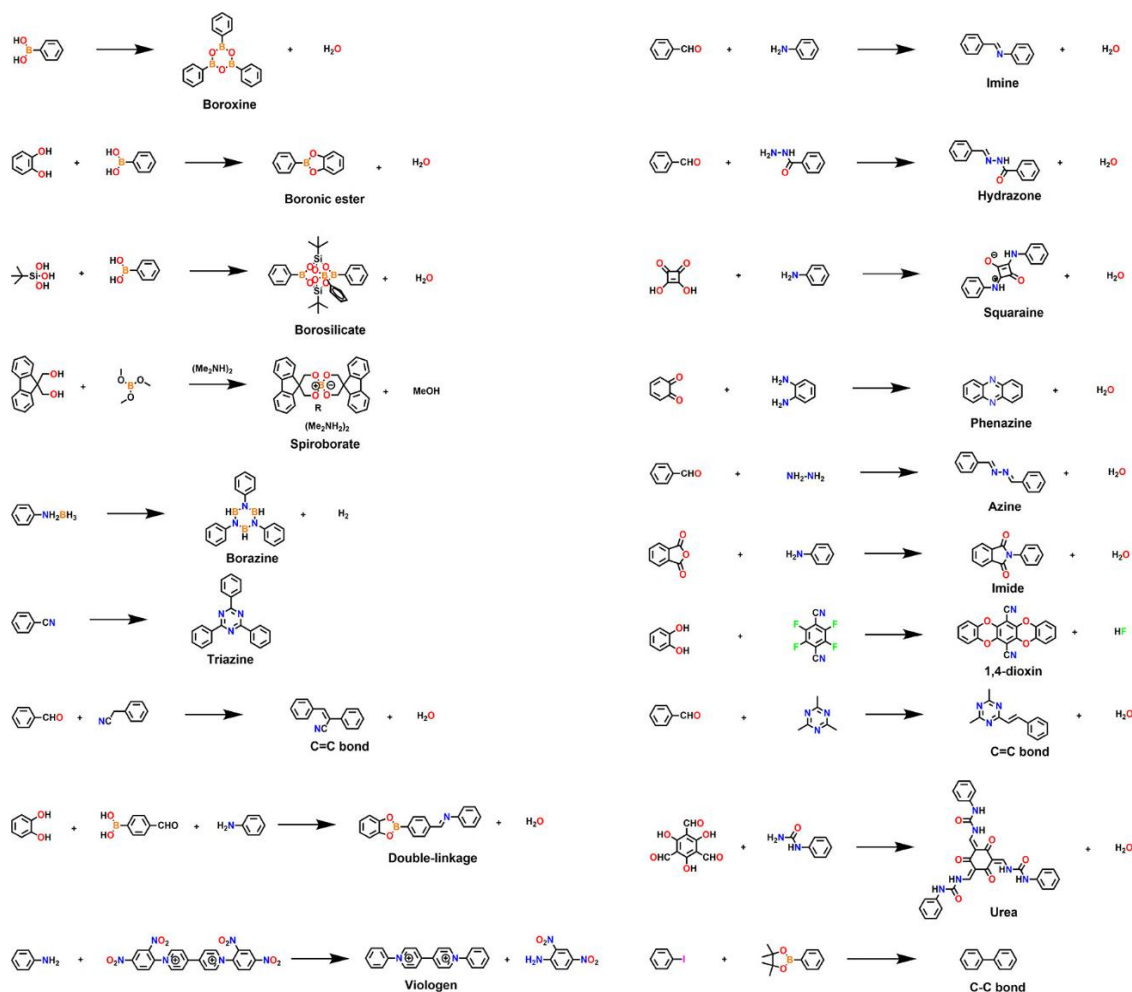


Figure 1.3 List of the various type of linkages used to prepare COFs. Reproduced with permission from ref.^[4]

As mentioned earlier, boroxines and catechol boronate esters were the first linkages to be developed and have been widely used ever since.^[28] The dynamic formation of boroxines and catechol boronate-ester can occur under a variety of reaction conditions (solvents, temperatures), allowing for the integration of a wide range of monomers into these networks. Furthermore, the high reversibility of these linkages allow to access single-crystalline mate-

rials.^[18,29] However, COFs held together by these linkages suffer from hydrolytic instability in presence of water (even as moisture), which is also intrinsically correlated with the high reversibility of the covalent bonds. The consequent trade-off between stability and crystallinity is a generally observed dichotomy in COFs, and for this reason, simultaneously obtaining a stable and highly crystalline material has become a central challenge in the field.^[6] In this direction, great effort has been devoted in developing new types of linkages seeking for the right balance between the two properties (**Figure 1.3**).

In 2009, Yaghi, Uribe-Romo, and coworkers introduced a new linkage motif based on the Schiff base reaction of amines and aldehydes to form an imine, marking the beginning of the development of a new category of COFs with nitrogen-based linkages.^[30] The first application of the dynamic imine formation involved the preparation of COF-300, a 3D framework formed through the condensation of tetra-(4-anilyl)methane and TP (terephthalaldehyde).^[30] This breakthrough was quickly followed in 2011 by a study that demonstrated the capacity of dynamic imine chemistry to produce periodic 2D networks, as Wang, Ding, and colleagues condensed 1,3,5-triformylbenzene and 1,4-diaminobenzene to produce a crystalline 2D COF (COF-LZU1).^[31]

Despite its easily reversible formation, the imine linkage offers better stability compared to the boron-based linkages.^[32] Chemists have explored further types of linkages based on the reversibility of the Schiff base reaction, such as hydrazone,^[33] azine,^[34] squaraine,^[35] β -ketoenamine,^[36] phenazine,^[37] oxazole,^[38] salen,^[39] and amina^[40] (**Figure 1.3**). However, in spite of the great variety of Schiff base linkages available the use of the simple imine bond has remained the most popular approach for the synthesis of 2D and 3D COFs.^[41] Schiff base reactions for the synthesis of COFs are generally conducted in the presence of an acid catalyst.^[42] The mechanism of the reaction begins with the protonation of the aldehyde which activates the carbonyl carbon for the nucleophilic attack of the amine to form a protonated hemiaminal. The tetrahedral intermediate undergoes intramolecular proton transfer and eliminates water to yield the target Schiff base (**Figure 1.4**). All the reaction steps are virtually reversible, provided that the water by-product is retained in the reaction mixture.

In parallel to the mentioned Schiff base and boronic acid-based reversible linkages, other chemistries have been developed for the crystallization of COFs, such as the triazine^[43] and borazine^[44] ring formations, imide,^[45] viologen,^[46] vinylene,^[47] amide,^[48] thianthrene,^[49] and dioxin,^[50] expanding the scope of COF synthesis. However, imine-linked 2D COFs represent the most widely synthesized and studied class of COF due to their crystallinity, the formal conjugation of their backbone and their robustness. Moreover, the experimental work per-

formed in this thesis directly involves this specific class of materials. For these reasons the next sections of the introduction focus mainly on imine-linked 2D COFs.

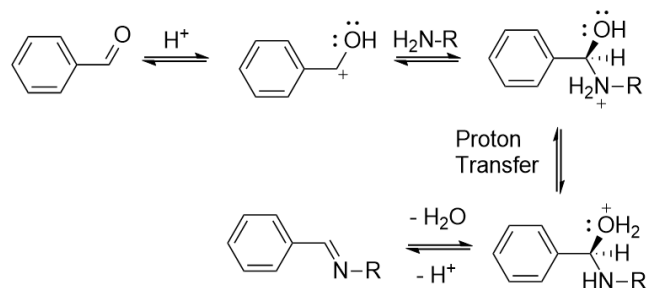


Figure 1.4 Mechanism for the acid-catalyzed Schiff-base showcased for the reaction between benzaldehyde and a primary amine.

1.5. Conversion and locking of the imine linkage

Despite the improved stability of the imine linkage compared to its boron-based equivalents, its robustness is challenged under harsh conditions, such as those involving strong acids, bases, or redox agents.^[51] Additionally, studies indicate that imine-linked 2D COFs are generally less thermally stable than their boronate-ester-linked counterparts.^[52] Consequently, such materials are not yet mature for industrial applications, such as catalysis, gas storage, or gas separation, which might involve the exposure of the material to a range of reactive species and severe physical conditions.^[53,54]

2D π -conjugated COFs are also receiving considerable attention due to their potential for use in electronic and electrochemical energy storage devices.^[55] These materials are predicted to possess semiconducting properties with highly customizable electronic properties.^[56] Despite the incorporation of (photo)electroactive units, such as porphyrins, pyrenes, thiophenes, and phthalocyanines, into the COF structure, 2D imine COFs exhibit limited in-plane π -conjugation owing to the inherent polarization of the C=N bond.^[57,58] Consequently, new methods to enhance the in-plane π -conjugation are highly desired.

This section is based on a Minireview that we published on *Angewandte Chemie* as a part of the work of the first year of the doctoral studies.^[59] It provides an outline of the various options available for the stabilization and functionalization of the imine bond in 2D COFs through chemical approaches.

The main strategy for enhancing the stability of the imine bond involves a reversible-

irreversible covalent reaction sequence that utilizes dynamic imine chemistry as the reversible step. This sequence produces crystalline 2D COFs with new linkages, ultimately resulting in kinetically blocked and chemically robust COFs. Moreover, specific synthetic strategies can lead to an improved in-plane π -conjugation or introduce additional functionalities, which confer novel physicochemical properties on the resulting COFs.

The strategies for the chemical locking of the imine linkage can be classified into two different categories: one-pot reactions and post-synthesis modifications (**Figure 1.5**). In one-pot reactions (OPRs), the formation of an irreversible bond is achieved by a series of reactions that occur at the same time as the crystallization. Self-locking linkages can be created by designing monomers with functional groups that undergo a second reaction after forming an imine bond. Another possibility is using a multi-component approach where a third component present in the reaction mixture triggers the locking reaction and becomes integrated into the linkage structure.

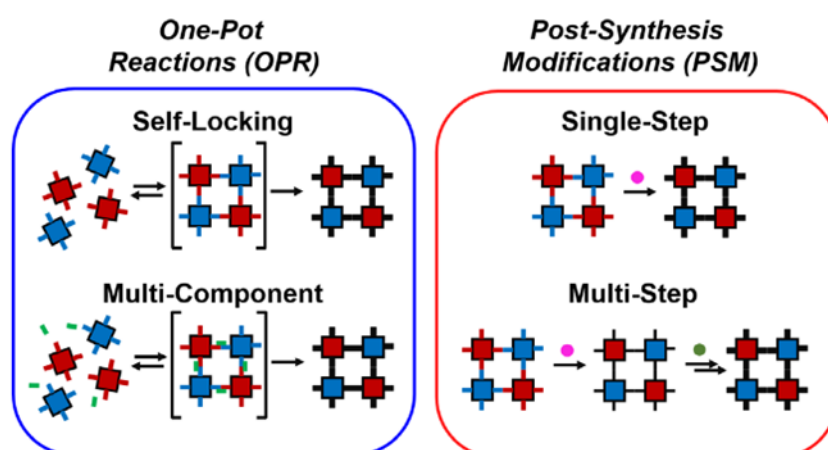


Figure 1.5 Classification of the approaches used for the locking of the imine bond: one-pot reactions (self-locking and multi-component) and post-synthesis modifications (single- and multi-step). Reproduced with permission from ref.^[59]

In OPRs, the reversible and irreversible steps are often entangled, which can compromise the crystallinity of the material. Meanwhile, the use of a post-synthesis modification (PSM) strategy enables the reversible imine formation and locking reaction to be completely separated. The crystalline imine COF is first synthesized and isolated conventionally. Only in the subsequent step, the C=N linkage is chemically converted into more functional and robust moieties via a solid-state reaction. Multi-step synthetic modifications have also been reported, allowing for the introduction of complex functionalities.

Self-locking OPRs involve reversible formation of imine followed by irreversible tautomeri-

zation or cyclization, which is typically triggered by reactive functional groups in the ortho-position of one or both monomers (**Figure 1.6a**). The most used self-locking OPR is the β -ketoenamine formation. First introduced by Banerjee and co-workers in 2012, it involves the reaction of an amine monomer with the 1,3,5-triformylphloroglucinol (Tp) trifunctional building block which induced the quantitative tautomerization of the enol-imine to the more robust keto-enamine form. The material exhibited a substantial stability improvement, in particular upon exposure to extremely acid environments. If the amine building block is functionalized with a nucleophilic group in the ortho-position, the reaction sequence involving imine formation and oxidative cyclization can be easily initiated in the presence of an oxidant. Hydroxyl (-OH), and amine (-NH₂) functional groups have been used and lead to the preparation of benzoxazole,^[60] and benzimidazole-linked COFs.^[61] A similar approach involves the reaction between a α -diketone and an α -diamine to form a stable and aromatic phenazine linkage through two consecutive condensations.^[62] The resulting materials exhibit high chemical stability and due to the aromatic stabilization of these linkages, furthermore they display promising improvement of the in-plane π -conjugation.^[60,63]

Multi-component OPRs involve the addition of a third component to the classical Schiff base reagents to create a linkage with improved stability and / or functionality (**Figure 1.6b**). Benzothiazole-linked COFs can be prepared from simple amine and aldehyde building blocks by adding elemental sulfur and an oxidant to the reaction mixture. In these conditions the imine bonds initially form and are then irreversibly cyclized to create high surface area, thermally and chemically stable benzothiazole-linked COFs.^[64] Another method using the Debus-Radziszewski reaction was reported to form benzimidazole-linked COFs with modest crystallinity and surface area, but high stability. The method involves the multicomponent reaction of a 1,2-diketone, an aldehyde, and ammonia.^[65] The Strecker reaction was used to create a stable α -aminonitrile-linked COF by adding trimethylsilyl cyanide (TSMCN) in presence of BF₃·OEt₂.^[66] Furthermore, by adding styrene, BF₃·OEt₂, and an oxidant, the aza-Diels-Alder reaction can be performed *in-situ*, converting reversible C=N linkages into robust and conjugated quinoline moieties.^[66] Finally, a multi-component OPR, known as A³-coupling reaction (aldehyde-alkyne-amine), was used to prepare a chiral propargylamine-linked COF.^[67]

The high and accessible surface area allows reactive chemical species to diffuse inside the pores and interact with bulk of the material and not only with its surface. Taking advantage of this feature, a series of PSMs at the solid state have been developed targeting the transformation of the linkage of imine COFs into stable and / or functional moieties, such as benzoxazoles, quinolines, and amides (**Figure 1.6c**).

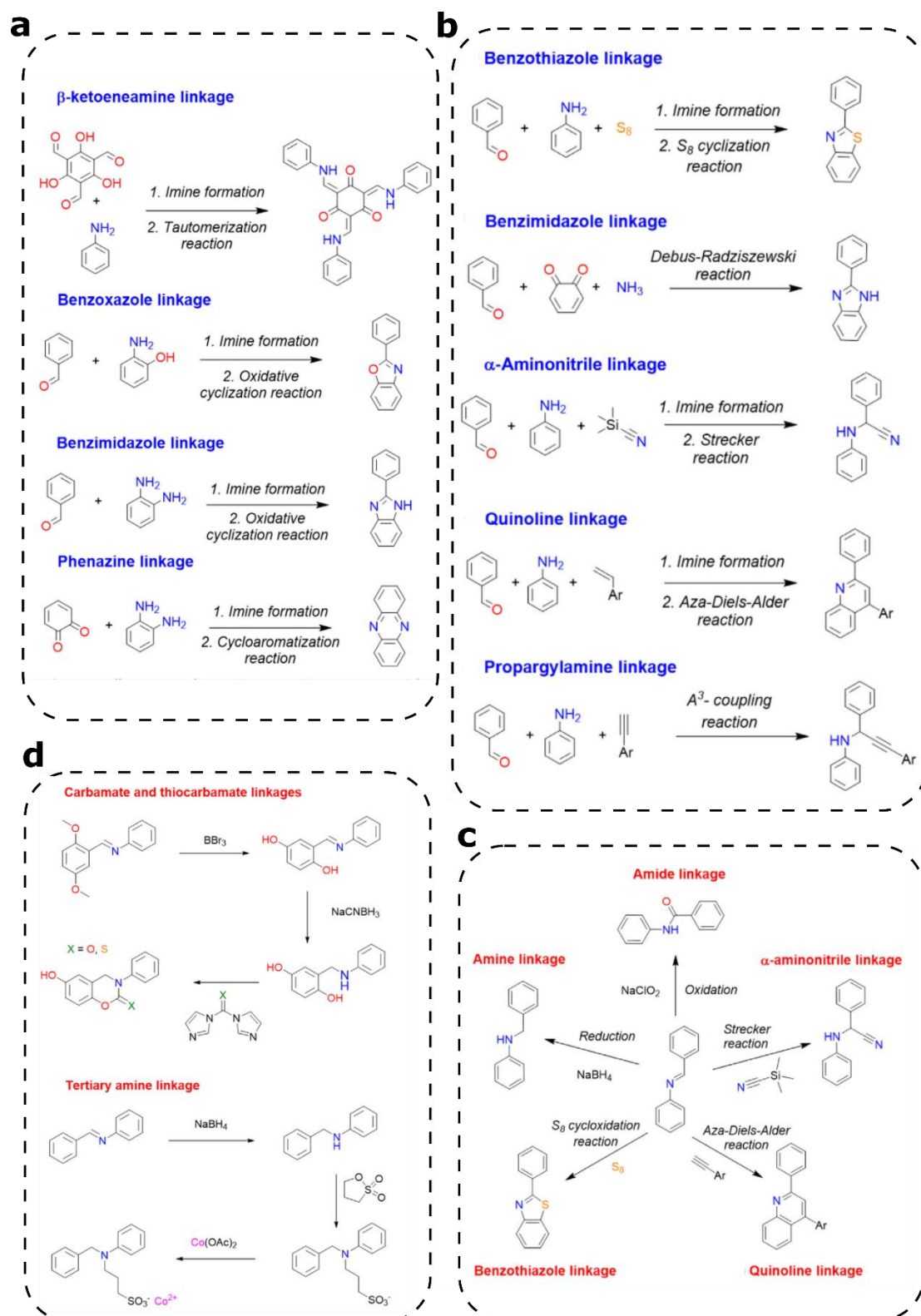


Figure 1.6 (a) List of the different types of self-locking OPR. (b) List of the different types of multi-component OPR. (c) List of the different types of single-step PSM. (d) List of the different types of multi-step PSM. Reproduced with permission from ref.^[59]

For example, the imine C=N bond can undergo direct oxidation to amide or direct reduction to secondary amine using suitable redox agents, which can be employed in solid-state synthesis to create kinetically stable amine- and amide-linked COFs. The reduction of the imine bond to a secondary amine was successfully achieved by PSM reaction of COF-300 and COF366-M with NaBH₄ in methanol in presence of terephthalic acid, resulting in minor changes in lattice parameters but improved chemical stability.^[68] Direct oxidation of the C=N bond using sodium chlorite was also applied to transform imine-linked COFs to isostructural amide-linked COFs, which demonstrated retention of crystallinity upon modification and higher stability toward the exposure to aqueous acid and basic environments.^[69]

The conversion of imine linkages in COFs to quinoline-linked COFs with extended π -electron delocalization is possible through reaction with aryl-alkynes or aryl-alkynes. This reaction can be carried out using both OPR and PSM methods. The PSM method involves the reaction of the pre-synthesized imine COF with phenylacetylene at 110 °C in the presence of BF₃·Et₂O and chloranil in toluene. The high crystallinity is preserved after the modification material was obtained, and stability upon exposure to aggressive chemicals was substantially enhanced, however the reaction is not quantitative, reaching a maximum of 20 - 30% conversion of the imine groups.^[51] The improvement of the π -electron delocalization resulted in a reduced optical bandgap of the modified materials.

A PSM version of the Strecker synthesis is also possible at the solid-state to modify imine-linked COFs. The reaction was carried out using TMSCN as the cyanide ion source and BF₃·Et₂O in toluene.^[66] Compared to the OPR route, the PSM method resulted in an α -aminonitrile-linked COF with slightly lower degree of crystallinity.

A further method for modifying pre-synthesized imine COFs consists in reacting them with elemental sulfur, to yield their respective benzothiazole-linked COFs. The molten reactant is infiltrated into the COF at 155 °C, and the temperature is raised to 350 °C, resulting in the conversion of the linkage from imine to benzothiazole.^[70] The improved stability of the modified materials induced enhanced endurance to high energy TEM electron-beam and improved contrast, allowing the study of structural defects of the material such as grain boundaries. The proposed mechanism involved the nucleophilic attack of the elemental sulfur to the imine carbon, forming an intermediate thioamide group which then undergoes oxidative cyclization to thiazole ring while reducing the elemental sulfur to H₂S.

In some cases, multi-step solid state reactions have been reported, allowing for the creation of complex functionalities while preserving the overall framework connectivity. Yaghi *et al.* demonstrated the feasibility of a multi-step PSM approach to the synthesis of complex

cyclic carbamate- and thiocarbamate-linked COFs, starting from imine-linked COF-170.^[71] In the first step the methoxy groups side groups were demethylated using BBr_3 , then the reduction of the imine linkage was achieved by treatment with NaCNBH_3 . Finally, the cyclic carbamate- and thiocarbamate-linked COFs were obtained by reaction of the adduct with carbonyldiimidazole or thiocarbonyldiimidazole, respectively.

A multi-step PSM was employed to integrate catalytic active sites into the walls of a COF structure with open channels.^[72] The imine group of TFPPy-PyTTA-COF was reduced to secondary amine with NaBH_4 , and successively modified by reaction with 1,3-propane sultone to create a sulfonic acid-functionalized COF with a tertiary amine linkage. The Co(II) salt of the acid was then obtained by metathetical reaction with cobalt acetate. The resulting ionic COF was used as a catalyst in the cycloaddition reaction of CO_2 to epoxides with good recyclability and excellent catalytic activity.

1.6. Structural and chemical diversity in 2D COFs

2D COFs based on the imine linkage have emerged as the most extensively researched class of COFs, owing to their distinctive advantages. Beyond the good chemical and thermal stability demonstrated by these materials, a further advantage is represented by the scope of the imine formation reaction. A diverse range of polyfunctional amines and aldehydes (showcased in **Figure 1.7**) can be accessed from commercial sources or through easy synthetic routes, allowing for the straightforward preparation of numerous frameworks. These advantages contributed to the popularity of imine-linked 2D COFs that are the most explored and diverse class of COFs, with this fact being demonstrated by the more than 200 different structures reported to date.^[2]

2D COFs are created by combining rigid, planar building blocks that form covalently linked 2D layers upon polymerization. The presence of a flexible sp_3 unit is typically enough to lead to the formation of amorphous polymer networks that can hardly rearrange to form a crystalline material. The 2D polymer sheets exhibit a net-like structure with an ordered backbone characterized by polygonal voids of specific shape and size. The overall geometrical features of the system define the topology of the net. The 2D polymer represents the primary-order structure, that upon stacking produces the bulk layered 2D COF. The ordered alignment of these layers perpendicular to the 2D polymer planes is driven by van der Waals and π - π interactions, resulting in open 1D channels that form the porous structure of 2D COFs. Consequently, the defined pore size and shape are determined by the underlying

The properties of 2D COFs can be controlled by the spatial arrangement of chemical functionality, that are determined by their 2D net topologies and their layer stacking behaviors. In terms of topologies the complexity ranges from simple nets with a single pore shape to more intricate multi-pore tiling. By means of topology diagrams (**Figure 1.8**) it is possible to design 2D COFs with specific net topologies by selecting the building blocks with the correct combination of symmetries, as described by Yaghi and Diercks.^[73] The topology-related nomenclature for the building blocks can vary, but usually the multifunctional monomers are termed “knots” or “nodes”, while linear difunctional monomers are termed “linkers”.^[2,74]

2D COFs exhibiting the hexagonal net (also indicated as honeycomb) can either be obtained by the $[C_3 + C_2]$ knot + linker combination (**Figure 1.8a**) or by the $[C_3 + C_3]$ knot + knot (**Figure 1.8b**) which typically leads to smaller pore sizes. Being the simplest possible topology, it is also the most common structure found in literature. The reaction of a tetrafunctional knot with C_4 symmetry can lead to a tetragonal (also indicated as square) lattice in the $[C_4 + C_2]$ knot + linker combination (**Figure 1.8c**), but also in the $[C_4 + C_4]$ knot + knot combination. Less common is the $[C_6 + C_2]$ knot + linker combination that can produce a trigonal (also indicated as triangular) structure (**Figure 1.8d**). Interestingly, when a tetrafunctional knot with D_{2h} symmetry is employed two different topologies become possible in the $[D_{2h} + C_2]$ knot + linker combination (**Figure 1.8e**). The first one is a rhombic lattice with one type of pore and the second one is a Kagome structure with a central hexagonal pore surrounded by six trigonal pores. The selectivity toward one of the two structures depends on the characteristics of the linker and knot molecules, and in particular their bulkiness and their interlayer interactions. Typically, D_{2h} knots with extensive π -systems have strong π - π interactions and preferentially form the rhombic square lattice.^[75,76] In contrast, more flexible knots with weaker interlayer interactions are stabilized through a docking mechanism and tend to induce the crystallization of Kagome structures.^[77]

While the pore shape depends on the symmetry of the monomers, the pore size can be controlled by varying their size. A common strategy consists in increasing the number of phenylene units in the linker or in the arms of the knot.^[45] The currently reported 2D COFs display a pore size that spans between 0.6 and 5.8 nm,^[78–80] placing these materials at the frontier between the microporous (< 2 nm) and mesoporous (2 – 50 nm) classification.^[81]

The net topology and the pore size also determine the π -density of the skeleton, which is an important factor to consider when designing 2D COFs with specific features related to the conjugated backbone, such as optical and electrical properties.^[8]

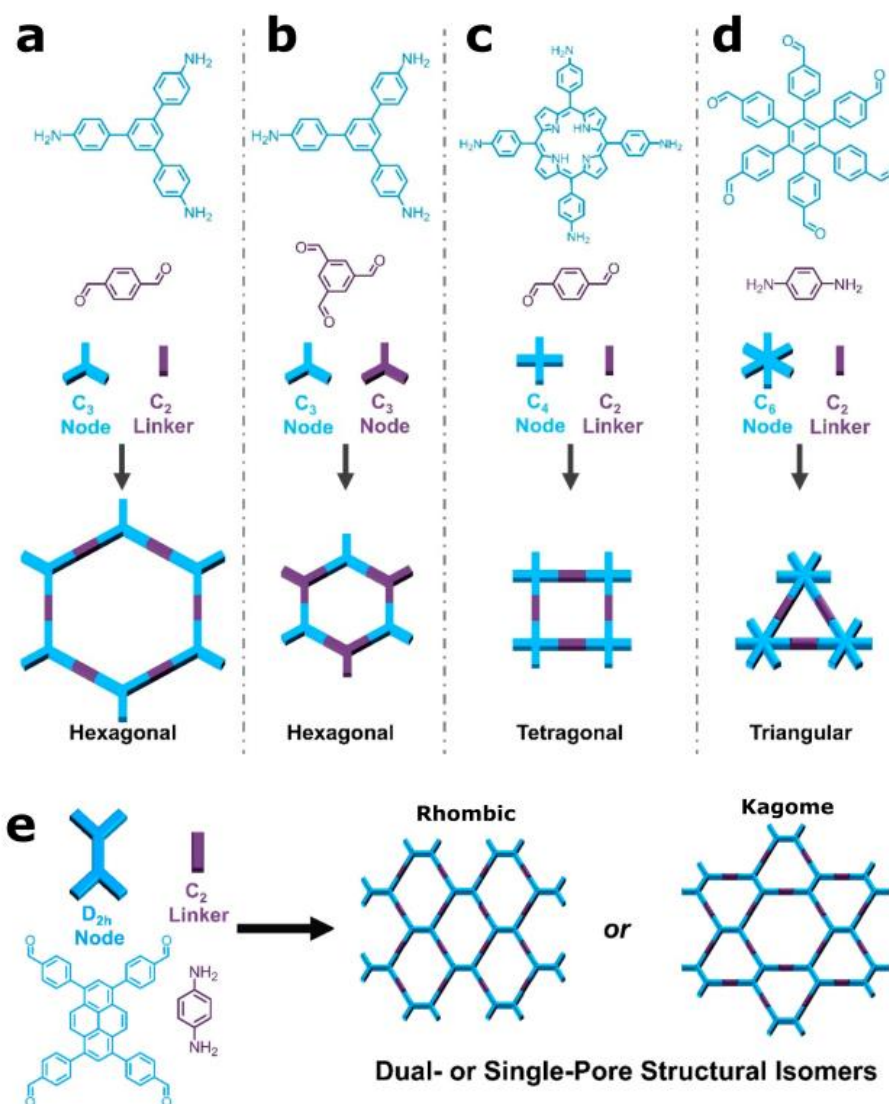


Figure 1.8 Representative selection of highly symmetric monomers and the relative 2D net topologies. Reproduced with permission from ref.^[2]

Beyond the multiple topologies that a 2D COF can display, another important structural feature that contributes to determine the macroscopic properties of these materials are the variety of configurations that the 2D layers can adopt upon aggregation and stacking in the third dimension. The stacking arrangements are determined by the weak non-covalent interactions between the 2D polymeric sheets, namely, π - π and van der Waals interactions which lead to the formation of a highly organized vertical structures comprising π -columns and 1D pores channel. The type of arrangement between the layers depends on a fine balance between attractive interlayer interaction and the repulsion between the polarized sections of the polymeric backbone.^[78,82] The possible different types of staking arrangements are

shown in **Figure 1.9**. Most 2D COFs reported to date adopt an eclipsed structure (AA alignment) in which the molecular building blocks are aligned on top of each other. On the other hand, very few cases of staggered structures (AB alignment, with the centers of the pores of one layer situated on top of vertex of the net of the second layer) have been reported.^[83,84]

Nonetheless, recent reports suggest that despite being the most reported model structure, the perfectly eclipsed stacking might not be the most realistic picture of the system. The local energetic minimum might be found when the layers assume a small relative offset (up to few angstroms).^[85,86] Depending on the directionality of the offset several quasi-eclipsed layering patterns are possible, namely inclined (each layer is shifted in the same direction respect to the layer below), serrated (each second layer is shifted in the same direction respect to the layer below and above), and rotated (each layer is twisted of a small angle in the same direction respect to the layer below). Combination of these layering patterns are also possible, as well as the manifestation of a random offset.^[87,88]

Some cases have been reported in which chemists have been able to exert some degree of control over the formation of specific stacking arrangements. Cao, Yang, and coworkers showed that a staggered AB kinetic product could be obtained instead of the thermodynamically stable AA eclipsed phase, by carefully choosing the reaction conditions.^[89] Cui, Wu, and coworkers demonstrated that it is possible to selectively obtain thermodynamically stable non-AA phases by introducing a steric hindrance effect by the introduction of bulky side-groups in the backbone.^[83] Finally, a stimuli-responsive behavior has also been reported for the stacking arrangement. Zhao, Kang, and coworkers showed that for certain 2D COFs the staking arrangement can be reversibly switched from AA layers to quasi-AB by solvent intercalation.^[84] Meanwhile, Medina, Sick, and coworkers reported that in some cases the exposure to solvent vapors can disrupt the eclipsed structure of the materials and lead uncorrelated layers, and the initial state can be recovered only by treatment of the solids with supercritical CO₂.^[90]

The stacking modes of layered materials exert a significant influence on the structural and physical properties of the resulting 2D COFs. The pore dimensions and shape are modified as the layers transit from an eclipsed to a staggered state, leading to a reduction in pore size. Besides, these stacking modes impact several physical properties of the 2D COF, including guest inclusion,^[91,92] fluorescence,^[82] and charge transport capabilities,^[93] among others.

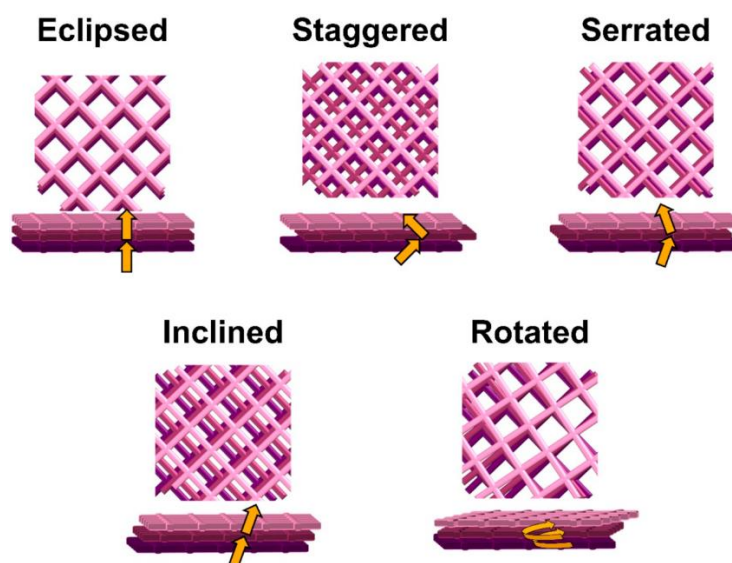


Figure 1.9 Scheme of some of the possible layer stacking arrangements in 2D COFs. Reproduced with permission from ref.^[2]

1.7. Synthesis and morphology control

The preparation of materials with long-range order and intrinsic porosity depends not only on the selection of appropriate linkage and building blocks but also on the implementation of an adequate synthetic strategy. Moreover, 2D COFs can be obtained in a variety of morphological shapes including polycrystalline powders, colloidal dispersions, nanofibers, membranes, gels, and films (**Figure 1.10**).^[9,94] Many strategies have been established to synthesize 2D COF materials with the desired crystallinity and porosity (nanoscale structure, < 100 nm) but also with tailored morphologies at the mesoscale (100 nm - 500 μm) and macroscale (> 500 μm).^[94]

Currently, the vast majority of 2D COFs are obtained as insoluble polycrystalline powders by solvothermal synthesis.^[4] This morphology represents an obstacle for an application-oriented development of these materials, as polycrystalline powders are unsuitable for several property measurements such as those that might involve the use as a membrane or the integration in an electronic device. For this reason, several techniques have been devised to prepare 2D COFs into more useful forms, such as the film morphology.^[95] Ultimately, it would be desirable to develop general methods that allow the fabrication of 2D COFs with desired morphologies and degree of crystallinity, a goal that has yet to be accomplished.

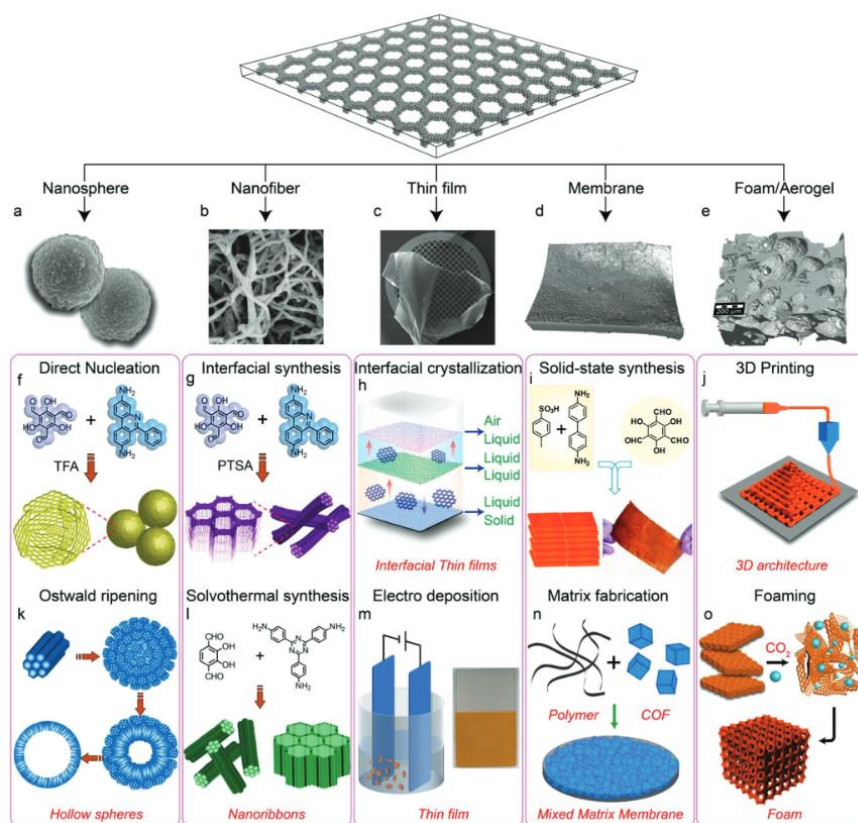


Figure 1.10 Morphological landscape in 2D COFs. The formation of the different morphologies can be controlled by selecting the right the building blocks and synthetic conditions. Reproduced with permission from ref.^[9]

As powder and film are the most common morphologies and are also the focus of the experimental part of this thesis, the following sections will provide a concise introduction to the most common synthetic strategies for producing 2D COFs with these morphologies.

1.7.1. Synthesis of COF powders

Solution-phase synthesis

The solution phase approach is the most widely used method for the synthesis of COFs. It typically involves dissolving or suspending the building blocks and the catalyst in a solvent mixture in a sealed vessel that is heated for several days, in solvothermal conditions. The success of the crystallization heavily relies on the choice of solvents, reaction time, and temperature, which must be tailored to the type of linkage and combination of building blocks. For example, mild temperatures of 80 - 120 °C are sufficient for the synthesis of boron-based COFs^[28] and imine-linked COFs,^[41] while for imide-linked COFs adequate reversibility is en-

sured only at higher temperatures ($> 150\text{ }^{\circ}\text{C}$).^[96] Precisely controlling the solvent mixture and its ratio is important to enable controlled diffusion of building blocks into the solution and to promote controlled crystallite growth. Solvothermal reactions are usually conducted in sealed Pyrex tubes or microwave vials to prevent solvent evaporation. Moreover, as the crystallization of COFs relies on condensation reactions, the closed reaction vessel ensures that the condensation by-product (often water) is kept available in the reaction mixture even at temperatures above its boiling point. The presence of the by-product ensures the backward reaction through hydrolysis of the linkage and enables the error correction mechanisms required for the formation of crystalline products. To enhance the reversibility of the COF formation reaction, various catalysts are used, and in particular for imine-linked COFs aqueous acetic acid is the most common choice.^[42]

Overall, these liquid-phase synthesis approaches enable the production of COFs at a scale ranging from a few milligrams to grams. The resulting COFs exhibit good to high crystallinity, with crystallite size approximately ranging between 20 and 100 nm. As for their morphology, the COFs form polycrystalline particles that can range in size from approximately 100 nm to a few micrometers. These particles can take on spherical, irregular, or regular shapes, and are typically found to aggregate into a powdery material.

Insights in the reaction mechanism

A precise explication of the polymerization - crystallization mechanisms of 2D COFs is of fundamental importance as it is the basis for the rational synthesis of novel frameworks. However, mechanistic insights into the 2D COF growth pathways are still scarce, due to the challenge posed by the investigation of such a heterogeneous process.^[97]

The nucleation-elongation mechanism consists in the initial formation of small nuclei of crystalline species that continue to grow in an ordered way by further polymerization and stacking. This mechanism, with the interlayer interaction as main driving force, was found to be in place for some boronate ester-linked 2D COFs.^[98,99] In this context, a way to control the growth of the crystals is to lower the concentration of the monomers disfavoring the nucleation of new particles.^[18] A similar effect can be achieved by the addition of monofunctional modulators, which slow down the reaction and favor the growth in the out-of-plane direction.^[100] The problem of the precipitation of a solid polymer in the early stages of the reaction introduces an irreversible step, which limits the solution-phase growth and obstructs the mechanistic investigation. To avoid this problem a colloidal 2D polymerization method based on the use of nitrile solvents was developed by the group of Dichtel.^[101]

For imine-based 2D COFs a less obvious crystallization mechanism appears to be in place. Initial studies based on the isolation of the reaction intermediates, reported the quick formation of an amorphous polymer network precipitate, and assumed a slow amorphous-to-crystalline transition at the solid state that generates the ordered material over several days.^[42] A similar mechanism was found to be in place when the material was homogeneously grown through a colloidal polymerization approach and investigated by *in-situ* techniques.^[102] However, more recent reports seem to dispute the previous findings proposing a model in which the reaction does not produce a amorphous polymer network, even at the incipient stages of the reaction. Instead, the authors reported the quick formation of micrometer-sized few-layers 2D sheets with random alignment along the *c*-axis, which slowly rearrange to form the 2D COF with an ordered layer stacking.^[103]

Expeditious synthesis

Solvothermal synthesis uses thermal energy to drive the reaction toward the formation of crystalline products, and this involves extended reaction times requiring great energy inputs. To eliminate this drawback, expeditious synthetic methods have been developed, using diverse energy sources like microwave,^[104] ultrasound,^[105] mechanical,^[106] and light irradiation,^[107] have been employed to accelerate the crystallite nucleation process, thereby enhancing the overall efficiency of the synthetic process. Recently, water-tolerant Lewis acids catalysts namely metal triflates have been developed for the synthesis of imine COFs. For instance, thanks to the high catalytic activity of $\text{Sc}(\text{OTf})_3$ for both imine formation and transimination, highly crystalline COFs could be obtained at room temperature within 10 minutes from the addition of the catalyst.^[108] Compared to the solvothermal method, COF synthesis under mild conditions could be an attractive strategy for fragile linker molecules, sensitive substrates, or to reduce the energy consumption.

1.7.2. Synthesis of COF films

All the above-mentioned synthesis methods result in insoluble powders that are unprocessable, thus limiting their potential range of applications. Therefore, new methods for the preparation of 2D COFs in the continuous film morphology are highly sought for.^[109] To this end a number of methods have been developed for the preparation of films targeting different thicknesses, here classified as single-layer (atomic thickness), few-layers (up to 10 nm), thin films (10 nm to 500 nm), and thick films (thicker than 500 nm).

A well-established method for the preparation of single-layer 2D COFs is the templated

growth on crystalline substrates such as highly oriented pyrolytic graphite (HOPG) and Au(111).^[110–112] However, despite being of incredibly insightful for the study of the dynamic of the 2D polymerization this method rarely yields large area films, and the a further challenge is presented by the impossibility of decoupling the film from the templating material which limits the potential use of the materials.^[113,114]

Further methods developed for the synthesis of few-layer, thin and thick films. These include the solvothermal growth, interfacial polymerization, and solution processing that allow to prepare films with different characteristics in terms of homogeneity, thickness, mechanical robustness, and crystallinity. These methods will be briefly described in the following sections.

Solvothermal growth on substrates

The most reliable approach for producing 2D COF films involves the direct polymerization of the material on a solid substrate immersed in the solution containing the monomers. This method is also known as solid – liquid interfacial synthesis. The reaction conditions used are similar to those utilized for the solvothermal synthesis of COF powders.^[115] The method relies on the assumption that the heterogeneous nucleation barrier is lower than the homogeneous nucleation barrier, so the material preferentially nucleates and grows at the solid - liquid interface, eventually generating a continuous film.^[109] This method is widely applicable, and many 2D COFs have been prepared as films on different substrates such as graphene, silicon, and indium tin oxide.^[116–118] Often, this synthetic method yields films where the layers of the 2D COF are aligned parallel to the substrate.^[119] The films are typically composed of a continuous and polycrystalline material with limited crystallite size, similar to those obtained by bulk powder syntheses (approximately 20 - 100 nm domain size).^[119] The possibility of generating oriented 2D COF films makes this approach the method of choice for the preparation of materials suitable for optoelectronic characterization.^[118,120] However, this method presents certain drawbacks, such as the limitations in scale-up, the restricted choice of substrates to those compatible with the solvent mixture, and the presence of a significant contamination from insoluble powder aggregates, that are also generated during the polymerization process.

Water - air interfacial polymerization

The water - air interfacial polymerization has shown great potential for the preparation of single-layer or multi-layer films of 2D COFs. Typically, large-area films can be prepared and are robust enough to be transferred from the liquid interface to arbitrary substrates, includ-

ing spanning holes of several microns, without collapsing.^[121]

Two date two different approaches have been reported to obtain good quality films: the Langmuir–Blodgett (LB) method and the surfactant monolayer assisted interfacial synthesis (SMAIS) method. In the LB method hydrophobic monomers are confined on the water surface of a LB trough and form a film upon polymerization when activated by the increasing surface pressure controlled by the movable barriers.^[121–123] In the SMAIS method, films of 2D COF are prepared by exploiting the templating effect of a surfactant, which pre-organizes one the building blocks at the water-air interface (typically a porphyrin-based monomer), while the second monomer, partially soluble in water is injected in the subphase and by slow diffusion reaches the interface where it reacts to generate a highly crystalline 2D COFs.^[124–127] The 2D COFs films prepared with this method are among the highest quality materials prepared to date. Large area films and remarkable crystalline domain sizes of up to $60 \mu\text{m}^2$ were achieved, making them suitable for integration into electronic devices.^[126] However, the scope of water - air interfacial methods remain remains limited and poor control of thickness can be exerted.

Liquid - liquid interfacial polymerization

Crystallization of free-standing 2D COF films has also been achieved through liquid - liquid interfacial polymerization. This method involves the segregation of the monomers or the monomers and the catalysts into two immiscible phases, consequently restricting the polymerization to the solvent - solvent junction. This technique has been widely used to prepare various thin and thick films with homogeneous properties and controllable thicknesses.

One of the most representative examples of liquid – liquid interfacial polymerization is the synthesis of β -ketoenamine-linked COF films which was reported by Dey, Banerjee, and co-workers.^[128] The large-area films were prepared in a beaker dissolving the aldehyde (Tp) in a dichloromethane (DCM) bottom phase and a series of ammonium salts of the desired amine co-monomers with *p*-toluene sulfonic acid (PTSA) in a water top layer. After 72 hours of reaction at room temperature crystalline free-standing thin films were obtained and could be transferred onto various substrates. The thickness of the films ranged from 50 to 200 nm and controlling the concentration of the precursors ensured the fabrication of thick films up to a few μm . Notably, upon transfer on the target substrates the materials maintained their integrity, even in case of the thinnest film. The size of the reaction vessel significantly represented the main limitation for the lateral dimension of the grown films.

In another example, Matsumoto, Dichtel, and colleagues showed that imine-linked COFs could be prepared at an organic – water interface by using $\text{Sc}(\text{OTf})_3$ as catalyst.^[129] In this case both the aldehyde and the amine co-monomers were dissolved in the organic bottom phase and while the Lewis catalyst preferably dissolved in the water top layer. This spatial segregation enabled a selective acceleration of the reaction at the liquid junction and the mechanically robust and crystalline films could be separated from the liquid after 72 hours. The thickness of the films could be varied between 20 nm and 100 μm by controlling the concentration of the monomers and the reaction time.

However, despite the good crystallinity achieved in the aforementioned cases, no preferential orientation of the crystallites was observed. Only recently, Zhang, Chen, and colleagues developed a strategy to synthesize highly crystalline and oriented films of 2D COFs by exploiting the self-polymerization of an A_2B_2 type monomer.^[130] Specifically, the 1,6-bis(4-formylphenyl)-3,8-bis(4-aminophenyl)pyrene (BFBAPy) was dissolved in DCM and a diluted aqueous acetic acid solution was stratified on top, which confined the reaction at the liquid junction. Depending on the reaction time, films with a thickness ranging from 150 to 900 nm could be obtained.

In summary, the liquid - liquid interfacial synthesis is currently the most straightforward, flexible and reliable way to prepare self-standing, large-area few-layers films and thin films. However, the method requires long reaction times and despite the success reported by Chen and co-workers, producing oriented films using this approach remains a challenging task.^[130]

Solution processing

Alternative methods for preparing 2D COF thin and thick films include the solutions processing of colloidal suspensions.^[101,131] Burke, Dichtel, and colleagues developed a method for exfoliating 2D COF powders by protonating the imine-linkages with trifluoroacetic acid (TFA), resulting in stable suspension of nanosheets that can be drop-cast to form large-area films.^[10] During exfoliation TFA partially depolymerizes the 2D COF structure into soluble monomers and oligomers, which then repolymerize as the solvent evaporates during the casting process yielding homogeneous films with controllable thickness from 50 nm to 20 μm . Barnes, Lambeth, and colleagues subsequently demonstrated that similar films could be prepared directly from a solution of the monomers in water - TFA.^[11]

Kandambeth, Banerjee, and colleagues developed a scalable method for synthesizing β -ketoenamine-linked 2D COF thick films.^[132] They prepared a slurry of COF particles suspended in water using PTSA as catalyst. The resulting paste was knife-cast onto substrates

and baked in an oven to generate large-area, freestanding 2D COF films. The presence of the catalyst during the solvent evaporation likely promoted the cross-linking between the COF sheets, resulting in mechanically robust 2D COF films that are flexible, defect-free, and crack-free, and with thicknesses ranging from 200 to 700 μm .

Khalil, Verduzco, and colleagues introduced a novel method for preparing imine and hydrazone-linked 2D COF films by suppressing the precipitation.^[133] Using a polar solvent, such as dimethylacetamide, and a modified mixing approach that slows down COF growth, the authors reported the formation of a nanoparticle suspension that is stable at high temperatures. However, upon cooling, the suspension is destabilized and generates a crystalline and porous COF gel, with this transformation found to be thermo-reversible. The temperature-dependent gelation process enables the fabrication of highly crystalline and porous COF films with thickness ranging from 100 μm to 1 mm.

Yao, Lotsch, and colleagues utilized the stable colloidal suspension of 2D COF particles to prepare imine-linked 2D COF films via spin-coating.^[134] The colloidal suspension was obtained by reacting the monomers in acetonitrile (MeCN) with $\text{Sc}(\text{OTf})_3$ as catalyst, and was demonstrated to be stable at room temperature for several months. By controlling the precursor concentration, either a nanosphere or nanoplate morphology of the particles could be selectively formed. Spin-coating the suspension onto substrates such as glass or silicon resulted in the production of continuous, large-area supported films with thicknesses ranging from 120 to 660 nm, depending on the number of coating cycles. Films generated using the nanoplate suspension exhibited a small preferential orientation of the crystallites notably with the 2D layers aligned orthogonal to the substrate.

In summary, solution processing is a promising approach for preparing thin and thick films of 2D COFs, by exploiting already established and scalable techniques such as drop-casting, spin-coating, knife-coating, and spray-coating. However, these approaches applied to 2D COFs are still underexplored due to the difficulty of generating solutions or suspension of these materials. Therefore, further research in this field is required with a particular focus dedicated to the development of new methods to prepare high-quality oriented films, which are currently missing.

1.8. 2D COF composites

To tailor or enhance the performance of 2D COFs, it can be useful to synthesize composites by incorporating other materials.^[16] In this regard, 2D COFs are advantageous due to their

open and accessible channels that can accommodate nanosized materials, as well as their polymeric backbone that offers a surface for the construction of composites through direct growth or physical mixing with a diverse range of other materials. Following these principles, 2D COFs composites were synthesized using functional materials such as metal nanoparticles,^[135] metal oxides,^[136] silica,^[137] carbon materials,^[138,139] polymers,^[140] MOFs,^[141] and quantum dots^[142] (**Figure 1.11**). By combining the advantages of two different materials, COF-based composites offer a flexible platform for creating functional smart materials with desired properties, which can be customized to satisfy the specific requirements of each application. However, despite the growing interest demonstrated in the past few years, this sub-field of study of COFs remains today largely unexplored.

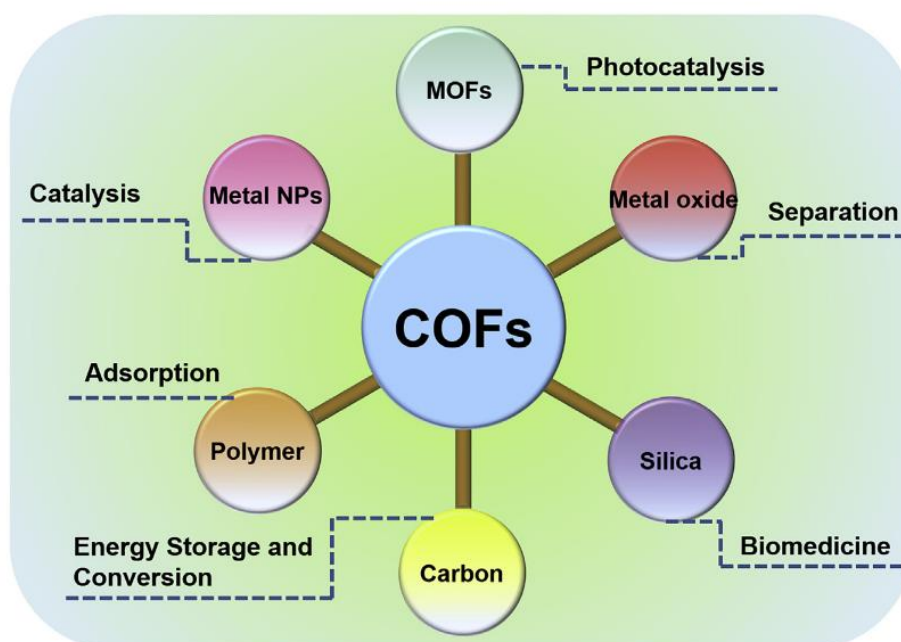


Figure 1.11 Overview of the filler materials that can be combined with 2D COFs and their proposed applications. Reproduced with permission from ref.^[16]

1.9. Properties and Applications of 2D COFs

2D COFs are increasingly attractive materials due to their unique structure formed by the layered stacking of covalently-linked ordered 2D polymers. These structural features generate crystalline, anisotropic, permanently porous, chemically robust, and low-density materials. Furthermore, the synthetic modularity of 2D COFs allows adjusting the pore size / shape and the functionality of the backbone, making them ideal platforms for various applications.

Therefore, since their discovery, 2D COFs have been studied for applications in gas separation and storage, liquid-phase molecular and ionic separation, catalysis, sensing, optoelectronics, and electrochemical energy storage (**Figure 1.12**).^[17] However, the development of these materials is still in the embryonal stage, and many challenges related to the limited crystallinity, the processability, and the scalability are hindering the implementation in real-world applications. This section provides a brief overlook of the potential applications of 2D COFs.

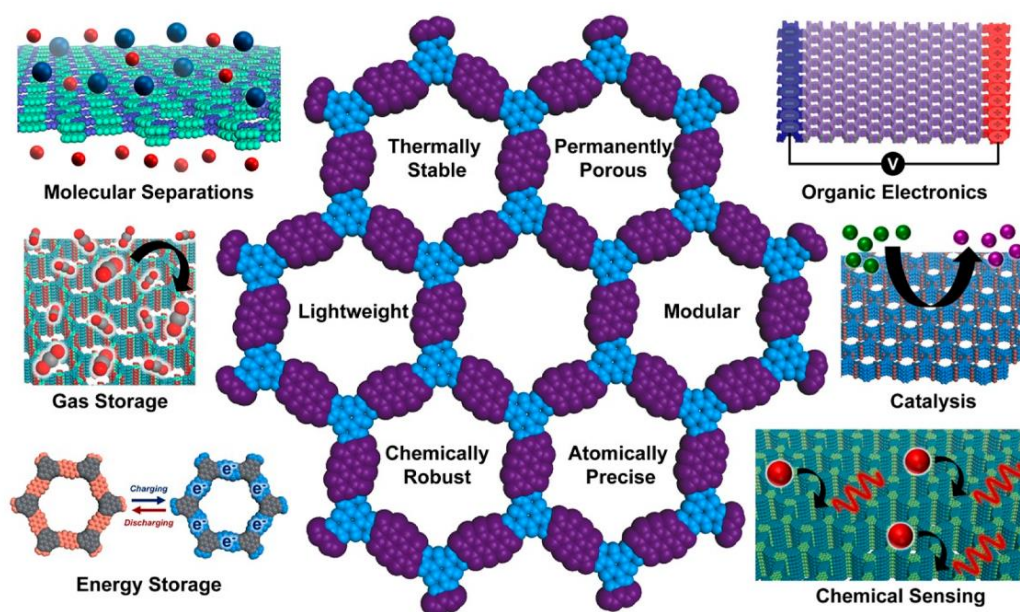


Figure 1.12 A selected collection of the most promising applications of 2D COFs. Reproduced with permission from ref.^[2]

1.9.1. Gas storage and separation

2D COFs are receiving increasing research attention due to their permanent porous structure and high specific surface area, properties that make these materials promising for gas-phase adsorption and separation of molecules. Indeed, their tunable pore size / shape and pore wall functionalities provide opportunities for the development of selective binding sites. Gas storage studies have primarily focused on small molecules such as hydrogen,^[143] carbon dioxide,^[144] and water vapor,^[145] with recent interest in methane^[146] and ammonia.^[147] For gas separation, 2D COF-based membranes could emerge as a cost-effective alternative to conventional distillation methods. Examples of proposed gas separations include H_2 / CO_2 ,^[148,149] H_2 / CH_4 ,^[149] H_2 / N_2 ,^[149] $\text{CO}_2 / \text{CH}_4$,^[150] and CO_2 / N_2 .^[150] While for the

application in gas storage the polycrystalline powder morphology is sufficient, for separation membrane the use of 2D COF films is more suitable.^[151]

1.9.2. Liquid-phase molecular and ionic separation

The development of thin polymeric films with precise pore size and connected by stable covalent bonds has inspired research into 2D COFs for liquid-phase molecular and ionic separation.^[152] With 2D COFs, it is possible to precisely adjust the size and the shape of the pore apertures, thus enabling the separation of guest molecules depending on their van der Waals volumes. Additionally, controlling the functionality and the hydrophobicity / hydrophilicity of the pore channels enables a further selection mechanism related to the attractive or repulsive host-guest interactions. Thanks to these intrinsic properties, 2D COFs have attracted great attention in the membrane separation field. Nevertheless, the synthesis and the processing of precisely oriented and mechanically robust 2D COFs films continues to be a challenge that hampers their use as membranes. Despite the synthetic difficulty, few examples have been reported for the study of 2D COFs as filtration membranes, achieving promising separation performances in water treatment^[153] and organic solvent nanofiltration.^[123]

1.9.3. Chemical sensing

The unique combination structural diversity, of accessible pores that allow the uptake of guest molecules, and rigid and conjugated backbones that often can exhibit a charge migration or fluorescent behavior make of 2D COFs promising materials for chemical sensing.^[154] Several examples have been reported in which 2D COFs have demonstrated useful in different sensing fields such as explosive sensing,^[155,156] biosensing,^[157] humidity sensing,^[158] pH detection,^[159] gas sensing,^[160] metal ion sensing,^[161,162] and acid vapor sensing.^[163] The most typical sensing mechanisms of guest molecules are the fluorescence quenching, the colorimetric detection, and the electrochemical detection.

1.9.4. Catalysis

The unique features of 2D COFs, including their high surface area and the modularity their components, make them versatile platforms for accommodating catalytic sites for various heterogeneous catalytic reactions.^[164] The catalytic activity of 2D COFs can be built on a vari-

ety of principles, including pore spatial confinement, pore wall functionalization, π -backbone design, and π -column organization. Exploring COF-based catalysts involves designing the various features that control interactions between excitons, electrons, holes, molecules, and ions, which in turn control the overall kinetics and thermodynamics reaction, thereby determining the catalytic activity, the selectivity, and the efficiency.^[4] For example, 2D COFs with conjugated π -backbones and chromophores well-organized in space, can be used as photocatalysts, particularly for singlet oxygen generation,^[165] and hydrogen evolution reaction (HER).^[166] In addition, the π -columns and in-plane conjugation of 2D COFs can serve as ordered pathways for charge carrier transport, making these materials useful as electrocatalysts for oxygen reduction reaction (ORR),^[167] oxygen evolution reaction (OER),^[168] and CO₂ reduction.^[169] Moreover, 2D COFs have been demonstrated to be useful as heterogeneous catalytic supports for metal ions such as Pd(II) or metallic nanoparticles for catalyzing organic reactions such as the Suzuki-Miyaura coupling^[31] or the Sonogashira coupling.^[170] The COF side walls can present pendant groups that protrude from the pore walls, and in this context the introduction of chiral groups has been demonstrated to be effective for asymmetric organocatalysis.^[32]

1.9.5. Optoelectronics

2D COFs are considered a promising class of materials for organic electronics due to their crystalline and conjugated structure. Indeed, the charge transport in these materials can proceed both in-plane along the π -conjugated 2D polymeric backbone, and out-of-plane, through the 1D π - π stacked assemblies forming layered materials.^[8] These structural features could in principle provide a strong electronic coupling within the material and for this reason 2D COFs are predicted to exhibit interesting optoelectronic behaviors.^[56,171] Being organic polymers, 2D COFs possess a highly modular skeleton, and in particular π -extended and redox-active structural units can be easily included in the framework.^[172] By selecting the right molecular components is therefore possible to prepare p-type,^[173] n-type,^[174] or ambipolar^[175] semiconducting materials. The integration in the backbone of both electron-donating and electron-accepting building blocks can be used to develop materials with smaller band gap and better conductivity.^[176] A similar strategy can be implemented by the employment of guest molecules.^[13] Additionally, it has been shown that the geometry and the connectivity of the building blocks which determines the 2D lattice symmetry can also influence the electronic structure of the final material.^[177]

For a deeper understanding of the charge transport properties of 2D COFs, it is important to describe the charge transport mechanism at microscopic scale. In general, charge transport in organic materials can happen either by band transport or by hopping.^[178] The band transport mechanism is commonly seen in organic single crystals, and it is achieved when a significant overlap of molecular orbitals is present and it is analogue to the case of inorganic semiconductors, such as silicon or graphene. Conversely, in amorphous materials or crystalline materials with poor overlap of the molecular orbitals, a weak electronic coupling, and a relatively strong electron-phonon coupling are observed, resulting in the prevalence of the hopping mechanism, according to which the charge carriers move by hopping between different localized states.^[179] Currently, the study of the charge transport properties of 2D COFs typically involves determining their crystal and band structures, by theoretical calculations, assuming a band transport mechanism.^[177] However, due to their anisotropic structure it is possible that charge transport processes may have different mechanisms depending on the transport direction within the crystalline domain.^[118] A complete picture of the charge transport mechanism in 2D COFs is still under elucidation.

Because of these interesting features a great effort is being dedicated to investigating the performances of these materials in proof-of-concept applications. Several examples of (opto)electronic devices were realized using 2D COFs, such as transistors,^[180] photovoltaic,^[181] light emitting,^[182] and sensor devices.^[8,160]

1.9.6. Electrochemical energy storage

2D COFs have earned significant attention due to their semiconductive nature and unique, well-defined, and adjustable porous structure that results in high surface areas. The porosity of 2D COFs is constituted of highly ordered 1D pore channels that have adjustable sizes and shapes, providing a fixed path for mass transport within the material for small species such as ions and molecules. This characteristic imparts 2D COFs with ion conduction properties, which, combined with their electrical conductivity and the functionalization with redox-active sites, make them highly attractive for electrochemical applications, especially in energy storage.^[178] One commonly investigated application is their use as electrode materials in supercapacitors, where they can store electrical energy via the electrical double-layer capacitance, pseudocapacitance, or a combination of the two processes.^[183] Furthermore, 2D COFs have the potential to be used as electrodes for various battery types,^[184] such as lithium-ion,^[185] lithium-sulfur,^[186] sodium-ion,^[187] and potassium-ion batteries.^[188] Recently,

COFs have also been investigated for their potential use in multivalent ion systems, including zinc-ion,^[189] magnesium-ion,^[190] and aluminum-ion^[191] energy storage devices.

2. Experimental tools for the characterization of 2D COFs

The scientific advances in the synthesis and the characterization of the properties of 2D COFs are only possible using advanced analytical techniques. This chapter provides a summary of the most significant instrumental techniques used to characterize various chemical, structural, morphological, and electronic properties of 2D COFs. Far from being exhaustive, the chapter aims to introduce the readers that are less familiar with the field of 2D COFs to the various methods.

2.1. Chemical characterization

2.1.1. Fourier-Transform Infrared Spectroscopy (FTIR)

Infrared (IR) spectroscopy is a technique that investigates the vibrational transitions that molecules and materials undergo when IR radiation is absorbed.^[192] The necessary conditions for the absorption of the radiation are the equivalence of the energy of the transition with the energy of the incoming radiation and a non-zero dipole moment change during the corresponding vibration. The energy at which the transitions occur are specific to the chemical bonds present in the material and in the Harmonic oscillator approximation for a diatomic system, the frequency of the transition is given by Hooke's law:

$$\tilde{\nu} = \frac{h}{2\pi c} \sqrt{\frac{k}{m_1 m_2 / (m_1 + m_2)}}$$

where $\tilde{\nu}$ is the wave number of an absorption maximum (cm^{-1}), h is the Planck constant, c is the velocity of light (cm s^{-1}), k is the force constant of the bond (dyne cm^{-1}), and m_1 and m_2 are the masses of the two atoms. Therefore, the information on the radiation absorbed in the mid infrared region ($400 - 4000 \text{ cm}^{-1}$) can be used to qualitatively identify chemical the composition of the material analyzed.

Modern IR instruments work in Fourier transform (FTIR), meaning that the polychromatic light produced by the source is not dispersed into its components before the interaction with the analyte, but rather passed through a Michaelson interferometer and then shone on

the sample. The resulting interferogram is converted back to the frequency by a Fourier transformation, obtaining a complete IR spectrum. This method allows a faster data collection and a better signal-to-noise ratio.

Attenuated Total Reflection (ATR) FTIR spectroscopy is a variation of FTIR used to easily measure solid and liquid without requiring sample preparation.^[193] This technique uses an internal reflection element, typically a diamond crystal, to enhance the surface sensitivity. The sample is placed in contact with the crystal and during the internal reflection of the light a component, known as evanescent wave, interacts with the surface of the sample and collects the information on its composition.

Within this thesis work the FTIR spectra were acquired with a ThermoScientific Nicolet iS50 spectrometer equipped with ATR Diamond and a DTGS KBr detector.

2.1.2. Nuclear Magnetic Resonance (NMR)

Nuclear magnetic resonance (NMR) is a powerful analytical technique that is used to retrieve information on the presence and the electronic environment of magnetically active nuclei such as ^1H , ^{13}C , and ^{19}F . The principle of the technique is that when a stationary magnetic field B_0 is applied to the sample, the magnetic dipoles of the nuclei align with a precessional motion around the direction of the external field. In this situation, for a common nucleus with a spin of one-half two distinct energy states are possible, corresponding to the alignment with or against the magnetic field.^[192] A perturbation of the spin orientations can be induced by the introduction of an electromagnetic wave with radiofrequency ν_1 in resonance with the Larmor precession frequency ν_L of the nucleus in analysis:

$$\nu_1 = \nu_L = \frac{\gamma}{2\pi} B_0$$

where γ is the gyromagnetic ratio of the nucleus in analysis and B_0 is the strength of the magnetic field. The resonance condition, the radiofrequency can be absorbed inducing the transition between the low and the high energy states. The nuclei in the high energy state return to the ground state through two possible non-radiative relaxation processes: the spin-lattice relaxation (loss of energy by transfer toward lattice vibrations and rotations) and the spin-spin relaxation (loss of energy by transfer toward other nuclei). Meanwhile, the rotating magnetization vector induces a current in receiver coil, which is detected and amplified to give an oscillating signal that decays in time known as free-induction decay (FID). The FID is processed by Fourier transform into readable spectrum containing the information on

the resonance frequency.

The presence of the electrons around the nuclei partially shield it from the external magnetic field. Moreover, the specific chemical environment around a nucleus in a molecule induces different degrees of shielding, with the result that each nucleus will experience a different magnetic field and will have its own resonance frequency depending on the type, arrangement, and chemistry of the surrounding atoms.

The most used routine NMR experiment is ^1H NMR that easily enables the determination of the composition and the structure of organic molecules and macromolecules. For a proper measurement the molecules need to be solubilized in a deuterated solvent with approximately a minimum concentration of 1 mM.

NMR spectra shown in chapter 3 were recorded on a Bruker Ascend Avance Neo – 500 MHz spectrometer or on a Bruker Avance III HD 400 MHz. Chemical shifts are reported in parts per million (ppm) relative to the tetramethylsilane TMS signal (small amount added before each analysis, $\delta_{\text{TMS}} = 0$ ppm).

2.1.3. X-ray Photoelectron Spectroscopy (XPS)

X-ray Photoelectron Spectroscopy (XPS) is a surface characterization technique that allows to study the chemical composition of a solid material.^[194,195] The working principle relies on the detection of the photoelectrons emitted when a sample is irradiated with a monochromatic X-ray radiation. It can be used to qualitatively detect any element of the periodic table (except for hydrogen and helium), but also to perform a semi-quantitative analysis of the relative composition of the surface with a detection limit of about 0.1 - 1 %. When a monochromatic X-ray radiation interacts with atoms constituting a material several phenomena can take place, such as the photoelectric effect or the Auger effect. In both cases the radiation is inelastically scattered, and electrons are expelled from the material with kinetic energies characteristic of the specific atoms, their oxidation states, and their chemical environments. The determination of the binding energy BE of the electrons involves the subtraction of the measured kinetic energy KE and a work function-like term Φ from the known energy of X-ray photons E_p :

$$BE = E_p - (KE + \Phi)$$

This process enables the identification of elements present on a material's surface and quantitative analysis of its elemental composition using available reference data on atomic sensitivity factors and binding energies. XPS spectra also provide additional information on

the chemical state, electronic structure, and density of states in the material. While the characteristic binding energy of core electrons for each element lies within a range of approximately ± 2 eV compared to the reference value for an atom forming pure covalent bonds, the energy can be shifted if the atom is bound to other atoms with polar bonds. By fitting XPS peaks of each element and considering the sample's surface elemental composition and additional chemical information, insight into oxidation states and relative fractions of each element associated with specific compounds or chemical species can be obtained. The analysis is typically operated in ultra-high vacuum ($< 10^{-7}$ mbar) and the sampling depth of the photoelectron effect is around 5-10 nm. Samples in thin film or powder can be analyzed.

Within this thesis work, XPS spectra were collected at room temperature by using a ThermoScientific K-Alpha X-ray photoelectron spectrometer equipped with an Al X-ray source (1486.7 eV) at a working pressure of 10^{-8} - 10^{-9} mbar. The spot of the wide elliptical X-ray beam was set at 400 μm . Survey spectra were recorded with a pass energy of 200 eV and with an energy step of 1 eV. The spectra of the elements were recorded with a pass energy of 50 eV and an energy step of 0.1 eV.

2.1.4. Thermogravimetric analysis (TGA)

Thermogravimetric Analysis (TGA) is a widely used analytical technique that enables the study of thermal behavior of a material by measuring its mass variations as it is subjected to controlled heating or cooling.^[196,197] TGA can provide insights into the thermal stability and the purity of a sample in addition to a range of other phenomena such as phase transitions, adsorption and desorption, and solid-gas reactions. TGA can be either carried out in isothermal mode or in dynamic mode. In isothermal TGA the sample is kept at a constant temperature in air or inert atmosphere and the change of weight is recorded as a function of time. More common in the routine characterization of COFs is the dynamic TGA. In these experiments the sample is exposed to a rising temperature ramp in air or inert atmosphere. The changes of mass that occur during this type of analysis are typically interpreted as related to the release of volatile components generated by desorption or by decomposition of the sample to form small molecules.

Within this thesis work, TG profiles were recorded in the range of 30 – 900 °C operating under air or nitrogen atmosphere with a heating rate of 10 °C min⁻¹ on a Mettler Toledo TGA/SDTA851e system.

2.1.5. Raman Spectroscopy

Raman spectroscopy is a useful technique for the investigation of the vibrational modes of the compounds in a sample at the solid, liquid, or gas states.^[198] In this technique, the light from a monochromatic source (typically a laser) in the visible, UV, or NIR region is used to irradiate the sample. The photons do not typically carry sufficient energy to promote an electronic excitation, but the molecules can still absorb the light when, their polarizability allows for the creation of an oscillating induced dipole moment by interaction with the electric field of the radiation. Through this mechanism the molecules can be excited to a “virtual” energy state which by decay is responsible for the scattering of the light. Most of the light is elastically scattered by the sample meaning that the absorbed photons are then re-emitted at the same excitation wavelength (Rayleigh scattering). However, a small fraction of the light is inelastically scattered, and the corresponding re-emitted photons are either shifted to higher energies or to lower energies. Stokes scattering produces a scattered photon with lower energy than the incident photon, and the difference in energy corresponds to one or more quanta of vibrational energy, leading to the molecule being in a vibrationally excited state. Conversely, anti-Stokes scattering happens when the scattered photon has higher energy than the incident photon, and it results from a molecule in an excited vibrational state before the visible light excitation. In general, despite the low probability of such events, the analysis of inelastically scattered photons can provide valuable insights into chemical structures, offering also a unique vibrational fingerprint of the materials under analysis.

In this thesis work, Raman spectra were recorded under ambient conditions with a Renishaw inVia spectrometer with 532 nm laser under a 100× objective (numerical aperture 0.85). The power was kept below 1 mW to avoid local heating and damage effects.

2.2. Structural Characterization

2.2.1. Powder X-ray Diffraction (PXRD)

Powder X-ray diffraction (PXRD) is a quick, non-destructive method used for analyzing the internal structure of polycrystalline solids and determining the composition of phase mixtures.^[199] The working principle of any XRD analysis is based on Thomson scattering, where the incoming photon transfers its energy to an atom in the crystalline material, exciting it

and causing it to emit radiation at the same frequency as the incident photon, in a spherical pattern. If the scattering occurs at different atoms in the system, the resulting waves can interfere constructively or destructively. Constructive interference occurs when the path length difference is an integer number of the wavelength, as described by the Bragg equation:

$$n\lambda = 2d \sin \theta$$

where n is the order of diffraction, λ is the wavelength of the X-ray radiation, d is the spacing between a well-defined set of crystal planes and the diffraction angle is 2θ . The effect of constructive interference is maximized where this equation is satisfied for each set of crystallographic planes in the crystal lattice. Each Bragg reflection is consequently labelled with three integers, (hkl) , describing the respective crystallographic planes (Miller indexes). Reflection positions and intensities provide characteristic diffraction patterns for database-assisted crystal identification or structure determination, while peak shape and width can be used to determine average crystalline domain sizes by means of the Scherrer equation.^[200]

PXRD is normally carried out with the starting assumption that the sample is isotropic, meaning that during the data collection every possible orientation of the crystalline domains is sampled with equal probability. If this condition is satisfied the diffraction spots are averaged into cones and the diffraction pattern can be reduced to a 1D profile. However, this loss of information complicates structure resolution, and modern computer-assisted methods are necessary for structure refinement (such as the Rietveld refinement or the Pawley refinement).^[201]

The two most employed measurement configurations in PXRD are the Bragg-Brentano and Debye-Scherrer geometries. In both the configurations, the X-ray source and the X-ray detector are mounted on the opposite sides of the instrument, and their relative position is controlled by a goniometer. The sample is positioned at the center of the goniometer. In the Bragg-Brentano (reflection) geometry, the sample lays flat and horizontal. A divergent X-ray beam is focused onto the sample at a variable angle (θ). The X-rays that interact with the sample and are reflected are collected on the opposite side by the detector at twice the angle of incidence (2θ). In the Debye-Scherrer (transmission) geometry the sample is placed in a glass capillary that is mounted on a rotating holder. The X-ray incident radiation is collimated to produce a parallel beam that is directed on the sample. The X-rays that pass through the sample and are diffracted are then captured by the detector positioned on a circular track at a fixed distance from the sample. The Debye-Scherrer geometry is particularly

suitable for small sample quantities and enables the collection of a complete diffraction pattern in a single measurement. Moreover, in contrast to the Bragg-Brentano geometry, the distortions generated on the 1D diffractogram by samples with preferential orientation of the crystalline domains is reduced.

PXRD diffractograms in reflection have been acquired in air using a D8 Advanced with twin-twin optics (Bruker). The diffraction patterns of the powder samples have been acquired in 2-40 (2θ) range in Bragg-Brentano configuration, using Cu $K\alpha$ radiation ($\lambda=1.5418 \text{ \AA}$) at 40 kV and 40 mA and a LINXEYE 2 detector. Two 2.5 mm Soller Cu slits have been applied to the primary and secondary optics. In the latter, a Ni stopper has been added to filter Cu $k\beta$ radiations. An automatized blade has been mounted to limit the contribution of air scattering at low angles. The data has been acquired with a step of 0.02° and an acquisition time of 1 s per step.

PXRD diffractograms in transmission were performed on a Stoe Stadi P diffractometer (Cu- $K\alpha_1$, Ge(111)) in Debye-Scherrer geometry. The samples were sliced into thin pieces and were measured in sealed glass capillaries (diameter = 1.0 mm) and spun for improved particle statistics. Each powder pattern was collected in a 2θ range from 0° to 40° with a total scan time of 3 hours.

From the XRD diffractograms the peak position was calculated using the Bragg's law:

$$d_{hkl} = \frac{\lambda_{Cu K\alpha}}{2 \sin \theta}$$

Where d_{hkl} is the calculated inter planar distance (in \AA), $\lambda_{Cu K\alpha}$ is the wavelength of the XRD source (1.5406 \AA), θ is the scattering angle (radians). The crystallite dimension was derived from the Scherrer formula:

$$\tau = \frac{K \lambda_{Cu K\alpha}}{\Delta \cos \theta}$$

Where τ is the crystallite dimension (in \AA), K is the shape factor (0.89) and Δ is the broadening in radians.

2.2.2. Structural simulations and refinements

Structure modeling was initially performed with BIOVA Materials Studio 2017 (17.1.0.48. Copyright© 2016 Dassault Systèmes) software. Rietveld refinements were performed using TOPAS v6. The background was corrected with Chebychev polynomials (Order 7). Simple axi-

al and zero-error corrections were used together with additional corrections for Lorentzian crystallite size and strain broadening. The LP factor was adjusted for the device and fixed at 27.^[202]

2.2.3. Grazing-Incidence Wide-Angle X-ray Scattering (GIWAXS)

Grazing-incidence XRD (GIXRD) is a valuable technique used to analyze the crystallinity of very thin surface layers of materials.^[203] By irradiating the sample with a parallelly collimated X-ray beam at a very low incidence angle ($< 1^\circ$) the interaction between the X-rays and the surface is maximized. GIXRD measurements are carried out in a specific geometry, where the sample plane is defined by x and y, and the z-axis is perpendicular to it.

GIXRD data is usually recorded using 2D detectors, providing information about the orientation of crystal lattices and insights into the morphology and roughness by analyzing the diffuse scattering of the film. GIXRD experiments differentiate between GI wide-angle X-ray scattering GIWAXS and small-angle X-ray scattering GISAXS depending on the 2θ ranges. GIWAXS experiments generally use 2θ between 1.5° and 40° , while GISAXS experiments use angles less than 1.5° (for Cu K α radiation).

GIWAXS scattering patterns were collected with a Bruker D8 GADDS system (Cu K α lamp, Goebel mirror point beam collimation) equipped with a Vantec2000 area detector. Silver behenate and silicon powder were used as low- and high-angle calibration standards, respectively. The scattering patterns were recorded by using an incidence angle of 1° and a detector angle of 12° . Alternatively, larger scattering images were created by combining two scattering patterns obtained with an incidence angle of 1° and detector angles of 8° and 18° , respectively.

2.2.4. Gas sorption measurements

Gas sorption measurements are an essential tool for characterizing porous materials in terms of pore volume, pore size distribution, and surface area. The measurement of the nitrogen adsorption-desorption under isothermal is the most common experiment. Nitrogen sorption is classified as physisorption, as only weak van-der-Waals forces occur between the gas and the material.^[204] The isotherm plots present the adsorbed volume of gas against the relative pressure, which is determined as the ratio of the equilibrium pressure p to the saturated vapor pressure p_0 of the pure adsorptive. To carry out the measurement, a sample is first activated under a high vacuum and elevated temperatures to eliminate any guest mole-

cules from the pores. For the measurement the sample in the analysis chamber is exposed to increasing amount of gas while the relative pressure p/p_0 rises, thus producing the adsorption isotherm. The desorption isotherm is obtained by removing the gas from the analysis chamber thus reducing the relative pressure p/p_0 . The entire procedure is carried out keeping the temperature constant (at 77 K).

The shape of the isotherm is closely related to the pore sizes and shapes of the material. Pore sizes can be divided into three categories, namely micropores (< 2 nm), mesopores (2–50 nm), and macropores (> 50 nm). Six different isotherm types are classified by IUPAC, each describing different pore structures, sizes, and surface interactions.^[205]

The simplest mathematical model to describe the phenomenon of physisorption is the Langmuir model, which assumes monolayer formation on a homogeneous surface with equal binding sites and no interactions between adsorbed molecules. The Brunauer-Emmett-Teller (BET) model extends the Langmuir model by including multilayer formation.^[206] According to this method a BET plot is constructed from the adsorption profile in the low relative pressure range. The resulting curve is fitted using the BET equation:^[206]

$$\frac{1}{n(p_0/p - 1)} = \frac{1}{n_m C} + \frac{C - 1}{n_m C} (p/p_0)$$

Where n is the specific amount of the adsorbed gas at the relative pressure p/p_0 , n_m is the monolayer capacity of the adsorbed gas, p is the pressure, p_0 is the saturation pressure, and C is the BET constant (which is related to the energy of monolayer adsorption). The specific surface area a_s is obtained from the value of the monolayer capacity n_m according to the following equation:

$$a_s = n_m \cdot L \cdot \sigma_m / m$$

Where σ_m is the N_2 cross-sectional area, L is the Avogadro constant, and m is the mass of N_2 . However, the accuracy of the BET method can be limited in highly polar environments due to the quadrupolar moment of nitrogen molecules, which can lead to overestimation of surface areas. In such cases, argon can be used as an alternative adsorptive since it has no quadrupolar moment.

The determination of pore size distributions can be implemented using the Kelvin equation, which describes the thermodynamic relationship between the reduced pore radius and the relative vapor pressure. The Barrett-Joyner-Halenda (BJH) model extends the Kelvin equation by including the thickness of the monolayer. However, these models have limita-

tions in describing inhomogeneities on surfaces and assuming only perfectly ordered layers. Density functional theory (DFT) based calculations can overcome these limitations. Two different types of modeling are currently utilized for this purpose: non-local density functional theory (NLDF) and quenched-solid density functional theory (QSDFT). NLDF, while commonly used, neglects important factors such as surface roughness and heterogeneity, whereas QSDFT is a more recent development that takes these factors into account.^[204]

The nitrogen sorption measurements reported in chapter 3 were performed on a Quantachrome Instruments Autosorb iQ MP with Nitrogen at 77 K. The samples were degassed for 12 h at 120 °C under vacuum prior to the gas adsorption studies. The pore size distributions (PSD) were calculated with a model of N₂ at 77 K on carbon using the QSDFT (cylindrical pores, adsorption branch) in AsiQwin software v3.01. BET analyses were conducted using a program written by Alexander M. Pütz (<https://github.com/AlexanderPuetz>) in the Lotsch group based on the software BETSI by Osterrieth and Fairen-Jimenez.^[207] The fitting ranges were selected to meet all Rouquerol criteria and to minimize the pressure error of monolayer loading.

The nitrogen sorption measurements reported in chapter 4 were recorded on a Micromeritics ASAP 2050 surface area and porosity analyzer at 77 K and pressure up to 1 bar. Before the measurements, the samples were activated for 12 hours at 120 °C in vacuum. For multipoint BET surface area calculations, the partial pressure range of 0.05-0.35 was chosen.

2.3. Morphological Characterization

2.3.1. Scanning Electron Microscopy (SEM)

Scanning electron microscopy (SEM) is an imaging technique used to investigate the morphology of a sample at the nanoscale.^[208] SEM utilizes a focused electron beam produced by field emission gun with accelerating voltages between 0.1 and 30 kV in vacuum. The beam is scanned on the surface of the sample in a grid pattern. The interaction between the beam (primary electrons) and the sample generates the emission of several different signals that carry the information about the morphology and the composition of the analyzed material. Depending on the acceleration voltage used the primary electrons can penetrate at different depths in the sample and different information can be detected. The detected signals include backscattered electrons (primary electrons that are backscattered from the sample), secondary electrons (lower energy electrons expelled from the sample due to inelastic scatter-

ing of the primary beam), and element-characteristic X-ray radiation. The image can be created from the intensity map of the secondary electrons. Furthermore, the emitted X-ray radiation can be used to determine the elemental composition of the sample by energy-dispersive X-ray spectroscopy (EDX).

All SEM images in the thesis were obtained using a FEI Quanta 250 FEG microscope operated in high vacuum mode (10^{-6} mbar), with accelerating voltages of 10-30 kV for the incident beam.

2.3.2. Transmission Electron Microscopy (TEM)

Transmission electron microscopy (TEM) is an imaging method that provides resolutions up to the atomic-scale.^[208] This technique uses very highly accelerated electrons (60-300 kV) in ultra-high vacuum and is limited to thin samples (< 100 nm). In TEM the entire area of imaging is irradiated at the same time by the beam that is focused by a series of electromagnetic lenses. The image results from the fraction of electrons that are transmitted through the sample and interacted with it through scattering or diffraction. The resolution offered by TEM can reach few tens of a nanometer, making it a fundamental tool for the investigation of the atomic structure of materials, their crystallographic features, and their defects. However, factors such as spherical aberrations, chromatic aberrations, and astigmatism, can limit the resolution achievable. Moreover, the stability of the material in analysis of the high-energy electron beam is a factor of crucial importance in TEM.

TEM and HR-TEM images were obtained from a Philips Tecnai F20 transmission electron microscope equipped with a 200 kV field emission gun.

2.3.3. Atomic Force Microscopy (AFM)

Atomic Force Microscopy (AFM) is a widely utilized technique for analyzing surface topography at the nanometer scale.^[208] AFM probes comprise a sharp tip connected at the end of a cantilever that is raster-scanned across the surface of the sample in analysis. This process causes the deflection of the cantilever due to the forces between the tip and the surface. The magnitude of the deflection is detected and used to recreate an image of the topography of the sample. Three main imaging modes are possible: contact, tapping, and non-contact modes. The mode selected is dependent on the properties of the sample and the desired outcome. The contact mode is the most straightforward mode, and it provides high-resolution images of the topography by tracking the displacement of the extremity of the

cantilever with the tip is in mechanical contact with the surface. However, imaging soft samples can be challenging, as the tip can damage the surface. Additionally, the frictional forces can create artifacts in the image. In the tapping mode the cantilever is oscillated at a frequency slightly below its resonance and the tip is in intermittent contact with the surface, reducing the forces applied to the sample. This mode is frequently used to image soft or fragile samples. Non-contact mode is used to image very fragile or easily damaged samples. In this mode, the cantilever oscillates at slightly above its resonance frequency, and the tip interacts with the sample through Van der Waals forces. This mode is sensitive to the long-range forces between the tip and the sample and can provide information about the chemical and physical properties of the sample surface.

Probe material selection is also crucial for optimal imaging. For example, silicon nitride (Si_3N_4) tips are commonly used for contact mode imaging of hard materials, while silicon (Si) tips are used for intermittent contact imaging of soft materials. The tips are frequently coated with metals such as gold (Au), platinum/iridium (Pt/Ir), or aluminum (Al) to enhance the resolution and sensitivity of the AFM imaging.

AFM images were recorded with a Bruker Dimension Icon microscope under ambient conditions, operating in tapping mode and using TESPA-V2 tips with spring constant $k = 42 \text{ N m}^{-1}$. The images were captured at a scan rate equal to 1.0 Hz with 1024 lines per image.

2.4. Optoelectronic and Electrochemical characterization

2.4.1. UV-vis absorption spectroscopy

UV-vis absorption spectroscopy is used to study the phenomenon of light absorption and enables insights into the electronic structure of materials. ^[209] With different variants of this technique, it is possible to investigate solutions, bulk material, or thin films.

The sample is irradiated by electromagnetic light spanning from the ultraviolet (200-400 nm) to the visible (400-800 nm) but also the NIR region can be explored (800-2500 nm). The absorbed light induces electronic transitions from the highest occupied molecular orbital (HOMO) to the lowest unoccupied molecular orbital (LUMO).

In the simplest case, *i.e.* the study of a molecule in solution, the absorbance A at a certain wavelength λ is defined by the Lambert Beer law on the base of the transmitted intensity I and the intensity of the incident beam I_0 :

$$A(\lambda) = -\log_{10} \frac{I(\lambda)}{I_0(\lambda)} = \varepsilon(\lambda) c L$$

where $\varepsilon(\lambda)$ is specific absorption coefficient, c is the molar concentration, and L is optical path length. For not completely transparent samples, scattering particles can create difficulties in the determination of absorbed light. A solution is the use of an integrating sphere that collects all the scattered light eliminating this problem.

Diffuse Reflectance Spectroscopy (DRS) is a variant of UV-visible absorption spectroscopy that is used to investigate the light-absorption properties of the surface of materials. DRS measures the difference in the reflectance of the sample and a reference material as a function of the wavelength.

UV-vis spectroscopy can be employed for the determination of the band gap energy for semiconducting materials with a direct band gap. This is done by fitting of the linear region of the Tauc plot, obtained by mathematical transformation of the absorption spectrum.^[210]

The UV-Vis absorption spectra in solution were recorded in a 1 cm quartz cuvettes using a V-670 UV-Vis-NIR spectrometer (Jasco) equipped with a PAC-743R (Jasco) Peltier cell changer. The UV-Vis absorption spectra of thin films were recorded using a PAC-743R integrating sphere (Jasco) in transmission geometry. The UV-Vis absorption spectra of powders grinded in BaSO₄ were obtained using the same setup, but in diffuse reflectance geometry. All spectra were baseline corrected and processed using the Spectragryph software “simple baseline” algorithm.

2.4.2. Charge transport measurements

To characterize the charge transport properties of a material a sourcemeter is a fundamental tool. A sourcemeter, also known as source measure unit (SMU) is a measuring device that combines a direct current (DC) power supply, current source, and a sensitive multimeter in a single unit. With this instrument it is possible to apply variable voltage and current and record electric signals through multiple channels. It can also include a pulse generator, thereby integrating all these functions into the same housing. When connected to a device to be characterized, a SMU can force voltage or current through the circuit and simultaneously measure the voltage and current in the device. For the measurement to be performed a physical contact is necessary. The electrical properties of a material can be determined through two, three, or four-terminal setups, depending on the type of experiment.^[178]

Two-terminal measurements are the most straightforward experiments used to determine

the electrical response of a device. The measurement involves the application of a voltage to the source and drain electrodes to assess properties related to the resistivity of the device. It should be noted that the resistive contributions from the leads are also included, making the measurement more representative of the actual operation of a device, but potentially introducing additional unwanted contributions to the electrical properties of the material. Some commonly employed two-terminal measurements include chronoamperometry, which involves measuring the current versus time at a constant bias voltage, and current versus voltage (I-V) curves, which measure device resistivity by sweeping the voltage.

Three-terminal measurements involve the use of a third electrode to apply an additional bias voltage to the device. In particular, in an OFET device the material is contacted with a gate electrode, which can alter the charge carrier density in the conductive channel by changing its potential. Transistor characteristic curves, including transfer (gate voltage sweep at constant source-drain bias) and output (source-drain voltage sweep at constant gate bias) curves, are commonly employed in three-terminal measurements to determine OFET parameters such as charge carrier mobility, subthreshold slope, and threshold voltage.

Four-terminal measurements are valuable when intrinsic electrical properties of the material must be assessed without interference from the charge carrier injection electrodes. Four probes, or electrodes, are typically arranged in a line for classical 4-point probe measurement or in a square for Van der Pauw measurements. In the line configuration, a bias voltage is applied at the external electrodes to drive a constant current through the conductive channel, with the two internal electrodes serving to record the potential drop at a known distance. From this, the resistivity of the material can be derived from the ratio of the current value that passes through the channel and the voltage drop measured between the two internal electrodes at the known distance.

In chapter 4 the electrical characteristics were measured by a Janis cryogen-free probe station (Lake Shore CCR5) equipped with Keithley 4200A-SCS parameter analyzer at room temperature and under vacuum (2 mbar) or air atmosphere.

In chapter 5 a Keithley 2636B SYSTEM SourceMeter was used for the two and three-terminal electrical measurements. Four-terminal measurements were carried out on a Jan-del probe, Model RM3000.

2.4.3. Electrochemical impedance spectroscopy (EIS)

Although SMUs are commonly used for DC and pulse experiments, potentiostats and im-

pedance meters are prevalent in the field of electrochemistry and AC measurements. Electrochemical impedance spectroscopy (EIS) is a versatile and non-invasive analytical technique that combines AC and DC inputs for the electrical characterization of materials, and it is particularly valuable in the analysis of electrochemical systems.^[211] EIS data correlates the electrical current and applied voltage in the frequency domain. During an EIS experiment, the electrochemical system under study experiences a small perturbation in the form of a sinusoidal signal of voltage (in potentiostatic mode) or current (in galvanostatic mode). The resulting data set is a complex function, called impedance (Z), which depends on the signal frequency. From the analysis of the EIS data, it is possible to identify and describe the elementary steps of a global mechanism, such as the double layer charging, electrochemical charge transfer, mass transport, and adsorption. To analyze EIS spectra, Z is fitted with equivalent circuit models comprising various electrical elements, such as resistors, capacitors, inductors, or other generalized impedance elements, resulting in a finite circuit whose behavior can be mathematically described.

The EIS experiments were executed with an Autolab PGSTAT 128N instrument.

2.4.4. Cyclic voltammetry

Cyclic Voltammetry (CV) is a powerful electrochemical technique used for the study of redox reactions and the determination of electrochemical parameters of a molecule or a material.^[212] The method involves applying a linear change in potential to a working electrode, while monitoring the resulting current. CV is typically performed with a three-electrode system consisting of the working electrode, counter electrode, and reference electrode immersed in a solvent containing the electrolyte. The analyte is either dissolved in the solution or, if insoluble it is grinded in solvent together with an inert binder polymer and then applied as coating on the working electrode. The current is measured between the working and counter electrodes, while the potential is measured between the working and reference electrodes. This setup allows for precise control and measurement of the electrochemical reactions occurring at the working electrode, while maintaining a stable electrochemical environment through the use of the counter and reference electrodes. The electrode potential is scanned in a predetermined window at a fixed scan rate, and the resulting current is plotted against the applied potential. When the potential of the working electrode reaches a specific value, a current starts to flow, indicating the beginning of an electron transfer between the electrode and the redox-active substance. The potential is swept in a cyclic man-

ner allowing for the observation of both oxidation and reduction peaks. The analysis of the peak position, intensity, and shape can be used to obtain valuable information about the redox properties of the species involved in the reaction, including their oxidation and reduction potentials, electron transfer rates, and diffusion coefficients.

The measurements reported in chapter 4 were carried out using a three-electrode system setup with a Pt-wire as counter electrode and an Ag/AgCl as reference electrode. The powder material was grinded with a small quantity of N-methyl-2-pyrrolidone (NMP) and polyvinylidene fluoride (PVDF) as binder and deposited on a glassy carbon electrode for the measurement. The material was dried from the solvent in vacuum overnight. The measurement was run in dry MeCN previously degassed with argon maintained under continuous argon flux during the measurement. 1 M tetrabutylammonium tetrafluoroborate (NBu_4BF_4) was used as electrolyte. A scan rate of 10 mV/s was applied, and the potential was swept positively first. As a reference, after running the measurement a small amount of ferrocene was added to the sample and measured.

The CV experiments were executed with an Autolab PGSTAT 128N instrument.

3. Kinetic suppression of nucleation enabling strain crystallization of oriented self-standing 2D COF films

3.1. Oriented and self-standing 2D COF films

2D COFs are a highly tunable, crystalline, and porous materials that have been considered promising for a range of applications.^[2] The true potential of 2D COFs arises from the 2D macromolecular nature of their covalent backbone, which places them among the family of topologically planar 2D materials that also includes graphene and transition-metal dichalcogenides (TMDC).^[213] Furthermore, in contrast to other 2D materials, 2D COFs possess a honeycomb 2D lattice, intrinsic to the topology of the building units. Stacking of these 2D layers results in the emergence of a higher-order structure, constituted of alternating π -stacked columns and 1D pore channels.^[74] Modifications of the chemical structure of the building units, offer the possibility of fine-tuning the pore size, the topology, the chemical functionality, and chemical bonding. This systematic approach provides easy access to the development of new materials with pre-designed properties that may have promising applications across various fields.

In particular, the application of 2D COFs for energy-efficient membrane-based separations is one of the most promising area of research.^[214] 2D COFs offer excellent thermal and chemical stability and their porous structure can be rationally designed to have specific chemistry and size. 2D COFs can be synthesized with 1D pore channels with diameters ranging from 0.6 to 6 nm, and while they are too large for efficient gas separations, they may be ideal for liquid-phase molecular nanofiltration.^[214] Up to date 2D COFs-based membrane have been tested for the selective separation of salts and organic dyes.^[215] However, the full potential of 2D COFs in this field is hampered by the discontinuous morphology and the randomly oriented polycrystalline nature of the material that is typically produced with the conventional polymerization methods.^[216] Consequently, these polycrystalline materials consists of non-oriented crystalline domains and amorphous regions, which is very far from the idealized structure with continuous and aligned 1D pore channels.

In this regard, the morphological modulation during 2D COF synthesis is often overlooked despite its paramount impact on the material properties. By controlling the reaction condi-

tions, it is in theory possible to obtain 2D COFs with distinct morphologies, such as spheres, fibers, films, foams, or more elaborated hierarchical structures.^[94] These variations in morphology can confer unique properties to COF microstructures, making them more appropriate for specific applications.^[9]

The realization of molecularly precise membranes for selective separation processes requires highly crystalline and oriented films. Therefore, a frontier in the development of 2D COFs is the synthesis of continuous, self-standing, mechanically robust, and oriented films. However, like thermosetting polymers, 2D COFs do not melt and are not soluble in any organic solvents, and consequently they cannot be post-synthetically processed into films. To address this issue, bottom-up interfacial polymerization methods have been developed to prepare membranes (μm -sized thick films), thin films (from hundreds of nm down to few layers) and even single-layer materials.^[115] The class of interfacial polymerizations include solid-liquid, air-liquid, and liquid-liquid methods. While the preparation of films at the solid-liquid interface can occasionally lead to highly oriented materials, the prepared thin films are generally strongly adherent to the supporting substrate.^[119,134,173,217] If both liquid-liquid and liquid-air methods have been developed for the preparation of self-standing films, air-liquid interfacial synthesis is typically dedicated to the preparation of few-layers or monolayer materials,^[123,124,218] while liquid-liquid interfacial synthesis represents currently the most appealing method for the preparation of self-standing membranes.^[129,130] Because the mechanism of formation of the crystalline films typically relies on the growth and coalescence of 2D COF particles or fibers, these materials generally display low orientation and poor mechanical properties.^[128,219] For this reason, a method to prepare free-standing, mechanically robust, oriented 2D COF films needs to rely on alternative mechanisms. In this regard, a general method for the synthesis of high-quality films is still missing. In particular, the kinetic and thermodynamic aspects of the crystallization process are often poorly investigated or overlooked, while proper understanding of these fundamentals is crucial to the modulation of the morphology and the crystallinity of the material.

Currently imine linked 2D COFs constitute the most widely utilized class of these materials.^[41] While for boronic-ester 2D COFs the crystallization is based on a classical nucleation-growth mechanism, for imine COFs a less obvious crystallization mechanism appears to be in place. Pioneering studies focusing on the isolation of the reaction intermediates, indicated the quick formation of crosslinked 3D polymeric network precipitate, that subsequently undergoes a slow amorphous-to-crystalline transition at the solid state to generate the ordered material over several days at elevated temperature.^[42] A similar mechanism was

found for homogeneously grown 2D COF nanoparticles through a colloidal polymerization approach and supported by *in-situ* techniques.^[102] More recent reports seem to dispute the previous finding proposing a mechanism in which the reaction does not produce a cross-linked polymer network, even at the initial stages of the reaction. Instead, the process proceeds through the fast formation of micrometer-sized few-layers 2D sheets with random alignment along the *c*-axis, which slowly rearrange to form a 2D COF with an ordered layer alignment.^[103]

In this chapter we show a method to prepare free-standing, mechanically robust, oriented 2D COF films that relies on the kinetical trapping of the amorphous polymer network phase, rather than on the thermodynamic control over the material growth. A combination of trifluoroacetic acid (TFA) and water as a solvent enabled the processing of a solution of low-molecular weight polyimine (**PI_m**) into a polymer film by the solution casting method. Owing to the capillary forces-related tensile stress exerted on the drop-cast mixture during the drying process the generated film displayed an unprecedented highly oriented layered structure, but low crystallinity. A post-synthesis re-crystallization protocol facilitated the conversion of this amorphous **PI_m** film into a highly crystalline and porous 2D COF membrane, simultaneously preserving the high orientation of the pristine material. Furthermore, we investigated the mechanism of the polymerization reaction in solution and at the solid state with the full step-by-step description of the system. We show that the polymerization resulted in a 3D rather than 2D structure behaving like amorphous branched polymer network with a distinct gel point, owing to the suppression of the auto-templating effect derived from the interlayer interactions by the protonation of imine linkages by TFA.^[220,221]

It is our belief that our research will contribute to the development of the methodologies for the preparation of 2D COF in a radically new direction by drawing new connections with the consolidated field of polymer networks.

3.2. Synthesis by polymer solution casting

The first example reporting the use of a water-TFA mixture to process 2D COFs into thin film is a top-down method reported by Burke in 2020.^[10] They demonstrated that imine-based 2D COF powders could be exfoliated and dissolved in organic solvents by protonation of the basic linkages by TFA and at least partial hydrolysis of the 2D macromolecules to smaller oligomers thanks to the presence of water. The generated dispersions could be processed into the film morphology by the spin coating technique. In a more recent study,

Barnes *et al.* found that the binary water-TFA mixture can be directly employed as solvent and catalyst for the formation of imine-linked 2D COFs.^[11] By doctor-blading a solution of 1,3,5-tris(4-aminophenyl)benzene (**TPB**) and terephthalaldehyde (**TP**) on a flat substrate, a crystalline and self-standing film of **TP-TPB-COF** is formed after the solvent evaporation. However, none of the reported materials displayed any preferred orientation of the crystalline domains.

Here, we demonstrate that under specific conditions highly oriented, self-standing films can be synthesized from a water-TFA solution of **PIm**. We investigated the mechanism of formation of the oriented film and our findings indicate that the crystallization does not take place through the nucleation-growth-assembly-coalescence of particles but rather with a mechanism that involves the formation of a series of intermediate states: namely an amorphous **PIm** gel which upon drying collapsed into a poorly crystalline but highly oriented **PIm** film. We show that the reaction in solution proceeded through step-growth polymerization and displayed a defined sol-gel phase transition and forms a chemical gel which recrystallizes in time into 2D COF particles. When the reaction was carried out in a cast droplet, the outward tensile stress generated by the evaporating solvent induced the deformation of the gel, while the fast rate of the evaporation kinetically suppressed the nucleation of 2D COF particles. Eventually, the strain induced the alignment of the polymeric network and the crystallization of a continuous and oriented **PIm** film with the stacking direction normal to its underlying substrate.

3.2.1. Synthesis of an oriented **PIm** film

The oriented **PIm** films were synthesized by polymer solution casting from a 5% water-TFA (v/v) polymer solution (**Figure 3.1**). To prepare the polymer solution, concentrated solutions of **TPB** and 2,5-dimethoxy terephthalaldehyde (**MeOTP**) were mixed in a stoichiometric 2:3 molar ratio at room temperature, resulting in a dark red ink, which indicated the formation of a protonated imine linkage. TFA which is both a good solvent and a mildly strong acid with a Hammett acidity function of $H_0 \approx -2$ catalyzed the Schiff-base reaction to quickly form a protonated **PIm** in solution. Noteworthy, water can be mixed with TFA up to 10 % in volume without changing the strength of the acidic media.^[222] The formation of a charged **PIm** prevented the π -interaction-induced aggregation between the polymer chains. Additionally, the presence of water precluded the formation of high molecular weight polymers and avoided precipitation of a solid up to high concentrations.

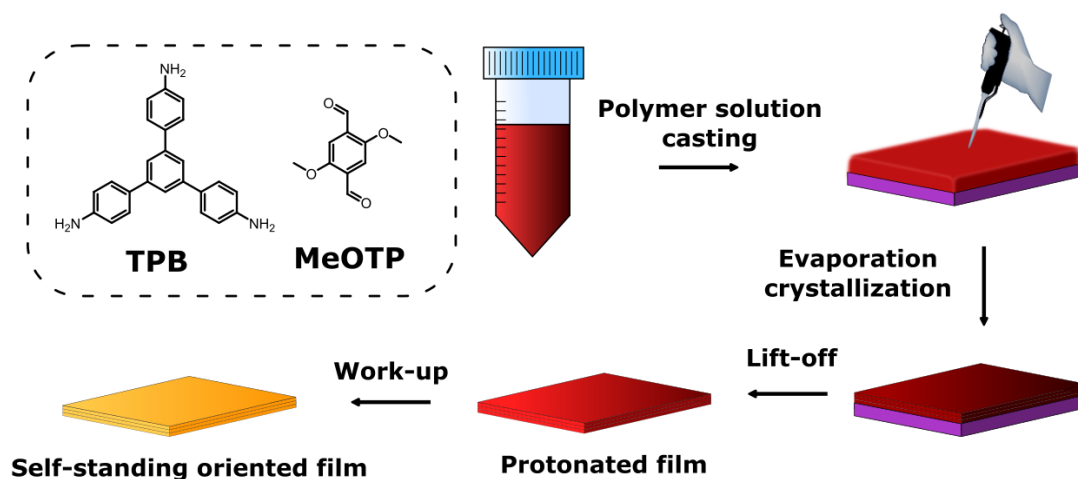


Figure 3.1 Schematic of the synthesis method: the polymer solution was processed by drop-casting and the evaporation of the solvent led to the formation of a poorly crystalline but oriented **Pim** film. The film was lifted off the substrate by immersion in MeOH and then neutralized with a TEA solution.

In a typical reaction, a squared silicon wafer of 15 mm side length was fully coated with a droplet of the $C_0 = 150$ mM solution (C_0 = functional group concentration) by drop casting, and the evaporation rate of the solvent was controlled by adjusting the temperature on a hotplate. The drying process was carried out in semi-enclosed environment which provided higher and more homogeneous solvent partial vapor pressure (a covered Petri dish of 5 cm in diameter and 1 cm of height). In absence of cover the abrupt and nonuniform solvent evaporation caused the cracking, the warping and the delamination of the film coatings.^[223] At 40 °C the reaction was complete after 4 hours and the homogenous dark-red light-reflective coating (**Figure 3.2a**) could be lifted-off the silicon wafer by immersion in a polar solvent such as methanol (MeOH). A dark-red colored self-standing film was obtained, and it could be easily manipulated without breaking (**Figure 3.2b**). The film was then washed with a triethylamine (TEA) solution in MeOH (10% v/v) to remove the residual adsorbed TFA. A color change from red to yellow indicated the successful neutralization of **Pim**.^[130,163] The material was then Soxhlet extracted with tetrahydrofuran (THF) for 12 hours to remove the unreacted monomers. After exchanging THF for *n*-pentane, solvent with a reduced surface tension of 15.5 mN m⁻¹, the film was dried in air at room temperature. Despite the low surface tension of *n*-pentane, if the material is left to dry flat on one side, it is subjected to substantial capillary forces that cause a permanent mechanical strain and the warping upward of the film edges.^[224] To avoid this problem and obtain a flat film the initial drying was carried out by hanging the film to achieve a uniform evaporation form both sides. After 1 hour

hanging, the material was further dried at reduced pressure overnight at 50 °C. Alternatively, the activation of the material by supercritical CO₂ equally yielded a flat film. The material was finally obtained as yellow, transparent film, with a yield of 95 % (**Figure 3.2c**).

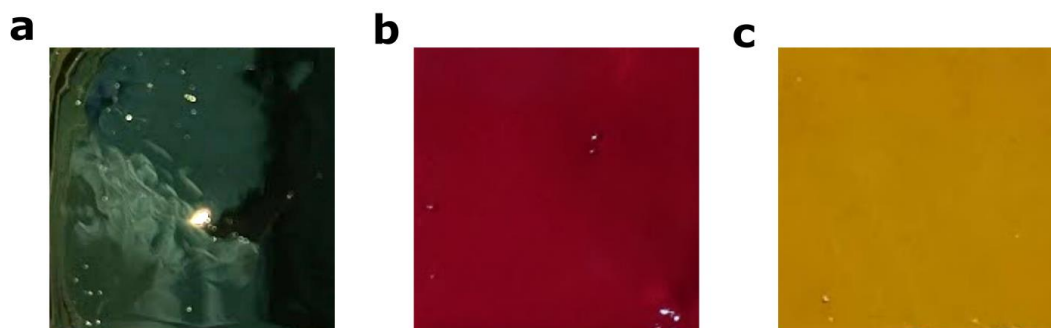


Figure 3.2 Camera photographs of the (a) “as synthesized” P1m film, containing a substantial amount of TFA; (b) P1m film after immersion in MeOH; (c) P1m film after the neutralization with TEA. Images size: 1.5 x 1.5 cm².

3.2.2. Morphological and structural characterization

Scanning Electron Microscopy

The films were imaged by Scanning electron microscopy (SEM) and the obtained micrographs showed a smooth and homogenous surface from the centimeter down to the micrometer scale (**Figure 3.3a**). The cross-section images (**Figure 3.3b-c**), indicated that the film was about 50 μm in thickness, and it was characterized by a clear layered morphology, with the layers stacking in the direction normal to the film face, as pages of a book. Such a highly organized morphology is reminiscent of bulk precursors of inorganic 2D materials and to the best of our knowledge is unreported for 2D COFs.^[225,226]

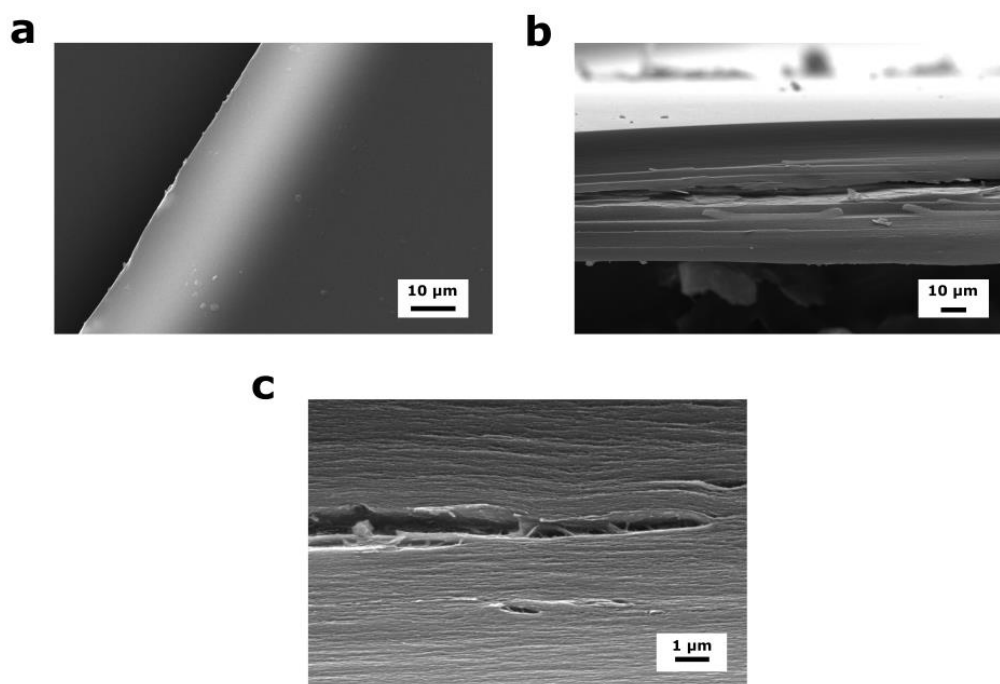


Figure 3.3 SEM images of the **PIm** film **(a)** top surface; **(b)** cross-section; **(c)** high magnification cross-section revealing the layered structure.

PXRD and 2D GIWAXS

The structural order of the film was analyzed by powder X-ray diffraction (PXRD), as well as by 2D grazing-incidence wide-angle X-ray scattering (2D GIWAXS). Notably, when the PXRD analysis carried out in the 2θ reflection geometry, it revealed a single, broad, yet intense diffraction peak at $2\theta = 25.3^\circ$ (**Figure 3.4a**). The reflection was ascribed to the local order generated by the π -stacking of the polymer chains, with an average spacing of $d = 0.35$ nm, while the substantial peak width indicated a weakly ordered material. The Scherrer analysis allowed the estimation of the structural coherence length from the peak breadth.^[200] The full width at half maximum (FWHM) of the reflection at 25.3° was determined as 6.0° which implied an average size of the semi-ordered domain of 1.3 nm along the π -stacking direction, equivalent to 3 – 4 polymer layers.

To explore the orientation preferences of the **PIm** film, the material was analyzed by 2D GIWAXS (**Figure 3.4b**). As expected, the scattering pattern was dominated by the π -stacking distance-related reflection. Remarkably, this peak was concentrated along the z direction, and together with two weaker reflections observed only in the xy direction (at 5.2° and 10.3° , **Figure 3.4c**), it indicated that the material presented a strong structural anisotropy. In particular, the polymer that constituted the film was oriented with the π -stacking

direction normal to the film face in which could explain the peculiar morphology observed by cross-sectional SEM.

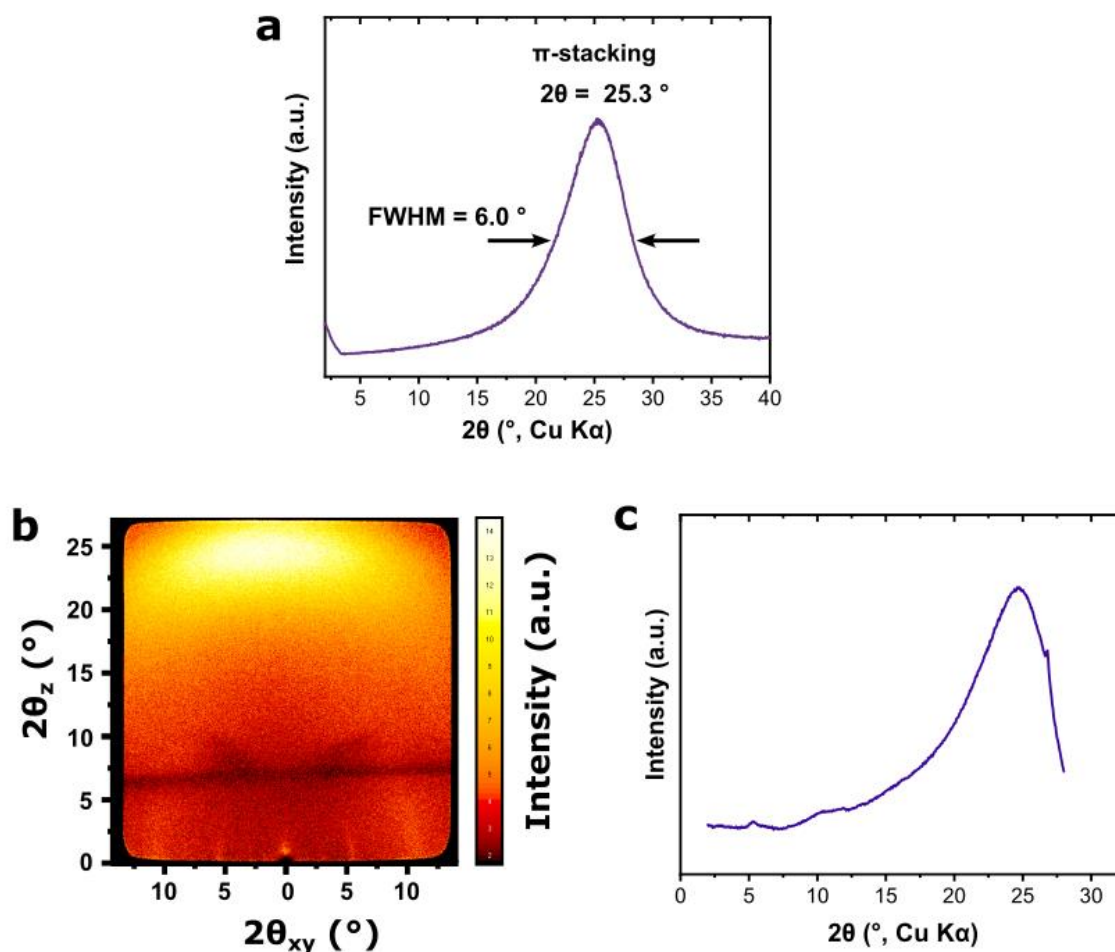


Figure 3.4 (a) PXR D of the PIIm film measured with a 2θ reflection geometry (Bragg-Brentano). (b) 2D GIWAXS of the PIIm film. (c) Radial integration of the 2D GIWAXS profile.

Nitrogen adsorption

The porosity of the material was probed by measuring a nitrogen adsorption-desorption isotherm at 77 K. As shown by the curves in **Figure 3.5** the material did not exhibit any relevant adsorptive property, with a total gas uptake at $p/p_0 = 1$ below $50 \text{ cm}^3 \text{ g}^{-1}$. These results clearly indicated that the PIIm film did not exhibit a porous structure, and consequently a very poor surface area (however, the estimation of the surface area was not carried out as, the low data quality did not allow for a BET Brunauer, Emmet, Teller analysis).

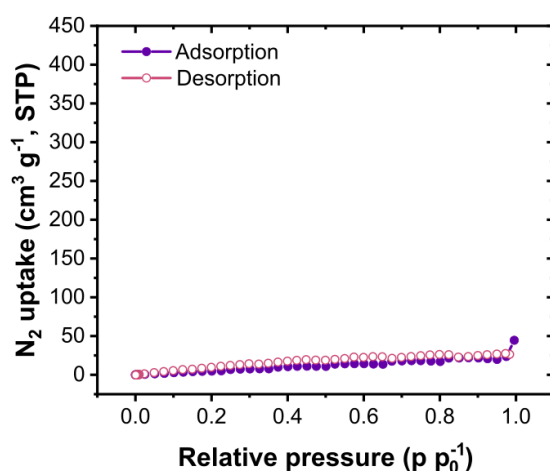


Figure 3.5 N₂ adsorption - desorption isotherm of PIIm.

3.2.3. Chemical characterization

Infrared spectroscopy

The presence of the imine bond after the polymerization at the solid state was verified by Fourier-transform infrared attenuated total reflectance (FTIR-ATR) spectroscopy (**Figure 3.6**). The spectrum obtained from the **PIIm** was compared with the spectra of the respective monomers and with the model compound **An₂-MeOTP** obtained by double Schiff-base formation reaction of **MeOTP** with aniline (**An**).

The spectrum of **MeOTP** (**Figure 3.6a**, yellow line) was characterized by two moderately intense bands at 2770 and 2760 cm⁻¹ characteristic of the aldehydic C-H stretching, an intense band at 1394 cm⁻¹ characteristic of the bending of C-H and a strongly absorbing C=O stretching vibration at 1668 cm⁻¹ which had an overtone centered at 3336 cm⁻¹. Moreover, aromatic, and aliphatic C-H stretching were also clearly visible with multiple absorption bands in the 3150-3000 cm⁻¹ and 3000 cm⁻¹ 2800 cm⁻¹ regions, respectively.

The spectrum of **TPB** (**Figure 3.6a**, grape-red line) showed two intense bands ascribed to the asymmetrical and symmetrical N-H stretching at 3442 and 3354 cm⁻¹, respectively. The N-H bending generated an intense band at 1605 cm⁻¹ which has an overtone at 3207 cm⁻¹ while the band originating from C-N stretching is clearly visible at 1278 cm⁻¹. At 1620 and 1513 cm⁻¹ two strong absorption bands were present, related to the aromatic ring modes. Finally, several medium-intensity bands in the range 3070-2960 cm⁻¹ could be ascribed to stretching of the C-H bonds connected to the aromatic rings.

The model compound **An₂-TPB** (**Figure 3.6b**, dark-blue line) was also characterized by

FTIR-ATR. The spectrum showed an intense band at 1614 cm^{-1} which was related to the stretching of the C=N bond and two intense bands at 1585 and 1574 cm^{-1} characteristic of the aromatic ring modes. The region between 3100 and 2800 cm^{-1} presented a sequence of medium-intensity bands that were related to the aromatic and aliphatic C-H stretching.

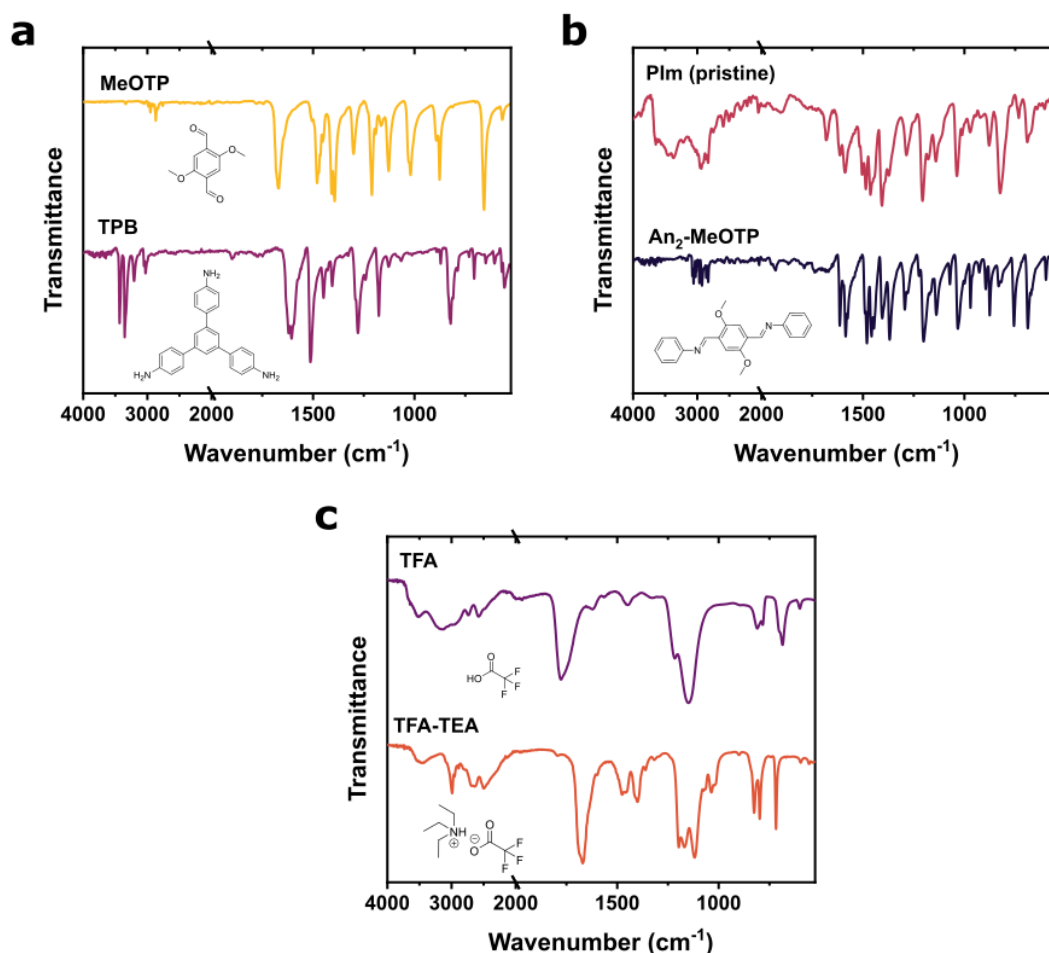


Figure 3.6 FTIR spectra of: (a) the monomers; (b) the PIm and the model compound An₂-MeOTP; (c) TFA and its salt with TEA (TFA-TEA).

In the FT-IR spectrum of the polymeric film (**Figure 3.6b**, red line) the stretching of the newly formed C=N bond was observed as a band of strong intensity at 1613 cm^{-1} , which corresponds to the value obtained for the model compound. At slightly lower frequencies, the aromatic ring mode was observed as an intense band with a maximum at 1588 cm^{-1} . A C=O stretching band of medium intensity was present at 1680 cm^{-1} , shifted by 12 cm^{-1} toward the higher frequency in respect to **MeOTP** which was ascribed to the formyl group of the mono-reacted aldehyde, that is a terminal group of a polymer branch. The related aldehydic C-H stretching generated two weak bands at 2760 and 2750 cm^{-1} . Finally, two bands at 3456 and

3375 cm^{-1} were present for the asymmetrical and symmetrical N-H stretching. As for the C=O stretching in the film, the maxima were shifted toward higher frequencies with respect to the monomer (by 14 and 21 cm^{-1} respectively) which was assigned to the NH_2 vibration of the terminal moiety. Moreover, the vibration modes of NH_2 overlapped with a broad band characteristic of O-H stretching, located between 3700 and 2700 cm^{-1} originating likely from the presence of the residual TFA and water trapped in the polymer matrix. Characteristic $\text{N}^+\text{-H}$ stretching bands were present at 2596, 2507, 2441 cm^{-1} and could be related to the presence of trapped TFA-TEA salt or to some residual protonation of the C=N linkage.^[227-229]

To confirm the assignments in the FTIR-ATR spectrum of **PIIm**, the spectra of TFA and the correspondent salt with TEA (TFA-TEA) were recorded and analyzed. The FTIR-ATR spectrum of TFA (**Figure 3.6c**, violet line) features a broad pattern in the range 3400-2500 cm^{-1} related to the O-H stretching hydrogen-bonded dimers, which is centered at 3000 cm^{-1} with maxima at 3520, 2578 and 2736 cm^{-1} . Furthermore, the carboxylic C=O stretching was observed as an intense band at 1778 cm^{-1} . A strong band characteristic of stretching in CF_3 moiety was visible at 1149 cm^{-1} . In comparison to TFA, in the spectrum of the TFA-TEA salt (**Figure 3.6c**, orange line), the OH stretching were missing and the region 3100-2800 cm^{-1} was occupied by the bands characteristic of the stretchings of C-H bonds in aliphatic chains which was consistent with the presence of TEA as protonated ammonium salt. The characteristic pattern of carboxylate ion consisting of asymmetric C=O stretching at 1671 cm^{-1} and weaker symmetric at 1401 cm^{-1} was distinguishable, proving the deprotonation of the acid. At 2688, 2635 and 2498 cm^{-1} the spectrum displayed the typical bands for a tertiary amine salt. Finally, an intense band characteristic of stretching in CF_3 moiety is present in the 1220-1090 cm^{-1} region.

3.3. Non-porous PIIm to oriented COF

3.3.1. Solvent annealing (recrystallization)

Despite the remarkable layered and oriented structure of **PIIm**, the overall long-range order of the material was found to be very limited, and the material did not show any adsorptive property. Moreover, the **PIIm** film contained trapped TFA and TFA salts. These guest species were highly stable: separately, no thermal treatment or extensive solvent Soxhlet extraction could remove them from the host polymer.

In the effort of improving the crystallinity and removing the trapped small molecules several recrystallization conditions were tested. After an extensive screening it was found that

annealing the film at 100 °C for 24 hours in MeCN with 10 M acetic acid (HOAc) could recrystallize the **PIm** to the corresponding **TPB-MeOTP-COF**. This treatment led to the opening of the pores thereby facilitating liberation of the entrapped species. The phase transition proceeded without any loss of the preferential orientation of the crystallites. The crystalline material was obtained in high yield 90% and while the original shape and size were preserved, the optical properties changed, from yellow translucent to gold opaque (**Figure 3.7**).

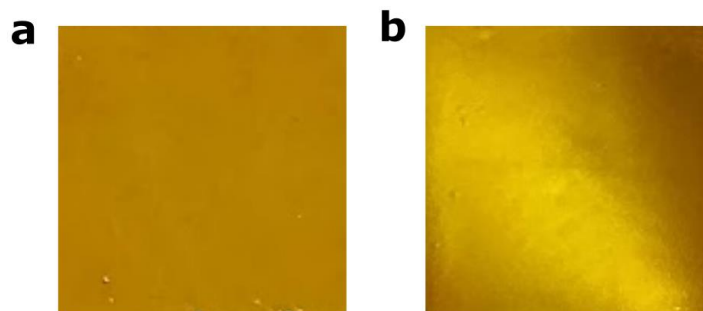


Figure 3.7 Camera photographs of the (a) film before the annealing; (b) film after the annealing. Images size: 1.5 x 1.5 cm².

3.3.2. Morphological and structural characterization

Scanning Electron Microscopy

While the macroscopic shape and size of the film were unchanged after the recrystallization, the microscopic morphology was drastically altered. The SEM analysis (**Figure 3.8**) showed that the recrystallized film was composed of coalesced elongated particles with about 1 : 3 aspect ratio (approximately 500 nm in length and 100 - 150 nm in diameter). These rod-like particles were aligned to compose a strongly anisotropic hierarchical assembly: 2 to 3 stacked arrays of rods assembled to generate a layer of material, with a thickness of about 1 - 2 μm . The overall film consisted of a stack of these layers along the direction normal to the film face, somewhat reminding the orientation of the layered polymer constituting the pristine material.

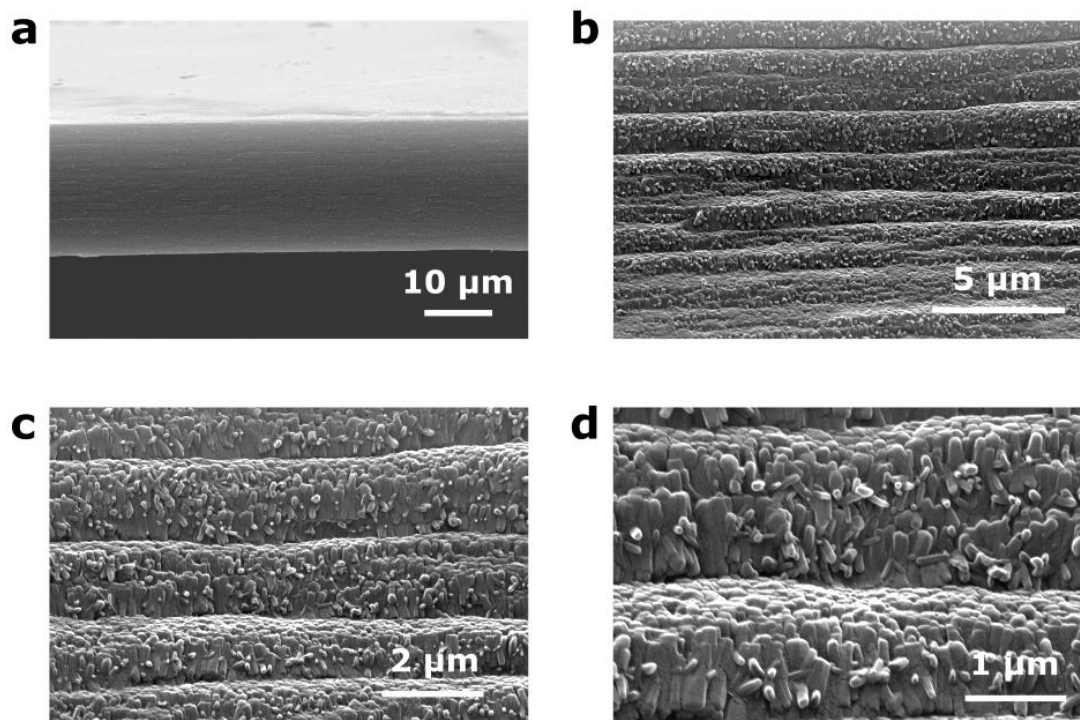


Figure 3.8 SEM micrographs of the cross-section of the film after annealing, at increasing magnifications from **a** to **d**.

PXRD and 2D GIWAXS

The evolution of the structural order upon annealing of the **TPB-MeOTP-COF** film was followed by PXRD both in transmission and reflection modes, as well as by 2D GIWAXS. PXRD in transmission was measured using a Co $K\alpha_1$ radiation and with sample packed in a capillary. The sample was spun to average any preferential orientation effect. The analysis revealed that upon recrystallization a highly crystalline material was obtained. Well-resolved reflections were present at 3.21, 5.58, 6.48, 8.60, 11.25, and 29.31 °, which were assigned to the (100), (110), (200), (210), (220) and (001) facets respectively.^[230] The pattern matched with a structure based on a ordered 2D polymer with a hexagonal topology and eclipsed AA-type stacking of the layers.^[32] Rietveld refinement was further used, and it well reproduced the PXRD pattern. According to the refinement, the structure adopted a P6/M space group symmetry with unit-cell parameters of $a = b = 36.35 \text{ \AA}$, $c = 3.56 \text{ \AA}$, $\alpha = \beta = 90^\circ$ and $\gamma = 120^\circ$. The overall good quality of the fit was confirmed by the low profile residual R_p and low weighted profile residual R_{wp} of 6.34 % and 8.73 %, respectively.

The measurement in reflection mode (Cu $K\alpha$ radiation) showed, as in the pristine **PIm**, a single and intense diffraction peak at 25.3 ° for the polymer π -stacking that in this case matches with the (001) plane (**Figure 3.9a**). As a result of the recrystallization the peak nar-

rowed from 6.0° to 1.5° which corresponded to an increase of the estimated average crystallite size to 5.3 nm along the c direction, equivalent to 15 - 20 COF layers.

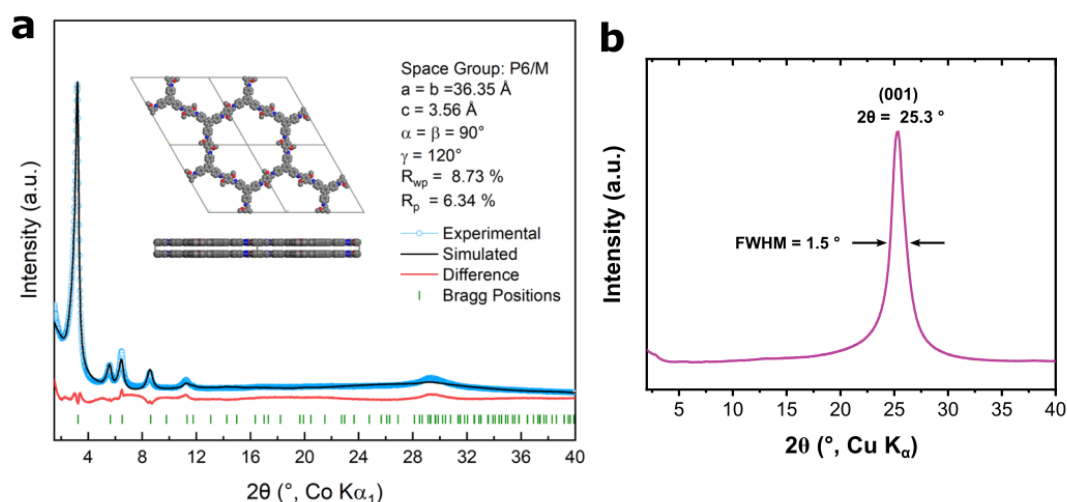


Figure 3.9 PXRD patterns of (a) the TPB-MeOTP-COF film measured in transmission (Co, $K\alpha_1$) with relative Rietveld refinement; (b) the TPB-MeOTP-COF film measured in reflection (Cu, $K\alpha$).

The 2D GIWAXS analysis on the recrystallized film showed high anisotropy with two sets of very sharp reflections oriented orthogonal to each other (**Figure 3.10**). The in-plane reflections for the $(hk0)$ planes were very well centered on the xy axis while the diffraction from the (001) plane was centered only on the z axis. The obtained pattern represented a clear signature of the high anisotropic nature of the 2D COF film, which was inherited from the alignment of the precursor **PIIm**.

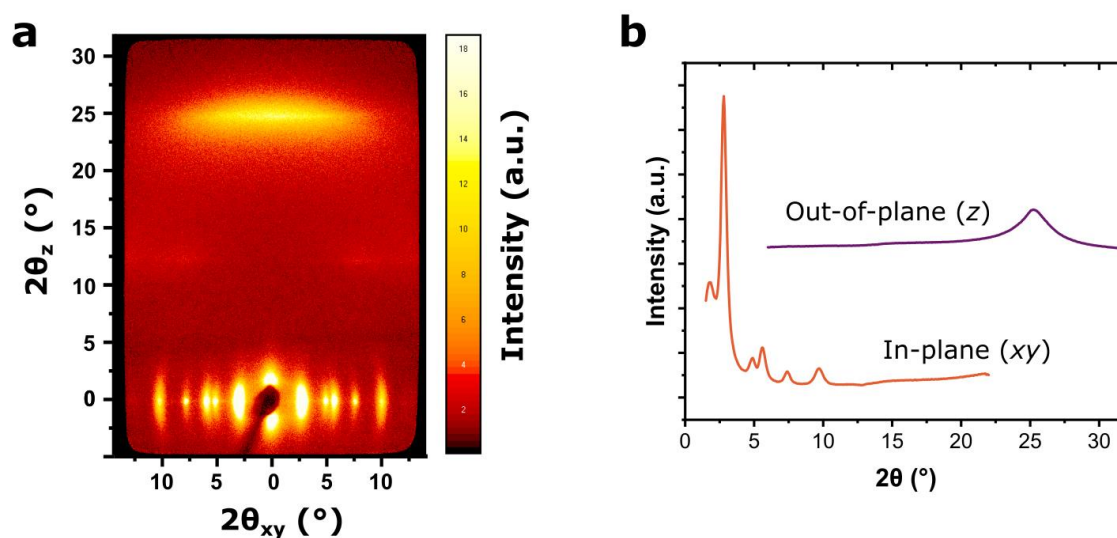


Figure 3.10 (a) 2D GIWAXS pattern of the recrystallized film (Cu, $K\alpha$). (b) Stacked plot of the in-plane (orange line) and out-of-plane (violet line) radial integrations of the 2D GIWAXS profile.

Nitrogen adsorption

The porosity of the specific surface of the recrystallized **TPB-MeOTP-COF** were investigated by nitrogen adsorption-desorption isotherm at 77 K (**Figure 3.11a**). The material displayed a rapid uptake at low relative pressure ($p/p_0 < 0.2$) followed by a step and a slower uptake at higher relative pressure ($p/p_0 > 0.3$), with a small hysteresis between the adsorption and the desorption branches. The shape of the curve allowed to classify it as type IV isotherm, which is typical of mesoporous materials.^[206] To evaluate the surface area a BET plot was constructed based the adsorption profile in the low relative pressure range. From the fitting of the data (see **Chapter 2** for more details) the BET specific surface area was determined to be $554 \text{ m}^2 \text{ g}^{-1}$, indicating the success of the recrystallization protocol in producing an ordered material with significantly higher porosity. The pore size distribution (**Figure 3.11c**), was calculated using the QSDFT method on the N_2 adsorption branch of the isotherm and assuming cylindrical pores. The plot showed a broadened size distribution centered at 3.2 nm, which was in agreement with the value obtained from the simulated structure and with the literature values.^[32,145] However, despite the improvement in the absorptive properties, the surface area of the film is substantially lower than the theoretically calculated one which is approximately $2100 \text{ m}^2 \text{ g}^{-1}$.^[32] This consideration, together with broadened pore size distribution, and the adsorption-desorption hysteresis of the isotherm could be ascribed to the a mixed effect of the thick film morphology and the presence of the residual amorphous **PIIm** in the sample.

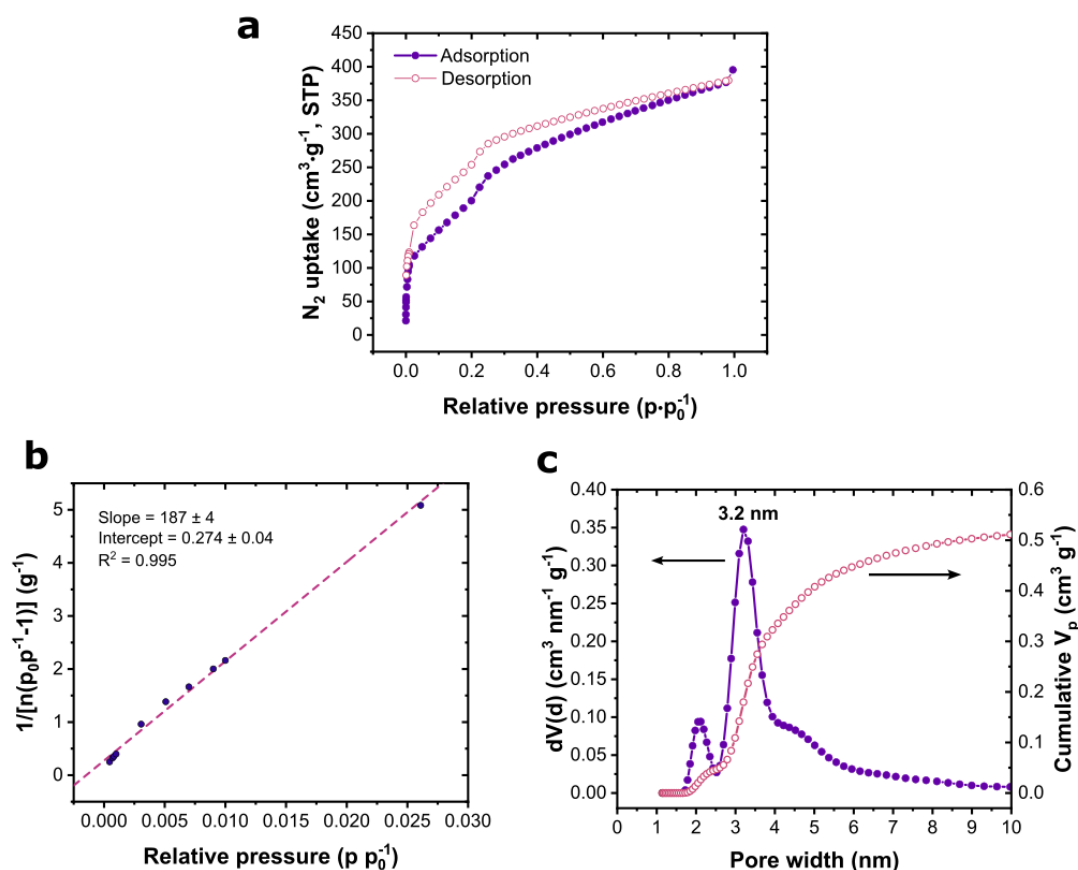


Figure 3.11 (a) N₂ adsorption - desorption isotherm of TPB-MeOTP-COF. (b) BET plot and linear fitting of the low relative pressure data of the N₂ adsorption branch. (c) Pore size distribution (violet line) and cumulative pore volume (pink line) profiles obtained by QSDFT calculation on the N₂ adsorption branch.

3.3.3. Chemical characterization

Infrared spectroscopy

FTIR-ATR spectroscopy confirmed the removal of the TFA-derived guest species (**Figure 3.12**). The disappearance of the dimeric O-H stretching band in the 3700 and 2700 cm⁻¹ region and of the N⁺-H stretching in the 2700-2500 cm⁻¹ region proved the successful elimination of the solute residues trapped in the polymer. Moreover, a strong decrease in intensity of both the aminic N-H vibration modes (3456 and 3375 cm⁻¹) and the aldehydic C=O stretching (1680 cm⁻¹) suggested that the annealing procedure further increased the extent of the reaction at the solid state, by healing the defects related to the unreacted end-groups of the polymer.

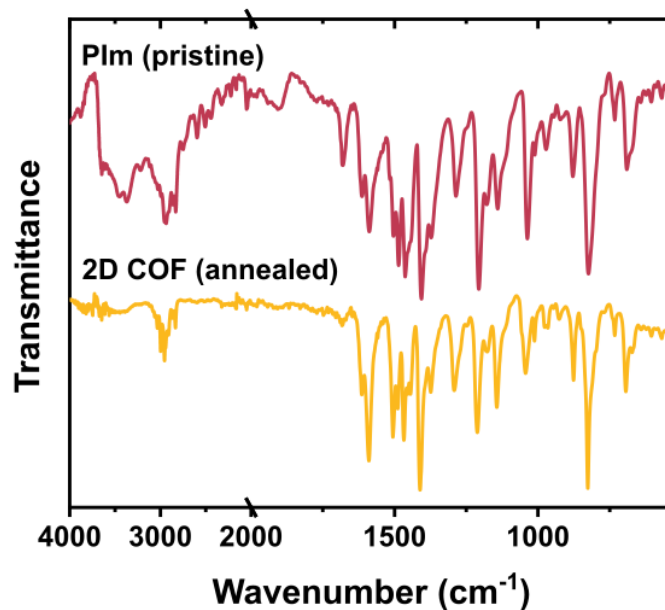


Figure 3.12 FTIR-ATR spectrum of the film of **TPB-MeOTP-COF** obtained by annealing of **PIm** at 100 °C in MeCN.

Thermogravimetric analysis

The thermal stability of the **TPB-MeOTP-COF** film was probed by thermogravimetric analysis (TGA) under inert atmosphere and compared with the pristine **PIm** film (**Figure 3.13**). The materials were dynamically heated at a rate of 10 °C min⁻¹ from 30 to 800 °C. Between 150 and 250 °C both materials showed an initial mass loss of about 3 % of the starting value, likely related to the desorption of volatile molecules trapped in the polymeric matrix. Both materials showed rapid degradation at temperatures higher than 400 °C, with the crystalline material being somewhat more stable in the 250 - 400 °C region. The recorded thermal stability profile of the crystalline material was consistent with the reported data for the same material in the bulk powder morphology, thereby supporting the chemical and structural resemblance of the film to the bulk powder.^[32]

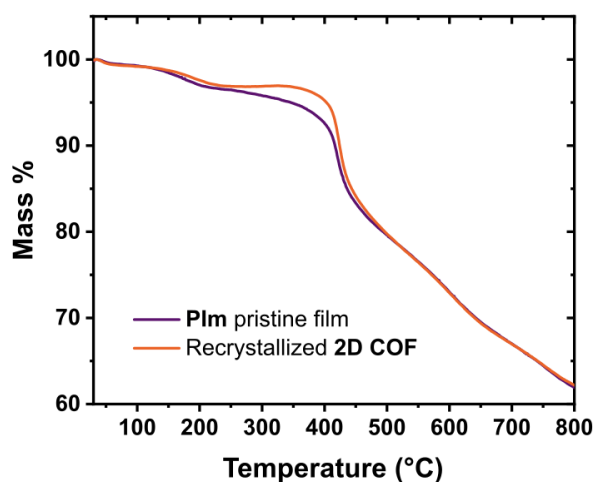


Figure 3.13 TG curves of the recrystallized TPB-MeOTP-COF film (orange line) vs the PIIm pristine film.

3.4. Mechanism of the reaction in solution

The formation of PIIm with high preferential orientation and its use as template to grow an oriented 2D COF film is unprecedented. Therefore, understanding the underlying mechanism for the formation of the layered PIIm is of paramount importance to the further development of the method, which could potentially be applied to prepare a variety of imine-linked 2D COF oriented films.

In general, the solidification of a film coating from a polymer solution is a complex process that simultaneously involves physical and chemical phenomena. The evaporation of the solvent is an irreversible process that has consequences both on the physics (capillary flow, Marangoni effect, skin formation) and on the chemistry (increase of concentration, concentration gradients).

In this first section dedicated to the mechanism of the formation of the oriented PIIm film we describe our findings related to the chemistry of the polymerization in solution. **Section 3.5** instead, is dedicated to the physical aspects of the film drying process.

The reaction of 2D COF building blocks in solution in typical conditions results inexorably in the formation of a solid precipitate or a colloidal suspension which hinders further analysis and imposes the use of model compounds to investigate the chemistry of the reaction.^[102] By completely solubilizing both monomers and the polymer, the water-TFA solvent system offered a rare opportunity for investigating and unveil the mechanism of the polymerization reaction through solution-based characterization techniques, such as nuclear magnetic res-

onance (NMR) and UV-vis absorption spectroscopies. To shed light on the polymerization and orientation mechanisms, the nature of the **PIm** in solution was investigated in different conditions, in particular concentration, temperature, and solvent composition. The analysis of the results led to the conclusion that the monomers reacted quickly in water-TFA, to form a dynamic protonated **PIm** with a 3D polymer network topology rather than a 2D topology. The molecular weight distribution of the polymer at equilibrium was dependent on the concentration, the temperature, and the solvent composition. When the conversion of imine (extent of reaction) reached a critical value, a gel formed. This behavior is typical of hyper-branched polymers, and a sol-gel transition was also the first process happening on the drying solution after the casting.^[231,232]

3.4.1. The sol-gel transition

The polymer solution was prepared by mixing the concentrated solutions of the separate monomers in 5 % water-TFA. Different concentrations of the monomers were tested, and all the experiments were carried out with an equimolar functional groups' ratio ($r = 1$), *i.e.* $C_0 = 3 \times [\text{MeOTP}]_0 = 2 \times [\text{TPB}]_0$. At $C_0 > 0.3$ mM, upon mixing, an immediate color change from yellow to bright red indicated the formation of a soluble protonated **PIm** (Figure 3.14). By increasing the concentration, the solution became progressively more viscous and at $C_0 > 225$ mM a gel-like solid was obtained upon few seconds of reaction at room temperature.

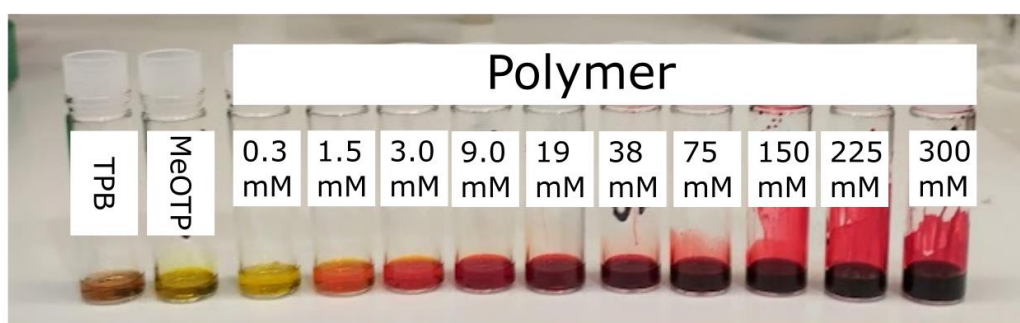


Figure 3.14 Photograph of the monomer solutions and the polymer solutions at different concentration.

The sol-gel transition was found to be temperature-dependent and fully reversible: the polymer solution exhibited viscous liquid properties at temperatures higher than the critical gelation temperature T_{gel} and elastic solid properties at temperatures below it. A sol-gel

phase diagram (**Figure 3.15**) was constructed by the test tube inversion method.

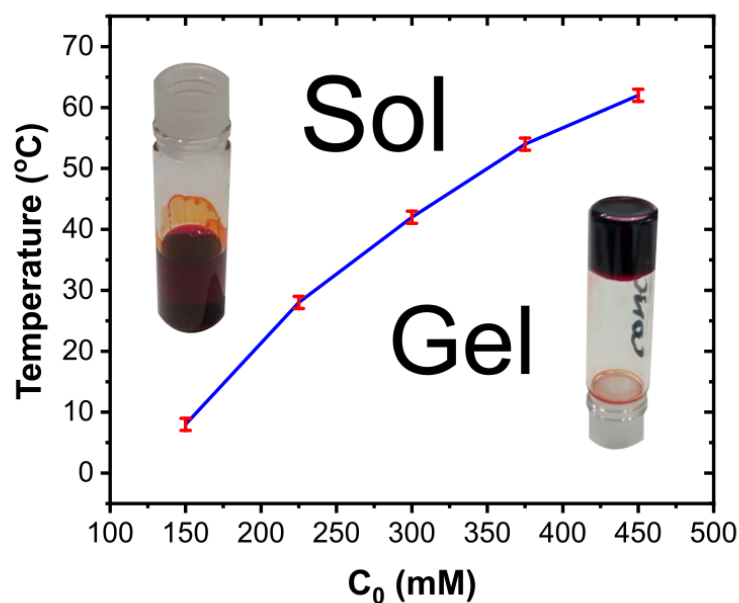


Figure 3.15 Sol-gel phase diagram for **Plm** in 5% water-TFA. Insets show photographs of sol (left) and gel (right).

3.4.2. Characterization of the gel

A gel is composed of a 3D network of colloidal or polymeric nature that extends throughout the whole volume of the system and it is swollen with the solvent along with the low molecular weight components in solution.^[233] To isolate and characterize the solid component of the gel, TFA and water were exchanged with acetonitrile (MeCN). MeCN quickly dissolved the low molecular weight oligomers and did not promote any significant depolymerization of the polymer solid on the experiment timescale. The MeCN-wet sample was freeze-dried to avoid the collapse of the 3D network upon solvent removal. The SEM image (**Figure 3.16a**) revealed a foam-like macroporous material composed of irregular fibers, that are strongly entangled with each other. PXRD of the freeze-dried gel showed only broad amorphous halo corresponding to the average intermolecular distance in the glassy solid, thereby indicating that the structure is fully amorphous (**Figure 3.16b**).

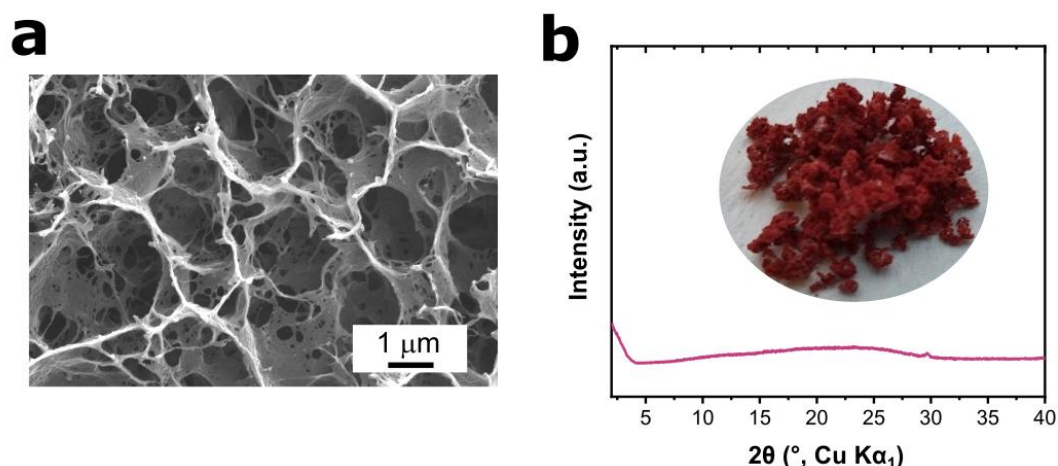


Figure 3.16 (a) SEM image of the **PIm** gel isolated by quenching with MeCN followed by freeze-drying. (b) PXRD of the gel and photo of the dry material.

Even though the monomers used in this reaction are rigid and predesigned to form a thermodynamically stable 2D polymer, the polymerization in water-TFA did not yield the typical crystalline precipitate characterized by nanosphere morphology. Instead, the polymer solution displayed gel point at defined concentration and temperature which is characteristic of 3D polymer networks formed by step-growth polymerization of polyfunctional monomers. The growth of the 3D structure was enabled by rotational degrees of freedom around the single bonds which allow for branching of the network in 3D. Noteworthy, in a growing 2D structure the number of available reactive groups (n) on the perimeter scales as the square root of the number of already incorporated monomers ($n^{1/2}$). On the contrary, 3D spherical structures grow much faster as the available reactive group on the surface scale with a factor $n^{2/3}$.^[234]

3.4.3. Step-growth polymerization of PIm

To get further insight into the mechanism of formation of the **PIm** gels, solutions at various concentrations were analyzed by proton nuclear magnetic resonance (^1H NMR). The presence of the methoxy groups on the polymer backbone was used as chemical probe for the NMR analysis, as the correspondent resonances had a distinct chemical shift from all the protons in the mixture, while the imine CH protons were overlapping with the residual solvent resonance. **Figure 3.17a** shows the high field region for the polymer solutions in a range of concentrations in TFA- d with 5% D_2O as solvent for the reaction. The four singlets are re-

lated to the protons of the methoxy groups of the **MeOTP** units (**Figure 3.17b**). The resonance at 4.51 ppm was assigned to the doubly reacted molecule (protons a), while the two signals at 4.44 ppm and 4.18 ppm were assigned to the asymmetrical, mono-reacted aldehyde polymer branch terminating unit (respectively protons b and c). Finally, the resonance at 4.10 ppm was related to the unreacted aldehyde (protons d).

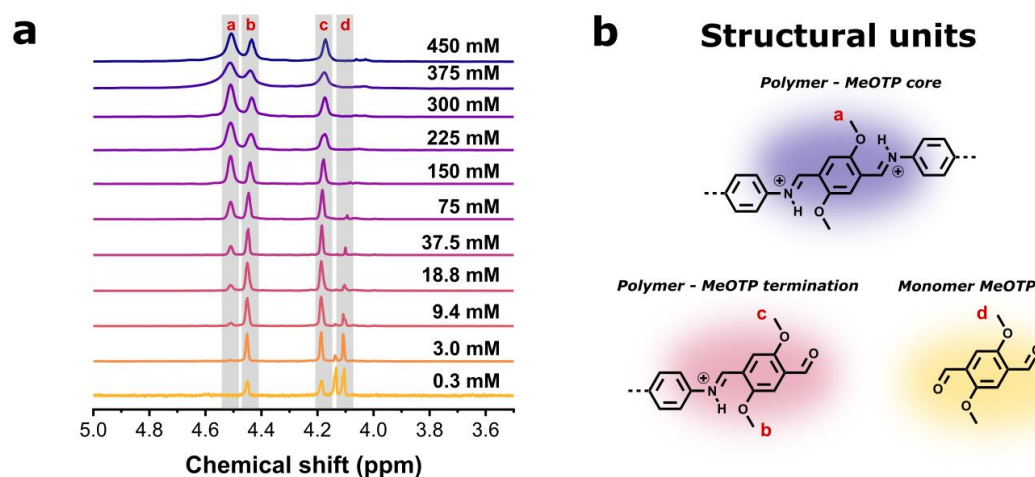


Figure 3.17 (a) High-field region of the ^1H NMR spectra at various C_0 measured at 23 °C in 5% D_2O -TFA- d . (b) Structural units followed by ^1H NMR.

To rationalize the NMR data, the relative amount of the species participating to the equilibrium were computed from the relative area of the NMR resonances. The relative amount of each functional group was plotted versus C_0 between 0.3 mM and 450 mM (**Figure 3.18**). We assumed that the polymerization reaction in this range of concentration was fully under thermodynamic control, which was ensured by the long equilibration time between the preparation of the solution and the measurement. The polymer solution was composed of macromolecules with a broad molecular weight distribution in which the polymer species are in dynamic equilibrium with each other and with the leaving water molecules.

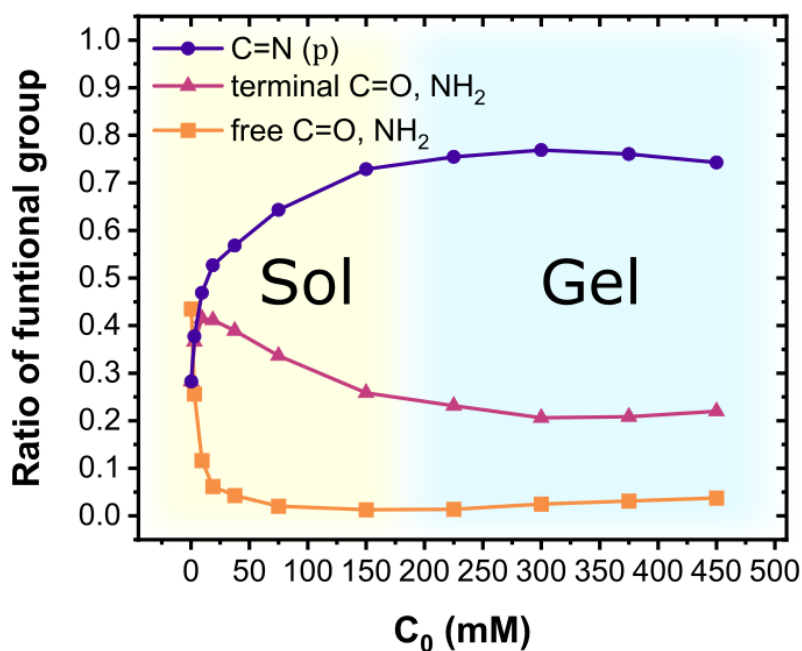


Figure 3.18 Relative amount of each functional group as a function of the concentration.

In a step-growth polymerization all monomers are reactive and combine in the initial stages of the reaction to form low-molecular weight oligomers. As expected, we observed that increasing the initial concentration of the monomers resulted in a shift of the equilibrium toward higher conversion of imine group (extent of reaction, p). In particular, we found that the relative amount of free monomers quickly approached zero by increasing the concentration between 0.3 and 10 mM with a concomitant increase in the relative amount of imine (Figure 3.18, blue line) and terminal C=O or NH₂ groups (Figure 3.18, grape-red line). The nearly 1:1 ratio between the terminal functional groups and the C=N linkage suggested that in this range of concentrations the monomers reacted to form low molecular weight oligomers, in particular **MeOTP-TPB** and **MeOTP₂-TPB** (Figure 3.19).

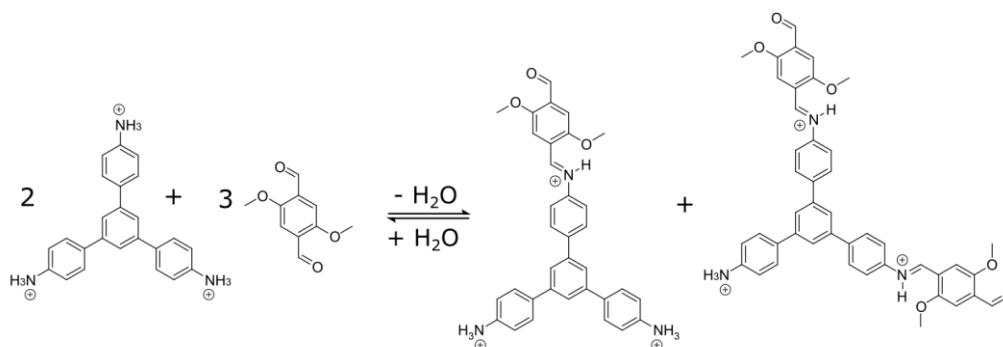


Figure 3.19 Reaction to form the **MeOTP-TPB** and **MeOTP₂-TPB** structural units. A stoichiometric mixture of these two oligomers results in a 1:1 ratio between terminal C=O or NH₂ groups and C=N group.

For $C_0 > 10$ mM, we observed a gradual decrease of the fraction of terminal functional groups and with a concomitant increase of p . In this range of concentration, **MeOTP-TPB** and **MeOTP₂-TPB** reacted to gradually form larger polymers. As p reached the critical value of $p_c = 0.76$ at $C_0 = 225$ mM the solution underwent an abrupt transition and became a gel. The presence of a clear gel point implied that under the applied conditions, the crystallization of 2D COF particles was suppressed, and the system behaved instead as a $A_3 + B_2$ 3D polymer network.

The Carothers model and the Flory-Stockmayer model are two classical approaches to predict the relationship between gelation and p in a step-growth non-linear polymerization. According to Carothers,^[23] gelation occurs when the average number degree of polymerization \bar{X}_n approaches infinity. For a step-growth polymerization containing equivalent numbers of A and B groups, Carothers derived that p_c at the gel point is given by the following equation:

$$p_c = \frac{2}{f_{avg}}$$

Where f_{avg} is the average functionality of the monomers involved in the reaction, weighted for the number of molecules of each monomer; for a $A_3 + B_2$ (with 2:3 ratio) $f_{avg} = 2.4$ and the model predicts a $p_c = 0.83$. As the model assumes that $\bar{X}_n \rightarrow \infty$ and in practice the gelation occurs when just one of the molecules approaches an infinite size, this model overestimates p_c and therefore constitutes an upper limit of gelation, meaning that gelation must happen below this critical value of reaction extent.

The second theory was developed by Flory and Stockmayer and uses a mean-field method in which the network formation is modeled as percolation on a Bethe lattice.^[235,236] This approach takes into account the presence of the fraction of macromolecules with high molar masses. The following equation gives the analytical solution for p_c according to this model:

$$p_c = (f_A - 1)^{-1/2}$$

Where f_A is the functionality of the branching unit A. In our case $f_A = 3$ for which the model predicts a $p_c = 0.71$. This model typically underestimates p_c since it does not account for the intramolecular cyclization, while in practice the formation of closed loops is not necessarily negligible, thereby constituting the lower limit of gelation, meaning that the gelation can occur above this conversion of the end-groups. The observed value for p_c in our case ($p_c = 0.76$), is intermediate between the two extremes predicted by the two classical theories, therefore fits perfectly into step-growth polymerization model. In addition, the relatively good agreement with the lower limit of gelation indicates somewhat limited extent of in-

tramolecular reactions.

According to the Flory-Stockmeyer model the number average degree of polymerization \bar{X}_n can be calculated according to the equation below:

$$\bar{X}_n = \frac{f_A/r + 2}{f_A(1/r - 2p) + 2}$$

Where in our case $f_A = 3$ and $r = 1$. **Figure 3.20** shows the calculated value for \bar{X}_n in function of the concentration.

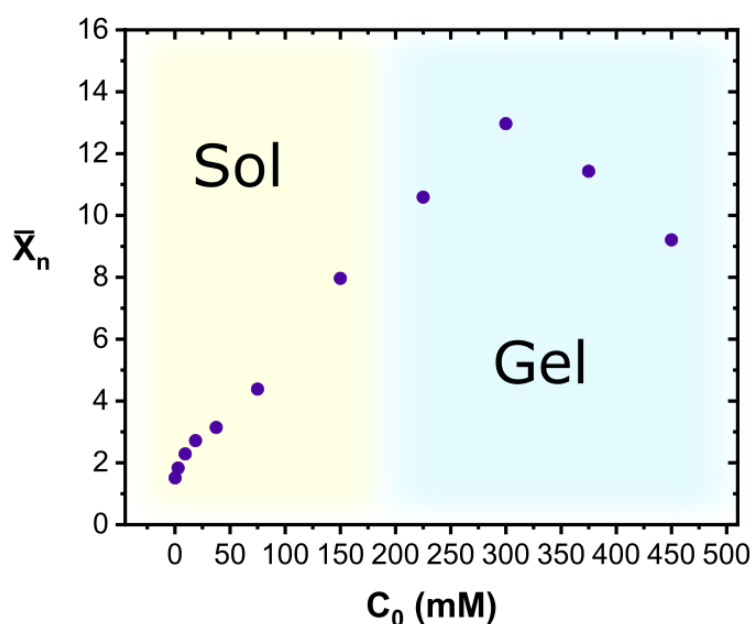


Figure 3.20 Calculated average number degree of polymerization (\bar{X}_n) as a function of the concentration.

Noteworthy, as the estimation of p was based on NMR measurements, the value of the calculated \bar{X}_n reflected only the properties of the molecules in solution. The number average degree of polymerization was not very large, and the average molecule was composed of approximately 10 monomers at the gel point. In practice, the observed increase of viscosity originated from a small fraction of the monomers mass converted into very large molecules. At the gel point, ideally, only a single insoluble, infinitely large polymeric network extending throughout the entire volume was present. As most of the mass fraction of the **PIm** was still in solution slightly above the gel point concentration, the changes in the composition could still be monitored by solution ^1H NMR. Interestingly, after the gel point ($C_0 > 225$ mM), p went through a maximum and then decreased in favor of terminal and monomeric C=O and NH_2 groups. This was consistent with the higher probability for the larger macromolecules of attaching to the growing solid network, while the smaller oligomers continued to remain dis-

solved in the gel-entrapped solvent.

3.4.4. Thermodynamic parameters

A typical assumption for polycondensation reactions is that all steps (apart from the condensations between the monomers) have the same equilibrium constant (K_{eq}). For the formation of **PIm**, K_{eq} is given by the following equation:

$$K_{eq} = \frac{[C = N][H_2O]}{[C = O][NH_2]} = \frac{p[H_2O]_0 + C_0p^2}{C_0(1-p)^2}$$

Where $[H_2O]_0$ is the initial molar concentration of water. K_{eq} was calculated based on the 1H NMR data at 23 °C and only for concentrations below the gel point as the presence of undissolved polymer (NMR silent) after the gel point did not allow for a correct quantification of the species involved in the equilibrium. The results are displayed in the plot portrayed in **Figure 3.21** and are put in relations with \bar{X}_n . In diluted conditions ($C_0 < 20$ mM), monomers and **MeOTP-TPB** and **MeOTP₂-TPB** were predominant ($\bar{X}_n \leq 3$) and K_{eq} had an extremely elevated value (~ 5000 at $C_0 = 0.3$ mM) which decreased rapidly with the growth of the oligomers size. When the average oligomer became larger than a trimer ($\bar{X}_n > 3$), the value of K_{eq} became independent from the molar mass ($K_{eq} = 190$).

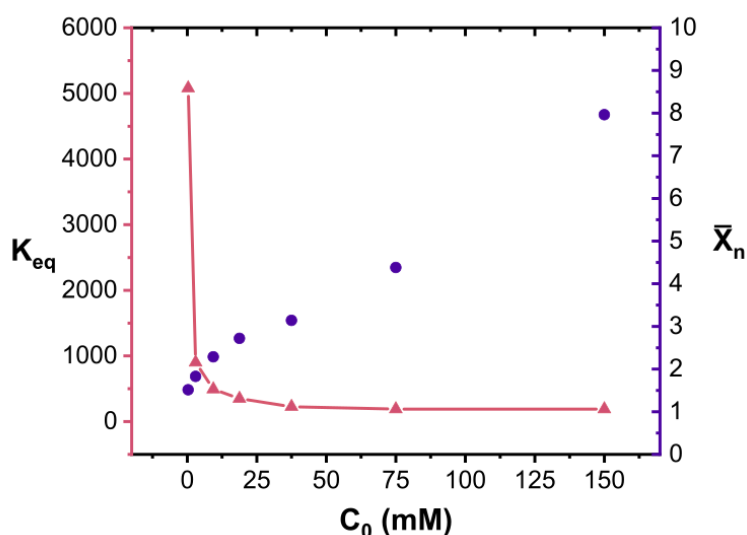


Figure 3.21 Equilibrium constant (K_{eq}) and average number degree of polymerization (\bar{X}_n) at different concentrations in the sol range.

The fact that the observed value of K_{eq} was higher for $\bar{X}_n \leq 3$ than for larger species was related to the higher reactivity of the monomers in forming the first **MeOTP-TPB** and **MeOTP₂-TPB** (**Figure 3.19**). Once these structural units were formed, they acted as building

blocks for the construction of the larger polymer molecules. Nevertheless, the value found for $\bar{X}_n > 3$, $K_{eq} = 190$ was surprisingly higher than the typical values for polyesterifications^[237] and in the same range as polyamidations,^[238] emphasizing the highly favorable thermodynamic forces that drive the polymerization.

To gain a deeper understanding of the thermodynamics of the polymerization process, the temperature dependency of the chemical reaction was investigated using variable temperature ^1H NMR. A **PIm** solution with $C_0 = 75$ mM was analyzed at different temperatures between 0 °C and 60 °C after an appropriate equilibration time. As shown in **Figure 3.22a**, the variation of the areas of the signals in the high-field region of the ^1H NMR spectra indicated that an increase in temperature led to the depolymerization of the material, which was expected for a reversible polycondensation process. To determine the thermodynamic contributions of the reaction, we used a linear fitting approach on the van't Hoff plot (**Figure 3.22b**) according to the following equation:

$$\ln K_{eq} = -\frac{\Delta H_p^\circ}{RT} + \frac{\Delta S_p^\circ}{R}$$

The reaction is moderately exothermic with a standard enthalpy of polymerization of $\Delta H_p^\circ = 8.26$ kJ mol⁻¹ and a standard entropy of polymerization of $\Delta S_p^\circ = 15.0$ J mol⁻¹K⁻¹. Based on these values we calculated a standard free energy of polymerization of $\Delta G_p^\circ(23\text{ °C}) = -12.7$ kJ mol⁻¹ and the corresponding equilibrium constant was calculated according to the following equation:

$$K_{eq}(T) = e^{\frac{-\Delta G_p^\circ}{RT}}$$

resulted in $K_{eq}(23\text{ °C}) = 175$, which was found in close agreement with the value of K_{eq} directly calculated from ^1H NMR data.

Importantly, the entropic contribution accounted for about around a third of the standard free energy change suggesting that the polymerization reaction was both enthalpy and entropy driven. The significant increase in entropy upon polymerization could be, at least partially, explained with the release of water molecules as by-product, which offset the loss of degrees of freedom associated with the formation of macromolecules. More importantly, such a significant entropic contribution was consistent the formation of a highly disordered 3D material with very minimal degree of intramolecular cyclization which is further supported by the extent of reaction at the gel point.

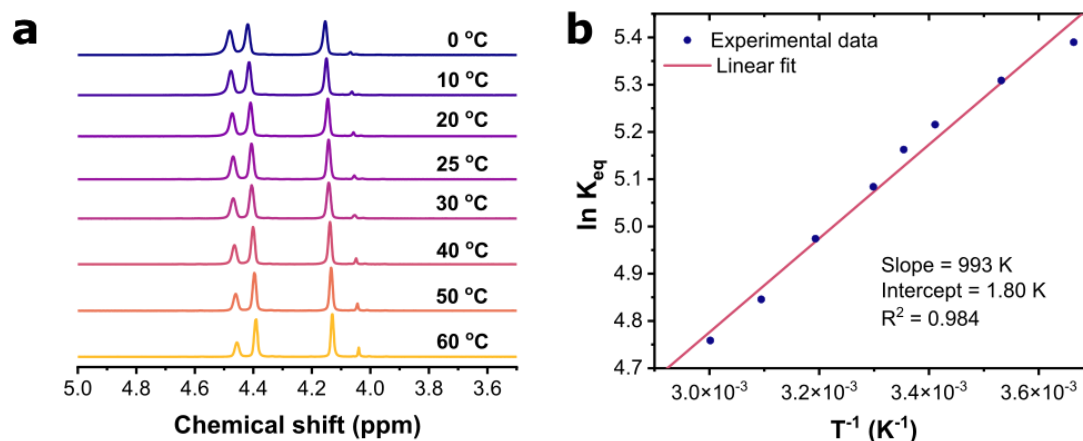


Figure 3.22 (a) High-field region of the ^1H -NMR spectra at different temperatures. (b) Van't Hoff plot and linear fitting of the experimental data.

3.4.5. The role of the solvent

Subsequently, we investigated the role of the solvent composition on the polymerization reaction. TFA was selected to run the polymerization reaction for its properties of highly polar and volatile solvent and its strong acidity which were demonstrated to be effective to form and dissolve charged **PIm**.^[10,11] Water was chosen as a co-solvent as to control the reaction equilibrium and avoid the formation high \bar{X}_n polymers which would lead to the formation of a non-processable gel at low concentrations. To gain further insights, we varied the solvent composition between 3% and 10% water, while maintaining a fixed temperature of 23 °C and a concentration of 75 mM. ^1H NMR analysis showed that the extent of the reaction could be finely tuned within the 0.68 – 0.57 range by varying the amount of water in the solvent mixture (**Figure 3.23a, b**). Interestingly, changes in the solvent composition led to variations in the apparent equilibrium constant (K_{eq}) as calculated by integration of the ^1H NMR resonances, which may be attributed to the increased contribution of **MeOTP-TPB** and **MeOTP₂-TPB** at high water percentages (**Figure 3.23b**).

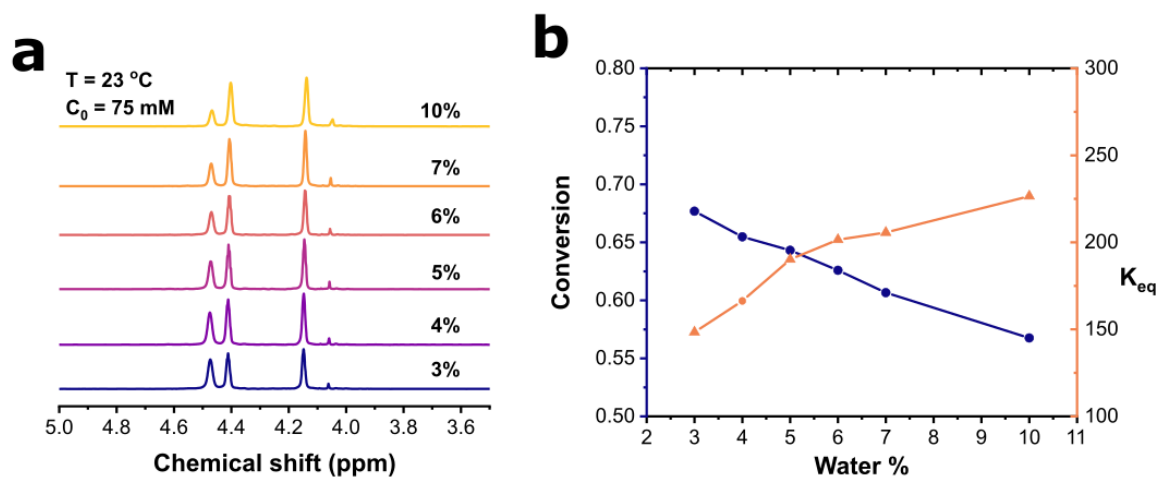


Figure 3.23 (a) High-field region of the ¹H-NMR spectra at different solvent compositions. **(b)** Extent of reaction and K_{eq} values at different solvent compositions.

3.4.6. Kinetic considerations

During the formation of the oriented **PIIm** films, as the solvent evaporated, the concentration increased and drove the reaction equilibrium in favor of higher molecular weights. The evaporation process was irreversible and relatively fast: it took around 10 minutes to form a solid film and 3-4 hours to release most of the trapped solvents. To determine if the **PIIm** growth reaction was thermodynamically or kinetically controlled during this process, a kinetic model for the condensation and hydrolysis reactions was needed.

The reaction between **MeOTP** and **TPB** in water-TFA to form the protonated **PIIm** produced a relevant variation of the color of the solution from pale yellow to intense red. Therefore, the reaction development could be conveniently followed by UV-vis absorption spectroscopy in solution. **Figure 3.24** illustrates the UV-vis absorption spectra of the monomers and **PIIm** in 5% water-TFA solution. While **TPB** absorbed primarily in the far-UV region of the spectrum and did not exhibit any significant absorption band in the 300 – 600 nm spectral window, **MeOTP** presented a featureless absorption band with an absorption maximum at 424 nm. In contrast, **PIIm** exhibited a strong and red-shifted absorption band with a resolved vibrational fine structure centered at 504 nm and two shoulders spaced by ca. 40 nm, that were assigned to transitions related to the protonated imine bond.^[163]

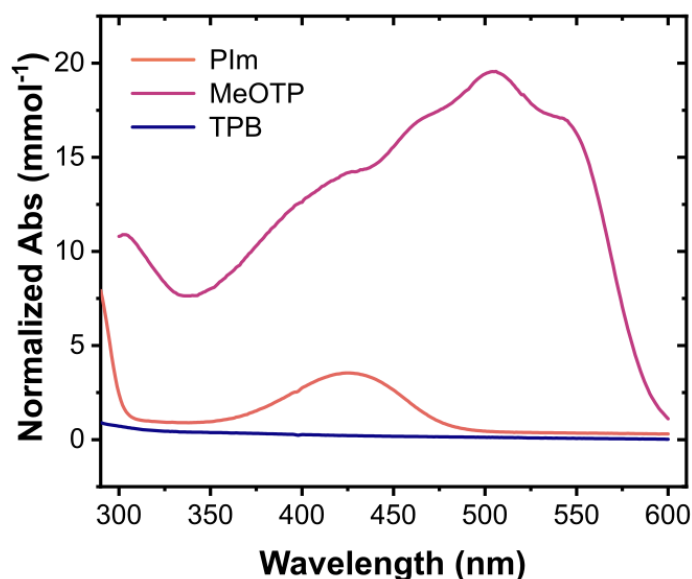


Figure 3.24 UV-vis spectra of TPB (violet line), MeOTP (orange line) and **Plm** (red line). The absorbance values were normalized by the respective C_0 .

We could speculate that the polymerization is a bimolecular reaction and it was expected to proceed according to a 2nd-order kinetic model. By neglecting the contribution of the reverse reaction (typical assumption for the incipient stages of the reaction), the differential and integrated rate equations could be expressed as follows, where the rate constant is denoted by k_p :

$$C = O + NH_2 \xrightarrow{k_p} C = N + H_2O$$

$$Rate_p = \frac{d[C = N]}{dt} = -k_p[C = O][NH_2] = -k_p[C = O]^2 \quad \text{for } [C = O] = [NH_2]$$

$$\frac{1}{[C = O]} = k_p t + \frac{1}{C_0}$$

Obtaining useful data on the rate of this reaction presented a challenge, as only the formation of **MeOTP-TPB** and **MeOTP₂-TPB** occurred at relevant concentrations for UV-vis analysis ($C_0 < 1$ mM), as confirmed by ¹H NMR. The formation of **MeOTP-TPB** and **MeOTP₂-TPB** was expected to proceed with a rate that differs from that of the formation of the relevant larger oligomers. Higher concentrations ($C_0 > 1$ mM) were suitable for a ¹H NMR analysis, but the rate of the reaction was too high to be investigated by this technique with a conventional equipment. Additionally, the presence of a high concentration of water as a component of the reaction solvent generated a non-negligible contribution of the hydrolysis

in determining the observed rate of polymerization. Due to the complexity of the system, it was not possible to investigate the kinetic of the polymerization reaction directly.

On the contrary, due of the great excess of water present in the 5% water-TFA solvent mixture, the hydrolysis could be easily studied as it was anticipated to follow a pseudo-1st-order kinetic, where k_h is the 2nd-order kinetic constant and k'_h is the pseudo-1st order kinetic constant:

$$C = N + H_2O \xrightarrow{k_h} C = O + NH_2$$

$$Rate_h = - \frac{d [C = N]}{dt} = -k_h [C = N][H_2O] = -k'_h [C = N] \quad \text{with } k'_h = k_h [H_2O]$$

$$\ln [C = N] = \ln [C = N]_0 - k'_h t$$

Where in this case, neglecting the contribution of the backward reaction (polymerization), is a more reasonable approximation, at least for the initial rate, as none of the products was present in the initial stage of the reaction. Furthermore, in the considered concentration range the rate of the forward reaction could be considered negligibly low, given the high dilution necessary for the UV-vis analysis.

Quick dilution was a simple and effective method to initiate the hydrolysis of **PI_m** to its components. With this method, the kinetics of the hydrolysis of **PI_m** was studied in 5 % water-TFA at 23 °C, in a UV-vis spectrophotometer. To initiate the reaction 1 μl of $C_0 = 150 \text{ mM}$ **PI_m** stock solution was added to 3.5 ml of solvent in the 1 cm quartz cuvette with rapid stirring. Under this dilution the initial concentration of the solution was $C_0 = 0.043 \text{ mM}$.

Upon dilution a clear and gradual change of the profile of absorption was observed in the first 30 minutes. The prominent absorption band centered at 504 nm progressively decreased, which was accompanied by appearance of new bands with maxima at 395 and 474 nm, which were assigned to the low molecular weight oligomers.

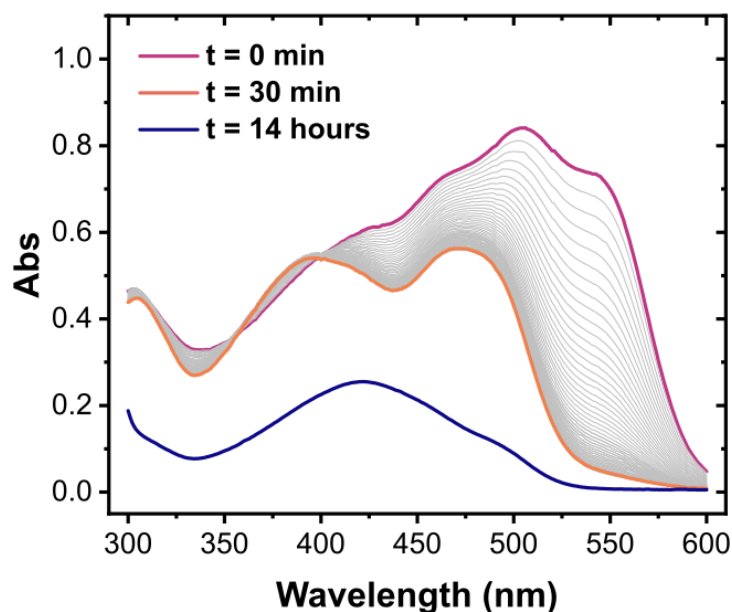


Figure 3.25 Temporal evolution of the UV-vis absorption during the hydrolysis of **PIm**.

Furthermore, no isosbestic point was maintained throughout the hydrolysis indicating a stepwise depolymerization consistent with first fast hydrolysis to **MeOTP-TPB** and **MeOTP₂-TPB**, followed by slow hydrolysis of these species.



This mechanism was further supported from the analysis of absorbance decay profile at $\lambda = 545 \text{ nm}$. The evolution of the absorbance in time (A_{525}) is showed in **Figure 3.26**. The data was alternatively visualized by plotting the logarithmic variation of A_{525} against time (**Figure 3.26**).

The logarithmic plot provided clear evidence of the occurrence of two pseudo-1st-order reactions as two consecutive linear intervals were observed. The fitting was performed in the 0 - 20 min time interval for the first reaction and 100 - 240 min time interval for the second reaction. It was assumed that in each of these intervals only the specific hydrolysis reaction took place, and no secondary or reverse reaction influenced the observed rate. Based on this model the two reactions proceeded with the kinetic constants $k_{obs}^1 = 1.63 \cdot 10^{-3} \text{ s}^{-1}$ and $k_{obs}^2 = 3.8 \cdot 10^{-5} \text{ s}^{-1}$.

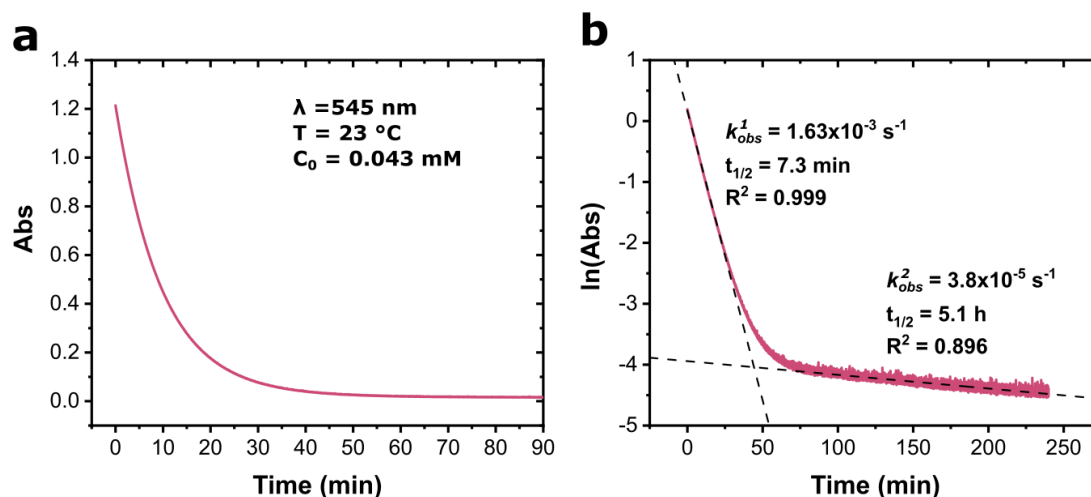


Figure 3.26 (a) Single-wavelength time course experiment at 545 nm for the hydrolysis of the polymer. **(b)** Logarithmic decay profile of the absorbance at $\lambda = 545$ nm. A pseudo-first order model has been used for the fitting.

In these conditions, a pseudo-1st-order half-life for the hydrolysis could be calculated according to the following equation:

$$t_{1/2} = \frac{\ln 2}{k}$$

It resulted that the hydrolysis of **PI_m** occurred with an observed half-life of $t_{1/2} = 7.1$ min and the hydrolysis of **MeOTP-TPB** and **MeOTP₂-TPB** occurred with an observed half-life of $t_{1/2} \sim 5$ h.

Notably, the two order of magnitude difference in the rate of hydrolysis of **PI_m** in comparison to the small oligomers, was consistent with the significant variation of the observed K_{eq} at low extent of reaction, when \bar{X}_n is equal or lower than 3. Indeed, at the equilibrium the forward and reverse reaction proceed with the same rate (principle of detailed balance) and the equilibrium constant equals the ratio of the rate constants according to:

$$K_{eq} = \frac{k_p}{k_h}$$

It could be concluded that the high observed K_{eq} at low \bar{X}_n were due to the much slower hydrolysis rate of **MeOTP-TPB** and **MeOTP₂-TPB** in respect larger oligomers.

To extract the contribution of the water amount to the observed hydrolysis rate, single-wavelength time course experiments were carried out in the same conditions but in different solvent compositions with the water volume fraction ranging between 3 and 12% (**Figure**

3.27a).

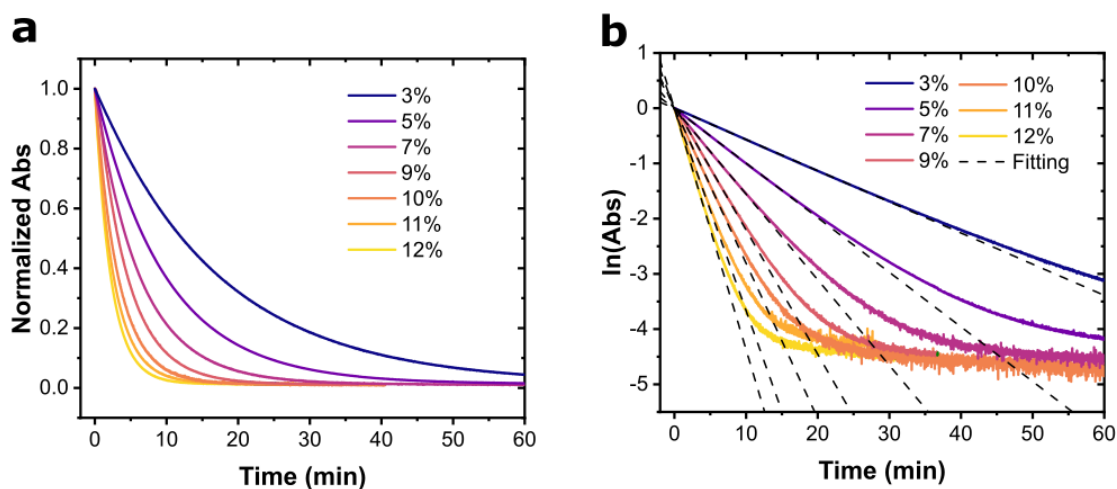


Figure 3.27 (a) Single-wavelength time course experiment at $\lambda = 545$ nm for the hydrolysis of **PIm** at 3, 5, 7, 9, 10, 11 and 12% of water. **(b)** Logarithmic decay profiles of the absorbance at $\lambda = 545$ nm. A pseudo-first order model has been used for the fitting.

As expected, the hydrolysis was faster at higher water contents and slower at low water contents. The linear fittings were performed on the logarithmic value of the A_{545} in function of time and considering only the initial rates (**Figure 3.27b**). The results are reported in **Table 3.1**.

Table 3.1 Summary table for the results of the fittings.

H ₂ O % (v/v)	[H ₂ O] (M)	k_{obs}^1 ($\times 10^{-3}$) s ⁻¹	Std. Err. ($\times 10^{-3}$) s ⁻¹	R ²
3	1.67	0.955	0.002	0.999
5	2.78	1.66	0.01	0.999
7	3.89	2.62	0.04	0.999
9	5.00	3.83	0.03	0.999
10	5.56	4.94	0.18	0.999
11	6.11	6.34	0.01	0.999
12	6.67	7.25	0.01	0.999

From the dependency of k_{obs}^1 on the [H₂O] it should be possible to determine the corresponding to the order of the hydrolysis respect to water. Both a linear and a quadratic dependency of the observed rate constant were probed with tentative fittings.

$$k_{obs}^1 = k_h[H_2O]$$

$$k_{obs}^1 = k_h[H_2O]^2$$

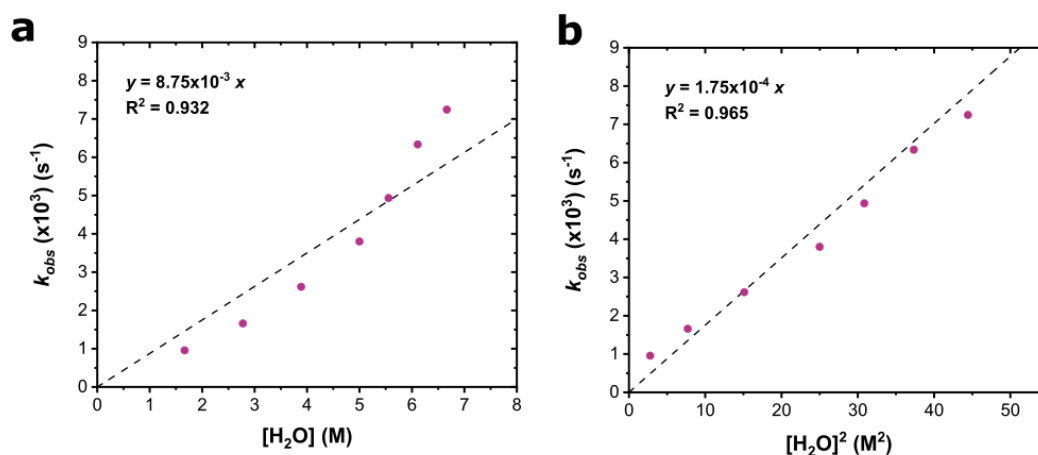


Figure 3.28 (a) Liner fitting of the variation of k_{obs}^1 with $[H_2O]$. (b) Liner fitting of the variation of k_{obs}^1 with $[H_2O]^2$.

The data analysis with the liner $[H_2O]$ dependency model provided an overall hydrolysis constant k_h of $8.75 \cdot 10^{-3} s^{-1} M^{-1}$, but the fit between the data and the model was poor ((a) Liner fitting of the variation of k_{obs}^1 with $[H_2O]$. (b) Liner fitting of the variation of k_{obs}^1 with $[H_2O]^2$. **Figure 3.28a**). A better description of the experimental data was obtained with the quadratic $[H_2O]$ dependency model (**Figure 3.28b**), which provided a k_h of $1.75 \cdot 10^{-4} s^{-1} M^{-1}$. These results may indicate that the hydrolysis of the polymer relied on a non-intuitive mechanism, whose elucidation would require further investigation which was beyond the scope of this study.

3.5. Structural evolution during gel consolidation

3.5.1. A plausible mechanism: evaporation-dependent strain crystallization

When the **PIm** solution was cast on the silicon substrate, the low solid-liquid interfacial tension caused the liquid to flow over the entire exposed solid surface, forming a full liquid layer coating. As the solution of the cast **PIm** dried, the concentration of the polymer increased. At 40 °C the evaporation rate of the solvent was rapid compared to room temperature, and after about 15 minutes the droplet had completely solidified. At the chemical level, the solidification of the droplet was expected to be the analogue of the sol-gel transition observed in the bulk solution and discussed in **Section 3.4.1**. Nevertheless, as it was observed, the structure of the solid film obtained upon solution casting was radically different from the material isolated after the bulk sol-gel transition. The difference was not only limited to the

macroscopic shape of the material (film vs powder), but it extended also to its microscopic morphological features, with the film being composed by a compact, layered, and oriented material and the bulk gel being characterized by a 3D, isotropic, macroporous, and highly entropic structure.

We speculate that these differences originated from the capillary forces that acted on the gel as it dried out during the film synthesis, phenomena that were absent when the gel was isolated from the bulk by freeze-drying. It is known that solventborne coatings are subject to tensile stress during the drying process and that this stress can result in elastic or viscous deformations of the coating.^[221]

3.5.2. Microfluidic flows in a drying sessile polymer droplet

When a solution containing a polymer is deposited onto a substrate, the evaporation of the solvent increases the concentration of the polymer. During this process the spatial distribution of the polymer chains within the film depends on the interplay between convective flows and the diffusion of the polymer segments.^[239] Typically, in a wet film the evaporation rate at the edge is higher compared to the center due to a combination of convective flow in the gas phase and high solvent vapor gradients near the contact line.^[221] As a consequence, the edges dry first and the polymer deposits pin the contact line, preventing the lateral shrinkage of droplet upon evaporation (**Figure 3.29a**). As drying continues, the droplet shrinks vertically and the contact angle decreases, inducing a capillary flow that effectively squeezes the fluid outwards to compensate for the liquid loss at the contact line.^[220] This flow drags the polymer chains from the center of the film toward the edges while the polymer diffusivity opposes this effect (**Figure 3.29b**). Furthermore, when the substrate is heated, the temperature at the edge is higher than at the top of the droplet, increasing further the evaporation rate at the contact line. The temperature gradient can have another non-negligible effect: the surface tension of the solution lowers with the increasing temperature inducing a gradient of surface tension that draws the fluid from the edge towards the top of the droplet along the liquid-vapor interface. This effect is known as Marangoni flow and it can partially contribute to the stress applied to the drying polymer.^[240]

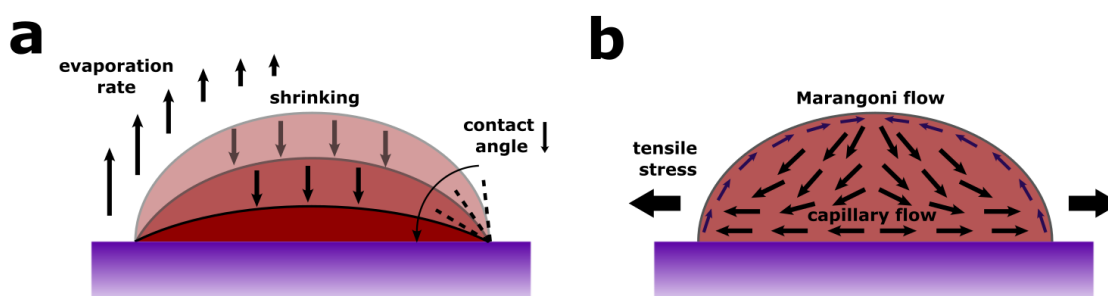


Figure 3.29 Schematics of a polymer droplet on a substrate. **(a)** Evolution of the droplet shape upon evaporation. The faster rate at the edges induces contact line pinning and a shrinking only in the vertical direction. **(b)** Flow fields within the droplet driven by the capillary (black vectors) and Marangoni (violet vectors) effects.

3.5.3. Morphological evolution of the drying polymer

It is plausible to assume that despite the increasing viscosity of the medium, **PIm** molecules in solution can be drawn and aligned according to the flow fields. Moreover, the sol-gel transition occurs once the gel point concentration has been reached and, in this situation, the **PIm** solid film still exhibits a solid-like viscoelastic response to applied stress can comply with the applied stress through deformation, resulting in the formation of the specific layered pattern.

To support this mechanistic hypothesis the morphological evolution of the film during the drying process was examined by SEM. To this end, different films were obtained after 5 minutes, 10 minutes, 15 minutes, 30 minutes, and 1 hour of reaction time at 40 °C. To isolate the polymeric material while avoiding the further evaporation of TFA (which would induce both chemical and physical changes to the film) the reaction was quenched by immersion in MeCN. Due to his polarity, this solvent was able to solubilize and remove the sol fraction, containing the low molecular weight protonated **PIm**, effectively arresting the chemical reaction. Additionally, the introduction of MeCN quickly induced the delamination of the film from the substrate (**Figure 3.30**). The solvent was then removed by freeze drying the samples, to avoid the effect of capillary forces resulting from the evaporation of MeCN which could further modify the morphology of the material.

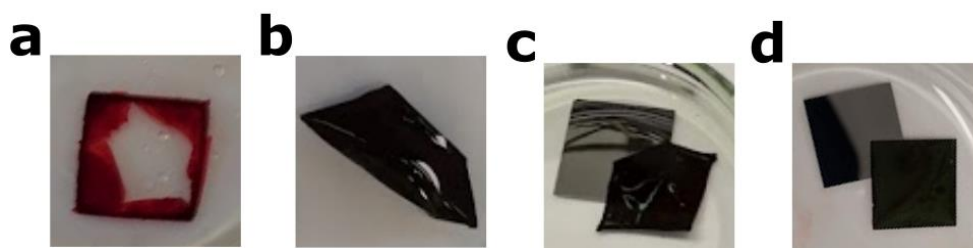


Figure 3.30 Photographs of the films isolated from the reaction on surface quenched at different reaction times: **(a)** 10 min, **(b)** 15 min, **(c)** 30 min, and **(d)** 60 min.

Below 5 minutes from the casting of the solution the droplet was still completely liquid. From 5 to 10 minutes of reaction, the films began to solidify, starting the edge. As a result, for the reaction quenched after 10 minutes only the rim of the film was isolated (**Figure 3.30a**).

The material was examined by SEM and as expected, the initial morphology of the solid polymer was analogue to that of the gel obtained from the bulk reaction (**Figure 3.31a, b**), indicating that the system underwent a sol-gel transition on substrate upon evaporation of the solvent. The material, however, presented regions with clear morphological inhomogeneities. In particular, in the area where the film dried at the contact with the vapor phase, the gel appeared to have collapsed to form a gradually more compact polymer skin layer (**Figure 3.31c, d**). Additionally, the top view of the polymer skin layer showed a highly fractured surface which is not surprising as the drying stress is the highest at the top surface of a coating: the exterior of the gel tries to shrink faster than the interior so large stresses are generated that cause the mechanical instability of the exposed surface of the network (**Figure 3.31c, d**).^[241]

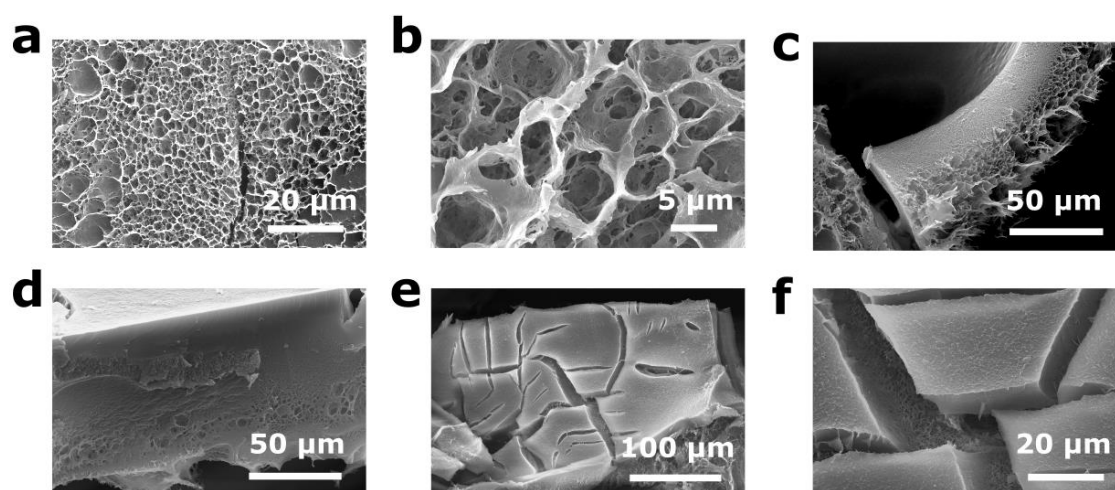


Figure 3.31 SEM micrographs representing different areas of the film obtained after about 10 minutes of reaction: **(a, b)** bulk region of the material that solidified into a macroporous gel; **(c, d)** cross-section image of a region that solidified in direct contact with the vapor phase, forming a skin layer; **(e, f)** images of the surface of the skin layer, presenting evident cracking.

A second reaction was quenched after 15 minutes of evaporation. Upon immersion in MeCN almost no **PIm** dissolved, as the films had completely solidified, meaning that after this time, the **PIm** concentration was well above the critical gel concentration. In turn, upon delamination from the silicon, the film immediately underwent permanent warping toward the drying side (**Figure 3.30b** and **Figure 3.32a, b**). As long as the film dried maintaining the adhesion to the substrate the component of the tensile stress that did not relax by the viscous deformation of the polymer was stored as elastic strain, which was compensated by the compressive stress on the substrate. If the film was left undisturbed, the elastic strain gradually dissipated as viscous deformation. However, if the film was accidentally or intentionally delaminated from the substrate before all the stresses were dissipated the unbalanced stored elastic strain was quickly released as plastic mechanical deformation by warping and cracking.^[241,242]

The morphology observed by the SEM was drastically different from the material isolated after 10 minutes. As result of the capillary forces, all the macroporosity collapsed, and the material appeared comparable to the final compact film. After 15 minutes, the layered structure of the film appeared evident. When the solution transitioned to the gel state the polymer network could hardly flow, however the relaxation of the stress induced by the anisotropic stretching took place through the network rearrangement. The excess of dangling functional groups facilitated the relaxation of the material through the formation of new

imine bonds and through error-correction resulting from hydrolysis and recondensation, owing to the relevance of these reactions over the timescale of consolidation. In this scenario, the entropic penalty associated with the loss of degrees of freedom was likely compensated by the formation of new intramolecular covalent bonds and intermolecular π -stacking between adjacent strands. The intramolecular cross-linking reactions result in the closure of loops of various orders, between which the most stable are the hexagonal macrocycles typical of the honeycomb lattice of **TPB-MeOTP-COF**. Despite the alignment of the **PI_m** strands parallel to the film surface, a long-range order in the lateral direction was not observed likely due to the electrostatic repulsion between positively charged imine linkages that overcame the van der Waals interactions over longer intermolecular distances.

Interestingly, after 15 minutes of reaction the layered structure seemed to orient along directions that are inclined respect to the film surface and curved in the proximity of the upper and lower surfaces (**Figure 3.32c-f**). This observed pattern matched closely with the hyperbolic streamlines of the flow field predicted by Hu and Larson using an analytical lubrication theory.^[243]

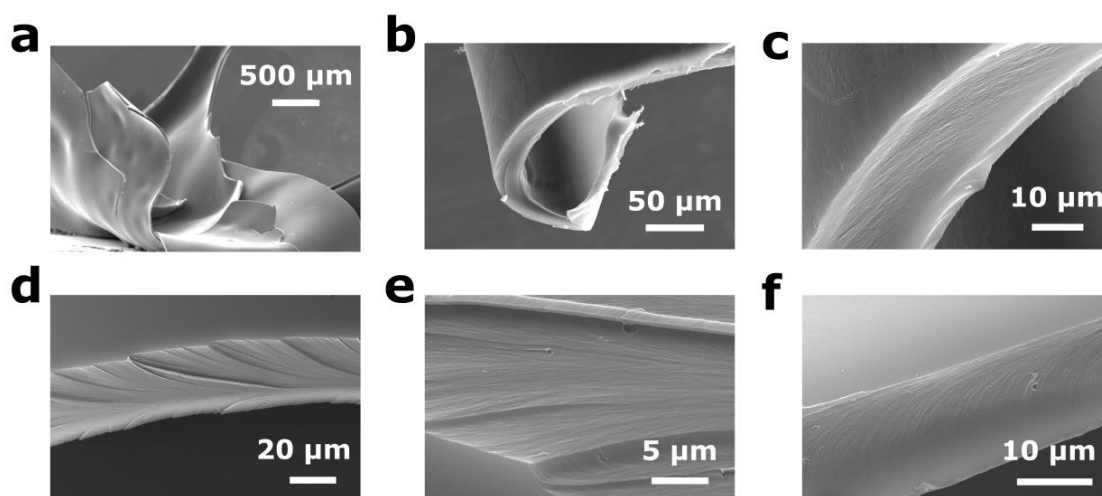


Figure 3.32(a-f) SEM micrographs representing different areas of the film obtained after about 15 minutes of reaction.

After 30 minutes of reaction (**Figure 3.30c**) the in-plane stress had gradually relaxed and from the SEM images of the film cross-section (**Figure 3.33a-c**) we observed that the layered pattern was almost completely aligned with the plane of the film. To completely dissipate the accumulated stress, the film was kept on the substrate at 40 °C for 4 hours (**Figure 3.30d**). Film prepared in these conditions did not undergo any mechanical deformation once delaminated from the substrate by means of a polar solvent. Cross-sectional SEM images (**Figure**

3.33d-f) show a highly oriented and stratified solid.

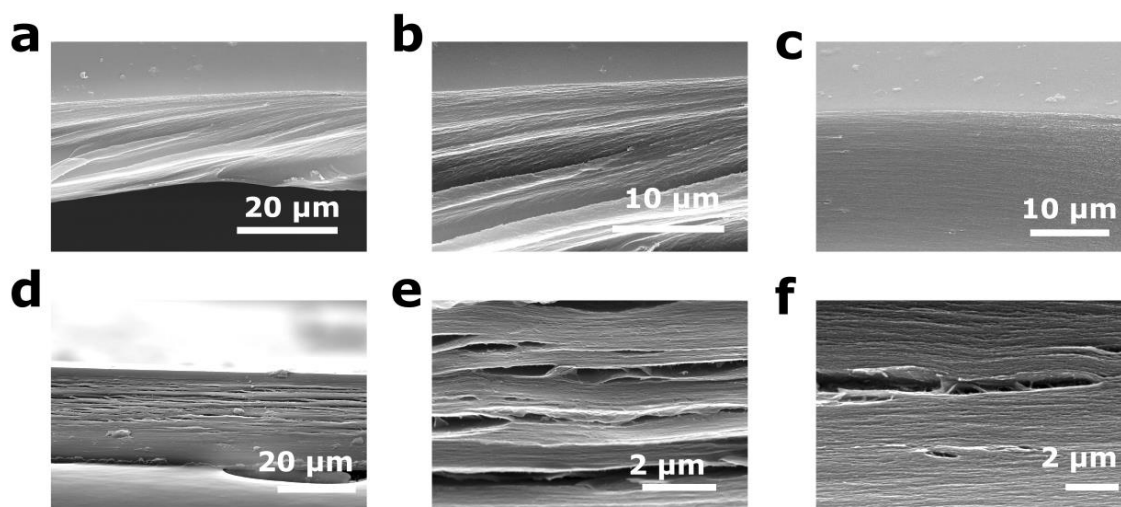


Figure 3.33 (a-c) SEM micrographs representing different areas of the film obtained after about 30 minutes of reaction; and **(d-f)** films obtained upon 4 hours reaction.

3.5.4. Structural evolution of the drying polymer

The morphological SEM study provided a general idea of the evolution of the structure of the material. However, SEM is a highly local characterization technique and, as the drying process is an intrinsically non-uniform transformation, electron microscopy could not provide a quantitative picture of the bulk structural characteristics of the solid.

For this reason, the information collected by microscopy was complemented with a time-dependent structural analysis with 2D GIWAXS. 2D GIWAXS is a non-destructive and fast technique, which does not require any sample preparation. Hence, quenching of the reaction and freeze-drying were in this case not necessary. Films were obtained by drying a drop-let of solution at 40 °C on silicon, and the diffraction pattern was recorded directly on the evolving system by temporarily displacing the cover of the petri dish.

Patterns were recorded at 10, 15, 30, 60, 90, 120, 180, and 225 minutes of delay time from the moment of the deposition of the solution on surface (**Figure 3.34**). After 10 minutes, the 2D pattern showed only a conical halo centered at $2\theta \sim 20^\circ$. This was related to the mean intermolecular distance of the molecule in the liquid phase and indicated the absence of any long-range order in the system, in agreement with the observed partially liquid, and partially porous gel structure evidenced in by SEM.

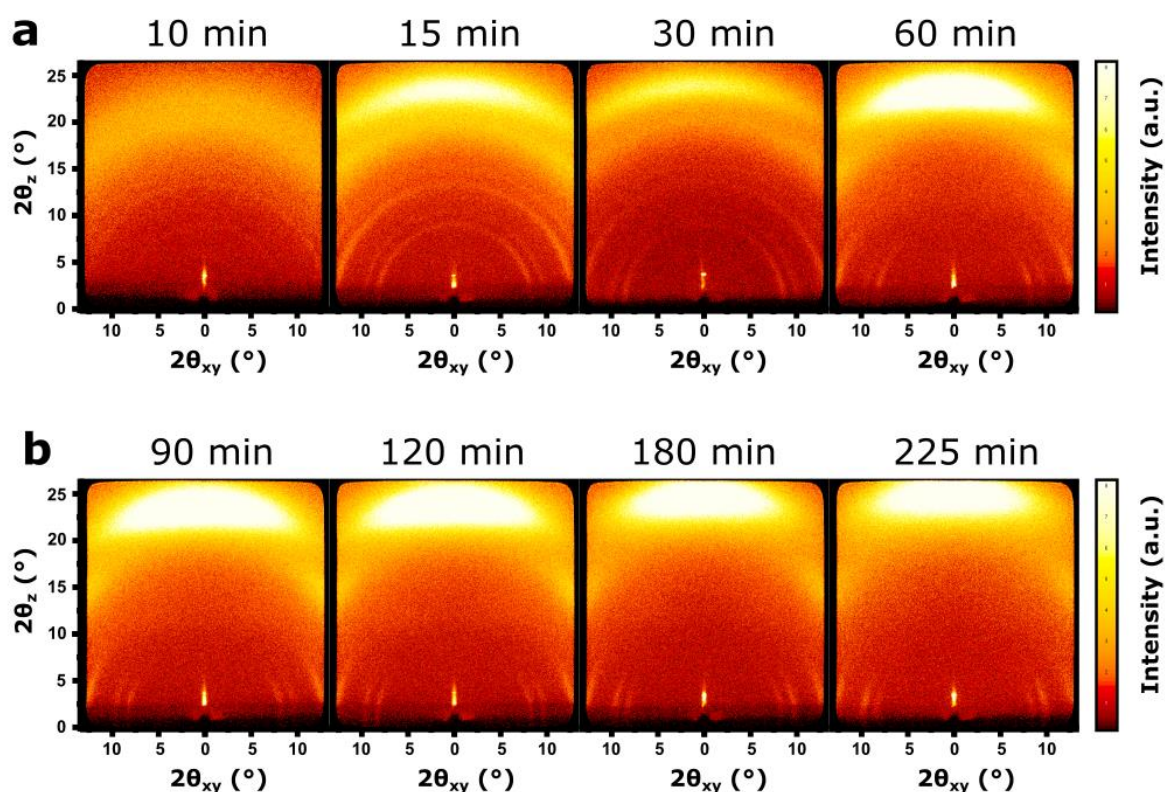


Figure 3.34 2D GIWAXS patterns sequences of the drying formed at different reaction times **(a)** at 10, 15, 30, and 60 minutes and **(b)** at 90, 120, 180, and 225 minutes.

After 15 minutes the material solidified, and the scattering pattern was characterized by weak conical reflections at low angles and a more intense reflection at higher angle. In particular, from the analysis of the profile obtained by integration of scattering signal over the whole measuring area (**Figure 3.35**) we observed that an intense scattering was present at $2\theta \sim 23^\circ$ that was assigned to the interlayer π -stacking of **PIm**. Moreover, five less intense reflections were present at $2\theta \sim 19.3, 14.3, 12.7, 9.6,$ and 8.3° . The reflection at $2\theta \sim 23^\circ$ appeared to be aligned along the z direction, consistently with the observed layering of the material. In contrast, the reflections at lower angles presented a conical shape, denoting a lack of preferential orientation in the corresponding diffraction planes.

At longer reaction time two main changes took place in the scattering pattern. First, the low angle reflections gradually orient along the xy direction between 15 and 90 minutes, suggesting that the diffractions planes related to these reflections progressively aligned perpendicular to the film surface. Second, starting from 60 minutes of reaction the reflection related to the π -stacking was subjected to a gradual shift toward higher angles, hence while no major structural change was taking place in this time interval the desorption of the sol-

vent caused a decrease of the interlayer distance. More importantly, a gradual increase in the orientation was observed over this period.

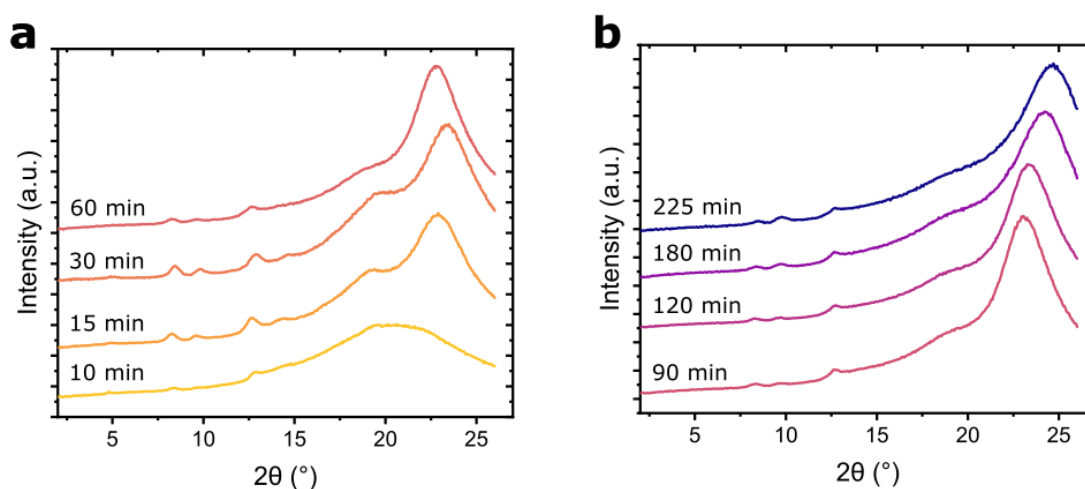


Figure 3.35 Staked plots of the radial integration of the signal intensity obtained from the previous 2D GIWAXS patterns at different times **(a)** at 10, 15, 30, and 60 minutes and **(b)** at 90, 120, 180, and, 225 minutes.

3.5.5. The effect of the evaporation rate

Controlling the evaporation rate was fundamental for the formation of a layered oriented film. We found that a 40 °C heated substrate in a semi enclosed reaction vessel (covered petri dish) offered the best conditions for the fast and precise formation of the desired material.

In this section we report and examine two counterexamples in which the droplet dried either at lower temperature or in an open reaction vessel. We anticipate that in neither of the two reaction conditions we could prepare a layered oriented material due to a combination of physical and chemical factors.

First, we examined the influence of the temperature on the outcome of the reaction. The synthesis was carried out by casting the solution on the silicon substrate at room temperature (about 20 °) in the semi enclosed reaction vessel. In these conditions, the reaction vessel quickly saturated with the solvent vapor and the rate of evaporation greatly decreased with respect to the standard reaction conditions, with the solidification of the material starting only after several hours. A seemingly dry film was isolated after 12 hours (**Figure 3.36**). The film was highly inhomogeneous with the edges appearing compact but partially delaminated and cracked and the central part showing a highly discontinuous material with a rough surface.

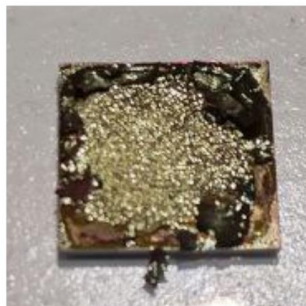


Figure 3.36 Photograph of the dry film after 12 hour at 20 °C in the semi enclosed reaction vessel. The image was taken before exposing the film to the solvents for the work-up procedure.

The rough central area of the film was analyzed by SEM. The film appeared discontinuous due to the high concentration of cracks and composed of islands of more compact material (**Figure 3.37a, b**). Cross-section images (**Figure 3.37c, d**) showed that the material was made of coalesced spherical particles of roughly 500 nm in size, which explained the poor mechanical properties of the film. Likely, after the initial sol-gel transition on surface the wet gel system became more and more concentrated, up to the point when π -stacking could overcome the electrostatic repulsion between the protonated branches of the macroporous 3D network. Beyond this point the new phase of **PIm** could nucleate and further grow following a nucleation-growth mechanism leading to typical spherical particle shape of 2D COFs. This observation supports the fact that, at least at the high concentrations preceding the complete drying of the material, the **PIm** gel is the kinetic product of the system, as spherical particles are observed only when the system is given enough time to equilibrate before the evaporation of the solvent and solidification of the system. For this process to take place the **PIm** must have enough time to hydrolyze from the kinetic gel state and repolymerize in the spherical morphology. Indeed, we have shown that the hydrolysis occurred with an estimated lifetime of about 7 minutes, which was not sufficiently rapid to effectively enable the equilibration from network to particles when the synthesis was carried out at 40 °C and solidification happened in ca. 10-15 min. These results indicated that the reaction at 40 °C under these conditions proceeded under kinetic control. Meanwhile, when the drying process was conducted at 20 °C, the evaporation was sufficiently slow for the hydrolysis to efficiently take place and the reaction was run under “pseudo-thermodynamic” control.

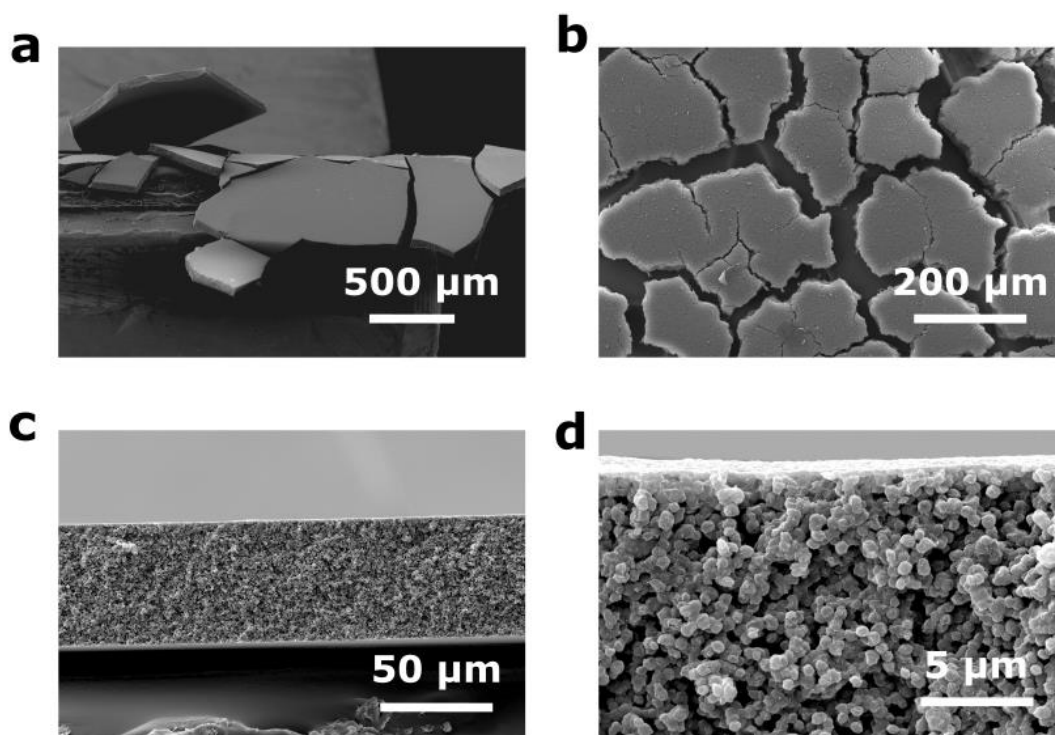


Figure 3.37 SEM images of the film synthesized at 20 °C. **(a, b)** Side and top views of the film. **(c, d)** Cross-section images of the film, clearly showing that it is constituted by particles.

The structural order of the film was characterized by PXRD in reflection geometry at different delay times from the start of the reaction. As in the initial part of the reaction the droplet was still completely liquid, only the period between 9 and 12 hour of reaction was analyzed (**Figure 3.38**). After 9 hour of reaction the film displays 6 reflections at $2\theta \sim 8.2, 9.5, 12.6, 14.3, 19.1,$ and 22.9° . Interestingly, the position of these reflections matched closely with the pattern found for the layered material prepared at 40 °C and reported in **Section 3.5.4** except from the fact that in this case the material did not assume a preferred orientation.

Further evolution of the scattering profile was associated with the drift of all the reflections toward higher angles, with the strongest shift being displayed by the reflection related to the π -stacking which gradually moved from 22.9 to 25.5° due to the desorption of solvent. Furthermore, the relative intensity of the peaks changed in time: in particular, the reflection at $2\theta \sim 8.2, 12.6, 14.3,$ and 19.1° became weaker and the reflection at 9.5° became more intense. This evolution may be related to the coexistence of two phases both showing short-range order whose ratio changes with the evaporation of solvent. Overall, the formation of the specific phases was independent from the morphology and was likely associated with

the arrangement of the protonated **PIIm** structural units in space.

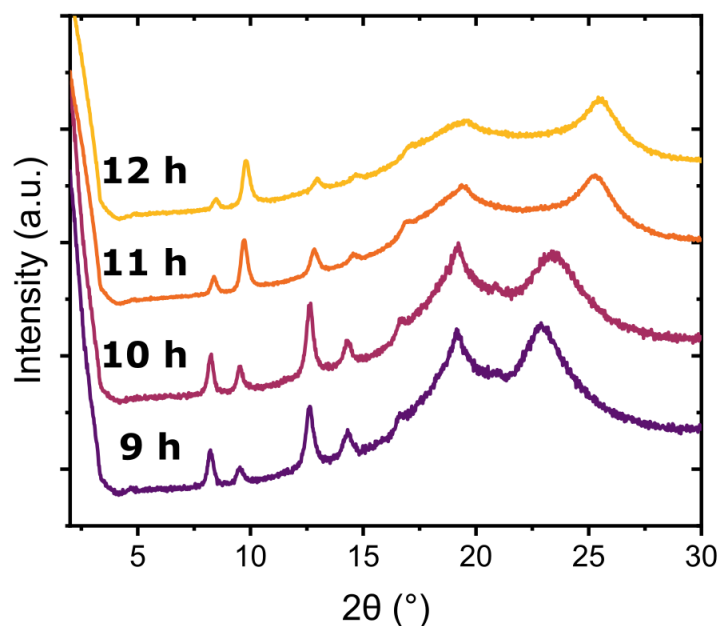


Figure 3.38 PXRD in reflection geometry of the drying film synthesized at 20 °C. The four patterns are related to different delay times from the beginning of the synthesis: 9, 10, 11, and 12 h.

In contrast, when the **PIIm** solution was cast on a preheated substrate at 40 °C in the open vessel, unoriented film was formed. Under these conditions the evaporation took place rapidly, due to the high gradient in vapor pressure. The film solidified within 5 minutes, but the generated stress on the polymer did not have time to relax as viscous deformation by rearrangement and alignment of the polymer strands. Instead, the stress was accumulated as elastic deformation which was compensated if the film adhered to the silicon substrate. Abrupt delamination and cracking and warping occurred when the stored elastic strain energy overcame the adhesion energy of the gel attached to the substrate (**Figure 3.39**).^[242] After 10 minutes the film had completely delaminated from the substrate.

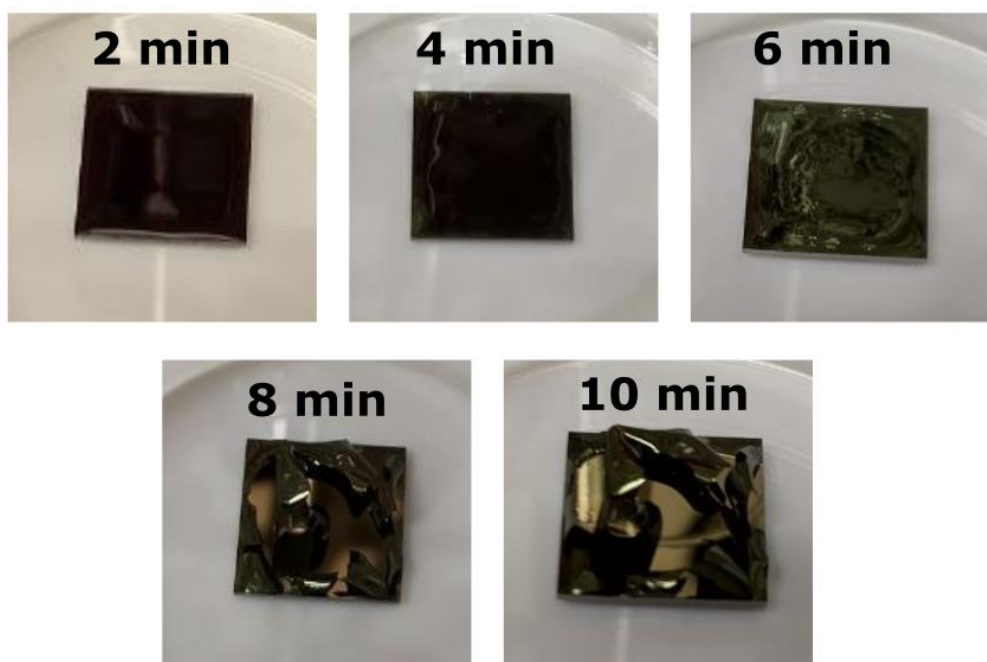


Figure 3.39 Photographs sequence of the film drying at 40 °C directly in the open environment.

The material was left to evaporate over 4 hours. After the workup the film was analyzed by SEM. As shown in **Figure 3.40**, the film in this case did not display neither a layered structure nor a spherical particle morphology, appearing different from both the standard reaction conditions and the reaction at low temperature. Indeed, the material appeared as overall homogeneous film (**Figure 3.40a**), whose fine structure, visible in **Figure 3.40b** was compact and continuous, but very rough. Under these conditions, the stress in the film was dissipated by abrupt plastic deformation concomitant with delamination from the substrate rather than viscoelastic rearrangement of the polymeric strands, and consequently, no orientation was observed. As most of the solvent quickly evaporated and most of the stress was dissipated in the initial period of the reaction, upon delamination of the film from the surface, the polymer gel did not have the time neither to stretch nor to repolymerize as particles, but instead, it shrunk and collapsed generating the observed morphology.

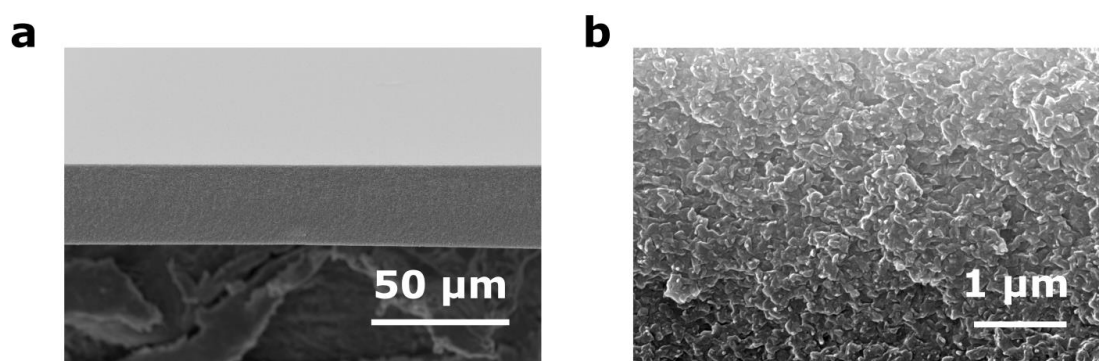


Figure 3.40 (a) Cross-section SEM image of the film prepared at 40 °C in the open environment. (b) detail of the morphology of the film.

The structure of the material was examined by PXRD in reflection (**Figure 3.41**). The scattering pattern obtained from solid presented five main reflections at: $2\theta \sim 8.5, 9.9, 13.0, 19.6,$ and 25.5° , which matched with both the pattern of the layer oriented **PIIm** and the unoriented **PIIm** particles, further demonstrating the common local structural order of polymer at the solid state, regardless of morphology of the material.

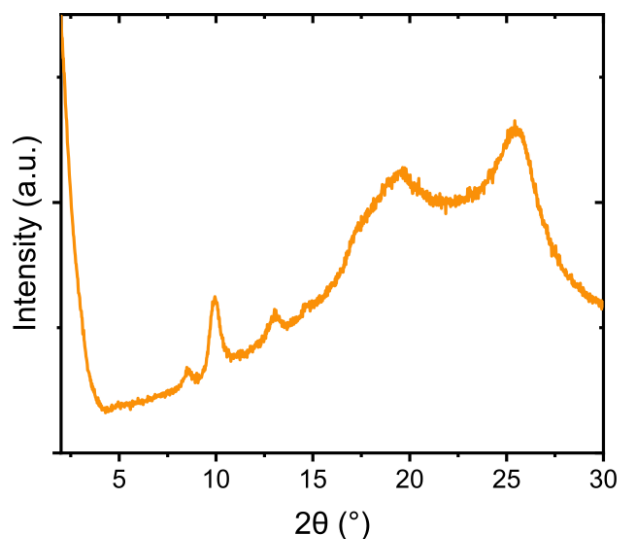


Figure 3.41 PXRD in reflection geometry of the drying film synthesized at 40 °C in the open environment.

3.6. Scope of the method

To demonstrate the generality of the synthetic procedure a 2D COF with rhombic lattice

was synthesized using TPPy (1,3,6,8-Tetrakis (4-aminophenyl) pyrene) as tetrafunctional knot and MeOTP as linker (**Figure 3.42**). This COF has been previously prepared using the solvothermal method.^[244,245]

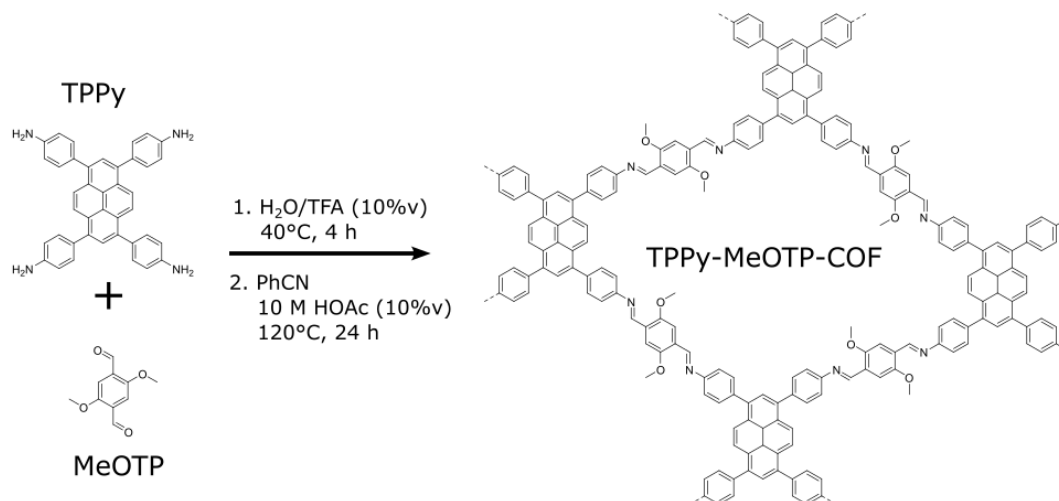


Figure 3.42 Reaction scheme for the preparation of **TPPy-MeOTP-COF** oriented films.

Initially the polymerization reaction was run using the same conditions used for the synthesis of **TPB-MeOTP-COF**. A solution of amine [TPPy] = 75 mM in H₂O - TFA (5 % v) was mixed with an equal volume of a solution of aldehyde [MeOTP] = 150 mM in the same solvent to obtain a final functional group concentration $C_0 = 150$ mM. The polymerization reaction between the two monomers quickly induced a change of color and viscosity of the solution, and a gel formed within few hours (**Figure 3.43a**). The formation of the gel phase indicated that in the selected conditions of concentration, temperature, and solvent composition, the extent of reaction p is higher than the critical point. Indeed, it is expected that in a $A_4 + B_2$ hyperbranched polymerization the critical extent of reaction p_c is comprised in the 0.58 – 0.75 range, where the extreme values were calculated with the theory of Flory - Stockmayer and Carothers respectively. Noteworthy, the theories predict the formation of a gel at lower extent of reaction for $A_4 + B_2$ polymer respect to a $A_3 + B_2$ system (0.71 – 0.83), due to the higher probability of cross-linking in presence of a tetrafunctional structural unit.

To avoid the formation of a gel it is necessary to shift the equilibrium of the polycondensation toward a lower value of extent of reaction. While maintaining the concentration and the temperature fixed, the formation of a stable polyimine solution was achieved by changing the solvent composition from 5 % to 10 % water content (in volume). The composition of the

resulting polyimine solution was studied by ^1H NMR using TFA-*d* and D_2O as solvents (**Figure 3.43b**). The ratio between the integrated area of the methoxy resonances at 4.02 ppm (monomer), 4.19 ppm and 4.46 ppm (terminal unit), and 4.54 ppm (core unit) was used to calculate the relative amounts of the species at the equilibrium. The extent of reaction was calculated as $p = 0.61^\circ$ and the equilibrium constant resulted as high as $K_{eq} = 153$.

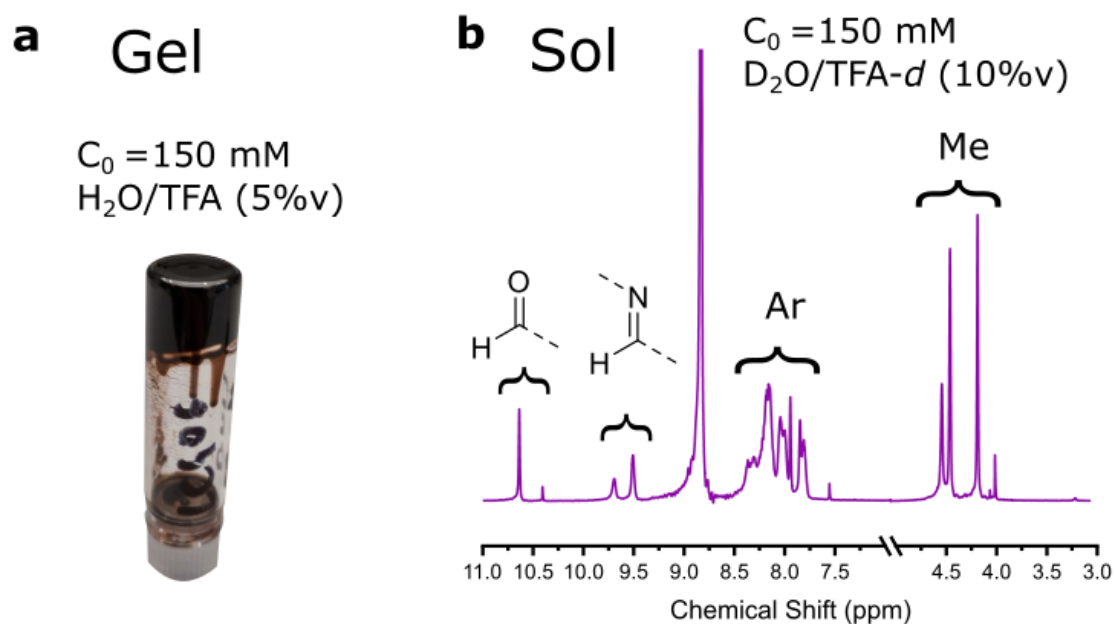


Figure 3.43 (a) Photo of the inverted vial containing the gel formed by polymerization of TPPy and MeOTP in $\text{H}_2\text{O}/\text{TFA}$ (5 % v). (b) ^1H NMR of the fully dissolved polyimine obtained by reaction of TPPy and MeOTP in $\text{D}_2\text{O}/\text{TFA-}d$ (10 % v).

The polyimine solution was used to prepare a film by polymer solution casting, at 40°C for 4 hours, using the same protocol described for **TPB-MeOTP-COF**. The product was obtained as continuous and robust orange film. The 2D GIWAXS analysis (**Figure 3.44**) showed a scattering pattern dominated by a π -stacking distance-related reflection centered at 22.6° . The peak was concentrated along the z direction, and together with the weaker reflections observed only in the xy direction (at 4.6° and 8.6°) indicated that the material presented a strong structural anisotropy. As in the case of the polyimine precursor of **TPB-MeOTP-COF**, the film was found to be oriented with the π -stacking direction normal to the film face.

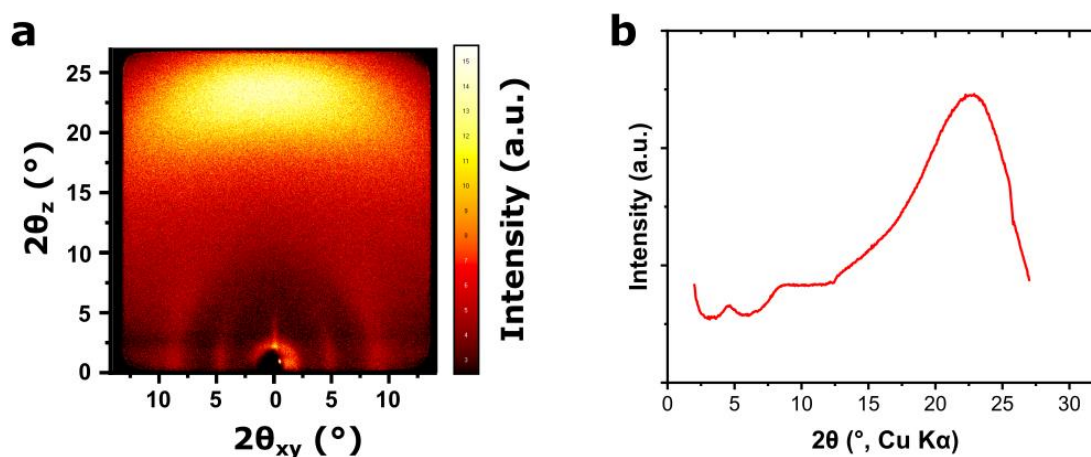


Figure 3.44 (a) 2D GIWAXS pattern of the polyimine film. (b) Radial integration of the 2D GIWAXS profile.

The polyimine intermediate displayed poor crystallinity, in accordance with the results obtained for the polyimine precursor of **TPB-MeOTP-COF**. To improve the degree of crystallinity, the material was recrystallized by annealing in benzonitrile (PhCN) at 120 °C for 24 hours with 10 M HOAc as catalyst. Notably, the annealing in MeCN, developed for **TPB-MeOTP-COF** failed to produce any improvement in crystallinity.

The annealed film was obtained with no significant mass loss and no observable alterations in its color or size. Upon performing a 2D GIWAXS analysis on the recrystallized film, high anisotropy was observed, with two distinct sets of sharp reflections oriented perpendicular to one another (as shown in **Figure 3.45**). Specifically, the in-plane reflections at 4.1 and 8.2 ° were centered on the xy axis and corresponded to the (110) and (300) planes, respectively.^[245] Additionally, the diffraction from the (001) plane was detected at 24.6 ° and centered on the z axis. These findings indicate that the **TPPy-MeOTP-COF** film exhibited high crystallinity and orientation, providing evidence for the generality of the synthetic method.

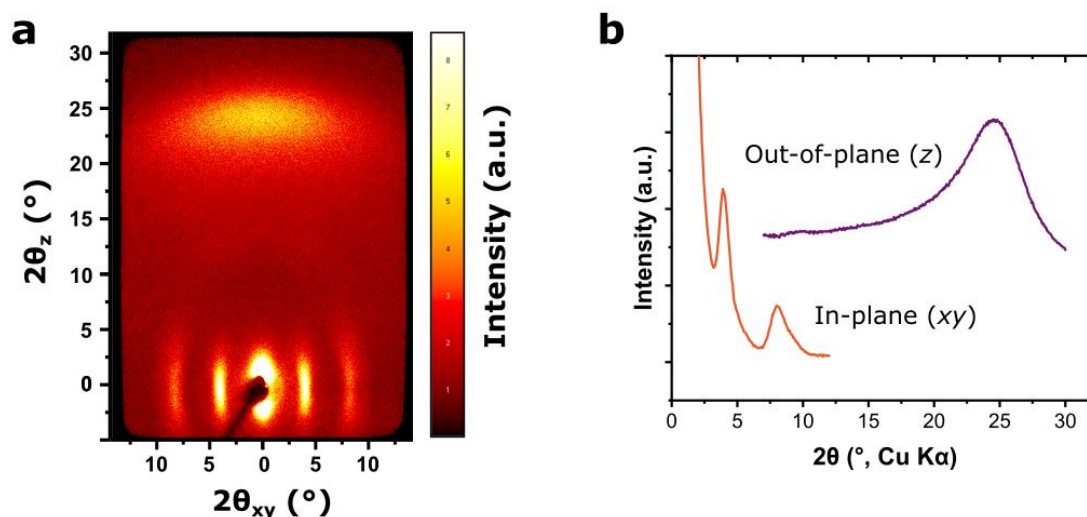


Figure 3.45 (a) 2D GIWAXS pattern of the recrystallized film. (b) Staked plot of the in-plane (orange line) and out-of-plane (violet line) radial integrations of the 2D GIWAXS profile.

3.7. Conclusions and perspectives

In conclusion, in this chapter we reported a radically new method for the preparation of crystalline, porous, and oriented films of 2D COF. The method consisted of two main steps. In the first step we prepared a layered and highly oriented polyimine film by solution cast polymerization, which displayed low crystallinity and no porosity. Afterwards we developed a protocol for the recrystallization of the polyimine film into a crystalline and porous COF, while preserving the overall orientation of the crystallites.

Furthermore, we investigated the origin of the orientation achieved in the polyimine film. Through a thermodynamic study we determined that the polymerization in water - TFA solution followed a step-growth mechanism, and resulted in a 3D polymer network, rather than a particle-based 2D COF. The subsequent morphological and structural investigations of a droplet of solution drying on surface demonstrated that the material initially solidified as 3D polymer network. Then it gradually stretched to generate an oriented layered structure under the outward tensile stress generated by the solvent evaporation. However, as demonstrated by our kinetic studies, the layered structure could be obtained only upon use of correct conditions of evaporation rate. A slow rate resulted in the nucleation and growth of polymer particles, proving that while this morphology was the thermodynamic product of the reaction, the stretched 3D polymer network represented a kinetic product. Additionally, when the evaporation was too fast, the elevated stress on the polymer film overcame the

adhesion energy with the substrate and the film delaminated. Once detached from the substrate, all the stresses on the polymer were abruptly dissipated, triggering a disordered collapse of the 3D network. A visual summary of the described mechanism is reported in **Figure 3.46**. Overall, this study demonstrated that the final morphology was highly dependent on the history of the material.

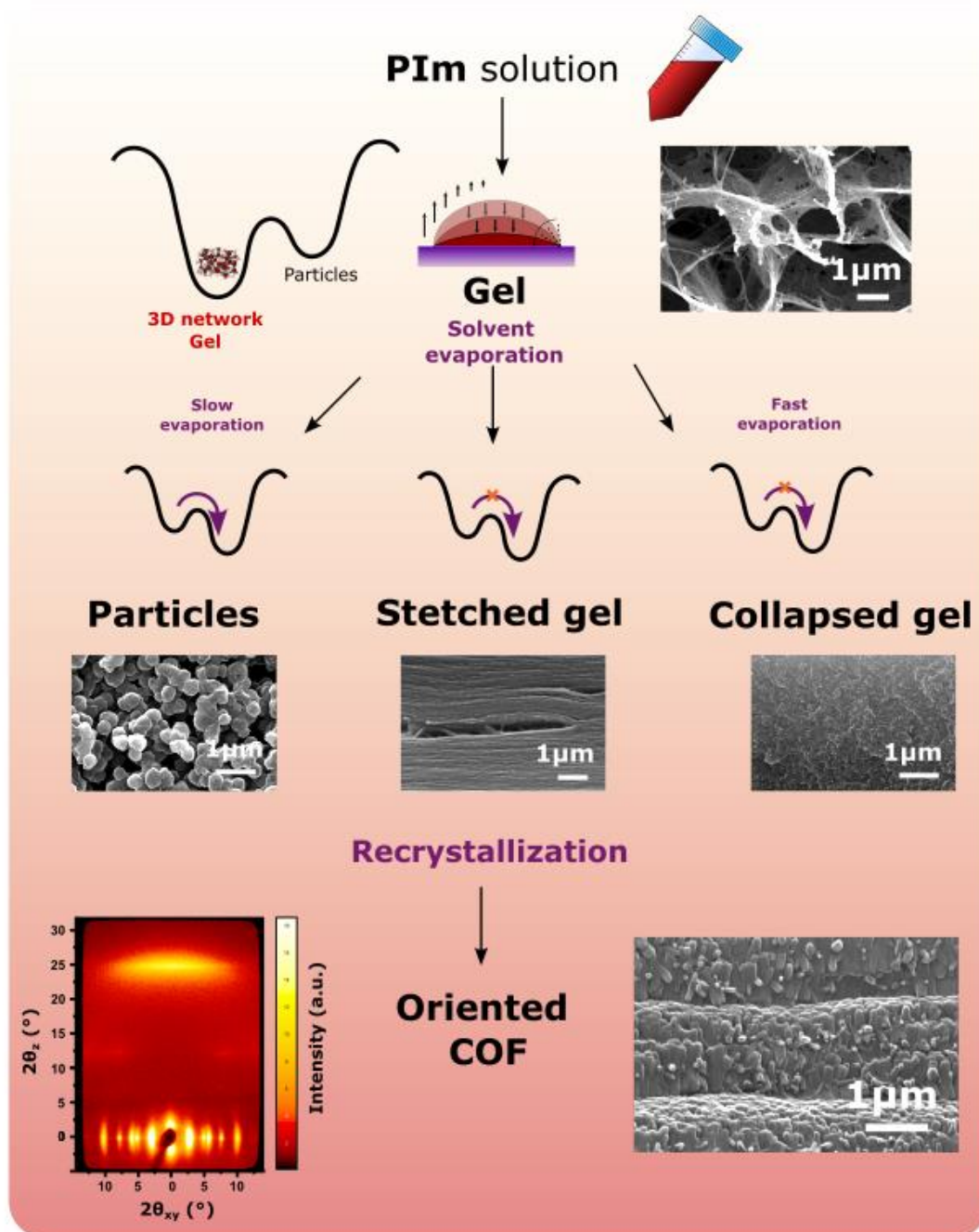


Figure 3.46 Hypothetical potential energy landscapes of the polymer solution in different conditions and SEM images of the respective obtained material.

At last, we successfully demonstrated the versatility of the synthetic protocol for the preparation of oriented, self-standing 2D COF films with different 2D topologies. Specifically, in addition to **TPB-MeOTP-COF**, we have also been able to apply this methodology to the preparation of **TPPy-MeOTP-COF**, showcasing the potentially broad applicability and adaptability of our protocol.

Future developments of this project, aim to further explore the scope of the method by investigating the film formation with different amine knots (such as 5,10,15,20-Tetrakis (4-aminophenyl)porphyrin, and 2,4,6-tris(4-aminophenyl)-1,3,5-triazine) and different aldehyde linkers (such as terephthalaldehyde, 2,5-difluoro terephthalaldehyde, 2,5-dihydroxyl terephthalaldehyde and others). We anticipate that the main factor in determining suppression of the particle nucleation seems to be related with the geometrical distortion of the amine backbone, which for example is highly reduced in monomer such as the flat 2,4,6-tris(4-aminophenyl)-1,3,5-triazine. Additionally, from preliminary experiments it was found that the 2,5 substitutions of the terephthalaldehyde with methoxy groups is crucial to obtain high degree of polymerization in the water – TFA mixtures. We speculate that this behavior could be mainly related to the stabilization of the protonated imine bond *via* intermolecular hydrogen bonding or by an electronic factor related to the substituents.

Crystalline and oriented porous films offer a great opportunity to study the anisotropic properties of 2D COFs. The 1D pore channels are oriented normal to the film section and we predict that such a structural feature, in conjunction with the morphological continuity and the mechanical robustness of the film can be successfully exploited for several application related to the capture and / or separation of molecules or ions in the gas or liquid phase.

3.8. Materials and methods

Materials

All reagents were purchased from commercial sources such as Sigma-Aldrich, TCI, abcr, BLD Pharm, FluoroChem and were used as received. Solvents were purchased from commercial sources such as Carlo Erba, Fischer Scientific, Carl Roth, Acros and used without any further purification. Deionized water was used in all the preparations. Silicon substrates were purchased from Fraunhofer and were directly used after rinsing with MeOH and drying with nitrogen flux.

Preparation of the **PIm** solutions (TPB-MeOTP)

Stock concentrated solution of the of the monomers were prepared by dissolving the re-

spective solids in a mixture of water and TFA. The monomers' solutions were then mixed in equimolar ratio at room temperature to produce the **PIm** solution.

In a typical reaction, [TPB] = 100 mM ($C_0 = 300$ mM) was prepared by dissolving in 175.7 mg of TPB (0.5 mmol) in 5 ml of 5% water-TFA (v/v), and [MeOTP] = 150 mM ($C_0 = 300$ mM) was prepared by dissolving in 145.6 mg of MeOTP (0.75 mmol) in 5 ml of 5% water-TFA (v/v). 2 ml of $C_0 = 150$ mM **PIm** solution were then prepared by transferring 1 ml from each monomer solution in a 5 ml vial and mixing by gently shaking. Upon mixing the solution rapidly changed color from yellow to bright red and the viscosity greatly increased. Before, further processing of the solution an equilibration time of 15 minutes was always respected.

For the preparation of solutions at lower concentrations the $C_0 = 150$ mM **PIm** solution was diluted by addition of the suitable amount of solvent. For **PIm** solutions/gels at higher concentrations the preparation of stock monomers' solutions with higher concentrations was necessary, with the upper limit of [TPB] = 400 mM and [MeOTP] = 600 mM, related to the limited solubility of TPB.

For the preparation of solutions with a different solvent composition the same procedure was adopted, but the new solvent mixture was directly used from the preparation of the solutions of the monomers.

For the preparation of the NMR solutions, deuterated solvents were used in place of the protonated ones. The preparation was carried out on a 0.5 ml scale.

Procedure for the preparation of the oriented films (TPB-MeOTP)

A 1.5 x 1.5 cm² silicon substrate was placed in a $\Phi = 5$ cm, $h = 1$ cm petri dish. The petri dish was placed on 40 °C pre-heated hotplate, taking care that the surface was horizontal, by means of a bubble level. Oriented films were prepared by carefully casting 0.15 ml of $C_0 = 150$ mM **PIm** solution on the surface of the substrate. After the deposition, the petri dish was quickly covered with the complementary glass cover. The film was left drying on surface for 4 hours resulting in a smooth golden reflective coating. Then the cover was removed, and the substrate was quickly immersed in MeOH, which caused the delamination of the film from the surface and the change of color to dark red. The self-standing film was then picked-up with tweezers and transferred in a 10% TEA-MeOH (v/v) solution, inducing the neutralization of the adsorbed TFA evidenced by the quick color change to bright yellow. The film was then Soxhlet extracted with THF for 12 hours to remove low molecular weight oligomers. THF was exchanged 3 times with *n*-pentane, solvent with a low surface tension (15.5 mN m⁻¹), and then dried in air. The drying up process was carefully carried out by suspending the film to favor an even evaporation of the solvent from both sides and avoid warping deformations. After 1 hour the film was transferred in a vacuum oven and the volatile residues of solvents were removed at 50 °C for 12 hours under reduced pressure. Alternatively, after the Soxhlet extraction the solvent was exchanged with MeOH and then dried using supercritical CO₂. The material was finally isolated as robust, flexible, homogeneous, transparent-yellow film, with a yield of 95%.

Procedure for the recrystallization of the film (TPB-MeOTP)

The recrystallization was carried out by placing the pristine **PIm** film in a 10 ml crimp seal vial together with 0.2 ml of MeCN and 0.02 ml of 10 M acetic acid. The vial was then placed

in an oven and heated to 100 °C for 24 hours. After cooling down, the film was washed with MeCN and THF, up until the solvent becomes colorless. Then THF was exchanged with *n*-pentane and dried according to the procedure reported for the pristine film. The recrystallized film was obtained as opaque-yellow film with a yield of 90%.

Procedure for the preparation of non-oriented films (TPB-MeOTP)

The non-oriented films were prepared by modification of the oriented film procedure. In particular, to obtain the “collapsed gel” morphology the reaction was carried out in the same conditions, but no cover was used to control the evaporation rate. In this case the solution quickly dries, cracks, and delaminates from the substrate. The reaction was still carried out for 4 hours and the same workup protocol was followed. The solid was finally isolated as brittle, fragmented, yellow film. To obtain the “particles” morphology the main preparation protocol was carried out, but the reaction was run at room temperature (20 °C) for 12 hours. The solid was finally isolated as highly brittle, highly fragmented, yellow film/powder.

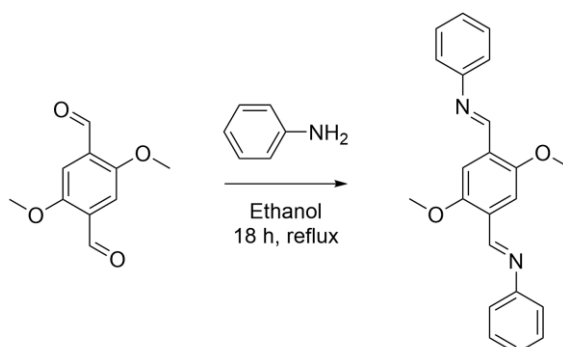
Procedure for the preparation and the isolation of the gel (TPB-MeOTP)

For the preparation of the gel [TPB] = 400 mM and [MeOTP] = 600 mM solutions in 5% water-TFA were mixed in equimolar ratio to obtain a $C_0 = 200$ mM **P1m** solution. In a few second from the mixing the sol-gel transition takes place. The reaction was equilibrated over 1 hour and then the solid was thoroughly washed with MeCN to remove the solvent and the low molecular weight oligomers, until the washing solvent was colorless. The resulting MeCN-wet solid was freeze-dried to isolate the final material as red powder.

Procedure for the reaction quenching experiment (TPB-MeOTP)

For the SEM analysis reported in **Section 3.5.3**, the reaction to from the oriented **P1m** film was quenched at different delay times. The quenching was carried out by quickly opening the reaction vessel (covered petri dish) and immersing the material with a large amount of MeCN. The film delaminated from the substrate and was further washed with MeCN until the solvent turned colorless. Then the MeCN-wet solid was freeze-dried to isolate the final material.

Synthesis of the An₂-MeOTP model compound



The An₂-MeOTP model compound was synthesized according to the reported procedure.^[71]

250 mg of MeOTP (1.3 mmol) 1.3 mmol, were dissolved in 60 ml of anhydrous ethanol in a 250 ml round bottom flask. Then 0.47 mL of aniline was added (5.15 mmol, 4 eq). The resulting mixture was heated at reflux for 18 h, then allowed to cool to ambient temperature, yielding a yellow precipitate. This was isolated by filtration and recrystallized in ethanol to yield An₂-MeOTP (371 mg, 1.07 mmol, 83 % yield). ¹H-NMR (500 MHz, CDCl₃, δ): δ 8.93 (s, 2H), 7.77 (s, 2H), 7.40 (m, 4H), 7.24 (m, 6H), 3.96 (s, 6H).

Synthesis of TFA-TEA

The TFA-TEA ionic liquid was synthesized modifying the reported procedure.^[229] 1 ml of TFA was placed in a ice bath under stirring. TEA was added dropwise, until pH neutrality is reached. The ionic liquid was dried under vacuum overnight to remove the reagents' residue. ATR-FTIR characterization is reported in the main text.

Procedure for the UV-vis hydrolysis (TPB-MeOTP)

Quick dilution is a simple and effective method to initiate the hydrolysis of **PI_m** to its components. With this method, the kinetic of the hydrolysis of **PI_m** was studied in 5% water-TFA at 23 °C, in a UV-vis spectrophotometer with thermostatted cell compartment. To initiate the reaction 1 μl of C₀ = 150 mM **PI_m** stock solution is added to 3.5 ml of solvent directly in the quartz cuvette followed by quick shaking of the cell to homogenize the solution. The measurement was conducted under stirring at 500 rpm.

Procedure for the preparation of the TPPy-MeOTP-COF oriented films

TPPy-MeOTP-COF oriented films were prepared using the same procedure reported for **TPB-MeOTP-COF**, with minor modifications.

In a typical reaction, [TPPy] = 75 mM (C₀ = 300 mM) was prepared by dissolving in 42.5 mg of TPPy (0.075 mmol) in 1 ml of 10 % water-TFA (v/v), and [MeOTP] = 150 mM (C₀ = 300 mM) was prepared by dissolving in 29.1 mg of MeOTP (0.15 mmol) in 1 ml of 10 % water-TFA (v/v). 2 ml of C₀ = 150 mM **PI_m** solution were then prepared by transferring 1 ml from each monomer solution in a 5 ml vial and mixing by gently shaking. Before, further processing of the solution an equilibration time of 15 minutes was always respected.

Oriented films were prepared by carefully casting 0.15 ml of C₀ = 150 mM **PI_m** solution on the surface of the substrate pre-heated at 40 °C and enclosed in a glass Petri dish. The film was left drying on the surface for 4 hours. The workup was carried out following the same protocol reported for **TPB-MeOTP-COF**. The material was finally isolated as robust, flexible, homogeneous, transparent-orange film, with a yield of 95 %.

The recrystallization was carried out in a 10 ml crimp seal vial with 0.2 ml of PhCN and 0.02 ml of 10 M acetic acid. The vial was then placed in an oven and heated to 120 °C for 24 hours. The film was obtained in a 90 % yield.

4. Design of an electron-rich imine-based 2D COF for optoelectronics and energy storage

4.1. Introduction

Organic semiconductors (OSCs) are carbon-based materials that gained increasing attention due to their potential use in a wide range of electronic devices, such as organic photovoltaics, organic light-emitting diodes, and organic field-effect transistors. They offer a series of advantages over traditional silicon-based electronics: they can be processed using low-cost techniques and deposited on flexible substrates. Their optical and electronic properties can also be easily tuned through organic synthesis. However, their charge transport properties are typically modest compared to their inorganic counterpart.^[246]

OSCs are composed of small molecules or polymers, characterized by extended π - π or π -n- π bonding systems, which are crucial for efficient charge delocalization and therefore high charge-carrier mobility. For OSCs to exhibit macroscopic electronic conductivity, the charge carriers need to efficiently move between adjacent molecules, forming percolation pathways which determine the final electronic properties of the material and depends strictly on the spatial organization of the molecules in the solid state. In the case of semiconducting polymers, the charge delocalization can extend over the conjugated covalent bonds thus facilitating the charge transport by bridging the adjacent crystalline domains with polymeric chains. Conversely, in small molecules, the π -conjugated system is localized in the core of the molecule, and the charge transport relies only on the overlap of the π clouds directed by the non-covalent intermolecular interactions.^[247]

In this context, 2D COFs are considered a new class of materials for organic electronics due to their crystalline and conjugated structure. Indeed, the charge transport in these materials can proceed both in-plane along the π -conjugated 2D polymeric backbone, and out-of-plane, through the 1D π - π stacked assemblies forming layered materials.^[8] These structural features could in principle provide a strong electronic coupling within the material and for this reason 2D COFs are predicted to exhibit interesting optoelectronic behaviors.^[56,171] Being organic polymers, 2D COFs possess a highly modular skeleton, and in particular π -extended and redox-active structural units can be easily included in the framework. Additionally, the geometry of the building blocks determines the 2D lattice symmetry which has been shown to influence the electronic structure of the final material.^[177] Because of these interesting

features a great effort is being dedicated to investigating the performances of these materials in proof-of-concept applications. Several examples of (opto)electronic devices were realized using 2D COFs, such as transistors, photovoltaic, light emitting, and sensor devices.^[8]

Moreover, 2D COFs have attracted even greater attention because in addition to the aforementioned semiconductive nature, they possess a unique, defined, and tunable porous structure which leads to high surface areas. The porosity is constituted by highly ordered 1D pore channels of tunable size and shape which offer a fixed path for mass transport within the material along the 1D channels. This feature endows 2D COFs with ion conduction properties, which in conjunction with the electrical conductivity and the redox activity, are particularly appealing for electrochemical applications, such as photocatalysis and energy storage.^[178]

The development of new porous, conjugated and electroactive 2D COFs for use in electronic and energy devices is crucial to expand their potential applications.^[178,248] This chapter reports on the synthesis and characterization of a COF material based on two known electroactive moieties: N,N,N',N'-tetraphenyl-1,4phenylenediamine (**BTA**) and thieno[3,2-*b*]thiophene (**TT**). **BTA** is triphenylamine derivative that has recently been employed as knot for the construction of 2D COF (**Figure 4.1**).^[249,13,185,250–252] Its tetragonal geometry has been shown to lead to the formation of a dual-pore Kagome-like 2D topology upon reaction with a bifunctional linear linkers.^[13,251] The triphenylamine structural unit, at the base of this molecule, is a thermally stable, propeller-shaped moiety that has been included in the skeleton of various polymers endowing these materials with photo- and electro-activity.^[12,253] These features are related to the stability of corresponding radical cation which easily generated by single-electron oxidation of the nitrogen center.^[254] Accordingly, **BTA**-based 2D COFs, are promising in several optoelectronic and energy-related applications and have already been tested as p-type semiconductors,^[13] in electrochromic devices^[250] and as electrodic material for energy storage.^[185,249,252] In particular Rotter et al. showed that a 2D COF constructed from **BTA** and thiophene-derived building blocks possess high conductivity both as “pristine material” $\sigma = 1.6 \times 10^{-3} \text{ m}^{-1}$, and doped material $\sigma = 3.7 \text{ S m}^{-1}$ where the latter was obtained by infiltration of an electron-acceptor molecule in the porous structure.^[13] Inspired by the properties of this material we decided to investigate the synthesis and the properties of a 2D COF with a similar structure.

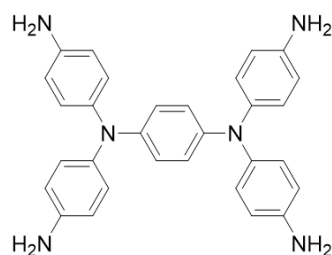


Figure 4.1 Structure of N,N,N',N'-tetraphenyl-1,4phenylenediamine (**BTA**).

On the other hand, thiophene and fused thiophene building blocks have been used in several cases to build electroactive 2D COFs.^[255] In particular, **TT** consists in two fused thiophenes and it results in a flat, rigid, and stable moiety, being ideal to build solid-state structures with strong intermolecular interactions (π - π and S \cdots S). The two fused thiophene rings, generate an electron-rich structure with an extended π -conjugation and a pronounced character of the quinoidal structure (**Figure 4.2**) which makes this moiety a prolific structural motif for the construction of p-type semiconductors.^[256]

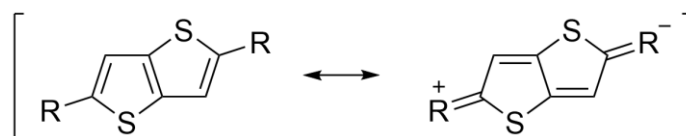


Figure 4.2 Resonance structures of thieno[3,2-*b*]thiophene (**TT**).

BTA-TT-COF was synthesized through dynamic Schiff-base chemistry. The imine linkage used for the construction of the polymer offers several advantages such as a good tradeoff between stability and reversibility and a formally conjugated bridge to connect the building blocks and extend the π -conjugation over the entire covalent structure.^[257] Using a solvothermal approach both a bulk powder polymer and a thin film at the solid / liquid interface were prepared. The first part of this chapter discusses the synthesis and characterization of the structure and chemical composition of both materials. In the second part, their charge transport properties and energy storage capabilities were analyzed by incorporating them into simple electronic and energy storage devices.

4.2. Results and discussion

4.2.1. Solvothermal synthesis of BTA-TT-COF

To prepare the **BTA-TT-COF** the tetra-amine **BTA** and the linear dialdehyde **TT** were reacted by acid-catalyzed dynamic Schiff-base polymerization (**Figure 4.3**). Solvothermal conditions were employed to obtain a crystalline powder.

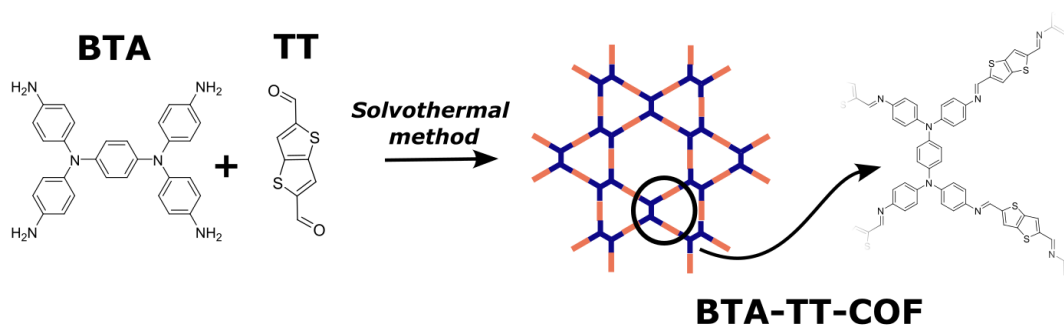


Figure 4.3. Reaction scheme for the synthesis of **BTA-TT-COF** from the building-blocks.

Despite the intensive research effort of the past two decades, general guidelines for the crystallization of a novel COF material have not yet been established. The exact synthetic protocols are typically defined each time by extensive screening of the reaction conditions. The key parameters influencing yield as well as crystallinity of the material to be optimized are the solvent composition, the type and the concentration of the catalyst, the concentration of water, the concentration of the monomers, the temperature, and the reaction time.

Following an unsuccessful screening of various reaction conditions reported in the literature for analogue COFs containing the **BTA** moiety (as shown in **Table 4.1**), the crystalline **BTA-TT-COF** was successfully synthesized by employing a 1 : 1 ratio of benzyl alcohol (BnOH) and glacial acetic acid (HOAc) as the co-solvent and reaction catalyst. In a typical reaction, the mixed solids were suspended in the appropriate amount of solvent in a pressure resistant Schlenk tube. The solids were dispersed by ultrasonication and then mixture was degassed by three freeze-pump-thaw cycles. The synthesis was performed by heating this mixture at 120 °C for 72 hours in an oven. The material was then filtered and washed with dimethylformamide (DMF) and acetone. The activation was carried out by exchanging acetone with *n*-pentane and the latter was removed first by room temperature evaporation and then at 80 °C in vacuum overnight (more details on the synthesis procedure are available in the

Materials and Methods section).

Table 4.1. Reaction conditions tested for the polymerization of **BTP-TT-COF**

Solvent and catalyst	Conditions	[BTA]	Outcome	Reference
BnOH / Mesitylene / 6 M HOAc 10 : 10 : 1	100 °C, 72 h	12 mM	Amorphous	[13]
<i>o</i> -DCB / <i>n</i> -BuOH / 3 M HOAc 5 : 5 : 1	120 °C, 120 h	23 mM	Amorphous	[185]
<i>o</i> -DCB / <i>n</i> -BuOH / 6 M HOAc 5 : 5 : 1	120 °C, 72 h	19 mM	Amorphous	[252]
<i>o</i> -DCB / <i>n</i> -BuOH / 6 M HOAc 15 : 15 : 2	120 °C, 72 h	31 mM	Amorphous	[250]
<i>BnOH</i> / <i>HOAc</i> 1 : 1	120 °C, 72 h	25 mM	<i>Crystalline</i> <i>Low yield</i>	<i>This work</i>
<i>BnOH</i> / <i>Mesitylene</i> / 15 M <i>HOAc</i> 3 : 3 : 2	120 °C, 72 h	25 mM	<i>Crystalline</i> <i>Good yield</i>	<i>This work</i>

However, despite the high quality of the resulting material, the yield of the reaction carried in pure HOAc and BnOH (1 : 1) was very low. To improve the yield, the volume of BnOH mixed with the HOAc was gradually increased and mesitylene was added as a third co-solvent together with a small amount of water (preserving all the other reaction parameters). However, an excessive dilution of HOAc resulted in the loss of crystallinity. The best tradeoff between crystallinity and yield was achieved by using a mixture of BnOH and mesitylene, along with 15 M aqueous HOAc as the catalyst / co-solvent in a volumetric ratio of 3 : 3 : 2. The final product was obtained following the workup as described above as a red powder with a 60% yield. The routine material characterization and the following application in energy storage devices reported in the further paragraphs of this chapter are related to the material synthesized in these reaction conditions.

By slightly modifying the reaction condition conditions it was also possible to scale up the synthesis from the tens of milligrams scale to the hundreds of milligrams scale, without the loss of crystallinity (see Materials and Methods section).

4.2.2. Structural and morphological characterization of BTA-TT-COF

The powder X-ray diffraction (PXRD) analysis evidenced the growth of a highly crystalline 2D COF with intense and well resolved reflections between 2 and 22 ° (**Figure 4.4a**). The main peaks appeared at 2.3 °, 3.9 °, 4.5 °, 6.0 °, 8.1 °, and 21.1 ° and were accompanied by less intense reflections at 6.8 °, 10.4 °, 11.4 °, 12.6 °. Due to the symmetry of the building-

blocks, either a single-pore tetragonal (*sql*) or a dual-pore Kagome-like (*kgm*) 2D nets could be expected (**Figure 4.4b**). Crystalline materials displaying the *sql* or the *kgm* topologies present highly different PXRD patterns which are sufficient for assignment of the structure.^[13,185,250] In particular, the pattern obtained for **BTA-TT-COF** matched the *kgm* model with an eclipsed stacking of the polymeric layers that was reported by He and collaborators.^[251] Based on this model the six main reflections of the PXRD pattern were assigned to the (100), (110), (200), (210), (220), and (001) planes, respectively. An interlayer distance of $d_{001} = 0.42$ nm was calculated from the position of the (001) reflection.

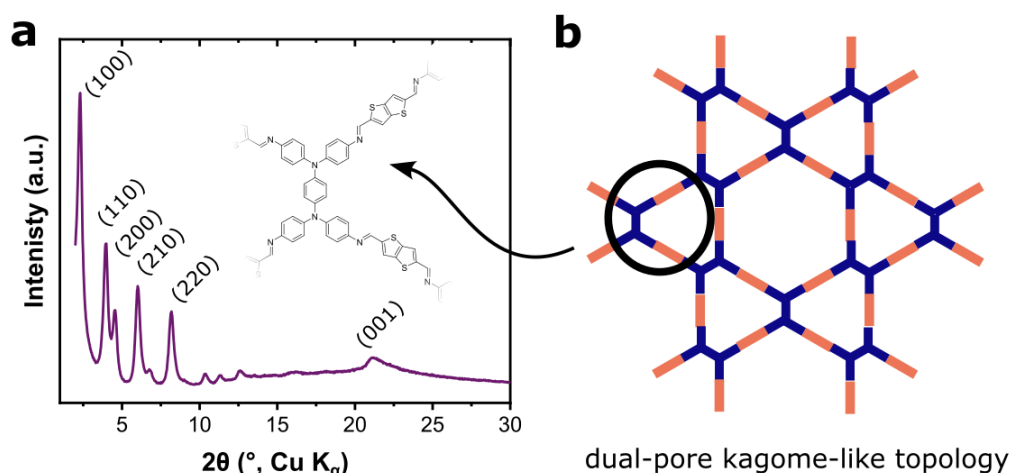


Figure 4.4 (a) Experimental PXRD pattern of **BTA-TT-COF**. **(b)** Schematic representation of the dual-pore kagome-like *kgm* topology.

The periodic structure was further studied by combining the PXRD results with a computational simulation. The COF was simulated with an eclipsed AA stacking model and optimized. It was found that the simulated PXRD shape matched the experimental results. Rietveld refinement was used (**Figure 4.5**) to reproduce the PXRD pattern. According to the refinement the structure adopted a P6/M space group with unit-cell parameters of $a = b = 45.22$ Å, $c = 4.20$ Å, $\alpha = \beta = 90^\circ$ and $\gamma = 120^\circ$. However, the overall quality of the fit was not satisfying exhibiting a somewhat high profile residual R_p and weighted profile residual R_{wp} of 7.58 % and 10.01 %, respectively. The poor fitting might have been related to distortion effects in the real crystals that altered relative intensities of the reflections. However, the structural model could still be considered an ideal representation with a geometry close to the actual structure.

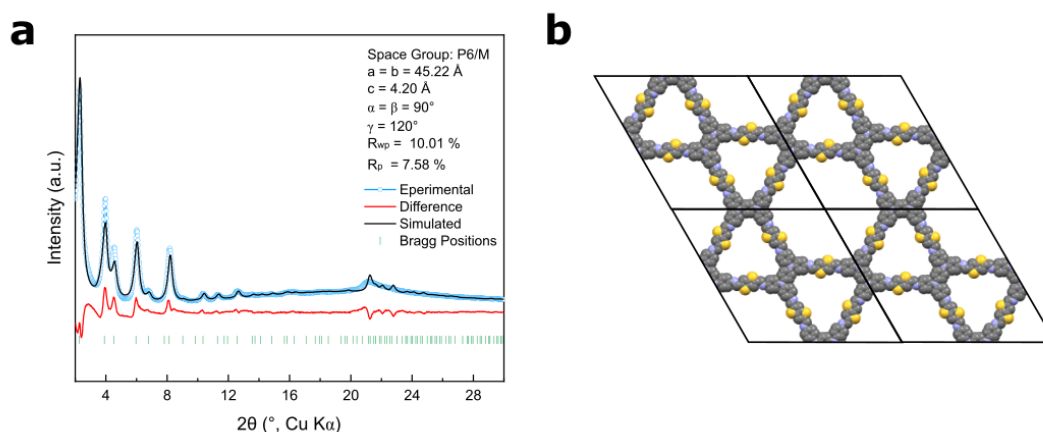


Figure 4.5 (a) Rietveld refinement of the **BTA-TT-COF**. **(b)** Schematic representation of the 2D unit cell of **BTA-TT-COF**.

A nitrogen adsorption-desorption isotherm at 77 K was measured to evaluate the surface area and pore size distribution of the porous powder. The material showed a type IV adsorption isotherm, typical of microporous materials (**Figure 4.6a**). To evaluate the surface area a BET plot was constructed (**Figure 4.6a**) from the adsorption profile in the 0.05 – 0.35 relative pressure range. The surface area was calculated from the fitting of the resulting plot (more details in **Chapter 2**). Average value of $720 \pm 50 \text{ m}^2 \text{ g}^{-1}$ was calculated from three independent samples. The pore size distribution was calculated using the BJH method on the N_2 desorption isotherm profile (**Figure 4.6c**). Two peaks appeared to be present in the expected mesoporous-microporous region of the, with maxima at about 2.3 and 3.8 nm. These calculated pore sizes were compatible with the dual pore structure (hexagonal and triangular) expected for the *kgm* structure.

The morphology of the powder material was investigated by SEM (**Figure 4.7**). To prevent the charging of the material during the imaging the sample was coated with a 7 nm thick gold film processed by sputter deposition. The **BTA-TT-COF** powder exhibited a distinctive morphology comprising roughly spherical aggregates, each with an average size of approximately $1 \mu\text{m}$. These aggregates were found to be composed of coagulated irregular particles of varying smaller sizes.

The powder material was analyzed using high resolution TEM imaging, which revealed a polycrystalline nature of the material with an irregular nanoscale morphology and an approximate size of 20 – 30 nm of the nanocrystalline domain (**Figure 4.8**). The crystalline domains with the *ab* plane oriented perpendicular to the electron beam direction exhibited an ordered hexagonal arrangement of mesopores. The ordered nature of the sample was confirmed by performing Fast Fourier Transform (FFT) of images **c**, **d**, and **e** of **Figure 4.8**. The

FFT patterns showed a periodicity of 3.2 - 3.4 nm, which approximately matches with the interplanar distance calculated for the (100) reflection in the PXRD ($d_{100} = 3.8$ nm) and with the larger pore size found by the BJH method from the N₂ desorption isotherm (3.8 nm).

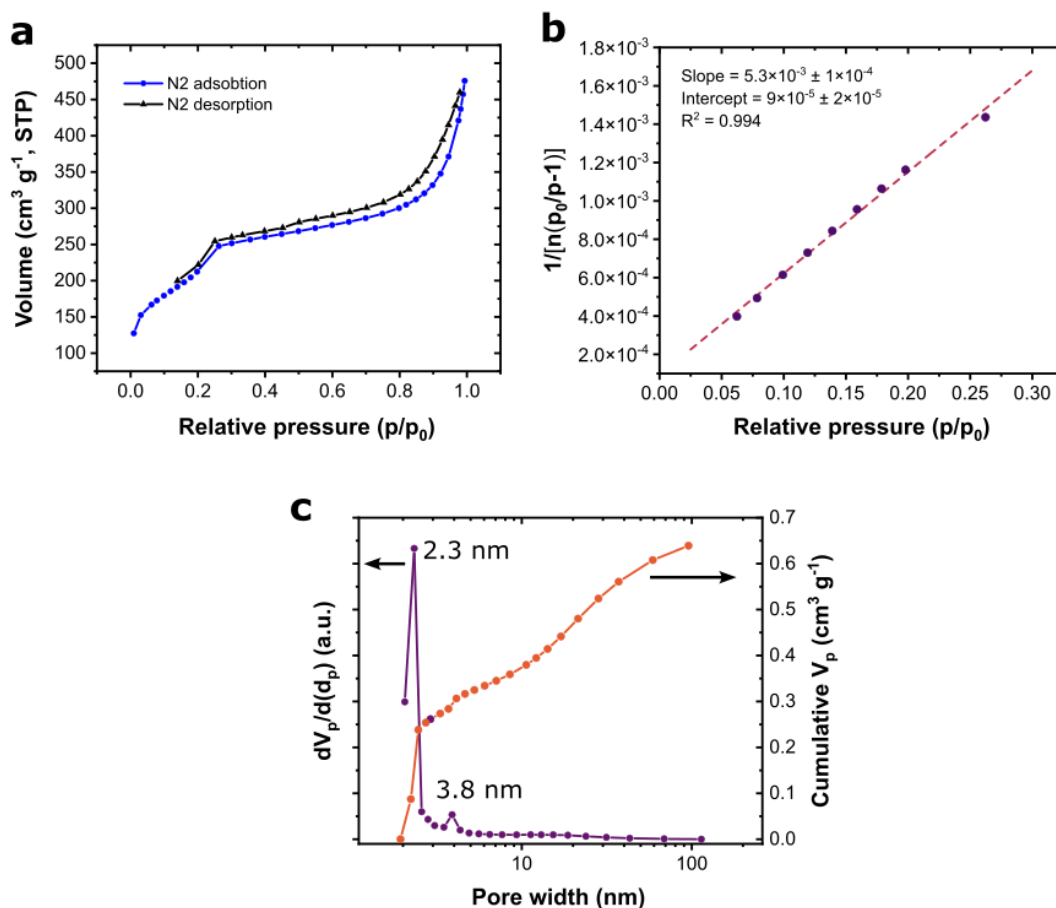


Figure 4.6 (a) N₂ adsorption-desorption isotherm of BTA-TT-COF. (b) BET plot and linear fitting of the low relative pressure data of the N₂ adsorption profile. (c) Pore size distribution (violet line) and cumulative pore volume (orange line) profiles obtained by BJH calculation on the N₂ desorption profile.

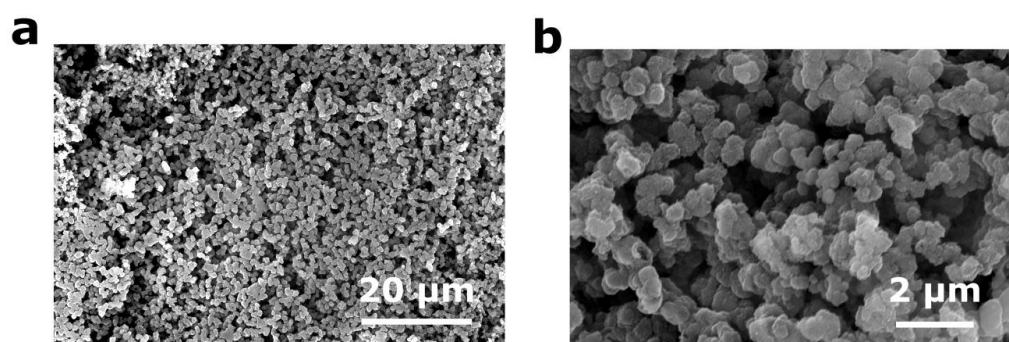


Figure 4.7 (a, b) SEM images of BTA-TT-COF at different length scales.

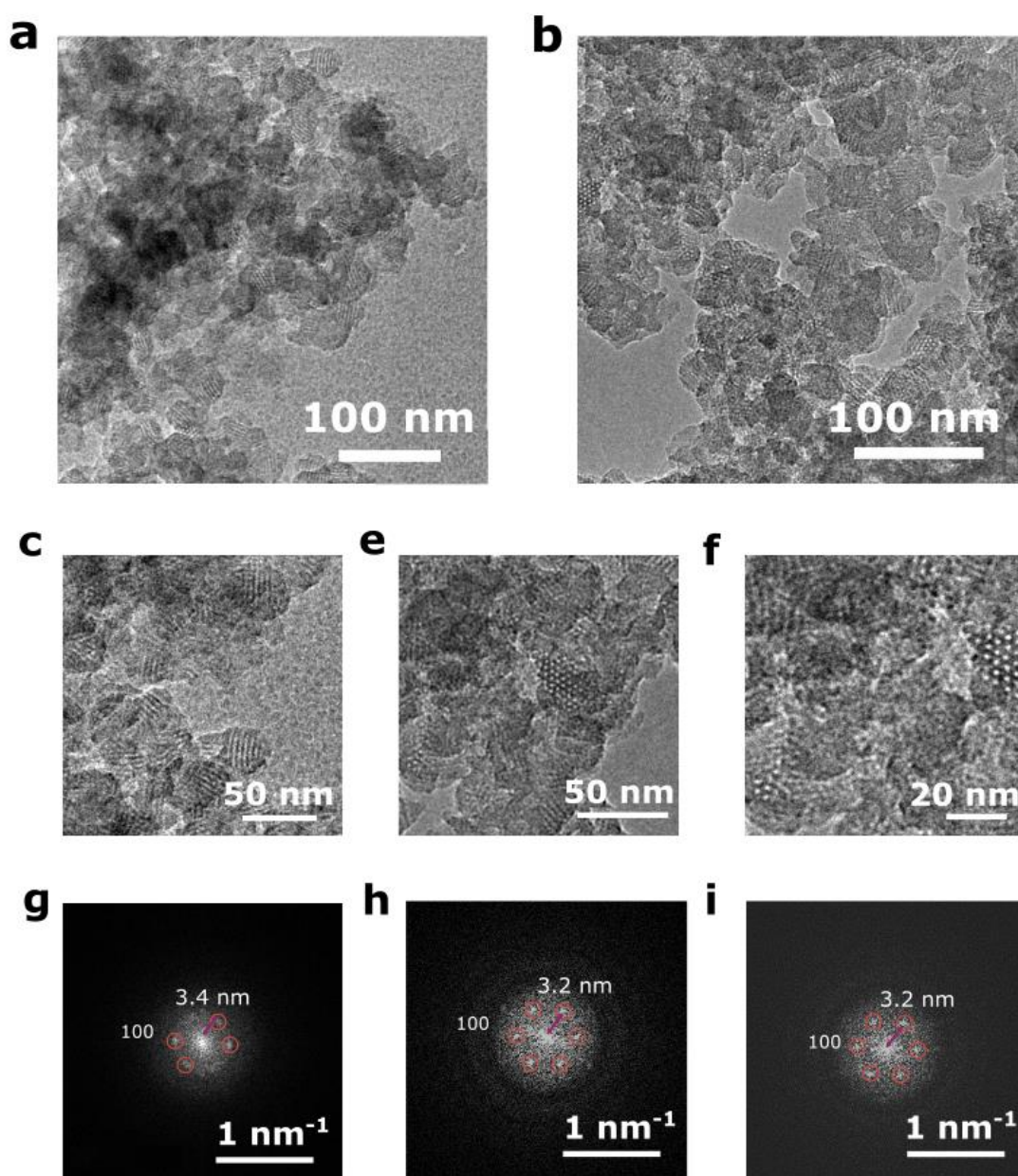


Figure 4.8 (a - f) TEM images of BTA-TT-COF at different length scales; (g - f) FFT profiles of the previous three images.

4.2.3. Chemical characterization of BTA-TT-COF

The formation of the imine polymer was assessed by ATR-FTIR, Raman spectroscopy and XPS by comparison with the spectra of the monomers. The FTIR spectrum of the tetra-amine BTA (Figure 4.9a, violet line) was characterized by the presence of two weak bands at 3442 and 3354 cm^{-1} characteristic of the asymmetric and symmetric N-H stretchings, respectively. The medium-intensity band at 1620 cm^{-1} was assigned to the N-H bending while the intense band 1496 cm^{-1} was ascribed to the aromatic ring mode. The presence of NH_2 groups was

further confirmed by a strong band for the N-H wagging vibration at 819 cm^{-1} .

The spectrum of the di-aldehyde **TT** (**Figure 4.9a**, red line) showed characteristic weak bands at 2875 and 2839 cm^{-1} for the stretching of the aldehyde C-H and a strong band at 1654 cm^{-1} related to the C=O stretching. Moreover, a single weak and sharp band was present at 3090 cm^{-1} for the C-H stretching of the aromatic backbone.

The spectrum of **BTA-TT-COF** (**Figure 4.9a**, yellow line) was characterized by a strong reduction in intensity of the bands related to the N-H stretching vibrations of the free amine groups. At the same time, the stretching vibration band characteristic of the carbonyl C=O stretching decreased in intensity and shifted from 1654 cm^{-1} to 1668 cm^{-1} . This shift was ascribed to the presence of the formyl group as a terminating moiety of the polymer branches. While the bands at 1499 and 1480 cm^{-1} were assigned to the aromatic ring modes, the intense absorption at 1606 cm^{-1} was tentatively attributed to the imine C=N stretching. The ambiguity on this band assignment was related to the relatively low frequency of vibration compared to similar structures reported in literature.^[258] Finally, the band at 1265 cm^{-1} was ascribed to the C-N stretching mode of the imine.

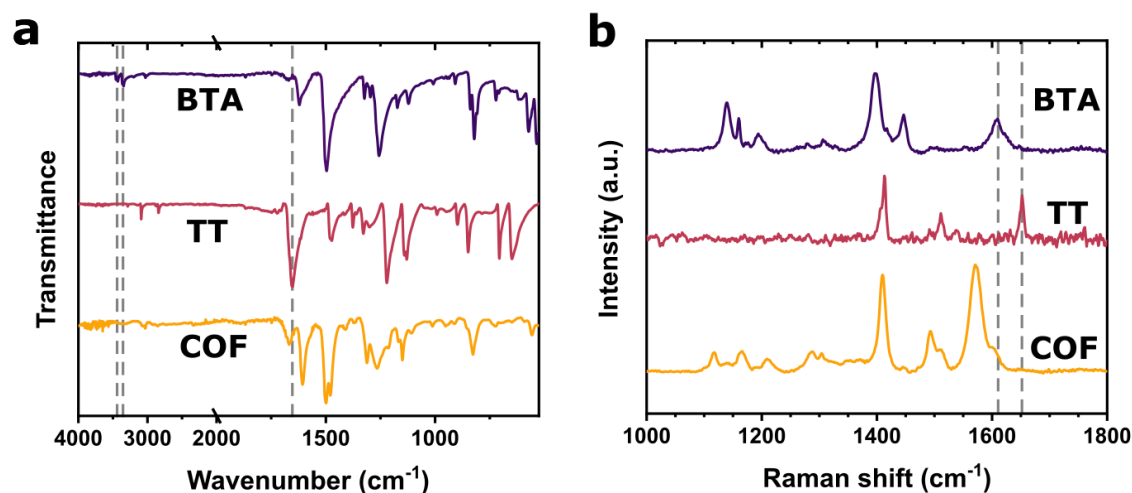


Figure 4.9 (a) FTIR and (b) Raman spectra of **BTA-TT-COF** (yellow line) compared to the corresponding monomers **BTA** (violet line) and **TT** (red line).

In the Raman, the monomers displayed characteristic peaks at 1609 cm^{-1} for the N-H bending of **BTA** and at 1652 cm^{-1} for the aldehyde C=O stretching of **TT**. These bands were not present in the spectrum of the product (**Figure 4.9b**, yellow line). However, a new peak assigned to the C=N stretching was observed at 1602 cm^{-1} . The signal appeared as shoulder of the more intense scattering signal at 1572 cm^{-1} which was ascribed to an aromatic ring

mode.

The XPS survey analysis (**Figure 4.10**) revealed the presence of oxygen, nitrogen, and sulfur in the material. Based on the survey results, an estimated C : N : S atom ratio of 82 : 12 : 6 was obtained, which is consistent with the expected theoretical ratio of 82 : 11 : 7. The oxygen signal at a binding energy of 532 eV was attributed to both unreacted formyl terminal groups possible oxidation by-products. Moreover, due to its high content (O to C ration of 1 : 5) we could not exclude a contribution from molecular oxygen species (such as H₂O, O₂, CO₂) that might be strongly adsorbed in the porous polymeric matrix.^[259]

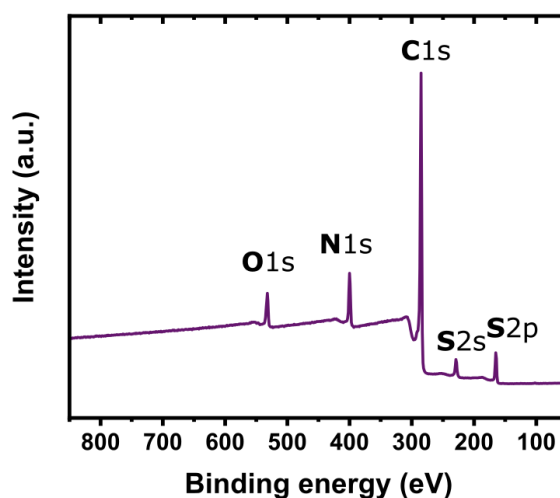


Figure 4.10 XPS survey of BTA-TT-COF powder.

High-resolution N1s and S2p spectra were recorded and analyzed for both the monomers and the COF. **BTA** displayed a single-component N1s signal at a binding energy of 399.0 eV for its primary and tertiary amine N (**Figure 4.11a**). After the reaction, for **BTA-TT-COF**, the N1s revealed the presence of multiple components which were fitted with Voigt functions (**Figure 4.11b**). A first component with a binding energy of 398.0 eV was assigned to the imine N. A second component at 399.1 eV was related to the tertiary amine N and the residual, unreacted primary amine N. A broader, less intense component was found at 400.3 eV which, due to the higher binding energy, was tentatively attributed to partially oxidized N or to N interacting with the adsorbed species in the porous structure. An alternative explanation for the presence of the component at higher binding energy is the formation of positively charged nitrogen species during the measurement (such as delocalized radical cations, *i.e.* polarons).^[260]

The S2p spectrum of **TT** displayed characteristic peak originating from a spin-orbit coupling

consisting of two components with maxima at 163.6 eV and 164.8 eV (**Figure 4.11c**) in 2:1 ratio. After the reaction, this peak shifted to somewhat higher binding energy presenting its components at 164.1 eV, 165.3 eV (**Figure 4.11d**).

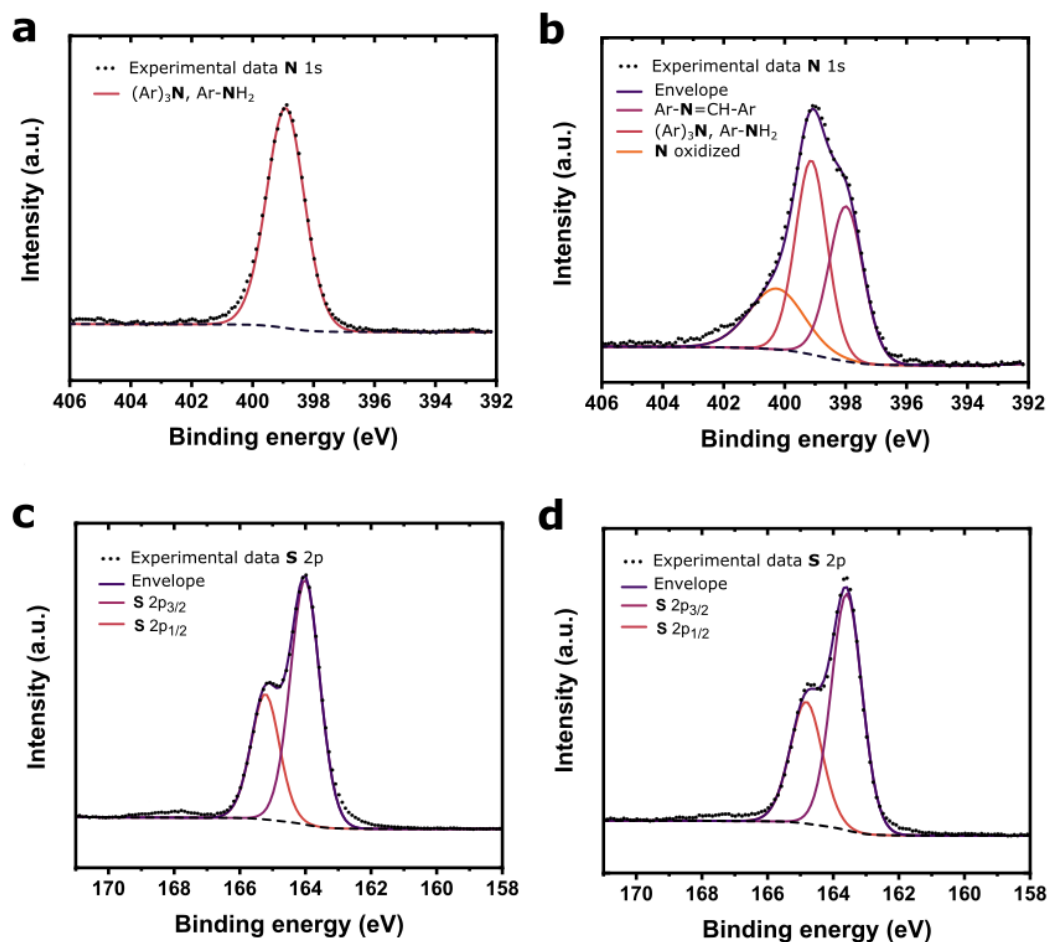


Figure 4.11 High-resolution XPS spectra of (a) N1s in the **BTA** monomer; (b) N1s in the **BTA-TT-COF**; (c) S2p in the **TT** monomer; (d) S2p in the **BTA-TT-COF**.

The thermal stability in inert atmosphere of **BTA-TT-COF** was tested by performing TG measurements (**Figure 4.12**, red line). The material exhibited a slow and gradual loss of mass up to 450 °C likely related to the desorption of small molecules, which is consistent with the presence of strongly adsorbed oxygen-containing species evidenced by XPS. Above this temperature, the rate of mass loss increased significantly, indicating a rapid decomposition of the material. A significantly lower stability was observed for the sample heated in air (**Figure 4.12**, violet line). Under these conditions the material showed stability only up to 370 °C. At higher temperatures the material quickly and fully decomposed.

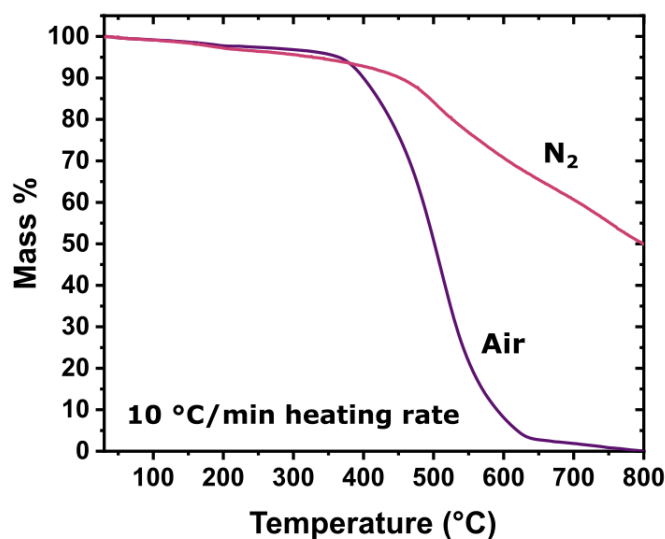


Figure 4.12 TG profile of BTA-TT-COF in inert atmosphere (red line) and in air (violet line).

4.2.4. Direct growth of BTA-TT-film in solvothermal conditions

The same synthetic procedure used to generate the polymer powder was employed to produce the BTA-TT-film as coating on a target substrate (Figure 4.13). This approach is also known as “direct-growth method” and it has been demonstrated to be the most versatile procedure for the preparation of 2D COF thin films. This protocol frequently leads to the formation of high quality films with the 2D layers oriented parallel to the substrate.^[2,7] In our case, in a typical synthesis, a flat substrate was vertically immersed in the initial monomers – solvent mixture, then the reaction vessel was sealed, and the mixture was heated up in an oven at 120 °C for 72 hours. After the reaction, the resulting red film-coated substrate was rinsed with acetone and briefly sonicated to remove co-synthesized powder material. Finally, the film was carefully dried using a nitrogen stream. This procedure was used to coat substrates such as silicon, quartz, glass, and gold-coated glass substrates.

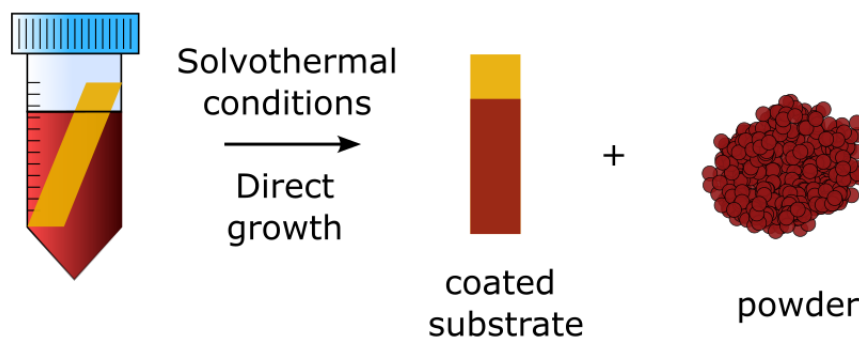


Figure 4.13 Simultaneous coating of a substrate with BTA-TT-film and powder formation.

Figure 4.14a and **b** display the optical microscopy images of the step edges of the films that were prepared on quartz and gold-coated glass. These images revealed the presence of a uniform, compact film with aggregates of various sizes located on its surface which were likely sediment of the co-synthesized powder material. Moreover, the continuity and mechanical stability of the sample was demonstrated by the presence of a folded portion of the film, as shown in **Figure 4.14b**.

The film prepared on quartz was imaged by SEM, and to prevent the electrical charging during the measurement, the material was coated with 7 nm thick gold film before the measurement. The resulting images (**Figure 4.14c, d**) demonstrated that the **BTA-TT-film** was homogeneous and had a continuous nature, even at the sub-micrometer scale. Additionally, the aggregates present on the surface were clearly identified as spherical particles of the co-synthesized powder material. Finally, as shown in **Figure 4.14d**, the presence of particles included in bulk of the film and emerging from its surface, suggested that the material might have formed via adsorption, aggregation, and coalescence of particles at the solid-liquid interface.

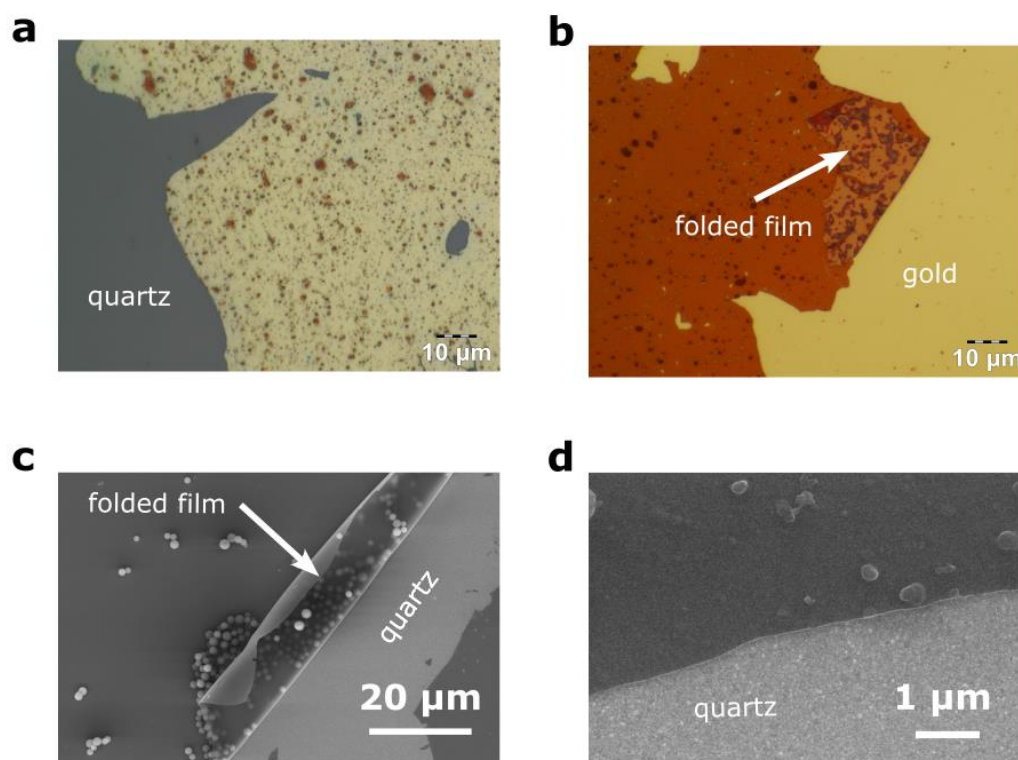


Figure 4.14 (a, b) Optical microscopy images of **BTA-TT-film** on quartz and on gold-coated glass; the film was imaged in an intentionally scratched area, to obtain a contrast with the underling substrate; **(c, d)** SEM images of **BTA-TT-film** on quartz at different length scales.

The thickness of the film at a step-edge of an intentionally scratched region of the surface was determined using atomic force microscopy (AFM). Two samples on silicon and glass substrates were measured to evaluate the reproducibility of the synthetic protocol over various supports (respectively **Figure 4.15a, b** and **Figure 4.15c, d**). The results revealed that the average thickness of the film was 92 ± 3 nm in the case of the silicon substrate and 90 ± 5 nm in the case of the glass substrate. The AFM measurements indicate that the synthetic protocol used in this study produces films with consistent and reproducible thickness across various reaction batches and substrate materials. Moreover, the small-scale images (**Figure 4.15b, d**) of both materials revealed a corrugated surface with an estimated root mean square roughness $R_{\text{RMS}} = 10$ nm for the sample on silicon and a $R_{\text{RMS}} = 5$ nm for the sample on glass (determined over an area of $2 \times 2 \mu\text{m}^2$). The corrugated topography of the film further suggested that the film could have formed from the aggregation and fusion on surface of particles that had nucleated in solution.

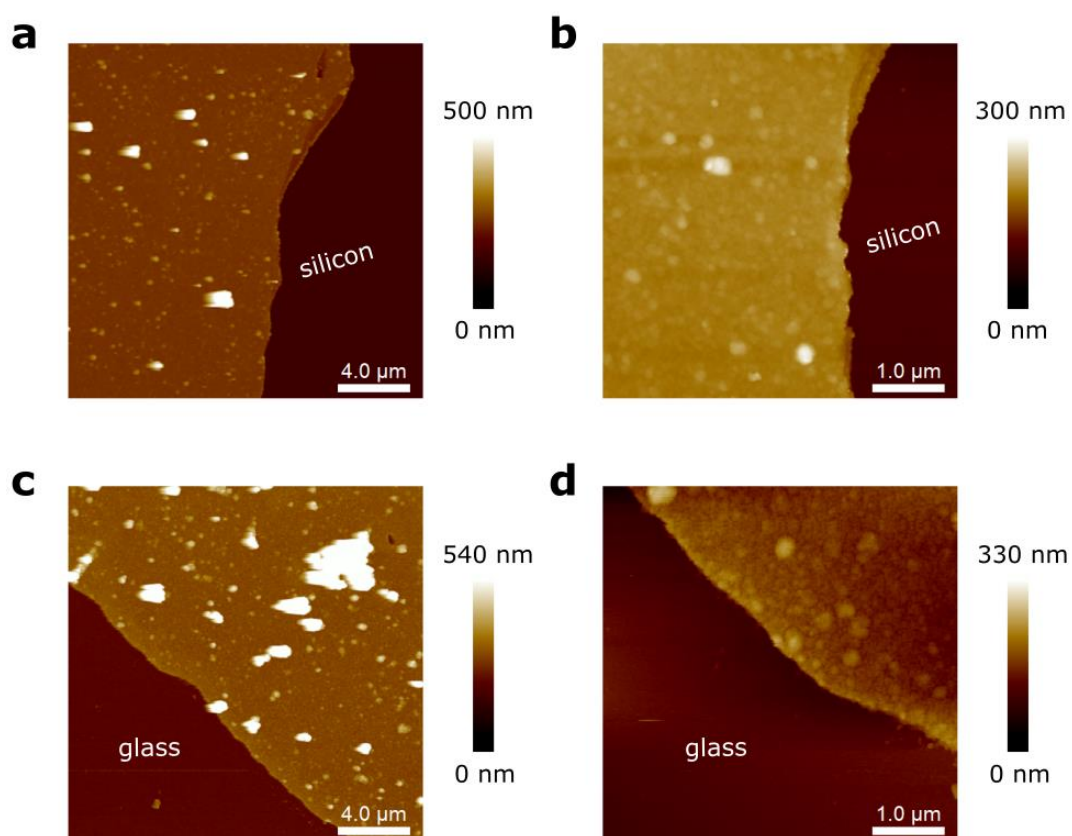


Figure 4.15 AFM topographical images of step-edges of the **BTA-TT-films** at different magnifications. The images were obtained from two different batches of synthesis: batch 1 (**a, b**), batch 2 (**c, d**).

To confirm that the structural order of the film matches with the **BTA-TT-COF** powder, a

2D GIWAXS analysis was performed on the sample (**Figure 4.16**). Unfortunately, likely due to the low thickness of the material, the quality of the resulting patterns is low (**Figure 4.16a**). Nevertheless, a strong diffraction cone was present at low angle, close to the beam stopper and a set of diffraction cones of low intensity could be observed at higher angles. Overall, the presence and the shape of these reflections indicated the existence of a crystalline material with no preferential orientation. From the vertical and horizontal linecuts of the 2D pattern (**Figure 4.16b**) the presence of the diffraction pattern was clearer. The reflections at 2.3° , 3.8° , 4.5° , 6.0° , 8.3° , 21.2° matched with the expected diffraction from the (100), (110), (200), (210), (220), and (001) planes, respectively, and were consistent with the pattern observed from the **BTA-TT-COF** powder. However, due to the low thickness of the material further analysis may require stronger X-ray sources (GIWAXS with synchrotron beam).

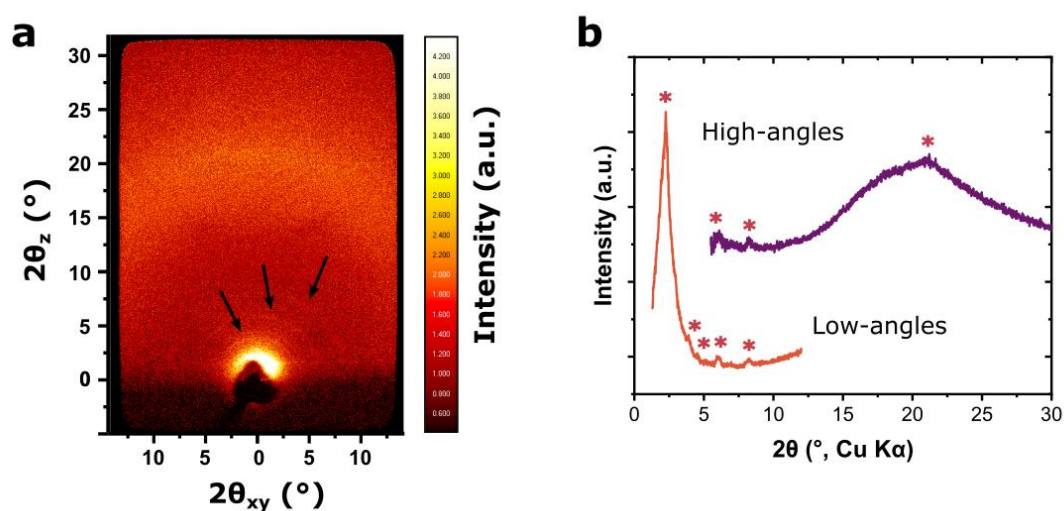


Figure 4.16 (a) 2D GIWAXS pattern of the **BTA-TT-film** on glass. (b) Staked plot of the low-angles (orange line) and high-angles (violet line) radial integrations of the 2D GIWAXS profile, the positions of the weak diffraction cones were marked with arrows. The positions of the reflections were marked with a star.

To confirm the chemical identity of the film coating the material was analyzed by Raman spectroscopy and XPS and compared to the **BTA-TT-COF** while recording the ATR-FTIR spectrum was not possible due to the low thickness of the sample. In contrast, the Raman spectrum (**Figure 4.17a**) revealed a pattern that matched almost perfectly with the spectrum of the powder COF, implying the same chemical nature of the two materials.

The XPS analysis was conducted on the film prepared on silicon. The elemental survey analysis (**Figure 4.17b**) indicated the presence of O, N, C, and S, consistent with the anticipated structure. The presence of the silicon constituting the substrates was not detected owing to the reduced penetration depth of XPS which is between few nm and few tens of

nm. The high intensity of the O1s peak (1 : 1 atom ratio vs C) was attributed to the presence of unreacted formyl groups, and oxidized species on the surface of the film and strongly adsorbed oxygenated species. From the survey a C : N : S composition of 76 : 17 : 7 was found, which is in line with the expected composition for the polymer. The high-resolution N1s peak (**Figure 4.17c**) was deconvoluted in three components, similar to the powder material: 398.5 eV for the imine nitrogen, 399.8 eV for the tertiary amine and the unreacted primary amines, and 401.0 eV for the oxidized / interacting nitrogen. A shift of about 0.5 eV towards higher binding energies with respect to the powder was found for all the components. For S2p, the high-resolution spectrum (**Figure 4.17d**) revealed the presence of a main signal with clearly distinguishable spin-orbit components at 164.1 eV and 165.4 eV, attributed to the thienothiophene moiety in the polymer backbone, and a second signal at 168.2 eV which spin-orbit components were not deconvoluted and that it was attributed to the partial oxidation of the thienyl ring to sulfoxide or sulfone, on the surface of the film.

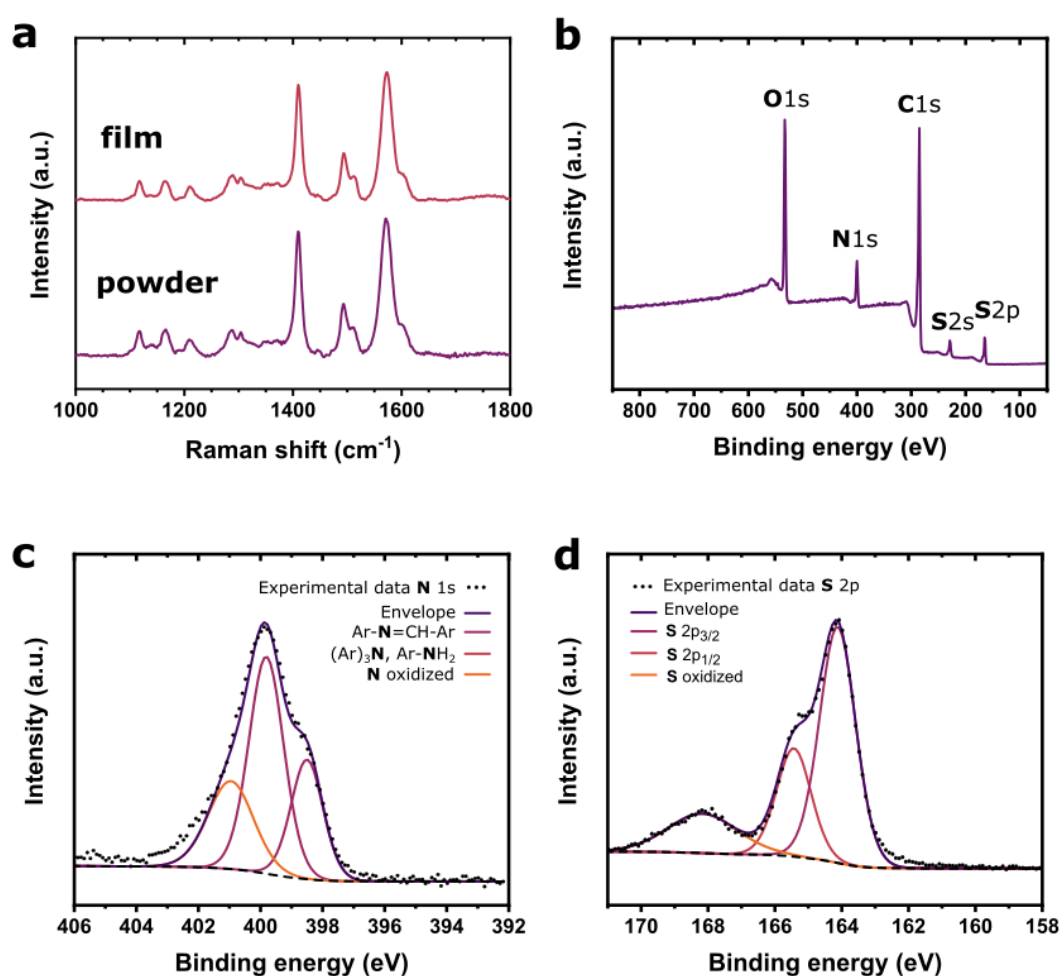


Figure 4.17 (a) Raman spectrum of **BTA-TT-film** compared to the corresponding powder material; (b) XPS survey of **BTA-TT-film**; (c) high-resolution XPS spectra of N1s and (d) S2p in the **BTA-TT-film**.

4.3. Optoelectronic properties of BTA-TT-COF and film

4.3.1. Energy levels

To estimate the positions of the valence and conduction band edges of the 2D COF, the material was characterized by UV-vis-NIR absorption spectroscopy and cyclic voltammetry (CV). The UV-Vis-NIR absorption spectra of the **BTA-TT-film** and **BTA-TT-COF** powder are shown in **Figure 4.18**. The film, prepared on quartz, was measured in transmission mode. The film absorbed strongly in the visible and UV regions, with an absorption onset at 600 nm and with two maxima at 340 and 493 nm. The **BTA-TT-COF** powder was measured by diffuse-reflectance spectroscopy (DRS) and despite the lower quality of the data, the absorption profile appeared matching the one of the film.

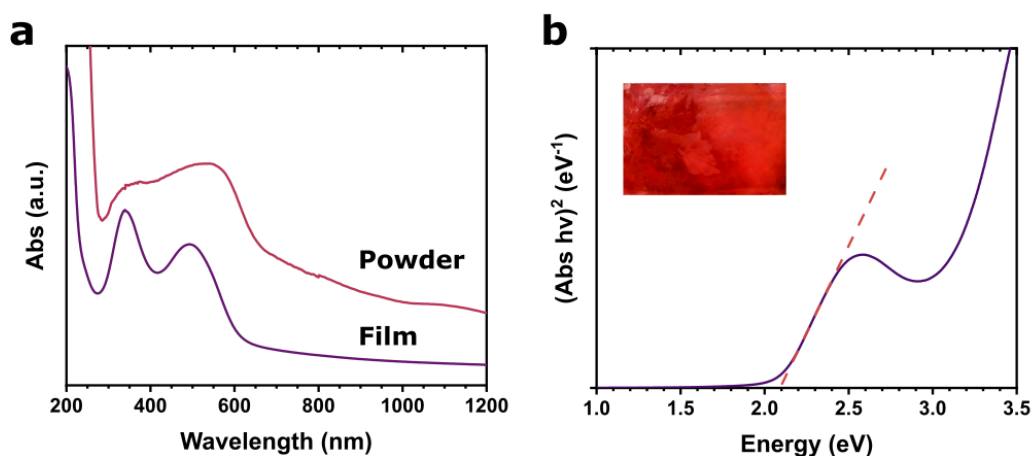


Figure 4.18 (a) Stacked plot of UV-vis-NIR absorbance spectra of **BTA-TT-COF** powder, measured in diffuse reflectance mode (red line), and **BTA-TT-film** on quartz measured in transmission mode (violet line); (b) Tauc plot analysis of **BTA-TT-film** on quartz assuming a direct band gap (the inset shows a photograph of the film synthesized on quartz).

A Tauc plot analysis was used to determine the optical bandgap from absorption profile of **BTA-TT-film**.^[210] Assuming a direct allowed transition,^[210] the optical bandgap was extracted from the x-intercept of the linear region of the fitting (red dashed line) obtaining an approximate value of $E_g^{opt} = 2.1$ eV. Additionally, this value was compared with the HOMO-LUMO energy gaps of the separate monomers obtained by Tauc plot analysis of their UV-vis spectra (**Figure 4.19**). Both **BTA** and **TT** in THF solution absorbed only in the UV region and their HOMO-LUMO energy gap was estimated as $E_g^{opt} = 3.3$ eV and $E_g^{opt} = 3.5$ eV respectively. The evident decrease of the energy gap to 2.1 eV for the COF suggested that upon polymeriza-

tion, the π -conjugation extends beyond the monomeric units.

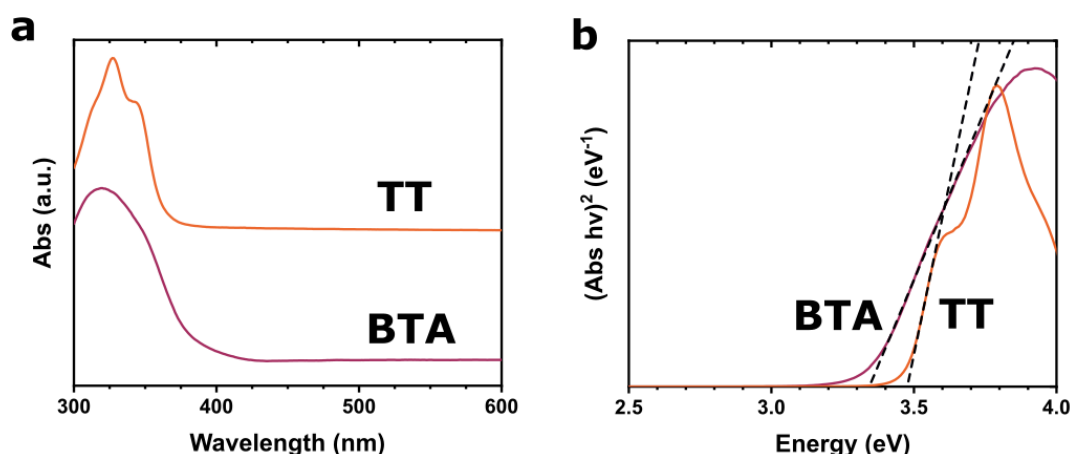


Figure 4.19 (a) Stacked plot of UV-vis absorbance spectra of the monomers **BTA** and **TT** in THF solution (b) Tauc plot analysis of the two monomers in solution assuming a direct band gap.

Cyclic voltammetry measurements (CV) were performed in 1 M NBu_4BF_4 in MeCN to investigate the redox properties of the material (**Figure 4.20a**). The COF powder was investigated in a three-electrode setup with a Pt wire as the counter electrode and an Ag/AgCl reference electrode. The power was deposited on a glassy carbon electrode. In the anodic trace two very well-defined current peaks were present at $E_{p,a}^1 = 0.2$ eV and $E_{p,a}^2 = 0.59$ eV vs Fc/Fc^+ which were attributed to the mono and di radical oxidation of the **BTA** unit (**Figure 4.20b**). The oxidation at relatively low potential and the shape of the profile matches with the reported electrochemical behavior of other BTA-COFs indicating that upon polymerization the redox properties of the material were mainly governed by the **BTA** rather than the **TT** moiety.^[13]

The absence of clear current peaks in the cathodic trace of the CV denoted the non-reversible nature of the oxidation process in the conditions of the measurement. In other words, after the material had been electrochemically oxidized, it reacted further to form stable species that could not be reduced back to the initial form of the COF. It is possible that despite the anhydrous and degassed conditions used during the measurement, traces of H_2O and O_2 were present and could react with the free radical species formed on the material during the positive current sweep.^[212]

The voltammogram showed an anodic peak onset of $E_{onset}^{ox} = -0.03$ eV vs Fc/Fc^+ . From this value the approximate position of the HOMO was determined to be $E_{HOMO} = -5.1$ eV according to the following equation:^[261]

$$E_{HOMO} = -E_{onset}^{ox}(\text{vs } \text{Fc}^+/\text{Fc}) + 5.1 \text{ eV}$$

Using the optical bandgap, the corresponding LUMO energy was calculated to be $E_{LUMO} = -3.0$ eV with respect to the vacuum level.

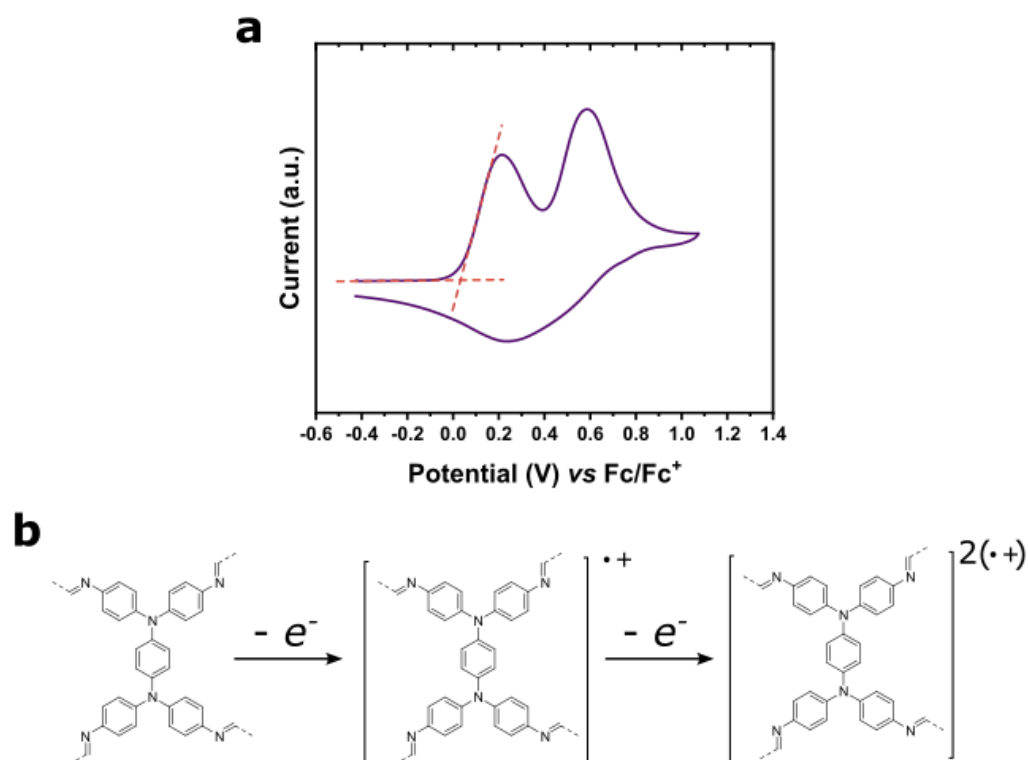


Figure 4.20 (a) Cyclic voltammogram of the **BTA-TT-COF** powder in MeCN. (b) Scheme of the two consecutive oxidation reaction of the **BTA** moiety in the polymer upon positive potential sweep.

At present, only the **BTA-TT-COF** powder has been characterized by CV. Albeit, the same behavior is expected for the **BTA-TT-film**, its CV characterization is currently being carried out. In parallel modifications of the measurement setup are being implemented in the attempt to avoid the irreversible degradation of the material upon oxidation.

4.3.2. (Photo)conductivity and molecular doping

To investigate the charge transport properties of the films a two-terminal, bottom-contact device was fabricated using a pre-patterned glass substrate and growing the **BTA-TT-film** on top (**Figure 4.21**). The contacts consisted in gold interdigitated electrodes with channel length of $L = 5 \mu\text{m}$ and channel width of $W = 3.4 \times 10^6 \mu\text{m}$.

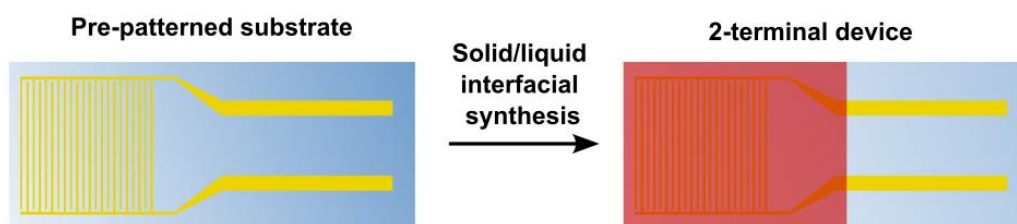


Figure 4.21 Scheme of the 2-terminal device, prepared by coating a glass substrate with pre-patterned interdigitated gold electrodes.

The electrical properties of the film right after synthesis were analyzed in a vacuum chamber (2 mbar). The current-voltage (I-V) curve (**Figure 4.22a**), measured in the -10 – +10 V window displayed a barely detectable current response, in the range of few tens of pA. The conductivity (σ) was extrapolated from the linear part of the I-V curve according to the following equation:

$$\sigma = \frac{\partial I / \partial V \cdot L}{W \cdot t}$$

where $\partial I / \partial V$ is the slope of the I-V curve, t is the thickness of the film, L is the channel length and W is the channel width. The film exhibited a conductivity in vacuum of $\sigma = 4 \times 10^{-11} \text{ S m}^{-1}$ which is an extremely low value compared to those calculated for similar materials measured in air.^[13] Moreover, the I-V curve showed a broad hysteresis, which indicated a partially capacitive response of the system to the applied voltage. Regardless of the low conductivity in vacuum, the material showed an extremely rapid photoresponse (< 350 ms) when irradiated with a white light-emitting diode (LED) (**Figure 4.22b**). Upon illumination through the glass window of the vacuum chamber the current increased of one order of magnitude, which was attributed to the increase of the number of charge carriers upon light absorption and subsequent HOMO-LUMO transition. The photocurrent behavior was recorded for several light pulses and always showed a reproducible response without deterioration and with stable on and off currents.

Owing to the semiconducting and electron-rich nature of the material it was expected that the electrical properties would vary upon exposure to an ambient environment. In particular, the role of atmospheric oxygen is an often overlooked factor in scientific literature when analyzing and comparing the conductivity performances of 2D COFs.^[13] These materials are known to possess a porous open structure and vast surface areas, which make it easy for gases to diffuse in the material. This volumetric interaction between the polymer and the

gas has the potential to lead to wide variation of the properties. Moreover, as most of the proposed applications for 2D COFs entail the use of these materials in atmospheric conditions, the study of the interaction with oxygen is of key importance.

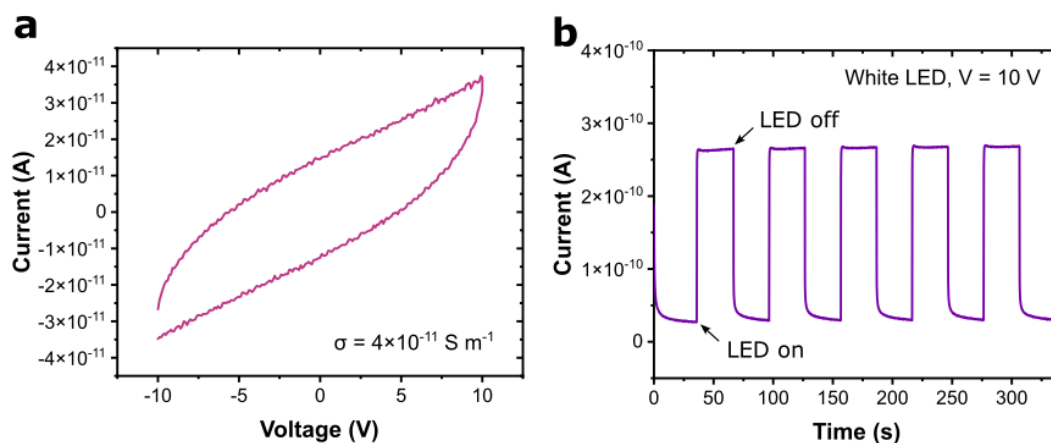


Figure 4.22 (a) I-V curve of the two-terminal device in vacuum (2 mbar). (b) Electrical current variation in time following the illumination of the device with white LED pulses.

After being stored in vacuum for several hours, the **BTA-TT-film** was exposed to ambient conditions (light, oxygen, humidity). Under these conditions I-V curves were measured at different delay times (**Figure 4.23a**). As the measured currents greatly and swiftly increased, the voltage window was limited to $-0.1 - +0.1$ V. In air, the curves followed a linear trend, suggesting the Ohmic character of semiconductor-metal contact. A low energy barrier between gold electrodes work-function and the material Fermi level is reasonable considering that for a p-type semiconductor the Fermi level is close to the HOMO ($E_{HOMO} = -5.1$ eV) which is well aligned with the gold electrodes work-function.^[262] Upon exposure to ambient conditions the conductivity increased from $\sigma = 4 \times 10^{-11} \text{ S m}^{-1}$ in vacuum to $\sigma = 2 \times 10^{-8} \text{ S m}^{-1}$ immediately after the exposure to air. This value further increased up to $\sigma = 3 \times 10^{-6} \text{ S m}^{-1}$ upon 10 – 20 hour of exposure (**Figure 4.23b**) resulting in a boost of five orders of magnitude of the conductivity respect to the vacuum levels and reaching values that are comparable those reported in literature for similar COF films.^[263] Moreover, preliminary experiments suggested that the effects of the air exposure could be (at least partially) reversed by bringing the sample back to vacuum.

This effect was attributed to p-doping induced from the electron acceptor molecules present in the atmosphere, and in particular O_2 that can diffuse into the polymer layer. It was shown that electron rich organic polymers such as poly(3-hexyl-thiophene-2,5-diyl) (P3HT) can interact with oxygen and form reversible polymer- O_2 charge transfer (CT) complexes.^{[264–}

^{266]} However, in our case the initial increase in conductivity during the first day of exposure was followed by a rapid loss of the charge transport properties during the following day ($\sigma = 1 \times 10^{-7} \text{ S m}^{-1}$ after 48 hours), which was attributed to the occurrence of (photo)oxidation reactions that could degrade the sample and interrupt the π -conjugation.^[267] The occurrence of irreversible oxidation is supported by the high amount of oxygen found in the XPS survey analysis (**Section 4.2.4**). However, a more detailed study on the reversible and irreversible reactions of the material with oxygen is necessary and is currently being performed.

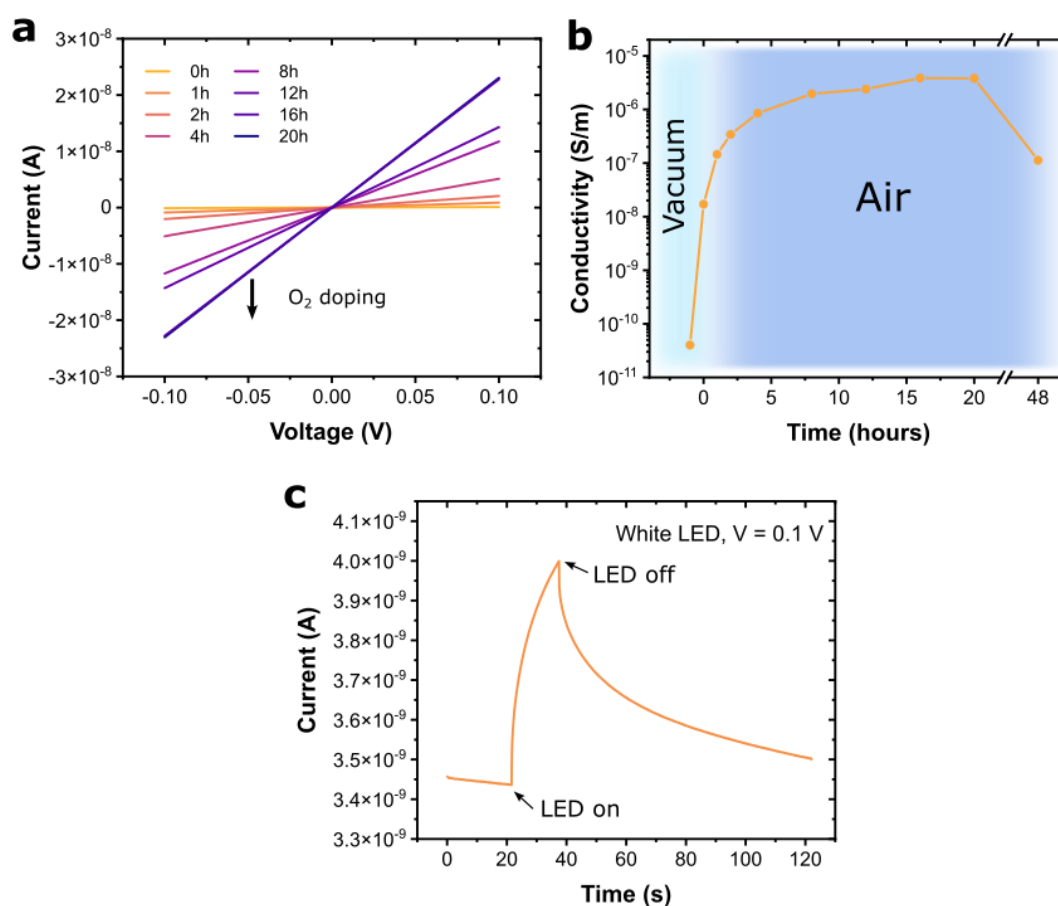


Figure 4.23 (a) I-V curves of the device recorded at different time delays after exposing the sample to ambient conditions. (b) Conductivity of BTA-TT-film in time calculated from the previous I-V curves. (c) Electrical current variation in time following the illumination of the device with a white LED pulse.

The current response of the film upon illumination with the white LED was also investigated in air. A clear difference in the photoresponse behavior was found for the sample exposed to air respect to the sample in vacuum. Upon irradiation of the sample with a white LED, a slow increase of current of only about 15 % was recorded (**Figure 4.23c**). The current returned slowly to the original level in dark condition (*i.e.*, LED off).

A doping method is considered significant if it results in a permanent and stable increase in

the conductivity of the material. Although the conductivity increased by five orders of magnitude upon O₂ doping, a loss of performance was recorded over time. To avoid this problem and induce a stable doping in the film, an organic electron-acceptor molecule was adsorbed as guest in the pores of the film. For this purpose, 2,3,5,6-tetrafluoro-tetracyanoquinodimethane (F₄TCNQ) was exploited. F₄TCNQ is commonly used to enhance the performance of electron rich conductive polymers due to its high electron affinity of 5.2 eV (**Figure 4.24**).

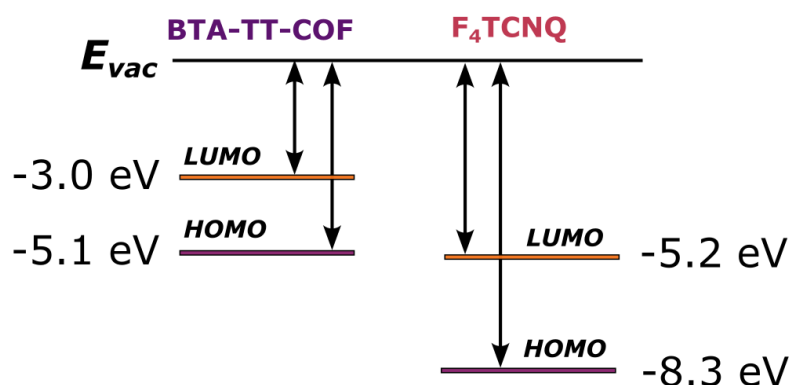


Figure 4.24 Scheme of the electronic structure of BTA-TT-COF and F₄TCNQ.

To achieve the doping **BTA-TT-film** was immersed for 5 minutes in a 0.1 mM solution of F₄TCNQ in MeCN. As soon as the film contacted the doping solution, an instant bleaching of the color from bright red to grey-red was observed, suggesting that a reaction took place, namely the formation of a polymer-F₄TCNQ adduct where the host polymer behaved as electron donor toward the guest molecule.^[13] The conductivity of the film increased substantially upon doping from $\sigma = 2 \times 10^{-8} \text{ S m}^{-1}$ (in air, right after the synthesis) to $\sigma = 2 \times 10^{-4} \text{ S m}^{-1}$ (**Figure 4.25a**). This boost of four orders of magnitude of the electrical conductivity was attributed to the efficient formation of CT complexes between the polymer and the dopant and it is in line with previous studies reporting the doping performances of F₄TCNQ. The presence of a CT from the polymer to the dopant is evidenced by the presence of two new absorption bands in the visible region (770 and 880 nm) that are related to the presence of the F₄TCNQ²⁻ anions (**Figure 4.25b**).^[268] The disappearance of these bands upon washing with MeCN suggested the reversibility of the doping / de-doping processes.

Concerning the stability of the F₄TCNQ doped material compared to the O₂ doped material, a comparative study is currently being performed.

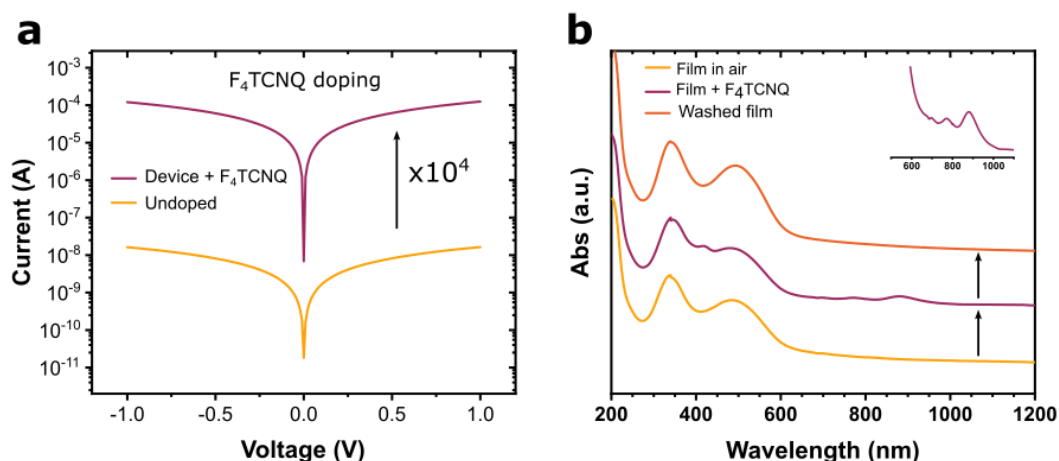


Figure 4.25 (a) I-V curves of the pristine film (undoped, yellow line) and the F₄TCNQ doped film (violet line). (b) Stacked UV-vis-NIR absorption spectra of the pristine film (yellow line), the F₄TCNQ-doped sample (violet line) and the de-doped sample (orange line). The inset shows the absorption related to the F₄TCNQ²⁻ anions.

4.4. Proposed applications for BTA-TT-COF and film

4.4.1. Active material in organic field effect transistor

The **BTA-TT-film** was integrated into a three-terminal device for a proof-of-concept demonstration that the material could be used as active channel for organic field-effect transistors (OFETs). A first solid-state OFET prototype of bottom-contact, bottom-gate device was prepared by growing the film on a Si/SiO₂ substrate with prepatterned gold electrodes.^[263] However, in this configuration no gate modulation of the current could be performed. A different possible way to achieve the current modulation is by using a liquid as dielectric. The liquid dielectric can penetrate the porous structure and through the formation of an electrical double-layer at the solid-liquid interface can improve the magnitude of the current modulation at lower voltages.^[269] Hence, a liquid-gated three-terminal device was constructed depositing a drop of deionized water on top of the transistor channel area (interdigitated electrodes of **Figure 4.21**) and a gold plate was positioned on the water surface to work as gate electrode (**Figure 4.26a**).

A transfer characteristic curve (I_{sd} vs V_g) was recorded by sweeping the gate voltage V_g from +0.4 V to -0.6 V with a fixed source-drain potential V_{sd} of 2 V (**Figure 4.26b**). The transfer curves appeared consistent with those expected for OFETs based on a p-type organic semiconductor and the device exhibited gate modulation in the negative bias regime with an

increase of the current of about 3 orders of magnitude in the on state (an $I_{\text{on}}/I_{\text{off}}$ ratio of $\sim 10^3$) and a threshold voltage V_{th} of -0.4 mV.

The product between the mobility μ and the volumetric capacitance C_v of the device was estimated as $\mu \cdot C_v = 4 \times 10^{-4} \text{ cm}^{-1} \text{ V}^{-1} \text{ s}^{-1}$ according to the following equation:^[270]

$$\mu \cdot C_v = \frac{g_m \cdot L}{V_{ds} \cdot W \cdot t}$$

where g_m is the transconductance $(\partial I_{\text{sd}}/\partial V_g)_{\text{MAX}}$ obtain from the linear regime of the transfer curve, V_{ds} is the voltage applied between drain and source, L is the channel length, W is the channel width, and t is the thickness of the film. The low $\mu \cdot C_v$ compared with similar devices^[271] could be attributed a low hole-mobility in the polymer potentially in combination with the detrimental effect of oxygen that might increase the off-state current. Additionally, the use of water as dielectric may not be the best choice, considering that it could chemicaly interact with the **BTA-TT-film** and contribute to the degradation of the electrical properties. However, the promising results obtained with this prototype suggest that the use of liquid-gating is a better solution than solid state gating when trying to integrate 2D COF materials as active layers in OFETs. This result was attributed to the opportunity for a liquid dielectric to penetrate the porous structure of the polymer and volumetrically modulate the current. For future developments, the water dielectric could be replaced with ionic liquids which have been shown to produce strong current modulation and might be less reactive toward the material and can be used in inert atmosphere (glovebox or under vacuum).^[272]

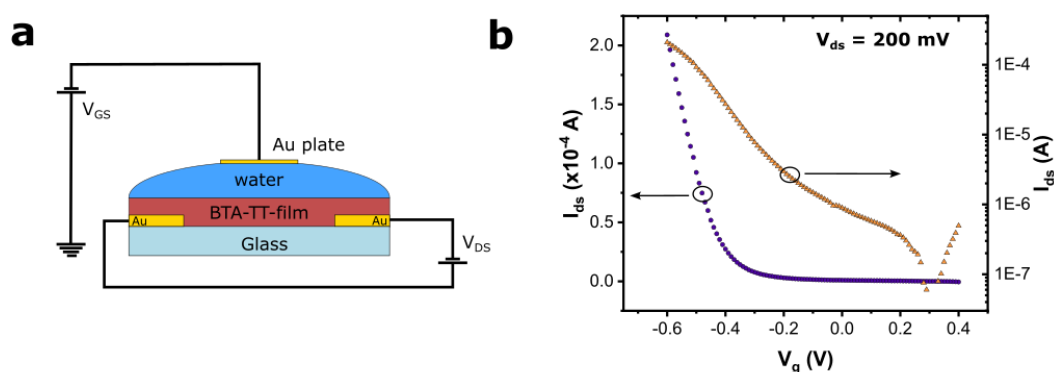


Figure 4.26 (a) Schematic diagram of the liquid-gated FET device using the **BTA-TT-film** as semiconductive materials. (b) Transfer plot of the FET device plotted with linear and logarithmic scales.

4.4.2. Symmetric pseudocapacitor

Pseudocapacitors are energy storage devices with high power density, high columbic effi-

ciency, fast charge-discharge rate, and long cycling life. These characteristics make them useful for many applications such as power tools, regenerative braking, power grids, and communication devices.^[273] In pseudocapacitors devices the energy can be stored through two parallel mechanisms: by the formation of an electrical double-layer (non-Faradaic processes) and by reversible electrodic redox reactions (Faradaic or pseudocapacitive processes).^[15] A simple pseudocapacitor consists of two symmetric electrodes separated by a membrane and immersed in an electrolyte solution as shown in **Figure 4.27**. The membrane allows ions to diffuse selectively during charging and discharging and prevents a short circuit by keeping the cathode and anode from touching. The electrolyte can consist either in an aqueous or in an organic solution depending on nature of the electrodes.

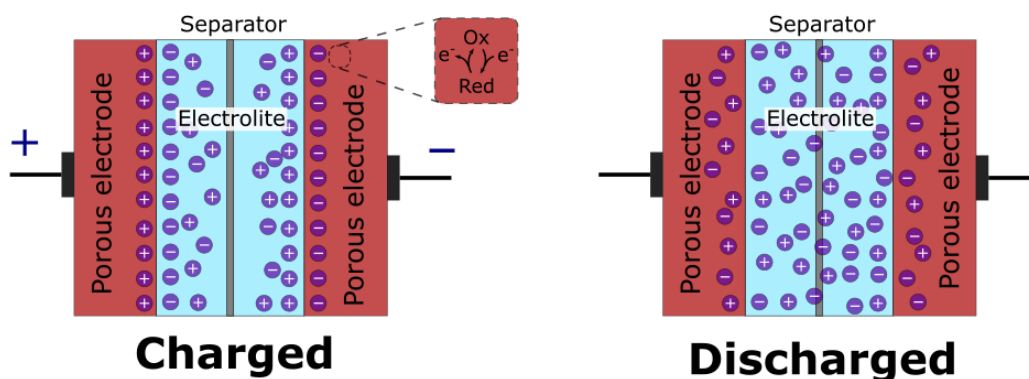


Figure 4.27 Schematic diagram of a symmetric pseudocapacitor presenting both double layer and pseudocapacitive energy storage mechanisms, in the charged and discharged states.

BTA-TT-COF is promising as active materials for pseudocapacitors because of their high surface area, the charge transport properties, and the presence of the electroactive **BTA** and **TT** units. Additionally, its crystalline and porous structure provides permanent pathways for the insertion / deinsertion of the electrolyte ions.

The performance of **BTA-TT-COF** as active material in a symmetric pseudocapacitor was examined by galvanostatic, voltammetry and impedance spectroscopy techniques with a two-electrode cell configuration. The electrodes were prepared from a N-Methyl-2-pyrrolidone (NMP) slurry of active material (70 wt %), conductive carbon (20 wt %), and polyvinylidene fluoride (PVDF) as binder (10 wt %). The slurry was cast onto carbon paper and dried in a vacuum oven at 80 °C for 18 hours. The two-electrode system was assembled in a coin cell containing 1 M NBu_4PF_6 in MeCN as supporting electrolyte. The electrodes were separated by inserting and electrolyte-soaked membrane (more details in the materials and methods section).

CV curves of **BTA-TT-COF (Figure 4.28a)** were recorded in the 0 - 2.5 V potential window at various sweep rates between 1 to 10 mV s^{-1} . The voltametric profile at 10 mV s^{-1} showed three broad current waves at 0.3 V, 1.5 V, and 1.9 V in the positive voltage sweep and no visible peak in the negative potential sweep. At lower scan rates, the position of the peaks gradually shifted toward lower voltages and at a scan rate of 1 mV s^{-1} two clear current waves appeared at 0.9 and 1.8 V in the negative potential sweep. Overall, the numerous current peaks demonstrated a rich redox activity of the material, but the general asymmetry of the voltammogram suggested the poor reversibility of the electrodic reactions in the experimental conditions.

The specific capacitance at different current densities was assessed through galvanostatic charge-discharge (GCD) cycles. The measurements were performed by applying a constant current to the system and monitoring the evolution of the potential in time. When the potential reached the limit values of 0 or 2.5 V, the direction of the current was reversed. As shown in **Figure 4.28b** the voltage time profiles exhibited the classic “shark-fin” shape indicative of double-layer capacitance. However, no clear voltage plateau was displayed suggesting a limited contribution of the redox processes to the overall measured specific capacitance. The specific capacitance was estimated from the discharge curves of the GCD cycles according to the following equation:

$$C_p(\text{F g}^{-1}) = \frac{2 \times i (\text{A g}^{-1}) \times \Delta t_d(\text{s})}{\Delta V(\text{V})}$$

Where i is the current density, Δt_d is the discharge time and the ΔV is the voltage difference between charged and discharged states, adjusted to exclude the initial voltage drop due to the internal resistance of the system.^[274] From the GCD cycle at 0.1 A g^{-1} a specific capacitance of 108 F g^{-1} was calculated and 62, 27, and 13 F g^{-1} from the cycles at 0.25, 0.5, and 1 A g^{-1} respectively. The important loss in capacitance observed upon the cycling the cell at increasing current density was attributed to the lack of reversibility of the redox reactions (as demonstrated by CV) which causes a gradual loss of the pseudocapacitive contribution at each cycle.

Electrochemical impedance spectroscopy (EIS) was carried out between 1 MHz and 10 mHz collecting 10 points per decade to evaluate the charge and ion transport dynamics (**Figure 4.28c**). In the Nyquist plot, the presence of a relatively small semicircle in the high-frequencies region indicated a low charge transfer resistance within the electrode and between the electrode and the current collector and as a consequence a good conductivity.^[275] In the low frequency region, the almost vertical line indicated a good mass transport dynam-

ic within the system and suggesting that the process is diffusion-controlled. Furthermore, the EIS data were fitted with a simple model represented by the equivalent circuit diagram of **Figure 4.28d**.^[276] In this circuit R_{ESR} represents the equivalent series resistance (comprising bulk electrolyte resistance, interfacial resistance, and apparent resistance of intra-particle pores),^[274] R_r the charge transfer resistance, C_p the pseudocapacitance, and C_{dl} the double-layer capacitance. The fitting according to this model provided the following values $R_{\text{ESR}} = 4.5 \Omega$, $R_r = 1.4 \Omega$, $C_p = 1.9 \text{ mF}$, and $C_{\text{dl}} = 5.6 \mu\text{F}$. The obtained capacitance components revealed that the material exhibited mainly pseudocapacitive nature, and in conjunction with the CV results, this conclusion justified the loss of capacitance observed upon cycling as correlated with the poor reversibility of the redox events in the electrode.

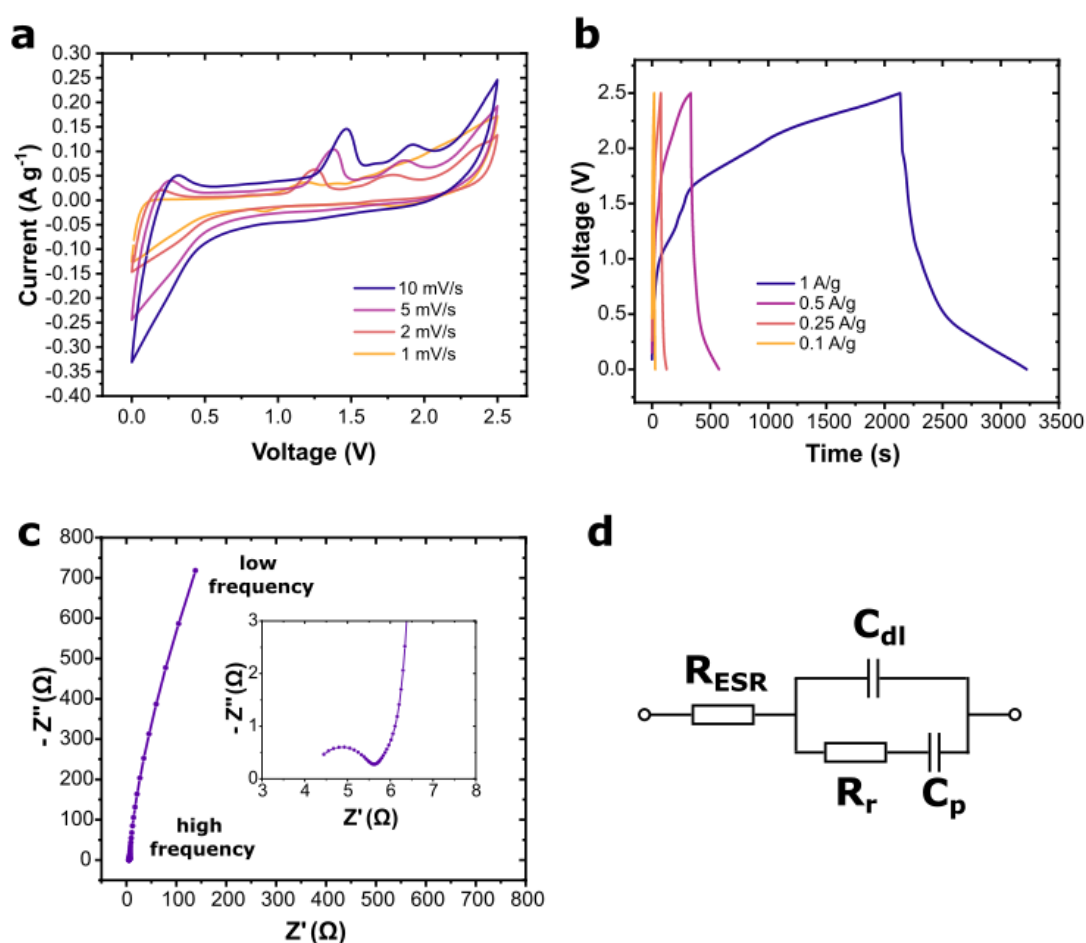


Figure 4.28 (a) Cyclic voltammograms at different scan rates of BTA-TT-COF. (b) Galvanostatic charge-discharge cycles at different current densities. (c) Electrochemical impedance spectroscopy (EIS) profile of the device measured in the 1 MHz to 10 mHz frequency range with 10 points/decade. (d) Equivalent circuit diagram that was used to model the electrical behavior of the cell.

In conclusion the value of gravimetric capacitance of 108 F g^{-1} at 0.1 A g^{-1} is in line with other β -ketoenamine and imine-linked 2D COFs containing electroactive moieties,^[277,278] but

still far from the best values obtained by EL-Mahdy for two other 2D COFs based on **BTA** as knot of the polymeric network (237 F g^{-1} and 189 F g^{-1} at a current density of 2 A g^{-1}).^[252] Overall, it was demonstrated that **BTA-TT-COF** could be integrated in an energy storage device as active material, thanks to its high surface area, good electrical conductivity, and good mass transport properties. It was also showed that to achieve a performing device the system requires further development, in terms of optimization of the cell composition (solvent, electrolyte, and electrode components). The careful choice of the materials is crucial to tackle the stability problem of the electrodes, which could be attributed to side reactions within the cell that strongly limit the Faradaic contribution to measured capacitance.

4.5. Conclusions and perspectives

In this chapter an electroactive 2D COF was synthesized as powder and as thin film on inert substrates. The powder exhibited high crystallinity upon PXRD and high-resolution TEM characterization, a high surface area of $720 \text{ m}^2 \text{ g}^{-1}$ estimated by nitrogen adsorption, and excellent thermal stability up to $450 \text{ }^\circ\text{C}$ under inert atmosphere, measured by TGA. The film, integrated in a two-terminal device exhibited a p-type semiconductor behavior with a valence band edge located at -5.1 eV , a conduction band edge at -3.0 eV , and an optical band gap of 2.1 V . The film displayed an electrical conductivity of $\sigma = 4 \times 10^{-11} \text{ S m}^{-1}$ in vacuum and $\sigma = 3 \times 10^{-6} \text{ S m}^{-1}$ after 20 hours in air. The conductivity could be further increased up to $\sigma = 2 \times 10^{-4} \text{ S m}^{-1}$ upon infiltration of small molecule with strong electron-acceptor properties such as F_4TCNQ . The difference between the conductivity in vacuum and in air was related to the tendency of the material to interact with O_2 , which caused an initial increase of the conductivity by p-doping followed by the deterioration of the charge transport performance upon longer exposure, likely due to irreversible (photo)oxidation reactions that disrupt the π -conjugation in the 2D polymer and the out-of-plane π overlap of the conjugated units. This behavior clearly demonstrated that, as a general rule, electron-rich 2D COFs must be handled with care when trying to measure their intrinsic electrical conductivities as the values can vary enormously depending on the time of exposure to the atmosphere.

Finally, as proof-of-concept, the film and the powder materials were integrated in an electronic and in an electrochemical energy storage devices and their performances were evaluated. In particular, the film was used as semiconductive material in a water-gated OFET. The device displayed three orders of magnitude of current modulation with a threshold voltage of V_{th} of -0.4 V . However, the device exhibited a particularly low value of $\mu \cdot C_v$, which was at-

tributed to a low hole-mobility in the COF layer and possible detrimental effects derived from the exposure of the device to both water and oxygen. The envisioned development for this type of application is the use of a water-free liquid dielectric (such as an ionic liquid) and the operation of the device in an inert atmosphere.

The powder material was tested as active electrodic material in a symmetric pseudocapacitor, using a 1 M NBu_4PF_6 solution in MeCN as supporting electrolyte. The device exhibited a specific capacitance of 108 F g^{-1} at 0.1 A g^{-1} which is in line with the values reported in literature for other electroactive 2D COFs.^[277,278] Nevertheless, the device displayed an important loss in performance at higher current density and the voltametric characterization highlighted a problem of reversibility of the redox reactions in the measuring conditions. Overall, these results showcase the potential and the limitations of the use of electron-rich 2D COFs such as **BTA-TT-COF** for the development of high-performance materials for pseudocapacitors. The further advancements of these project will go in the direction of solving the irreversibility issue of the redox reactions, by matching the COF with the right materials (electrolyte salt, solvent, conductive carbon, binder) and by assembling the cell in a water and oxygen-free environment (glovebox) to make sure that these species do not interfere with the Faradaic processes at the electrodes.

4.6. Materials and methods

Materials

All reagents were purchased from commercial sources such as Sigma-Aldrich, TCI, abcr, BLD Pharm and were used as received. Solvents were purchased from commercial sources such as Carlo Erba, Fischer Scientific, Carl Roth, Acros and used without any further purification. The glass substrates prepatterned gold electrodes were purchased from MetroOhm. The Quartz substrates and ITO substrates were purchased from Ossila. Si/SiO_2 (230 nm) substrates were purchased from Fraunhofer.

Instrumental methods

GCD experiments were carried out on a Neware Battery Tester (BTS-4008T-5V/10mA).

Solvothermal synthesis of **BTA-TT-COF** in concentrated acetic acid

In a 15 ml pressure-vessel 23.6 mg of BTA (0.05 mmol, 1 equiv.) and 19.6 mg of TT (0.10 mmol, 2 equiv.) were dispersed by ultrasonication in a mixture of benzyl alcohol (1.0 ml) and glacial acetic acid (1.0 ml). The suspension was degassed by three freeze-pump-thaw cycles then heated at $120 \text{ }^\circ\text{C}$ for 72 hours. After cooling down the red precipitate was

filtered and washed abundantly with dimethyl formamide (DMF), then Soxhlet extracted with acetone for 12 hours. Acetone was then exchanged with *n*-pentane (Soxhlet extracted, 2 hours) and finally the powder was dried first in air and at 120 °C in a vacuum oven for 12 hours. The product was obtained as a red color solid with a yield of 20%.

Solvothermal synthesis of BTA-TT-COF

In a 15 ml pressure-vessel 47.3 mg of BTA (0.10 mmol, 1 equiv.) and 39.3 mg of TT (0.20 mmol, 2 equiv.) were dispersed by ultrasonication in a mixture of benzyl alcohol (1.5 ml), mesitylene (1.5 ml), and water (0.10 ml). Then glacial acetic acid (1.0 ml) was added, and the suspension was degassed by three freeze-pump-thaw cycles then heated at 120 °C for 72 hours. After cooling down the red precipitate was filtered and washed abundantly with dimethyl formamide (DMF), then Soxhlet extracted with acetone for 12 hours. Acetone was then exchanged with *n*-pentane (Soxhlet extracted, 2 hours) and finally the powder was dried first in air and at 120 °C in a vacuum oven for 12 hours. The product was obtained as red color solid with a yield of 60%.

Scale up of the solvothermal synthesis of BTA-TT-COF

In a 35 ml pressure-vessel 236 mg of BTA (0.5 mmol, 1 equiv.) and 196 mg of TT (1.0 mmol, 2 equiv.) were dispersed by ultrasonication in a mixture of benzyl alcohol (5.0 ml), mesitylene (5.0 ml), and water (0.50 ml). Then glacial acetic acid (3.0 ml) was added, and the suspension was degassed by three freeze-pump-thaw cycles then heated at 120 °C for 72 hours. After cooling down the red precipitate was filtered and washed abundantly with dimethyl formamide (DMF), then Soxhlet extracted with acetone for 24 hours. Acetone was then exchanged with *n*-pentane (Soxhlet extracted, 2 hours) and finally the powder was dried first in air and at 120 °C in a vacuum oven for 12 hours. The product was obtained as red color solid with a yield of 60%.

Solvothermal synthesis of BTA-TT-film

In a 15 ml pressure-vessel 47.3 mg of BTA (0.10 mmol, 1 equiv.) and 39.3 mg of TT (0.20 mmol, 2 equiv.) were dispersed by ultrasonication in a mixture of benzyl alcohol (1.5 ml), mesitylene (1.5 ml), and water (0.10 ml). Then the designed substrate (prewashed with acetone, isopropanol and UV-ozone cleaned for 30 min) was immersed vertically in the liquid suspension and glacial acetic acid (1.0 ml) was added, and the mixture was degassed by three freeze-pump-thaw cycles then heated at 120 °C for 72 hours. After cooling down the coated substrate was extracted from the reaction vessel and separated from the red powder precipitate. The film was washed with DMF and briefly sonicated to remove most of the attached powder material. Further washing was carried out in acetone and THF which was eventually exchanged with *n*-pentane. The film was dried under nitrogen flux.

Construction of the pseudocapacitor prototype

The electrochemical measurements were performed in a two-electrode system using a measuring cell containing two electrodes separated by an electrolyte-soaked separator. The cell was enclosed in a CR2032-type coin cell. The electrodes were prepared by creating a

dispersion of active material, conductive carbon (superP), and binding material (PVDF) in NMP in a 7:2:1 weight ratio. The resulting dispersion was drop-cast onto carbon paper and dried in a vacuum dryer at 80 °C overnight. The electrodes were separated by glassy fibrous paper (Whatman GF/G) soaked with the electrolyte (1M NBu₄PF₆ in MeCN).

5. Functionalized reduced graphene oxide as nanofiller for an asymmetrically conductive COF composite film

5.1. Introduction on COF composite materials and applications

The development of novel smart materials with unique features is a major research focus in the field of materials science.^[279] Smart materials are at the basis of many classical applications such as sensors and actuators, as well as in the new areas of soft robotics and bioelectronics.^[280] The increasing demand for advanced smart materials with multi-responsive properties requires the integration of multiple distinct functionalities to accomplish a broad range of tasks. In this context, 2D COFs are highly attractive for many applications, as it has been demonstrated that their surface area, pore size and shape, and functional group composition are highly customizable, which can potentially lead to the simultaneous expression of various unique properties within a single material.^[74,154] However, the use of 2D COFs as smart materials in macroscopic devices is hindered by some intrinsic drawbacks, such as the difficulty in processing them into robust macroscopic films and the modest charge transport properties displayed by most 2D COFs.

In **Chapter 3** we faced the first challenge, reporting on a simple method for processing 2D COFs into robust macroscopic films. In **Chapter 4** we faced the second challenge, testing the possibility of endowing the polymer with high intrinsic electrical conductivity by carefully selecting appropriate electroactive moieties as building blocks. However, the latter approach showed some limitations related to the modest electric conductivity performance to poor stability of the obtained electron-rich material.

A general alternative approach to endow 2D COFs with new properties is to combine them with other nanomaterials such as metal nanoparticles, silica, metal oxides, polymers, or carbon materials.^[16] Notably, carbon nanomaterials have often been used as fillers to modify the mechanical, electrical, and thermal properties of polymers.^[281,282] Among all, graphene has emerged as a highly attractive nanofiller in polymer matrices owing to its high thermal and electrical conductivities, large surface area, and remarkable mechanical properties.^[283,284] However, graphene exhibits strong interlayer van der Waals forces and poor in-

teraction with the polymer matrix, leading to a high tendency to aggregate and generate non-uniform composite materials.^[285] As a result, the full exploitation of graphene for the modification of polymers can be extremely challenging. A possible alternative approach involves the use of graphene oxide (**GO**) as a replacement.^[286] **GO** is the most common derivative of graphene and is composed of layered carbon sheets with a defective $sp^2 - sp^3$ carbon backbone, decorated with oxygen-containing functional groups (OFGs), such as hydroxyls, carboxyls, carbonyls, and epoxides.^[287] The presence of a high number of OFGs at the carbon basal plane and at the sheet edges promotes the formation of well-dispersed **GO** colloids in water and polar organic solvents, allowing for easy solution-based processing of the material, in contrast to graphene.^[288] Moreover, owing to the reactivity of the OFGs, **GO** represents a flexible platform for the attachment of additional organic functional groups, further improving its capability to interface with the target host materials through chemical modification.^[289] However due to the presence of the OFGs and the highly defective carbon backbone, **GO** displays extremely low electrical conductivity compared to graphene. The electrical performance of **GO** can be improved by partially removing the OFGs and thereby restoring, yet not fully, the extended π -conjugation. This reduction process can be carried out with a variety of chemical, electrochemical, and thermal methods and yields a conductive material known as reduced **GO** (**rGO**).^[290] Notably, thermal annealing is a simple and clean method that allows to obtain a **rGO** by inducing the desorption of small molecules such as H_2O , CO , and CO_2 which drives the decomposition of the OFGs and the sp^3 to sp^2 rehybridization of the carbon backbone.^[291]

In this chapter, we report a simple strategy for the preparation of an **rGO-COF** composite material in the film morphology, where the **COF** constitutes the matrix and the **rGO** is the nanofiller (**Figure 5.1a**). The method is based on the solution processability of the polyimines based on the **TPB** monomer in water-TFA mixtures developed in **Chapter 3**. As co-monomer **MeOTP** or 2,5-bis(octyloxy)terephthalaldehyde (**OctOTP**) were used. Initially, the formation of a **GO-PI** composite was studied, and a simple covalent functionalization step was presented to improve the uniformity of the **GO** distribution within the **PI** matrix (**Figure 5.1b**). Subsequently, the desired **rGO-COF** composite was obtained by two consecutive annealing steps (**Figure 5.1c**). The first was conducted in solvent at 100 °C and induced the recrystallization of **PI** to **COF**, whereas the second was carried out at 250 °C in inert atmosphere to induce the reduction of **GO** to conductive **rGO**. The final film exhibited high robustness toward exposure to organic solvents and water and remarkable mechanical stability. Moreover, upon **GO** reduction, the composite displayed an asymmetrical electrical conductivity on

the two sides of the film, attributed to a gradient in the concentration of **rGO** along the section of the film. This peculiar structure was leveraged to build a prototype of a strain-sensing device that showed a high electrical response to bending cycles, quantified with a gauge factor of 11.5.

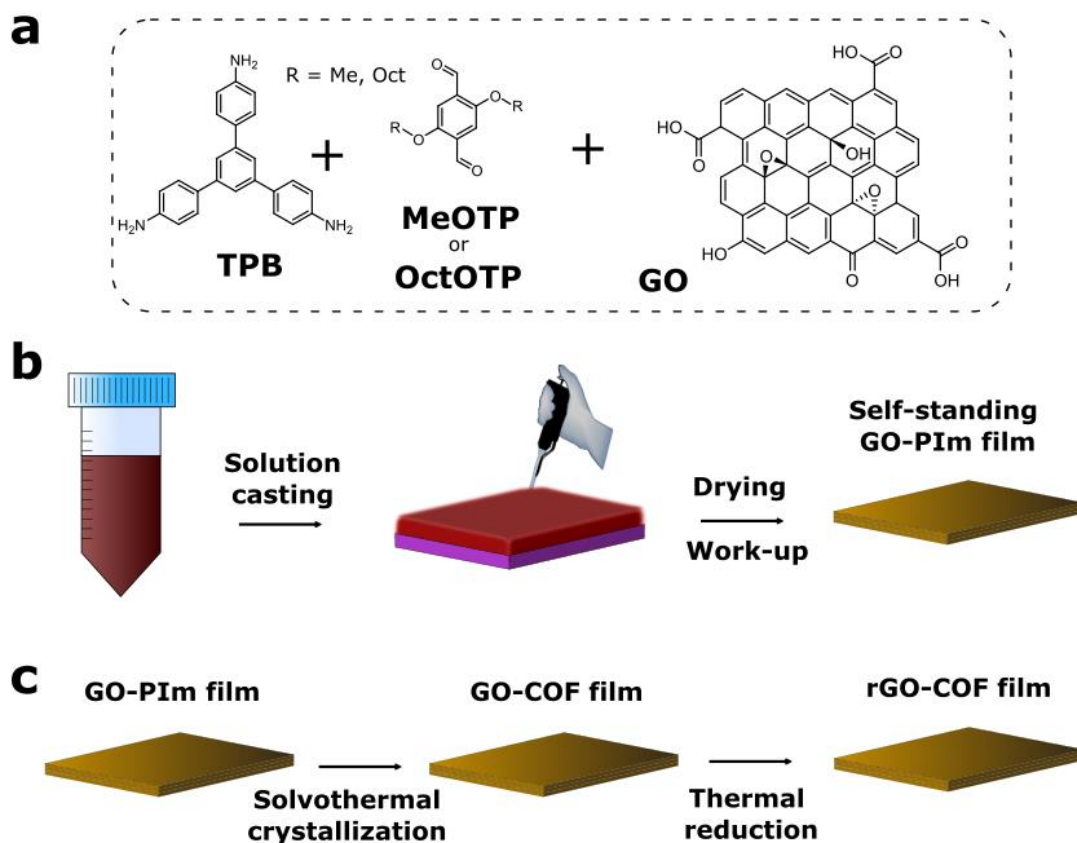


Figure 5.1 (a) Chemical structure of the components used for the construction of the **rGO-COF** composite. (b) Scheme for preparation of **GO-PIm** composite films using the polymer solution-casting method, followed by the lift off and neutralization of the film by immersion in MeOH and TEA. (c) Scheme of the preparation of the **rGO-COF** composite by post-synthetic treatment of the **GO-PIm** film, consisting in the solvothermal recrystallization of **PIm** to **COF** and thermal reduction of **GO** to **rGO**.

5.2. Synthesis and characterization of the GO-COF composite

5.2.1. Synthesis of the GO-PIm composite

To prepare the **GO-PIm_{Me}** and **GO-PIm_{Oct}** composites, solutions of **PIm_{Me}** (**MeOTP-TPB**) and

PIm_{Oct} (OctOTP-TPB) were used with a concentration of $C_0 = 150$ mM (total functional group concentration, see **Chapter 3**) in a 5 % v water-TFA solvent mixture. An appropriate amount of **GO** powder was added to these solutions to achieve a concentration of 2 mg ml^{-1} which resulted in solid materials with a **GO** content of about 6 % wt and 4 % wt, respectively. To obtain a fine dispersion of **GO**, the mixture was processed in a Cup Horn ultrasonic bath (200 W) for 30 min. The resulting black inks were used directly to prepare the films by casting 150 μl of the dispersions onto silicon or quartz substrates. The evaporation was performed in a semi-enclosed environment (covered Petri dishes) at 40 °C. In both cases (**GO-PIm_{Me}** and **GO-PIm_{Oct}**), solid films promptly formed after a few minutes of reaction, while the solvent drying process was continued for 4 hours at the same temperature. Subsequently, the film-coated substrates were immersed in a TEA solution in MeOH (10 % v), which simultaneously produced the delamination of the materials from the substrates and the neutralization of the remaining TFA, as evidenced by the clear color change from red to yellow. The films were then purified by a 12-hour Soxhlet extraction with THF, which was finally exchanged for *n*-pentane. The removal of *n*-pentane was first carried out at room temperature by hanging the films to allow even evaporation from both sides, and then in vacuum at 80 °C overnight (see **Section 5.6** for further details).

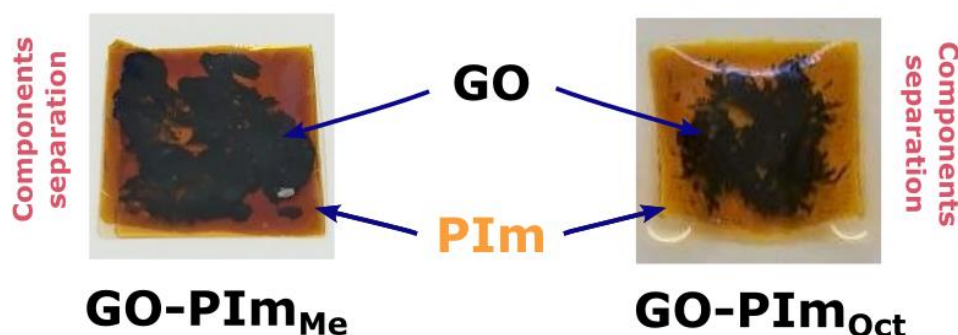


Figure 5.2 Photographs of **GO-PIm_{Me}** and **GO-PIm_{Oct}** composites at 2 mg ml^{-1} loading. Both materials showed separation of their components.

As shown in **Figure 5.2**, the **GO-PIm_{Me}** and **GO-PIm_{Oct}** films obtained using this method displayed a clear separation of the components, with a very high concentration of **GO** in the central part of the film, while almost no filler material was present at the edges. The origin of this segregation effect was researched in the stability of **GO** colloids in TFA. The formation of a stable colloidal suspension of **GO** in water and polar organic solvents is related not only to its hydrophilicity, but also to the electrostatic repulsion effect between the 2D sheets. Indeed, it has been demonstrated that the presence of ionizable OFGs, such as carboxylic ac-

ids, leads to the accumulation of a high negative charge on the 2D sheets when dispersed in a solvent.^[288] Moreover, it is known that in acidic conditions **GO** exhibit poor dispersibility, as the presence of carboxylate anions is unlikely.^[292] Therefore, the evident segregation from the **PIm** matrix was attributed to the limited dispersibility of **GO** in the solvent mixture.

5.2.2. Functionalization of **GO** with ethylene diamine (EDA)

To solve this issue, we developed a strategy to simultaneously compatibilize **GO** with the acidic reaction conditions and with the **PIm** matrix. The strategy consisted in the functionalization of the material with a basic moiety, such as a primary amine, which can improve the stability of the colloidal suspensions upon protonation in TFA and formation of positively charged sheets. Moreover, the presence of the primary amino groups on the surface can provide an anchoring point for cross-linking between **GO** and **PIm**. To achieve the functionalization, the presence of reactive epoxy groups on **GO** offers an easy platform to modify the material by ring opening reaction which occurs with S_N2 mechanism.^[289] On these grounds, **GO** was reacted with ethylene diamine (EDA) (**Figure 5.3**), which resulted in a material with exposed amino groups on the basal plane and edges of the 2D sheets (**GO_{EDA}**).

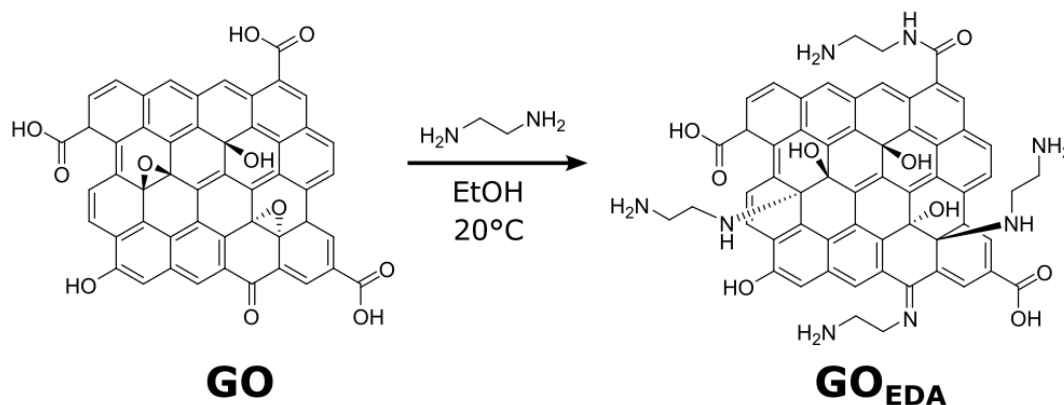


Figure 5.3 Scheme of the possible reactions occurring during the functionalization of **GO** with ethylene diamine (EDA).

The functionalization was carried out by slowly adding (over one hour) a suspension of **GO** in ethanol (EtOH) to a solution of EDA in EtOH in large excess.^[293] The order of mixing and the excess of EDA were chosen to avoid the cross-linking between **GO** sheets, which would cause aggregation of the material and the formation of a bulk network. The mixture was then stirred at 20 °C for 16 hours. Afterwards, the crude reaction mixture was separated

from the solution by centrifugation and removal of the supernatant. To completely remove unreacted EDA, the precipitate was washed thoroughly with EtOH, acetone, and water. The **GO_{EDA}** powder was obtained by freeze-drying (see **Section 5.6** for further details).

The functionalization of **GO** with EDA can occur through multiple reaction pathways, given the range of functional groups present on the material. Specifically, while the ring opening of the epoxides is favored even in mild conditions and in absence of acid catalysis, carbonyls, hydroxyls, and carboxylic acids are much less reactive toward amines, although a partial contribution from these functional groups cannot be completely excluded.^[289,294]

The **GO** functionalization was verified using XPS (**Figure 5.4**). While the pristine **GO** did not show any detectable amount of nitrogen, a clear peak appeared at ~ 400 eV in the survey spectrum of **GO_{EDA}**. Furthermore, the carbon / oxygen relative amount increased from 2.2 to 3.1 after the reaction because of the additional aliphatic chains of EDA (**Figure 5.4b** vs **Figure 5.4c**).

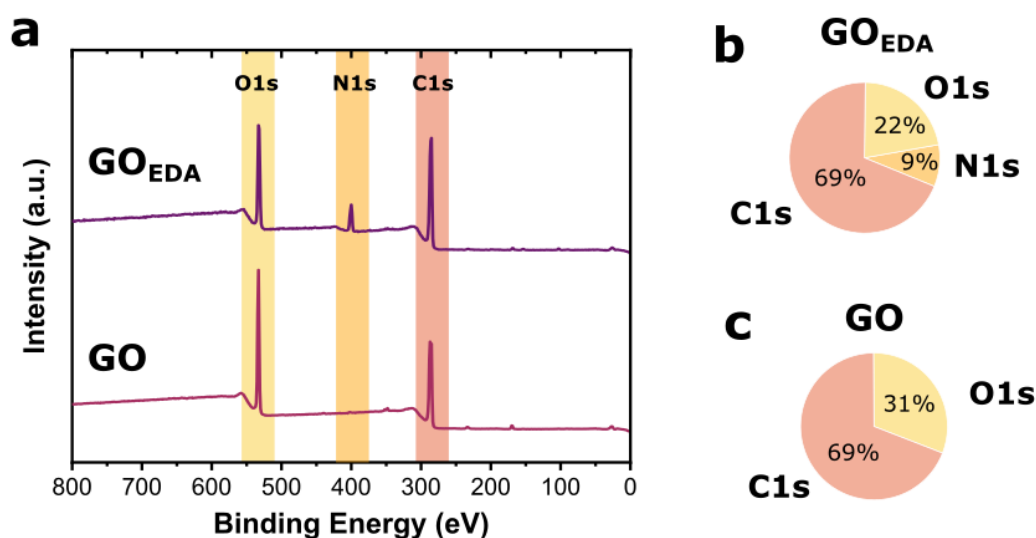


Figure 5.4 (a) Survey XPS profiles of **GO** and **GO_{EDA}**. (b) Elemental relative amounts in **GO_{EDA}**. (c) Elemental relative amounts in **GO**.

The XPS survey also provided semi-quantitative information regarding the composition of the **GO_{EDA}**. The degree of functionalization could be estimated from the relative abundance of nitrogen and carbon (**Figure 5.4b**) according to the following equation:^[294]

$$\frac{C_{GO}}{n_{EDA}} = \frac{C\% - N\%}{N\%/2}$$

where C_{GO}/n_{EDA} is the ratio between the number of carbon atoms in **GO** and the number of attached EDA molecules, and $C\%$ and $N\%$ are the relative abundances of carbon and ni-

trogen, respectively, obtained from the relative areas of the XPS peaks. The analysis revealed the presence of an EDA molecule every 13 **GO** carbon atoms, indicating a high concentration of exposed amino groups in the material.

The interaction of the functionalized material with TFA was tested by preparing a 2 mg ml^{-1} suspension of **GO**_{EDA} in water-TFA 5 % *v* and comparing it with a suspension of the **GO** precursor at the same concentration. It was observed that a few minutes after the ultrasonication treatment, the pristine **GO** flakes formed aggregates, while **GO**_{EDA} appeared finely dispersed after the same amount of time (**Figure 5.5**). Moreover, the **GO**_{EDA} dispersion remained stable for several hours before beginning to sediment, thereby constituting a more promising candidate for the formation of **GO-PIm** composites from TFA solution.



Figure 5.5 Photographs of a 2 mg ml^{-1} suspension of pristine **GO** and **GO**_{EDA} in 5% water-TFA a few minutes after ultrasonication clearly displaying the aggregation of the flakes in the case of pristine **GO** and the good dispersion obtained from **GO**_{EDA}.

It is most likely that the presence of protonated amino groups exposed on the basal plane and at the edges of the material could be the reason for the observed better dispersibility of **GO**_{EDA} compared to **GO** in TFA. Indeed, the electrostatic repulsion between the same positively charged **GO**_{EDA} layers helps to prevent the aggregation. However, the z-potential measurements of the dispersion have not yet been carried out; therefore, the origin of the colloidal stability improvement was not experimentally confirmed.

5.2.3. Synthesis of the **GO**_{EDA}-**PIm** composites

The **GO**_{EDA}-**PIm**_{Me} and **GO**_{EDA}-**PIm**_{Oct} composites were prepared using the same protocol described in **Section 5.2.1** and with a **GO**_{EDA} concentration of 2 mg ml^{-1} , which resulted in materials with a **GO**_{EDA} content of about 6 % and 4 % in mass respectively. The films obtained after the synthesis and workup displayed an improved distribution of **GO**_{EDA} in the **PIm** matrix (**Figure 5.6**). Notably, while the uniformity of the **GO**_{EDA}-**PIm**_{Me} composite still did not appear to be optimal, **GO**_{EDA}-**PIm**_{Oct} exhibited a nearly homogenous distribution of the graphene de-

rivative within the entire area of the film, as observed in the optical images. Additionally, both materials exhibited high stability toward exposure to organic solvents and to mechanical manipulations, with no degradation of the polymer and no visible release of the nano-filler.



Figure 5.6 Photographs of $\text{GO}_{\text{EDA}}\text{-PIm}$ composites.

The improved homogeneity obtained with PIm_{Oct} with respect to PIm_{Me} could be tentatively attributed to the effect of the octyl chains, which might help to improve the affinity between the polymer and the modified GO . Because $\text{GO}_{\text{EDA}}\text{-PIm}_{\text{Oct}}$ displayed much higher homogeneity respect to $\text{GO}_{\text{EDA}}\text{-PIm}_{\text{Me}}$, further characterization focused only on this material.

To investigate the morphology of the $\text{GO}_{\text{EDA}}\text{-PIm}_{\text{Oct}}$ composite, the material was analyzed using SEM and the obtained images were compared with those of the pristine polymer. Pristine PIm_{Oct} appeared as 50 μm -thick film, with a smooth and continuous surface (Figure 5.7a) and a compact and almost featureless cross-section (Figure 5.7b).

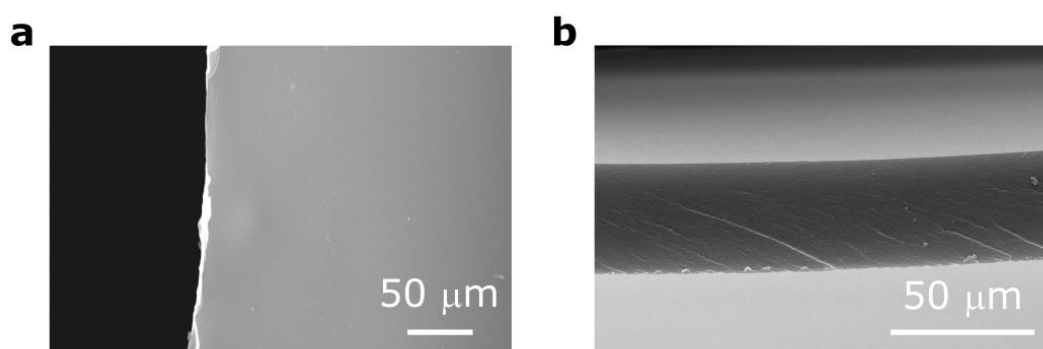


Figure 5.7 (a) Top and (b) cross-sectional SEM images of PIm_{Oct} without GO_{EDA} .

The SEM images of the composite are shown in Figure 5.8. Clearly, while retaining the same smooth surface as in the pristine PIm_{Oct} , the presence of GO_{EDA} evidently altered the morphology in the bulk of the material. Notably, the cross-sectional images (Figure 5.8b, c)

displayed a particularly corrugated structure, indicating limited uniformity of the GO_{EDA} distribution at the micrometer scale. However, such a morphology is expected for a nano-material dispersed in a polymer.^[286]

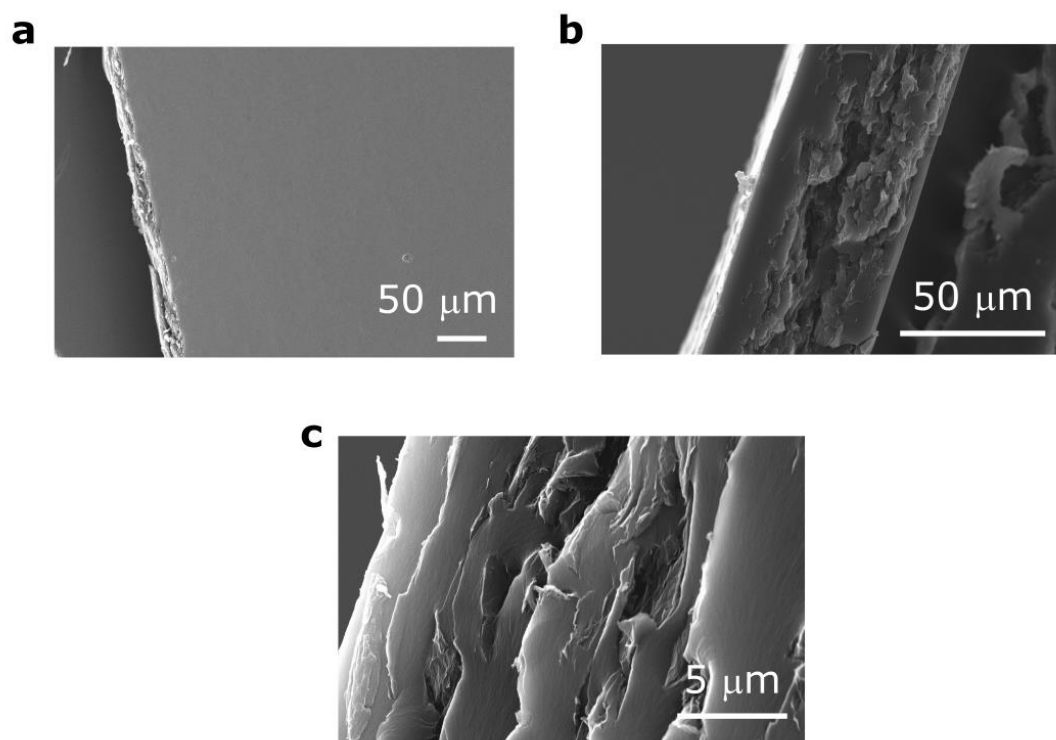


Figure 5.8 (a) Top and (b) cross-sectional SEM images of $\text{GO}_{\text{EDA}}\text{-PIIm}_{\text{Oct}}$ composite. (c) Details of the cross-section of the film showing a corrugated morphology related to the presence of GO_{EDA} sheets.

5.2.4. Characterization of the $\text{GO}_{\text{EDA}}\text{-PIIm}_{\text{Oct}}$ composite and recrystallization to $\text{GO}_{\text{EDA}}\text{-COF}_{\text{Oct}}$

Structural analysis of the composite

As thoroughly discussed in **Chapter 3**, the **PIIm** prepared through the polymer solution casting method generates a material with a limited structural order. The PXRD analysis in Bragg-Brentano (reflection) geometry (**Figure 5.9**) of $\text{GO}_{\text{EDA}}\text{-PIIm}_{\text{Oct}}$ confirmed the amorphous feature, displaying two very broad reflections at $2\theta = 6^\circ$ and 23° . The reflection at high angle was assigned to the π -stacking distance between the aromatic backbone of the polymer for a calculated d-spacing of approximately 0.39 nm. The asymmetry of the reflection was attributed to the presence of a second component in this peak at approximately 20° , which was related to the average intermolecular distance between the aliphatic octyl chains, with a corresponding d-spacing of approximately 0.44 nm. The low-intensity and broad reflection at 6° further indicated a very limited degree of order in the material. Given the low relative

amount of GO_{EDA} present in the material (approximately 4 % wt), it was not expected that the presence of the nanofiller would contribute to the observed diffraction pattern or alter the overall structure of the polymer. However, on this front, further analysis of the composite with different relative amounts of nanofiller is required and will be carried out in future experiments.

To improve the structural order, the material was recrystallized to the corresponding COF_{Oct} by solvothermal annealing at 100 °C in MeCN. For an efficient recrystallization, 10 M HOAc was added as a catalyst and the reaction was run for 24 hours. The recrystallized material was obtained in a 95 % yield and without any apparent optical or morphological alterations. The PXRD analysis (**Figure 5.9**) revealed a distinctive pattern with peaks at $2\theta = 2.9^\circ$, 5.9° , 10.0° , and 25.1° that were assigned to the (100), (200), (220), and (001) planes, respectively, and matched with the previously reported powder material.^[103] Despite the improvement, the crystallinity remained limited, in particular when compared to the same material prepared by the solvothermal method^[103] and to the COF_{Me} film prepared by polymer solution casting (**Chapter 3**). The diffraction halo related to the aliphatic octyl chains at approximately 20° remained clearly visible after the solvent annealing step.

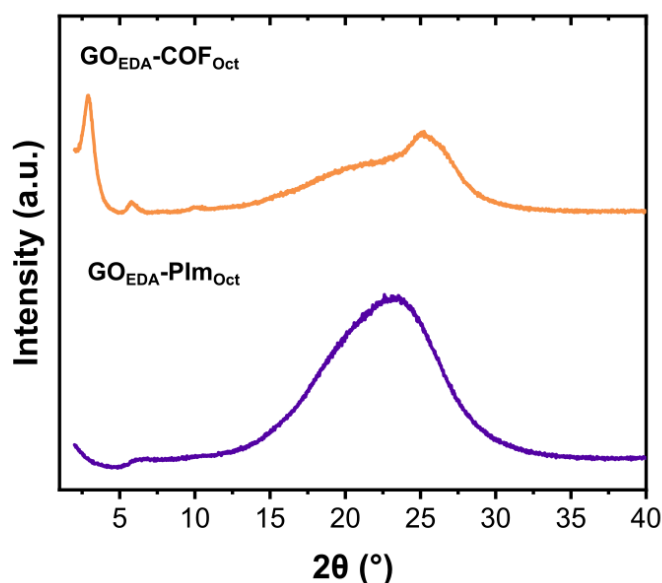


Figure 5.9 PXRD patterns of the $\text{GO}_{\text{EDA}}\text{-PIm}_{\text{Oct}}$ composite (violet line) and the $\text{GO}_{\text{EDA}}\text{-COF}_{\text{Oct}}$ composite (orange line) obtained by annealing the previous sample.

Interestingly, the presence of reflections related to both the ($hk0$) and ($00l$) planes in the PXRD in Bragg-Brentano geometry indicated the lack of a highly oriented structure, which is instead typical in the case of PIm_{Me} and COF_{Me} (see **Chapter 3**). To further elucidate the structure of the material, PIm_{Oct} and COF_{Oct} were investigated using GIWAXS with a 2D de-

tor. **PIm_{Oct}** presented a weak scattering pattern (**Figure 5.10**) with two visible diffraction cones at $2\theta = 6^\circ$ and 23° , confirming the results obtained using PXRD. The material displayed a weak orientation preference with the π -stacking direction orthogonal to the surface of the film, and the intensity of the $2\theta = 6^\circ$ reflection slightly increased in the in-plane (xy) direction, while the intensity of the $2\theta = 23^\circ$ reflection grew in the out-of-plane (z) direction. However, the lack of strong alignment of the polymer sheets justified the featureless morphology observed in the cross-sectional SEM images (**Figure 5.7**) compared with the highly layered structure observed for **PIm_{Me}** in **Chapter 3** (**Figure 3.3**).

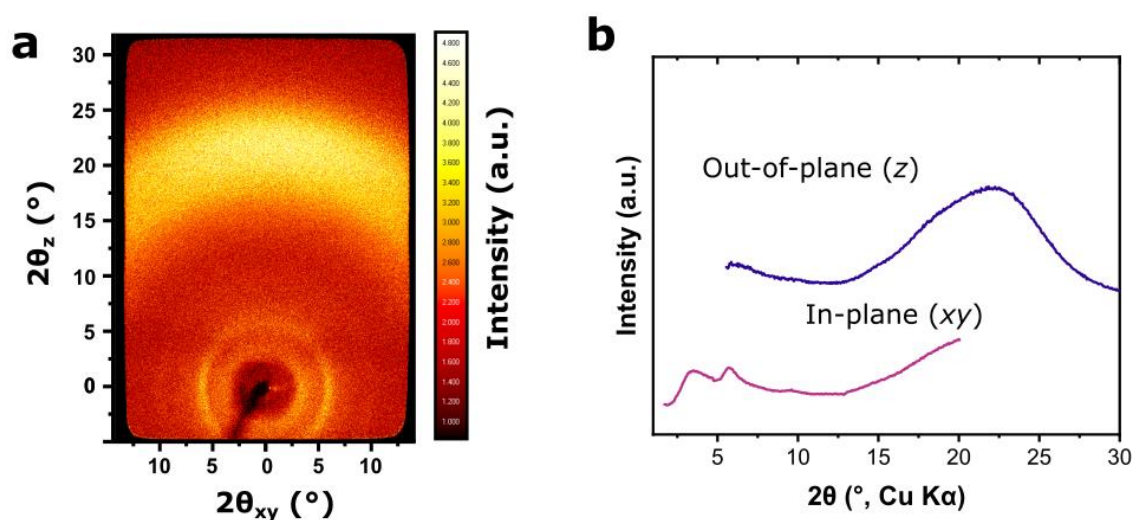


Figure 5.10 (a) 2D GIWAXS pattern of the self-standing **PIm** film (without **GO_{EDA}**). (b) Staked plot of the in-plane (violet line) and out-of-plane (blue line) radial integrations of the 2D GIWAXS profile.

The 2D GIWAXS analysis of the recrystallized **COF_{Oct}** (**Figure 5.11a**) confirmed the crystalline nature of material with intense reflection cones at $2\theta = 2.9^\circ$, 5.7° , 9.7° , 25.0° , and a diffused halo centered at 20° . As for the **PIm_{Oct}** precursor, the diffraction cones related to the ($hk0$) planes displayed higher intensity along the in-plane (xy) direction, while the diffraction cone related to the (001) plane showed higher intensity along the out-of-plane (z) direction. In conclusion, **COF_{Oct}** showed a small orientation preference, with the 2D polymer layers aligned parallel to the film surface, inheriting the anisotropic structure from the **PIm_{Oct}** precursor.

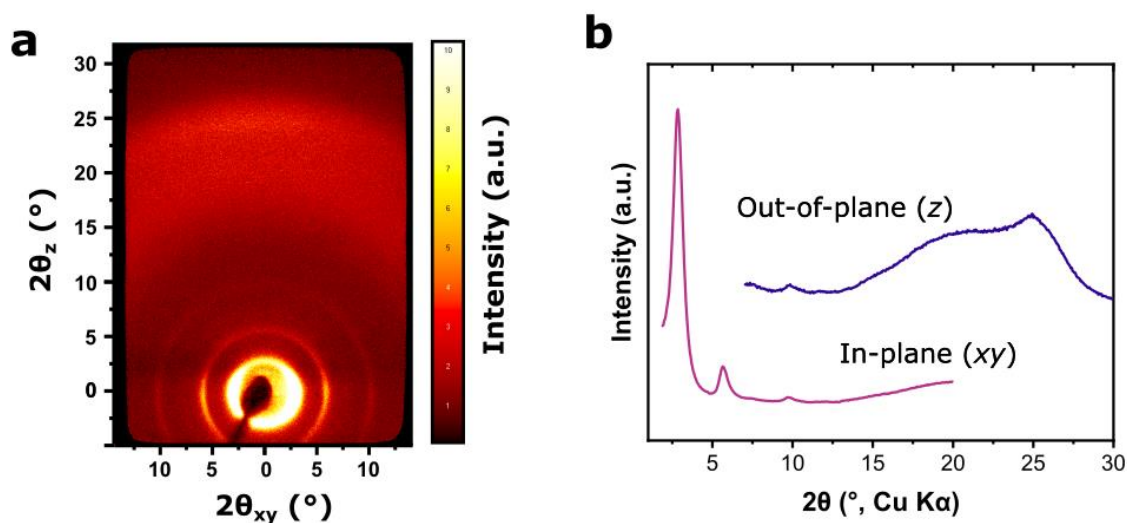


Figure 5.11 (a) 2D GIWAXS pattern of the self-standing COF_{Oct} film (without GO_{EDA}). (b) Staked plot of the in-plane (violet line) and out-of-plane (blue line) radial integrations of the 2D GIWAXS profile.

The nitrogen adsorption isotherm measurements allow the evaluation of the gas uptake properties of porous materials and the estimation of their surface area and pore size distribution. At the time of preparation of this manuscript, the results of the porosity assessment were not available. However, some considerations can be made regarding the nature of the composite films. As in the case of PIIm_{Me} reported in **Chapter 3**, which was not crystalline, PIIm_{Oct} is not expected to display gas-adsorption properties because of the extremely low surface area correlated to a non-porous nature. However, upon recrystallization to COF_{Oct} , the porous structure of the material is reconstructed, and the material should be able to exhibit a good gas uptake performance and high surface area, as reported by Feriante and Zhu for the corresponding COF material in powder (500 and 1200 $\text{m}^2 \text{g}^{-1}$, respectively).^[103,295] The effect of the presence of GO_{EDA} as nanofiller in the COF is unknown, but it is not expected to induce major changes in the microporous nature of the material, due to the low amounts present. The porosity studies using nitrogen adsorption measurements are currently underway.

Infrared-spectroscopy

The presence of the imine linkage upon polymerization and the changes upon the recrystallization step were verified by FTIR-ATR spectroscopy (**Figure 5.12**). The spectrum obtained from the $\text{GO}_{\text{EDA}}\text{-COF}_{\text{Oct}}$ composite was compared with the spectrum of the precursor $\text{GO}_{\text{EDA}}\text{-PIIm}_{\text{Oct}}$ and with the spectra of the respective monomers, **TPB** and **OctOTP**.

The spectrum of **TPB** (**Figure 5.12a**, violet line) showed two intense bands ascribed to the

asymmetrical and symmetrical N-H stretching at 3442 and 3354 cm^{-1} , respectively. The N-H bending generated an intense band at 1605 cm^{-1} , whereas the band originating from C-N stretching was clearly visible at 1278 cm^{-1} . The two bands at 1620 and 1513 cm^{-1} were related to the aromatic ring modes. The spectrum of **OctOTP** (Figure 5.12a, purple line) was characterized by several intense bands in the region of 3000-2800 cm^{-1} for the stretching of the C-H bonds of the octyl chains. Two weak bands at 3048 and 2760 cm^{-1} were assigned to the aromatic and aldehydic C-H stretchings, respectively. The characteristic intense band for the C=O stretching vibration appeared at 1677 cm^{-1} with an overtone at 3352 cm^{-1} .

In the FTIR spectrum of the **GO_{EDA}-PIm_{Oct}** film (Figure 5.12b, blue line) the stretching of the newly formed C=N bond was observed as a band of medium intensity at 1614 cm^{-1} . At slightly lower frequencies, the aromatic ring mode was observed as an intense band, with a maximum at 1588 cm^{-1} . A C=O stretching band of medium intensity was present at 1681 cm^{-1} , slightly shifted toward higher frequencies with respect to the monomeric **OctOTP** and was ascribed to the formyl group of the mono-reacted aldehyde, which is a terminal group of the polymer branch. Two bands at 3469 and 3377 cm^{-1} were present for the asymmetrical and symmetrical N-H stretching, respectively. As for the C=O stretching in the film, the maxima were slightly shifted toward higher frequencies with respect to the monomer, allowing to assign them to the NH₂ vibration of the terminal group of the polymer branch. Characteristic N⁺-H weak stretching bands were present at 2594, 2497, 2440 cm^{-1} and were attributed to the presence of trapped TFA-TEA salt or to some residual protonation of the C=N linkage.^[227-229]

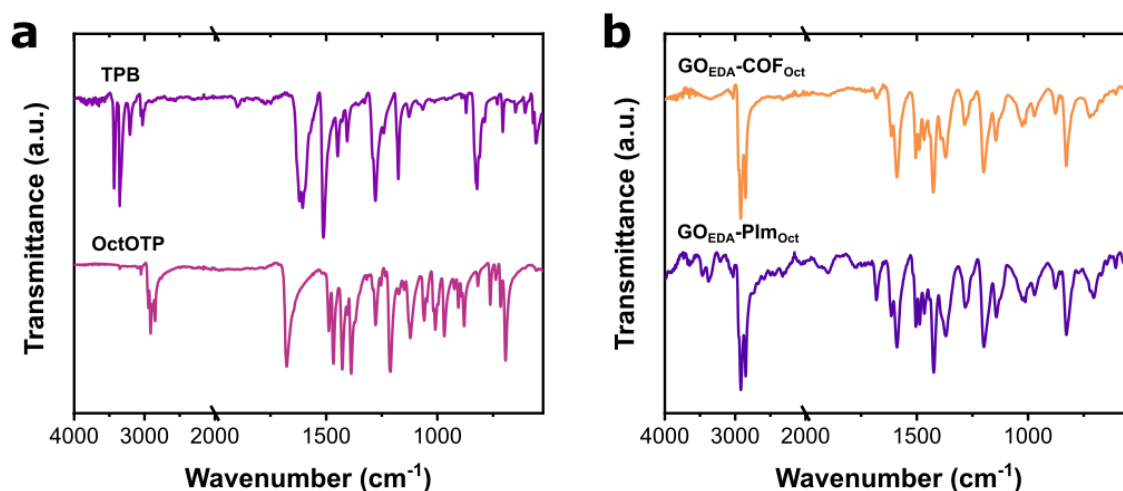


Figure 5.12 FTIR spectra of: (a) monomers TPB (violet line) and OctOTP (purple line). (b) **GO_{EDA}-PIm_{Oct}** composite (blue line) and **GO_{EDA}-COF_{Oct}** composite (orange line) obtained by annealing the previous sample.

FTIR-ATR analysis of the **GO_{EDA}-COF_{Oct}** composite after the recrystallization step confirmed the depletion of the terminal free aldehyde and amine groups and the removal of the TFA-derived guest species (**Figure 5.12b**, orange line). In particular, the spectrum showed a strong decrease in the intensity of both the aminic N-H vibration modes (3469 and 3677 cm^{-1}) and the aldehydic C=O stretching (1681 cm^{-1}), and the disappearance of the N⁺-H stretching bands in the 2700-2500 cm^{-1} region. In conclusion, the solvent annealing procedure not only affected the structural order of the branches of the polymer network, but also increased the extent of the reaction in the solid state by healing the defects and reducing the number of unreacted end-groups of the polymer.

5.3. Thermal Reduction and Conductivity Measurements

Owing to the presence of a high number of OFGs on the basal plane and on the edges of **GO_{EDA}**, the composites prepared with this material as nanofiller did not show any appreciable electrical conductivity. As anticipated, a thermal annealing treatment was developed to induce the reduction of the nanofiller to conductive **rGO_{EDA}**. In this regard, a recent systematic study by Valentini *et. al.* showed that the electrical properties of GO films could be finely adjusted by carefully selecting the annealing conditions, and namely the temperature, the time, and the gas atmosphere.^[291] Notably, the authors demonstrated that a form of rGO with low resistivity ($10^{-1} \Omega \text{ m}$) could be easily obtained after 4 hours at temperatures as low as 150 °C when the annealing was performed in air. Alternatively, when the annealing was performed in inert atmosphere, rGO showing low resistivity ($10^{-2} - 10^{-3} \Omega \text{ m}$) was obtained after 4 hours in the 200 – 300 °C temperature range.

The thermal stability of the **COF_{Oct}** matrix was investigated using TGA before the implementation of the annealing procedure for the **GO_{EDA}-COF_{Oct}** composite. **Figure 5.13** shows the TG profiles of **PIm_{Oct}** and **COF_{Oct}** exposed to a temperature ramp of 10 °C min^{-1} in nitrogen atmosphere from 30 to 600 °C (the inert atmosphere was chosen to avoid possible secondary reactions of the material with oxygen).

The two materials exhibited the same TG profiles, indicating that the structural rearrangements related to the recrystallization did not influence the thermal stability of the polymer. **COF_{Oct}** and **PIm_{Oct}** did not display any significant mass loss in the 30 – 400 °C temperature interval but rapidly degraded at higher temperatures, as indicated by the loss of 50 % of the total mass before reaching 450 °C. Interestingly, **COF_{Oct}** displayed the same degradation temperature as **COF_{Me}** (**Chapter 3, Figure 3.13**) but a much faster decomposition rate. This

finding might suggest a relevant role of the lateral chain fragmentation during the first stages of the thermal decomposition of the material, in partial contrast to what has been reported by Evans *et. al.*^[52]

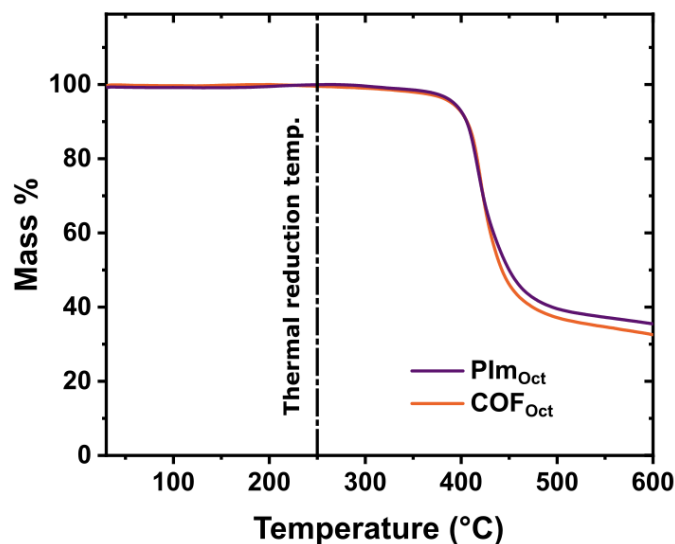


Figure 5.13 TG profiles of the **PIm_{Oct}** and **COF_{Oct}** (orange line). A temperature gradient of 10 °C min⁻¹ and nitrogen atmosphere were used. The temperature used for the subsequent thermal reduction of **GO_{EDA}** is indicated by the dashed line.

Having assessed the thermal stability of the **COF_{Oct}** matrix up to 400 °C in inert atmosphere and on the basis of the results reported for pure GO,^[291] a temperature of 250 °C and a reaction time of 4 hours were selected for the thermal annealing of the **GO_{EDA}-COF_{Oct}** composite (**Figure 5.14**). The reaction was performed in a tubular oven under an inert atmosphere (argon) to avoid potentially detrimental secondary reactions of the **COF_{Oct}** matrix with atmospheric oxygen. Upon thermal treatment, the film did not display any evident color morphology changes and retained its mechanical flexibility and robustness. It is known that during the annealing of GO, small, oxygenated molecules such as H₂O, CO, and CO₂ are released with a consequent increase in the C / O ratio. Moreover, after annealing at temperatures between 150 and 300 °C, Valentini *et. al.*, evidenced a gradual decrease in the amount of C_{sp3}-O-C_{sp3} and C_{sp3}-OH and a parallel increase in C_{sp2}-O and C_{sp2}=C_{sp2}.^[291] These findings indicated that during the annealing, the release of oxygenated moieties is accompanied by a rearrangement of the OFGs, which the authors identified as major contribution to the increase in conductivity of the thermally treated materials.

Owing to the low amount of **GO_{EDA}** nanofiller present in the **GO_{EDA}-COF_{Oct}** composite and the carbon nature of the **COF_{Oct}** matrix, it was not possible to directly examine the chemical changes of the material upon reduction using conventional techniques such as XPS and sol-

id-state NMR.^[291] However, the effects of the thermal treatment on the chemical structure of the material can be indirectly evidenced by the changes in the charge transport properties.^[291]

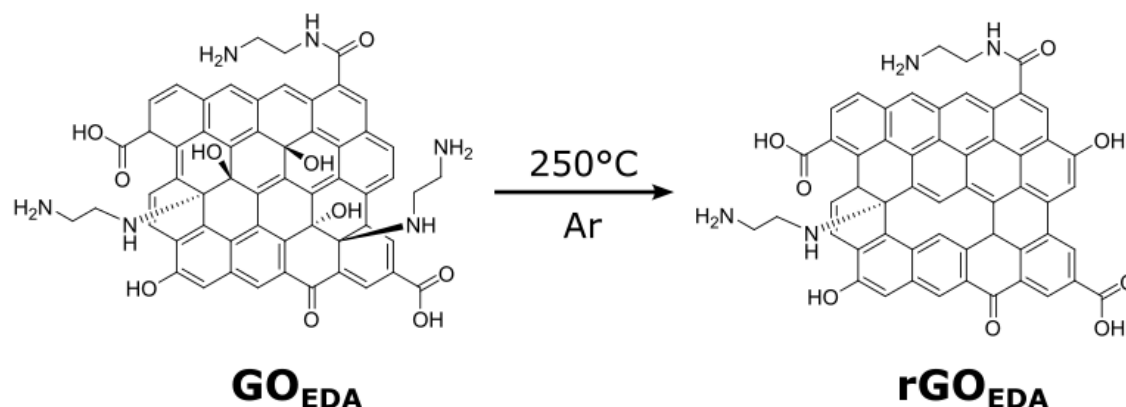


Figure 5.14 Scheme of the possible reactions occurring during the thermal reduction of GO_{EDA} to rGO_{EDA} by thermal treatment.

The electrical sheet resistance (R_s) was measured using the four-point probe technique (FPP) (**Figure 5.15a**). While before the annealing the $\text{GO}_{\text{EDA}}\text{-COF}_{\text{Oct}}$ composite exhibited a sheet resistance R_s beyond the detection limit of the employed instrument (*i.e.* $R_s = 10^7 \Omega \text{ sq}^{-1}$), after the thermal treatment the sheet resistance of the film dropped to $R_s = 1.3 \times 10^5 \Omega \text{ sq}^{-1}$. This value corresponds to a resistivity of $\rho = 6.5 \Omega \text{ m}$ (and a conductivity of $\sigma = 0.15 \text{ S m}^{-1}$) calculated according to the following equation:

$$\rho = \sigma^{-1} = R_s \cdot t$$

where t is the thickness of the composite film (in this case, $t = 50 \mu\text{m}$).

Interestingly, a large difference in electrical performance was observed between the two sides of the $\text{rGO}_{\text{EDA}}\text{-COF}_{\text{Oct}}$ film. In particular, the mentioned value of sheet resistance could be reproducibly measured over different batches of the material for the bottom side of the film (the side that was in contact with the substrate during synthesis). In contrast, the top side of the film (in contact with the air and the solvent vapors during the synthesis) always showed a sheet resistance beyond the instrumental limits. These results suggested an asymmetrical distribution of rGO_{EDA} in the COF_{Oct} matrix with a higher concentration on the bottom side of the film, which could have originated during the film drying-polymerization process. However, the presence of a concentration gradient was not obvious in the preliminary cross-sectional SEM analysis (**Figure 5.8**), and extra morphological characterization is needed to duly confirm this hypothesis.

To further examine the electrical properties of the composite films, a two-terminal device was prepared and tested. The film was cut into a rectangular shape (approximately 10×20 mm), and the two extremities were contacted with silver paste and copper wires on the conductive side (**Figure 5.15b**). The device exhibited a perfectly linear current response in the -0.1 - $+0.1$ V voltage interval, indicating the Ohmic character of the contacts. From the slope of the I-V curve, a conductivity of approximately $\sigma = 0.16 \text{ S m}^{-1}$ was calculated according to the following equation:

$$\sigma = \frac{\partial I / \partial V \cdot L}{W \cdot t}$$

where $\partial I / \partial V$ is the slope of the I-V curve, t is the thickness of the film ($50 \mu\text{m}$), L is the channel length (20 mm), and W is the channel width (10 mm). The calculated value matched the conductivity obtained from the FPP measurements and further confirmed the successful reduction of the GO_{EDA} nanofiller.

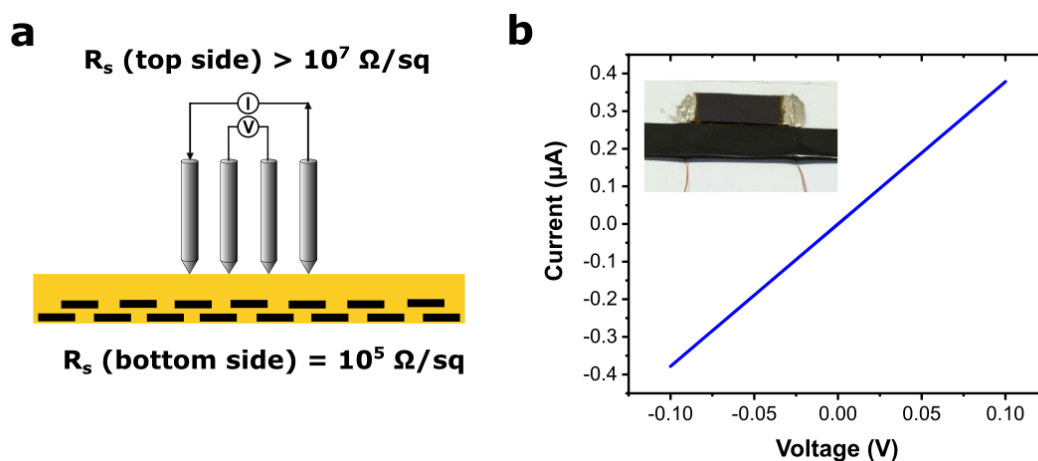


Figure 5.15 (a) Scheme of the four-point probe measurement of the sheet resistance on the two sides of the film. (b) I-V curve measured for the film on a two-terminal configuration. Inset: photograph of the two-terminal device obtained by contacting the material with silver paste and copper wires.

The conductive, self-standing, flexible, light, and porous structure of the $\text{rGO}_{\text{EDA}}\text{-COF}_{\text{Oct}}$ film makes it promising for several applications, ranging from energy storage to chemical and mechanical sensing. In the next section of this chapter, we show how, by taking advantage of the asymmetrically conductive nature of the film, the material could be exploited for the construction of a wearable strain sensor.

5.4. Strain sensing

Wearable strain sensors are becoming increasingly important for measuring the deformation or strain of materials under various mechanical stimuli. These sensors play a critical role in a wide range of applications, including health monitoring, biomedical devices, and robotics.^[296,297] Various sensing mechanisms can be exploited for strain sensing, such as changes in the resistive, capacitive, or optical properties of the sensor upon deformation. The development of new low-dimensional materials such as inorganic nanomaterials, carbon-based nanomaterials, and polymers as single components or composites has broadened the possibilities for the design of sensors with high sensitivity, durability, flexibility, and low weight.^[298,299] However, complex fabrication processes and poor structural material stability, which are often associated with nanomaterial-based sensors, constitute important challenges to address.^[300] Therefore, there is a great demand for the development of new types of strain sensors that can overcome these limitations and offer high performance and functionality coupled with convenient fabrication processes.

In this section, a proof of concept is proposed for the potential application of the **rGO_{EDA}-COF_{Oct}** composite material as a wearable piezoresistive strain sensor. To the best of our knowledge, this is the first report of a strain sensor in which a COF-based active material is applied.

The **rGO_{EDA}-COF_{Oct}** composite has significant advantages owing to its simple architecture and fabrication process. In fact, the device simply consisted of the self-standing film, where contacts on the conductive side were obtained with silver paste and copper wires to achieve a horizontal junction of the device with a channel width of approximately 1 cm (**Figure 5.16a**). Due to the flexibility and the robustness of the **COF_{Oct}** matrix, the device did not require any additional supporting material, which is typically needed to both support the active material and guarantee its structural integrity upon operation of the device.^[131]

For a simple proof-of-concept test, the prepared device was secured to the wrist, ensuring that it was flat when the wrist was in the resting position (**Figure 5.16b**). The copper wires were connected to a source meter to apply potential and monitor the current passing through the device at any time. Subsequently, tensile and compressive strains were applied by alternatively bending the wrist upward and downwards (**Figure 5.16c, d**).

Figure 5.16e shows the current output under 1 V bias, from a sequence of compression-tension bending cycles, initially at a low frequency and with small movements, and then at a high frequency with larger movements. The sensor showed a fast response (below 100 ms)

to the dynamic movement in both the compressive and tensile phases; in particular, the current increased under the compressive strain and decreased under the tensile strain. The change in the output current upon deformation was attributed to a variation in the material resistivity, consistently with a piezoresistive mechanism.^[301] According to this mechanism, when the material is compressed, the contact between the adjacent conductive **rGO** sheets increases, and the electrical resistivity decreases. On the contrary, when the material was stretched, the overlap between the **rGO** sheets decreased, and thus the resistivity increased.^[302] The higher current variations recorded in response to larger movements of the wrist suggested a good sensitivity of the system.

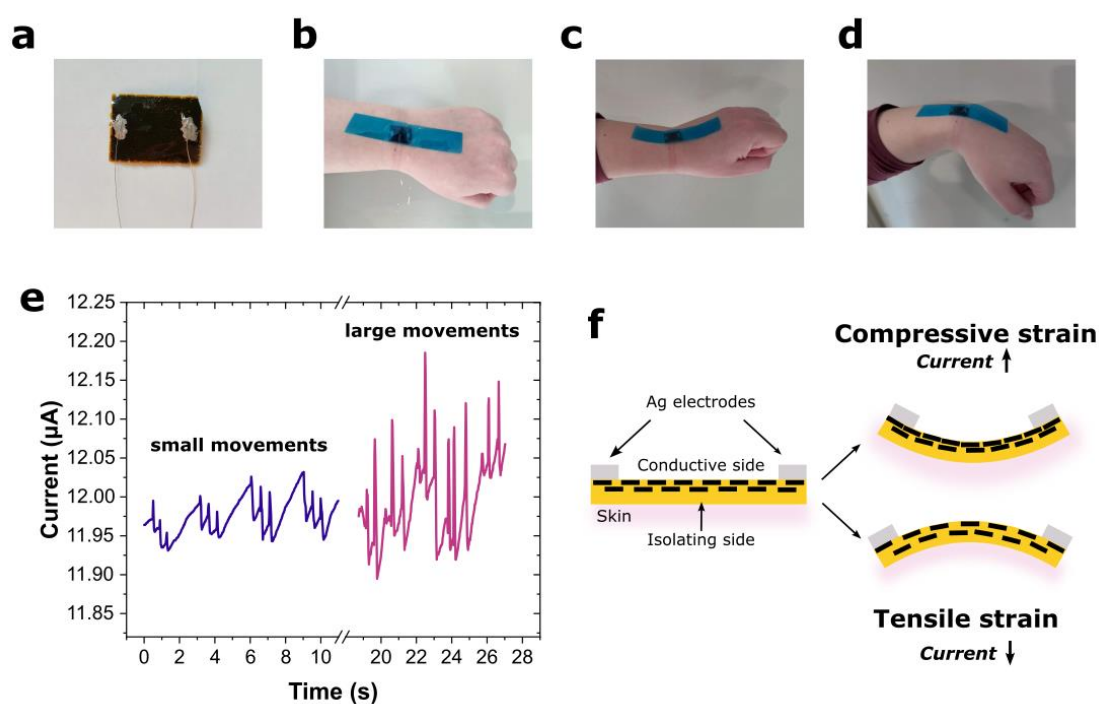


Figure 5.16 (a) Photograph of the sensing device. (b) Device applied to the wrist, using adhesive tape. (c, d) Upward and downward wrist movements. (e) Current output during periodic wrist bending, initially at low frequency and with small movements, and then at high frequency with large movements (Bias = 1 V). (f) Illustration of the compressive and tensile strains generated upon wrist bending with associated structural and resistivity changes in the **rGO_{EDA}-COF_{oct}** composite.

The performance of the sensor was quantified through the gauge factor (GF), which is a measure of the change in resistance upon deformation, according to the following equation:^[301,303]

$$GF = \frac{\Delta R/R_0}{\varepsilon}$$

where $\Delta R/R_0$ is the relative resistance variation and ε is the applied strain. Controlled

compressive deformations were applied to the sensor and the corresponding strain ε was calculated according to the following equation:^[131]

$$\varepsilon = \frac{t}{2r}$$

where t is the thickness of the film (in this case, $t = 50 \mu\text{m}$) and r is the bending radius of the device during the measurements (**Figure 5.17a**, rigid plastic frames, with a defined r were used). As shown in **Figure 5.17b**, under the experimental conditions of our tests, the relative resistance variation showed a linear variation with strain in the range of 0 % - 0.5 % with an extrapolated gauge factor of 11.5. This value of gauge factor is comparable to the literature values reported for other rGO-based sensors.^[297,303]

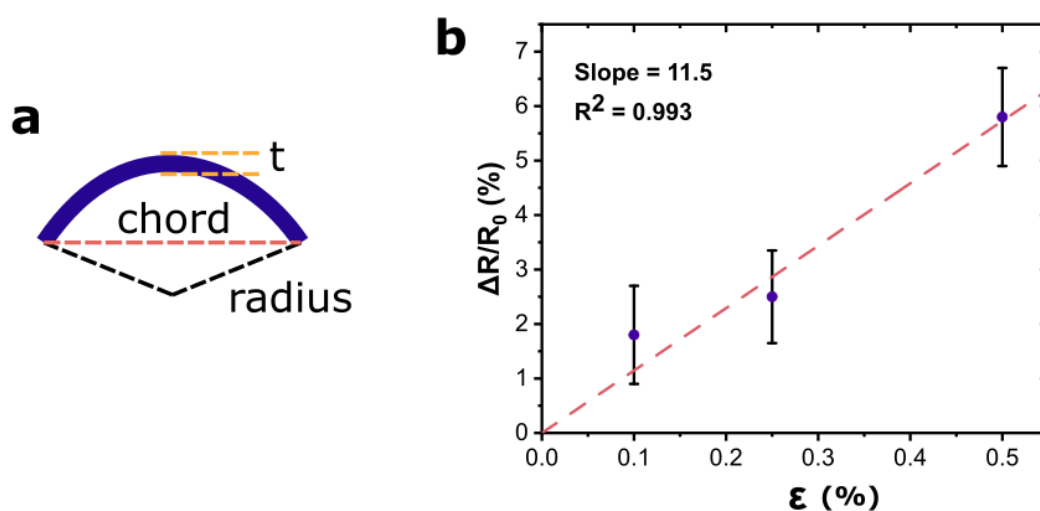


Figure 5.17 (a) Schematic of deformation geometry and extrapolation of relevant parameters for strain calculation. **(b)** Relative resistance changes as a function of the applied strain.

5.5. Conclusion and Perspectives

In conclusion, in this chapter we reported the synthesis, the characterization and the application of a novel **rGO-COF** composite as self-standing film. We showed how the combination of an amine-functionalized GO and octyloxy-functionalized polyimine in strong acid media could lead to an optimal compatibilization of the two nanostructured materials. The polymer solution casting method was used to process the material obtaining a film of **GO_{EDA}-PI_{mOct}** with thickness of about $50 \mu\text{m}$, that after recrystallization and thermal annealing yielded a conductive composite film of **rGO_{EDA}-COF_{Oct}**.

Interestingly, the films obtained with 4 % wt loading of **GO_{EDA}** displayed an asymmetry of

the conductive properties, with one side of the film showing a sheet resistance of $R_s = 1.3 \times 10^5 \Omega \text{ sq}^{-1}$ and the other one being electrically insulating. The origin of the anisotropic electrical properties has not been fully established yet, but further investigations are underway. However, it is reasonable to presume that during the synthesis, the capillary forces acting on the drying material could cause a gradient in the distribution of the GO nanofiller, which an excess of material on the bottom side of the film.

The asymmetrically conductive nature, in conjunction with the mechanical flexibility and robustness of the composite, endowed the material with interesting properties that could be harnessed for flexible electronics and for smart sensing materials. In particular, we demonstrate that the films could be directly used as piezoresistive strain sensors, as their intrinsic resistivity is proportionally increasing or decreasing depending on the type and the magnitude of the stress applied (compressive or tensile).

The next developments in this project include the preparation of rGO-COF composites with different relative amounts of GO-based nanofiller to investigate the effect of the composition on the structural, mechanical, and electrical properties of the film. Moreover, we are interested in the expansion of the scope of the possible COFs that could be efficiently modified with GO with this method. COFs with high porosity and specific chemical functionalities, able to interact with target molecules, could in fact be very appealing for the implementation of the material as chemical sensor. However, the development in this direction could be limited by the necessity of an octyloxy-functionalized backbone for an adequate compatibilization of the polymer with GO. To circumvent this problem, we began to develop a series of multicomponent 2D COF, using TPB as knot and complementary mixtures of MeOTP and OctOTP with different ratios as linkers. Having the same geometry and the same reactivity is expected that both monomers will be included in the backbone of the 2D COF with statistic distribution.^[304,305] Preliminary experiments were carried out by preparing **TPB-MeOTP_{0.95}-OctOTP_{0.05}**, **TPB-MeOTP_{0.80}-OctOTP_{0.20}**, and **TPB-MeOTP_{0.50}-OctOTP_{0.50}**, by means of the solvothermal method. This more established synthetic method was selected for the preliminary experiments, as it yields isotropic COF powders which are easier to characterize by PXRD due to the absence of preferred orientation effects. The PXRD analysis of the materials (**Figure 5.18**) revealed a gradual transition in the scattering pattern by increasing the amount of OctOTP in the framework, from the pure **TPB-MeOTP (COF_{Me})** to the pure **TPB-OctOTP (COF_{Oct})**. These results indicate the homogenous inclusion of the two monomers in the COFs and paves the way to a possible expansion to further aldehydes with specific functionalities.

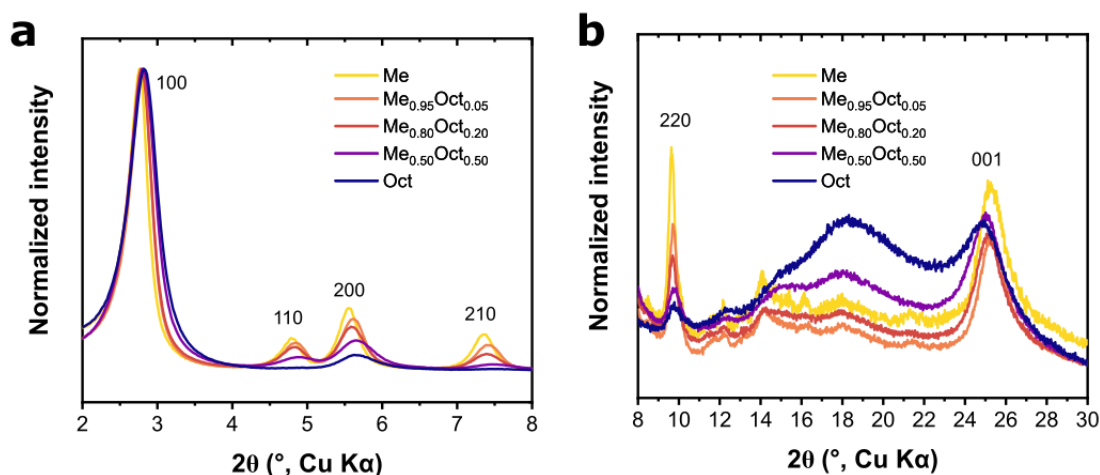


Figure 5.18 PXRD pattern of the series of TPB-MeOTP_x-OctOTP_{1-x} COFs synthesized by solvothermal method: **(a)** low angle window, **(b)** high angle window.

In our vision, this multicomponent COF strategy could be extended to the synthesis of the rGO-COF composite films prepared by polymer solution casting. The introduction MeOTP might allow us to endow the COF matrix with different properties, while retaining the good compatibility achieved by the presence of the octyloxy chains. For example, it is expected that the different MeOTP / OctOTP ratios would lead to a tunable average pore size and surface area.^[295] Moreover, the replacement of MeOTP in the three-components COF with a linker molecule carrying propargyl [HC≡C-CH₂-] side chains such as 2,5-bis(2-propynyloxy) terephthalaldehyde could enable the introduction of new functionalities in the channel walls via post-synthetic functionalization (for example, by azide-alkyne cycloaddition).^[32]

5.6. Experimental section

Materials

All reagents were purchased from commercial sources such as Sigma-Aldrich, TCI, abcr, BLD Pharm, FluoroChem and were used as received. Solvents were purchased from commercial sources such as Carlo Erba, Fischer Scientific, Carl Roth, Acros and used without any further purification. Deionized water was used in all the preparations. Graphene oxide (GO, 4 mg mL⁻¹, monolayer content > 95 %) was purchased from Graphenea). Silicon substrates were purchased from Fraunhofer and were directly used after rinsing with MeOH and drying with nitrogen flux.

Synthesis of GO_{EDA}

A solution of EDA (330 mg) in 30 mL ethanol was added to a solution of GO (230 mg) in

ethanol (50 mL) for 1 hour at room temperature. The reaction mixture was stirred for 16 hours at room temperature, and the crude reaction mixture was centrifugated (10000 rpm for 20 min) to remove the supernatant. The precipitate was washed with ethanol (3 × 50 mL), acetone (3 × 50 mL), and water (1 × 50 ML) to remove the excess EDA. The product was then dried for 24 h in a freeze-dryer.^[293]

Preparation of the **PIm** solutions and **GO-PIm** suspensions

Concentrated stock solutions of the monomers were prepared by dissolving the respective solids in a mixture of water and TFA. The monomer solutions were then mixed in equimolar ratio at room temperature to produce the **PIm** solutions.

In a typical reaction, [TPB] = 100 mM ($C_0 = 300$ mM) was prepared by dissolving in 35.1 mg of TPB (0.10 mmol) in 1 ml of 5 % water-TFA (v/v), and [OctOTP] = 150 mM ($C_0 = 300$ mM) was prepared by dissolving in 58.6 mg of MeOTP (0.15 mmol) in 1 ml of 5 % water-TFA (v/v). Then, 2 ml of $C_0 = 150$ mM **PIm**_{oct} solution was prepared by transferring 1 ml of each monomer solution in a 5 ml vial and mixing by gentle shaking. Upon mixing, the solution rapidly changed color from yellow to bright red, and the viscosity was greatly increased. Before further processing, an equilibration time of 15 minutes was maintained.

The same procedure was followed for the preparation of the **PIm**_{Me} solutions at $C_0 = 150$ mM, using [MeOTP] = 150 mM ($C_0 = 300$ mM) as the aldehyde solution. This solution was prepared by dissolving 29.1 mg of MeOTP (0.15 mmol) in 1 ml of 5 % water-TFA (v/v).

To prepare the **GO**_(EDA)-**PIm** suspensions, 4 mg of **GO** or **GO**_{EDA} were added to 2 ml of the **PIm** suspension (2 mg ml⁻¹). The mixture was then ultrasonicated (Cup Horn sonicator, 200 W) for 30 min to obtain a homogenous dispersion.

Procedure for the preparation of the composite films

A 15 × 15 mm² silicon (or, alternatively, a 15 × 20 mm² quartz) substrate was placed in a $\Phi = 5$ cm, $h = 1$ cm petri dish. The Petri dish was positioned on a 40 °C preheated hotplate, ensuring that the surface was horizontal by means of a bubble level. The films were prepared by carefully casting 0.15 ml of **PIm** / **GO**_(EDA)-**PIm** solution / suspension (0.20 ml for the quartz substrate) onto the surface of the substrate. After the deposition, the Petri dish was quickly covered with the complementary glass cover. The film was left to dry on the surface for 4 hours, resulting in a smooth gold reflective coating. Then, the cover was removed, and the substrate was quickly immersed in MeOH, which caused the delamination of the film from the surface and a change in color to dark red. The self-standing film was then picked up with tweezers and transferred to a 10% TEA-MeOH (v/v) solution, inducing the neutralization of the adsorbed TFA, as evidenced by the rapid color change to bright yellow. The film was then Soxhlet extracted with THF for 12 hours to remove the low-molecular-weight oligomers. THF was exchanged three times with *n*-pentane, a solvent with low surface tension (15.5 mN m⁻¹), and then dried in air. The drying process was carefully carried out by suspending the film to favor the even evaporation of the solvent from both sides and avoid warping deformations. After 1 hour most of the solvent evaporated and the film was transferred in a vacuum oven and the volatile residues of solvents were removed at 50 °C for 12 hours under reduced pressure.

Procedure for the preparation of the multicomponent COFs

The multicomponent COF powders were prepared by solvothermal synthesis. 70.3 mg of TPB (0.20 mmol) and 58.3 mg of MeOTP (0.30 mmol) were dissolved in 4 ml of 1,4-dioxane / mesitylene mixture (4 : 1) on a 20 ml microwave vial. 1 ml of 6 M HOAc was then added as a catalyst, the vial was sealed and heated at 70 °C for 4 hours. At the end of the reaction the solid obtained was filtered and washed with MeOH, then Soxhlet extracted with THF for 12 hours to remove the trapped oligomers. Finally, the powder was activated by evaporation of the solvent at room temperature followed by 12 hours in the vacuum oven at 80 °C. For the synthesis of the multicomponent COFs a complementary mixture of MeOTP and OctOTP was used instead of the sole MeOTP. All the COFs were obtained as bright yellow powder with a minimum yield of 90 %.

Strain sensor characterization

Electrical characterization was performed using a source meter (Keithley 2635 B System Source Meter) controlled by LabTracer 2.0. A potential of 1V was applied to the sensor. To calculate the gauge factor, three different devices were prepared, and the relative resistance change was measured as a function of strain.

6. Conclusion and outlook

In this thesis, the main objective was to develop functional 2D COFs-based materials with tailored physico-chemical properties and to characterize them at multiple length scales for their integration as active materials in sensing, electronic, and energy storage devices. The primary focus was on the preparation of materials in the film morphology as this form is ideal for the investigation of their properties. Additionally, the development of films with large lateral size and presenting oriented crystallites, is essential to improve the integration and performance of 2D COFs in applications such as filtration membranes, energy storage, and optoelectronics.

In each experimental chapter of the thesis, a single or a family of 2D COF-based materials are designed for a specific application, synthesized in the film morphology, and characterized. Each experimental chapter was designed to address one of the following challenges: 1. development of a new technique for solution processing to achieve specific morphology and orientation; 2. design of a conjugated 2D COF with semiconductor properties; 3. preparation of a composite rGO-COF materials for flexible electronics.

2D COFs are completely inert to conventional organic solvents, rendering them insoluble and non-processable once synthesized, analogously to thermosetting polymers. As such, precise control of the morphology during synthesis is crucial. In **Chapter 3** we introduced an innovative method for preparing large-area, self-standing, mechanically robust, and structurally oriented 2D COF films. Initially, we investigated the reaction between TPB and MeOTP. By utilizing a reaction solvent consisting of a water-TFA mixture, we were able to produce a soluble polyimine at ambient temperature. The method comprises two main steps. First, we created a layered and highly oriented polyimine film using solution-cast polymerization, which exhibited minimal crystallinity and porosity. Following this, we established a procedure for the recrystallization of the polyimine film into a porous and crystalline 2D COF while preserving the overall alignment of the crystallites.

In addition, this chapter elucidates the mechanistic details related to the transition from solution to solid. A thermodynamic analysis revealed that the polymerization process led to a reversible sol-gel transition via a step-growth mechanism upon increasing the concentration or decreasing the temperature. As a droplet of the solution dried on a surface, the increase in concentration induced the gel formation, while the evaporation of the solvent generated outward tensile stress that promoted the alignment of the polymeric segments in the direction of the force field. Furthermore, we showed that a slow rate of evaporation

gave rise to the nucleation and growth of polymer particles, indicating that the stretched 3D polymer network constituted a kinetic product. Collectively, the mechanistic exploration underscored the profound impact of the history of the material on its ultimate morphology.

Finally, we have successfully demonstrated the adaptability of our synthetic procedure in the fabrication of self-supporting, oriented imine-linked 2D COF films with diverse 2D topologies. Specifically, in addition to TPB-MeOTP-COF, we have also utilized this methodology for the preparation of TPPy-MeOTP-COF, which features pyrene-based building blocks as the amine knot. This expansion of our method to other imine-linked 2D COFs highlights the broad applicability and flexibility of our protocol, emphasizing its potential for widespread implementation.

The short-term developments of this project will be focused on the exploration of the scope of the methodology by investigating the formation of films with various amine knots, and different aldehyde linkers. In these regards, preliminary experiments have revealed that the functionalization of the 2,5 positions of terephthalaldehyde with and alkoxy groups is critical to achieve high degrees of polymerization in the water-TFA mixtures. We speculate that this behavior could be ascribed to the stabilization of the protonated imine bond via intermolecular hydrogen bonding. To prove this hypothesis, terephthalaldehyde could be functionalized with a different hydrogen bond acceptor at the 2,5 positions, such as the methyl thiolate group.

On a long-term perspective, the developments of this project should aim at the investigation of the anisotropy-related properties the properties of the oriented films. From an application standpoint, highly oriented, mechanically robust, and self-standing 2D COF films offer a unique opportunity to investigate the intrinsically anisotropic properties of 2D COFs. The 1D pore channels are perpendicular to the film plane, and we anticipate that this structural feature, coupled with the morphological continuity and mechanical stability of the film, could be exploited for various gas or liquid phase molecular or ion separation applications. Moreover, by extending the method to include electroactive monomers, conductive and oriented 2D COFs could be synthesized, enabling the study of in-plane and out-of-plane charge transport properties of the material.

The incorporation of (photo)electroactive building blocks into 2D COFs, along with their extended in-plane conjugation and out-of-plane columnar stacking, makes them promising candidates for use as active materials in (opto)electronics, such as light-emitting devices, photoconductive devices, solar cells, and field-effect transistors. In **Chapter 4**, a novel imine-linked 2D COF was designed and synthesized to include the electron-rich BTA and TT moie-

ties in its polymeric backbone, then its optoelectronic properties were investigated for use as an active material in FET and EES devices. The solvothermal synthesis of a 2D COF resulted in an insoluble powder material with high crystallinity, a Kagome-type topology, and an eclipsed AA stacking arrangement. However, the powder material was not suitable for studying charge transport properties. Thin films of about 90 nm were fabricated by direct growth in solvothermal conditions, immersing the designed substrate in the reaction mixture. When integrated into a two-terminal device, the film displayed p-type semiconductor behavior with a valence band edge at - 5.1 eV, a conduction band edge at - 3.0 eV, and an optical band gap of 2.1 eV. The film exhibited an electrical conductivity of $\sigma = 4 \times 10^{-11} \text{ S m}^{-1}$ in vacuum and $\sigma = 3 \times 10^{-6} \text{ S m}^{-1}$ after 20 hours in air. This increase was attributed to the tendency of the material to interact with O_2 , which induced the p-doping of the materials over time. However, this increase was followed by a decline of the charge transport performance upon longer exposure, likely due to irreversible (photo)oxidation reactions that degrade the material. The conductivity of the pristine film could also be increased by infiltrating small molecules with strong electron-acceptor properties, such as F_4TCNQ reaching values up to $\sigma = 2 \times 10^{-4} \text{ S m}^{-1}$.

Additionally, as a proof-of-concept, the thin film was utilized as the active channel in a water-gated OFET. The device exhibited a threshold voltage of -0.4 V and three orders of magnitude of current modulation. However, the device demonstrated a considerably low value of μC_v , which was ascribed to the low hole mobility within the COF layer as well as other potentially harmful effects arising from exposure of the device to both water and oxygen.

The powder material was employed as an active electrodic material in a symmetric pseudocapacitor exhibiting a satisfactory specific capacitance of 108 F g^{-1} at 0.1 A g^{-1} , which is consistent with values reported in the literature for other electroactive 2D COFs. However, the device showed a significant decrease in performance at higher current density, and the voltammetric characterization revealed a problem with the reversibility of the redox reactions under the experimental conditions. Taken together, these findings demonstrate both the potential and the limitations of electron-rich COFs, such as BTA-TT-COF, for the development of high-performance materials for pseudocapacitors.

This study highlights the importance of careful measurement of the intrinsic conductivity of electron-rich 2D COFs, as their values may vary considerably depending on the exposure time to the atmospheric environment. We anticipate that this study will encourage further research into the impact on charge transport properties of guest species in the pores of 2D COFs, particularly in the case of oxygen. The proof-of-concept application in a liquid-

gated OFET demonstrated that this type of device may be optimal for exploiting the potential of 2D COFs in electronics, given their unique porous structure. The short-term developments in this direction involve the use of a water-free liquid dielectric (such as an ionic liquid) and operating the device in inert atmosphere to avoid parasitic reactions with oxygen or water. The proof-of-concept application as active electrode material in pseudocapacitor devices confirmed that the material is electrochemically unstable. Further short-term advancements in this direction aim to address the irreversibility issue of the redox reactions by interfacing the 2D COF with the appropriate materials (electrolyte salt, solvent, conductive carbon, binder) and assembling the cell in a water and oxygen-free environment (glovebox) to ensure that these species do not interfere with the Faradaic processes at the electrodes.

On a longer-term perspective, research efforts should be dedicated towards devising new strategies for improving the poor intrinsic conductivities of conjugated 2D COFs. In particular, growing materials with larger single crystalline domains is crucial to reduce the impact of the lattice defects on the (opto)electronic properties.

In **Chapter 5**, we show the synthesis, characterization, and investigation of a potential application of a novel conductive composite material in the film morphology consisting of conductive rGO and a non-conductive 2D COF. The polymer solution casting method was employed to process the mixed materials and obtain a film with a thickness of approximately 50 μm . The combination of an amine-functionalized GO and octyloxy-functionalized polyimine as precursors was found to lead to an optimal compatibilization of the two nanostructured materials. Subsequently, recrystallization and thermal annealing were carried out to produce a conductive composite film. Remarkably, the films, which contained 4 % wt of GO_{EDA} , exhibited an asymmetry in their conductive properties, with one side of the film exhibiting a sheet resistance of $R_s = 1.3 \times 10^5 \Omega \text{sq}^{-1}$, while the other side was electrically insulating. This feature, coupled with the mechanical flexibility and durability, made the material suitable for flexible electronics. Specifically, we showed that the films could serve as piezoresistive strain sensors, as their inherent resistivity varies in proportion to the type and intensity of the stress applied (compressive or tensile).

In the short term, the future developments of this project involve synthesizing rGO-COF composites with varying amounts of GO nanofiller to explore the impact of composition on the structural, mechanical, and electrical properties of the film.

On a long-term perspective, we plan to expand the range of 2D COFs that could be effectively modified with GO using this method, with a particular focus on multicomponent 2D COFs that can introduce specific chemical functionalities to interact with target mole-

cules and potentially serve as chemical sensors. Furthermore, we anticipate that this study will motivate further investigations into the origin of the anisotropic electrical properties of the composite, which have yet to be fully elucidated.

In conclusion, this thesis attempted to tackle some open challenges in the fabrication of 2D COF films with customized structure and electrical properties. Our results bring a new perspective on the design and the construction of these materials. In particular, we believe that that our findings will serve as a reliable point of reference for researchers who are exploring new synthetic approaches and innovative designs for functional 2D COFs.

7. References

- [1] H.-G. Elias, *An Introduction to Polymer Science*, VCH, Weinheim, **2005**.
- [2] A. M. Evans, M. J. Strauss, A. R. Corcos, Z. Hirani, W. Ji, L. S. Hamachi, X. Aguilar-Enriquez, A. D. Chavez, B. J. Smith, W. R. Dichtel, *Chem. Rev.* **2022**, *122*, 442–564.
- [3] A. P. Côté, A. I. Benin, N. W. Ockwig, M. O’Keeffe, A. J. Matzger, O. M. Yaghi, *Science* **2005**, *310*, 1166–1170.
- [4] K. Geng, T. He, R. Liu, S. Dalapati, K. T. Tan, Z. Li, S. Tao, Y. Gong, Q. Jiang, D. Jiang, *Chem. Rev.* **2020**, *120*, 8814–8933.
- [5] O. M. Yaghi, M. J. Kalmutzki, C. S. Diercks, *Introduction to Reticular Chemistry: Metal-Organic Frameworks and Covalent Organic Frameworks*, Wiley, **2019**.
- [6] F. Haase, B. V. Lotsch, *Chem. Soc. Rev.* **2020**, *49*, 8469–8500.
- [7] H. Wang, Z. Zeng, P. Xu, L. Li, G. Zeng, R. Xiao, Z. Tang, D. Huang, L. Tang, C. Lai, D. Jiang, Y. Liu, H. Yi, L. Qin, S. Ye, X. Ren, W. Tang, *Chem. Soc. Rev.* **2019**, *48*, 488–516.
- [8] N. Keller, T. Bein, *Chem. Soc. Rev.* **2021**, *50*, 1813–1845.
- [9] S. Karak, K. Dey, R. Banerjee, *Adv. Mater.* **2022**, *34*, 2202751.
- [10] D. W. Burke, C. Sun, I. Castano, N. C. Flanders, A. M. Evans, E. Vitaku, D. C. McLeod, R. H. Lambeth, L. X. Chen, N. C. Gianneschi, W. R. Dichtel, *Angew. Chem. Int. Ed.* **2020**, *59*, 5165–5171.
- [11] M. G. Barnes, D. C. McLeod, R. H. Lambeth, *ACS Appl. Polym. Mater.* **2022**, *4*, 2017–2021.
- [12] H.-J. Yen, G.-S. Liou, *Polym. Chem.* **2018**, *9*, 3001–3018.
- [13] J. M. Rotter, R. Guntermann, M. Auth, A. Mähringer, A. Sperlich, V. Dyakonov, D. D. Medina, T. Bein, *Chem. Sci.* **2020**, *11*, 12843–12853.
- [14] M. T. Fontana, D. A. Stanfield, D. T. Scholes, K. J. Winchell, S. H. Tolbert, B. J. Schwartz, *J. Phys. Chem. C* **2019**, *123*, 22711–22724.
- [15] J. Li, X. Jing, Q. Li, S. Li, X. Gao, X. Feng, B. Wang, *Chem. Soc. Rev.* **2020**, *49*, 3565–3604.
- [16] Y. Liu, W. Zhou, W. L. Teo, K. Wang, L. Zhang, Y. Zeng, Y. Zhao, *Chem* **2020**, *6*, 3172–3202.
- [17] R. Freund, O. Zaremba, G. Arnauts, R. Ameloot, G. Skorupskii, M. Dincă, A. Bavykina, J. Gascon, A. Ejsmont, J. Goscianska, M. Kalmutzki, U. Lächelt, E. Ploetz, C. S. Diercks, S. Wuttke, *Angew. Chem. Int. Ed.* **2021**, *60*, 23975–24001.
- [18] A. M. Evans, L. R. Parent, N. C. Flanders, R. P. Bisbey, E. Vitaku, M. S. Kirschner, R. D. Schaller, L. X. Chen, N. C. Gianneschi, W. R. Dichtel, *Science* **2018**, *361*, 52–57.
- [19] H.-G. Elias, *Macromolecules. 3: Physical Structures and Properties*, Wiley-VCH, Weinheim, **2008**.
- [20] R. C. Thompson, S. H. Swan, C. J. Moore, F. S. Vom Saal, *Philos. Trans. R. Soc. B Biol. Sci.* **2009**, *364*, 1973–1976.
- [21] D. Crespy, M. Bozonnet, M. Meier, *Angew. Chem. Int. Ed.* **2008**, *47*, 3322–3328.
- [22] H. Staudinger, *Berichte Dtsch. Chem. Ges. B Ser.* **1920**, *53*, 1073–1085.

- [23] W. H. Carothers, *Trans. Faraday Soc.* **1936**, *32*, 39.
- [24] W. Kaminsky, Ed. , *Polyolefins: 50 Years after Ziegler and Natta I: Polyethylene and Polypropylene*, Springer Berlin Heidelberg, Berlin, Heidelberg, **2013**.
- [25] Y. Xu, S. Jin, H. Xu, A. Nagai, D. Jiang, *Chem. Soc. Rev.* **2013**, *42*, 8012.
- [26] J. S. M. Lee, A. I. Cooper, *Chem. Rev.* **2020**, *120*, 2171–2214.
- [27] H. M. El-Kaderi, J. R. Hunt, J. L. Mendoza-Cortés, A. P. Côté, R. E. Taylor, M. O’Keeffe, O. M. Yaghi, *Science* **2007**, *316*, 268–272.
- [28] L. Frey, J. J. Jarju, L. M. Salonen, D. D. Medina, *New J. Chem.* **2021**, *45*, 14879–14907.
- [29] A. M. Evans, I. Castano, A. Brumberg, L. R. Parent, A. R. Corcos, R. L. Li, N. C. Flanders, D. J. Gosztola, N. C. Gianneschi, R. D. Schaller, W. R. Dichtel, *J. Am. Chem. Soc.* **2019**, *141*, 19728–19735.
- [30] F. J. Uribe-Romo, J. R. Hunt, H. Furukawa, C. Klöck, M. O’Keeffe, O. M. Yaghi, *J. Am. Chem. Soc.* **2009**, *131*, 4570–4571.
- [31] S. Y. Ding, J. Gao, Q. Wang, Y. Zhang, W. G. Song, C. Y. Su, W. Wang, *J. Am. Chem. Soc.* **2011**, *133*, 19816–19822.
- [32] H. Xu, J. Gao, D. Jiang, *Nat. Chem.* **2015**, *7*, 905–912.
- [33] F. J. Uribe-Romo, C. J. Doonan, H. Furukawa, K. Oisaki, O. M. Yaghi, *J. Am. Chem. Soc.* **2011**, *133*, 11478–11481.
- [34] S. Dalapati, S. Jin, J. Gao, Y. Xu, A. Nagai, D. Jiang, *J. Am. Chem. Soc.* **2013**, *135*, 17310–17313.
- [35] A. Nagai, X. Chen, X. Feng, X. Ding, Z. Guo, D. Jiang, *Angew. Chem. Int. Ed.* **2013**, *52*, 3770–3774.
- [36] S. Kandambeth, A. Mallick, B. Lukose, M. V. Mane, T. Heine, R. Banerjee, *J. Am. Chem. Soc.* **2012**, *134*, 19524–19527.
- [37] E. Vitaku, C. N. Gannett, K. L. Carpenter, L. Shen, H. D. Abruña, W. R. Dichtel, *J. Am. Chem. Soc.* **2020**, *142*, 16–20.
- [38] D. A. Pyles, J. W. Crowe, L. A. Baldwin, P. L. McGrier, *ACS Macro Lett.* **2016**, *5*, 1055–1058.
- [39] L.-H. Li, X.-L. Feng, X.-H. Cui, Y.-X. Ma, S.-Y. Ding, W. Wang, *J. Am. Chem. Soc.* **2017**, *139*, 6042–6045.
- [40] S.-Y. Jiang, S.-X. Gan, X. Zhang, H. Li, Q.-Y. Qi, F.-Z. Cui, J. Lu, X. Zhao, *J. Am. Chem. Soc.* **2019**, *141*, 14981–14986.
- [41] C. Qian, L. Feng, W. L. Teo, J. Liu, W. Zhou, D. Wang, Y. Zhao, *Nat. Rev. Chem.* **2022**, *6*, 881–898.
- [42] B. J. Smith, A. C. Overholts, N. Hwang, W. R. Dichtel, *Chem. Commun.* **2016**, *52*, 3690–3693.
- [43] P. Kuhn, M. Antonietti, A. Thomas, *Angew. Chem. Int. Ed.* **2008**, *47*, 3450–3453.
- [44] K. T. Jackson, T. E. Reich, H. M. El-Kaderi, *Chem. Commun.* **2012**, *48*, 8823.
- [45] Q. Fang, Z. Zhuang, S. Gu, R. B. Kaspar, J. Zheng, J. Wang, S. Qiu, Y. Yan, *Nat. Commun.* **2014**, *5*, 4503.
- [46] G. Das, T. Skorjanc, S. K. Sharma, F. Gándara, M. Lusi, D. S. Shankar Rao, S. Vimala, S. Krishna Prasad, J. Raya, D. S. Han, R. Jagannathan, J.-C. Olsen, A. Trabolsi, *J. Am. Chem. Soc.* **2017**, *139*, 9558–9565.
- [47] X. Zhuang, W. Zhao, F. Zhang, Y. Cao, F. Liu, S. Bi, X. Feng, *Polym. Chem.* **2016**, *7*, 4176–4181.

- [48] H. L. Qian, F. L. Meng, C. X. Yang, X. P. Yan, *Angew. Chem. Int. Ed.* **2020**, *59*, 17607–17613.
- [49] W. J. Ong, T. M. Swager, *Nat. Chem.* **2018**, *10*, 1023–1030.
- [50] B. Zhang, M. Wei, H. Mao, X. Pei, S. A. Alshimmri, J. A. Reimer, O. M. Yaghi, *J. Am. Chem. Soc.* **2018**, *140*, 12715–12719.
- [51] X. Li, C. Zhang, S. Cai, X. Lei, V. Altoe, F. Hong, J. J. Urban, J. Ciston, E. M. Chan, Y. Liu, *Nat. Commun.* **2018**, *9*, 1–8.
- [52] A. M. Evans, M. R. Ryder, W. Ji, M. J. Strauss, A. Corcos, E. Vitaku, N. C. Flanders, R. P. Bisbey, W. Dichtel, *Faraday Discuss.* **2020**, *34*, 240–241.
- [53] S. Kandambeth, K. Dey, R. Banerjee, *J. Am. Chem. Soc.* **2019**, *141*, 1807–1822.
- [54] Z. Meng, A. Aykanat, K. A. Mirica, *Chem. Mater.* **2019**, *31*, 819–825.
- [55] M. D. Allendorf, R. Dong, X. Feng, S. Kaskel, D. Matoga, V. Stavila, *Chem. Rev.* **2020**, *60*.
- [56] S. Thomas, H. Li, C. Zhong, M. Matsumoto, W. R. Dichtel, J. L. Bredas, *Chem. Mater.* **2019**, *31*, 3051–3065.
- [57] E. Jin, M. Asada, Q. Xu, S. Dalapati, M. A. Addicoat, M. A. Brady, H. Xu, T. Nakamura, T. Heine, Q. Chen, D. Jiang, *Science* **2017**, *357*, 673–676.
- [58] S. Xu, H. Sun, M. Addicoat, B. P. Biswal, F. He, S. Park, S. Paasch, T. Zhang, W. Sheng, E. Brunner, Y. Hou, M. Richter, X. Feng, *Adv. Mater.* **2020**, DOI 10.1002/adma.202006274.
- [59] L. Cusin, H. Peng, A. Ciesielski, P. Samorì, *Angew. Chem. Int. Ed.* **2021**, *60*, 14236–14250.
- [60] P. F. Wei, M. Z. Qi, Z. P. Wang, S. Y. Ding, W. Yu, Q. Liu, L. K. Wang, H. Z. Wang, W. K. An, W. Wang, *J. Am. Chem. Soc.* **2018**, *140*, 4623–4631.
- [61] P. Das, S. K. Mandal, *Chem. Mater.* **2019**, *31*, 1584–1596.
- [62] J. Guo, Y. Xu, S. Jin, L. Chen, T. Kaji, Y. Honsho, M. A. Addicoat, J. Kim, A. Saeki, H. Ihee, S. Seki, S. Irle, M. Hiramoto, J. Gao, D. Jiang, *Nat. Commun.* **2013**, *4*, 2736–2736.
- [63] M. Wang, M. Ballabio, M. Wang, H.-H. Lin, B. P. Biswal, X. Han, S. Paasch, E. Brunner, P. Liu, M. Chen, M. Bonn, T. Heine, S. Zhou, E. Cánovas, R. Dong, X. Feng, *J. Am. Chem. Soc.* **2019**, *141*, 16810–16816.
- [64] K. Wang, Z. Jia, Y. Bai, X. Wang, S. E. Hodgkiss, L. Chen, S. Y. Chong, X. Wang, H. Yang, Y. Xu, F. Feng, J. W. Ward, A. I. Cooper, *J. Am. Chem. Soc.* **2020**, jacs.0c03418-jacs.0c03418.
- [65] P. L. Wang, S. Y. Ding, Z. C. Zhang, Z. P. Wang, W. Wang, *J. Am. Chem. Soc.* **2019**, *141*, 18004–18008.
- [66] X.-T. Li, J. Zou, T.-H. Wang, H.-C. Ma, G.-J. Chen, Y.-B. Dong, *J. Am. Chem. Soc.* **2020**, *142*, 6521–6526.
- [67] J. Wang, X. Kan, J. Shang, H. Qiao, Y. Dong, *J. Am. Chem. Soc.* **2020**, *142*, 16915–16920.
- [68] H. Liu, J. Chu, Z. Yin, X. Cai, L. Zhuang, H. Deng, *Chem* **2018**, *4*, 1696–1709.
- [69] P. J. Waller, S. J. Lyle, T. M. Osborn Popp, C. S. Diercks, J. A. Reimer, O. M. Yaghi, *J. Am. Chem. Soc.* **2016**, *138*, 15519–15522.
- [70] F. Haase, E. Troschke, G. Savasci, T. Banerjee, V. Duppel, S. Dörfler, M. M. J. Grundei, A. M. Burow, C. Ochsenfeld, S. Kaskel, B. V. Lotsch, *Nat. Commun.* **2018**, *9*, 2600–2600.
- [71] S. J. Lyle, T. M. Osborn Popp, P. J. Waller, X. Pei, J. A. Reimer, O. M. Yaghi, *J.*

- Am. Chem. Soc.* **2019**, *141*, 11253–11258.
- [72] Q. Yan, H. Xu, X. Jing, H. Hu, S. Wang, C. Zeng, Y. Gao, *RSC Adv.* **2020**, *10*, 17396–17403.
- [73] C. Diercks, M. Kalmutzki, O. Yaghi, *Molecules* **2017**, *22*, 1575.
- [74] D. Jiang, *Chem* **2020**, *6*, 2461–2483.
- [75] T.-Y. Zhou, S.-Q. Xu, Q. Wen, Z.-F. Pang, X. Zhao, *J. Am. Chem. Soc.* **2014**, *136*, 15885–15888.
- [76] X. Chen, N. Huang, J. Gao, H. Xu, F. Xu, D. Jiang, *Chem Commun* **2014**, *50*, 6161–6163.
- [77] L. Ascherl, T. Sick, J. T. Margraf, S. H. Lapidus, M. Calik, C. Hettstedt, K. Karghiosoff, M. Döblinger, T. Clark, K. W. Chapman, F. Auras, T. Bein, *Nat. Chem.* **2016**, *8*, 310–316.
- [78] S. T. Emmerling, R. Schuldt, S. Bette, L. Yao, R. E. Dinnebier, J. Kästner, B. V. Lotsch, *J. Am. Chem. Soc.* **2021**, *143*, 15711–15722.
- [79] S. Dalapati, M. Addicoat, S. Jin, T. Sakurai, J. Gao, H. Xu, S. Irle, S. Seki, D. Jiang, *Nat. Commun.* **2015**, *6*, 7786.
- [80] A. P. Côté, H. M. El-Kaderi, H. Furukawa, J. R. Hunt, O. M. Yaghi, *J. Am. Chem. Soc.* **2007**, *129*, 12914–12915.
- [81] J. Rouquerol, D. Avnir, C. W. Fairbridge, D. H. Everett, J. M. Haynes, N. Pernicone, J. D. F. Ramsay, K. S. W. Sing, K. K. Unger, *Pure Appl. Chem.* **1994**, *66*, 1739–1758.
- [82] P. Albacete, J. I. Martínez, X. Li, A. López-Moreno, S. Mena-Hernando, A. E. Platero-Prats, C. Montoro, K. P. Loh, E. M. Pérez, F. Zamora, *J. Am. Chem. Soc.* **2018**, *140*, 12922–12929.
- [83] X. Wu, X. Han, Y. Liu, Y. Liu, Y. Cui, *J. Am. Chem. Soc.* **2018**, *140*, 16124–16133.
- [84] C. Kang, Z. Zhang, V. Wee, A. K. Usadi, D. C. Calabro, L. S. Baugh, S. Wang, Y. Wang, D. Zhao, *J. Am. Chem. Soc.* **2020**, *142*, 12995–13002.
- [85] B. T. Koo, W. R. Dichtel, P. Clancy, *J. Mater. Chem.* **2012**, *22*, 17460.
- [86] E. L. Spitler, B. T. Koo, J. L. Novotney, J. W. Colson, F. J. Uribe-Romo, G. D. Gutierrez, P. Clancy, W. R. Dichtel, *J. Am. Chem. Soc.* **2011**, *133*, 19416–19421.
- [87] T. Hayashi, Y. Hijikata, A. Page, D. Jiang, S. Irle, *Chem. Phys. Lett.* **2016**, *664*, 101–107.
- [88] C. Kang, Z. Zhang, A. K. Usadi, D. C. Calabro, L. S. Baugh, K. Yu, Y. Wang, D. Zhao, *J. Am. Chem. Soc.* **2022**, *144*, 3192–3199.
- [89] S. Yang, X. Li, Y. Qin, Y. Cheng, W. Fan, X. Lang, L. Zheng, Q. Cao, *ACS Appl. Mater. Interfaces* **2021**, *13*, 29471–29481.
- [90] T. Sick, J. M. Rotter, S. Reuter, S. Kandambeth, N. N. Bach, M. Döblinger, J. Merz, T. Clark, T. B. Marder, T. Bein, D. D. Medina, *J. Am. Chem. Soc.* **2019**, *141*, 12570–12581.
- [91] A. Sharma, A. Malani, N. V. Medhekar, R. Babarao, *CrystEngComm* **2017**, *19*, 6950–6963.
- [92] C. J. Doonan, D. J. Tranchemontagne, T. G. Glover, J. R. Hunt, O. M. Yaghi, *Nat. Chem.* **2010**, *2*, 235–238.
- [93] S. Jin, T. Sakurai, T. Kowalczyk, S. Dalapati, F. Xu, H. Wei, X. Chen, J. Gao, S. Seki, S. Irle, D. Jiang, *Chem. - Eur. J.* **2014**, *20*, 14608–14613.
- [94] H. S. Sasmal, A. Kumar Mahato, P. Majumder, R. Banerjee, *J. Am. Chem. Soc.* **2022**, *144*, 11482–11498.

- [95] K. Liu, L. Wang, R. Dong, *J. Mater. Chem. C* **2020**, *8*, 10696–10718.
- [96] L. Jiang, Y. Tian, T. Sun, Y. Zhu, H. Ren, X. Zou, Y. Ma, K. R. Meihaus, J. R. Long, G. Zhu, *J. Am. Chem. Soc.* **2018**, *140*, 15724–15730.
- [97] X. Li, C. Yang, B. Sun, S. Cai, Z. Chen, Y. Lv, J. Zhang, Y. Liu, *J. Mater. Chem. A* **2020**, *8*, 16045–16060.
- [98] H. Li, A. M. Evans, I. Castano, M. J. Strauss, W. R. Dichtel, J. L. Bredas, *J. Am. Chem. Soc.* **2020**, *142*, 1367–1374.
- [99] H. Li, A. D. Chavez, H. Li, H. Li, W. R. Dichtel, J.-L. Bredas, *J. Am. Chem. Soc.* **2017**, *139*, 16310–16318.
- [100] I. Castano, A. M. Evans, H. Li, E. Vitaku, M. J. Strauss, J.-L. Brédas, N. C. Gianneschi, W. R. Dichtel, *ACS Cent. Sci.* **2019**, *5*, 1892–1899.
- [101] B. J. Smith, L. R. Parent, A. C. Overholts, P. A. Beaucage, R. P. Bisbey, A. D. Chavez, N. Hwang, C. Park, A. M. Evans, N. C. Gianneschi, W. R. Dichtel, *ACS Cent. Sci.* **2017**, *3*, 58–65.
- [102] R. L. Li, N. C. Flanders, A. M. Evans, W. Ji, I. Castano, L. X. Chen, N. C. Gianneschi, W. R. Dichtel, *Chem. Sci.* **2019**, *10*, 3796–3801.
- [103] C. Feriante, A. M. Evans, S. Jhulki, I. Castano, M. J. Strauss, S. Barlow, W. R. Dichtel, S. R. Marder, *J. Am. Chem. Soc.* **2020**, *142*, 18637–18644.
- [104] N. L. Campbell, R. Clowes, L. K. Ritchie, A. I. Cooper, *Chem. Mater.* **2009**, *21*, 204–206.
- [105] W. Zhao, P. Yan, H. Yang, M. Bahri, A. M. James, H. Chen, L. Liu, B. Li, Z. Pang, R. Clowes, N. D. Browning, J. W. Ward, Y. Wu, A. I. Cooper, *Nat. Synth.* **2022**, *1*, 87–95.
- [106] B. P. Biswal, S. Chandra, S. Kandambeth, B. Lukose, T. Heine, R. Banerjee, *J. Am. Chem. Soc.* **2013**, *135*, 5328–5331.
- [107] S. Kim, H. C. Choi, *Commun. Chem.* **2019**, *2*, 1–8.
- [108] M. Matsumoto, R. R. Dasari, W. Ji, C. H. Feriante, T. C. Parker, S. R. Marder, W. R. Dichtel, *J. Am. Chem. Soc.* **2017**, *139*, 4999–5002.
- [109] L. K. Beagle, Q. Fang, L. D. Tran, L. A. Baldwin, C. Muratore, J. Lou, N. R. Glavin, *Mater. Today* **2021**, *51*, 427–448.
- [110] G. Zhan, Z.-F. Cai, K. Strutyński, L. Yu, N. Herrmann, M. Martínez-Abadía, M. Melle-Franco, A. Mateo-Alonso, S. D. Feyter, *Nature* **2022**, *603*, 835–840.
- [111] N. Bilbao, Y. Yu, L. Verstraete, J. Lin, S. Lei, S. De Feyter, *Chem. Commun.* **2018**, *54*, 9905–9908.
- [112] J. Plas, D. Waghray, J. Adisoejoso, O. Ivasenko, W. Dehaen, S. De Feyter, *Chem. Commun.* **2015**, *51*, 16338–16341.
- [113] D. Cui, D. F. Perepichka, J. M. MacLeod, F. Rosei, *Chem. Soc. Rev.* **2020**, DOI 10.1039/C9CS00456D.
- [114] L. Grill, S. Hecht, *Nat. Chem.* **2020**, *12*, 115–130.
- [115] Y. Jin, Y. Hu, M. Ortiz, S. Huang, Y. Ge, W. Zhang, *Chem. Soc. Rev.* **2020**, *49*, 4637–4666.
- [116] J. W. Colson, A. R. Woll, A. Mukherjee, M. P. Levendorf, E. L. Spitler, V. B. Shields, M. G. Spencer, J. Park, W. R. Dichtel, *Science* **2011**, *332*, 228–231.
- [117] D. D. Medina, V. Werner, F. Auras, R. Tautz, M. Dogru, J. Schuster, S. Linke, M. Döblinger, J. Feldmann, P. Knochel, T. Bein, *ACS Nano* **2014**, *8*, 4042–4052.
- [118] D. D. Medina, M. L. Petrus, A. N. Jumabekov, J. T. Margraf, S. Weinberger, J. M. Rotter, T. Clark, T. Bein, *ACS Nano* **2017**, *11*, 2706–2713.

- [119] H. Wang, B. He, F. Liu, C. Stevens, M. A. Brady, S. Cai, C. Wang, T. P. Russell, T. W. Tan, Y. Liu, *J. Mater. Chem. C* **2017**, *5*, 5090–5095.
- [120] S. L. Cai, Y. B. Zhang, A. B. Pun, B. He, J. Yang, F. M. Toma, I. D. Sharp, O. M. Yaghi, J. Fan, S. R. Zheng, W. G. Zhang, Y. Liu, *Chem. Sci.* **2014**, *5*, 4693–4700.
- [121] W. Dai, F. Shao, J. Szczerbiński, R. McCaffrey, R. Zenobi, Y. Jin, A. D. Schlüter, W. Zhang, *Angew. Chem. Int. Ed.* **2016**, *55*, 213–217.
- [122] I. Gadwal, G. Sheng, R. L. Thankamony, Y. Liu, H. Li, Z. Lai, *ACS Appl. Mater. Interfaces* **2018**, *10*, 12295–12299.
- [123] D. B. Shinde, G. Sheng, X. Li, M. Ostwal, A.-H. Emwas, K.-W. Huang, Z. Lai, *J. Am. Chem. Soc.* **2018**, *140*, 14342–14349.
- [124] K. Liu, H. Qi, R. Dong, R. Shivhare, M. Addicoat, T. Zhang, H. Sahabudeen, T. Heine, S. Mannsfeld, U. Kaiser, Z. Zheng, X. Feng, *Nat. Chem.* **2019**, *11*, 1–7.
- [125] H. Qi, H. Sahabudeen, B. Liang, M. Položij, M. A. Addicoat, T. E. Gorelik, M. Hamsch, M. Mundsinger, S. Park, B. V. Lotsch, S. C. B. Mannsfeld, Z. Zheng, R. Dong, T. Heine, X. Feng, U. Kaiser, *Sci. Adv.* **2020**, *6*, eabb5976.
- [126] S. Park, Z. Liao, B. Ibarlucea, H. Qi, H. Lin, D. Becker, J. Melidonie, T. Zhang, H. Sahabudeen, L. Baraban, C. Baek, Z. Zheng, E. Zschech, A. Fery, T. Heine, U. Kaiser, G. Cuniberti, R. Dong, X. Feng, *Angew. Chem. Int. Ed.* **2020**, *59*, 8218–8224.
- [127] Z. Ou, B. Liang, Z. Liang, F. Tan, X. Dong, L. Gong, P. Zhao, H. Wang, Y. Zou, Y. Xia, X. Chen, W. Liu, H. Qi, U. Kaiser, Z. Zheng, *J. Am. Chem. Soc.* **2022**, *144*, 3233–3241.
- [128] K. Dey, M. Pal, K. C. Rout, S. Kunjattu H, A. Das, R. Mukherjee, U. K. Kharul, R. Banerjee, *J. Am. Chem. Soc.* **2017**, *139*, 13083–13091.
- [129] M. Matsumoto, L. Valentino, G. M. Stiehl, H. B. Balch, A. R. Corcos, F. Wang, D. C. Ralph, B. J. Mariñas, W. R. Dichtel, *Chem* **2018**, *4*, 308–317.
- [130] B. Zhang, X. Song, Y. Li, Y. Li, Z. Peng, L. Ye, L. Chen, *Chem. Commun.* **2020**, *56*, 3253–3256.
- [131] C. Huang, Y. Yao, V. Montes-García, M. Stoeckel, M. Von Holst, A. Ciesielski, P. Samorì, *Small* **2021**, *17*, 2007593.
- [132] S. Kandambeth, B. P. Biswal, H. D. Chaudhari, K. C. Rout, S. Kunjattu H., S. Mitra, S. Karak, A. Das, R. Mukherjee, U. K. Kharul, R. Banerjee, *Adv. Mater.* **2017**, *29*, 1–9.
- [133] S. Khalil, M. D. Meyer, A. Alazmi, M. H. K. Samani, P.-C. Huang, M. Barnes, A. B. Marciel, R. Verduzco, *ACS Nano* **2022**, *16*, 20964–20974.
- [134] L. Yao, A. Rodríguez-Camargo, M. Xia, D. Mücke, R. Guntermann, Y. Liu, L. Grunenberg, A. Jiménez-Solano, S. T. Emmerling, V. Duppel, K. Sivula, T. Bein, H. Qi, U. Kaiser, M. Grätzel, B. V. Lotsch, *J. Am. Chem. Soc.* **2022**, *144*, 10291–10300.
- [135] D. Rodríguez-San-Miguel, A. Yazdi, V. Guillerm, J. Pérez-Carvajal, V. Puentes, D. MasPOCH, F. Zamora, *Chem. - Eur. J.* **2017**, *23*, 8623–8627.
- [136] D. Chakraborty, S. Nandi, D. Mullangi, S. Haldar, C. P. Vinod, R. Vaidhyanathan, *ACS Appl. Mater. Interfaces* **2019**, *11*, 15670–15679.
- [137] L.-L. Wang, C.-X. Yang, X.-P. Yan, *ChemPlusChem* **2017**, *82*, 933–938.
- [138] S. Mohata, K. Dey, S. Bhunia, N. Thomas, E. B. Gowd, T. G. Ajithkumar, C. M. Reddy, R. Banerjee, *J. Am. Chem. Soc.* **2022**, *144*, 400–409.
- [139] P. Wang, Q. Wu, L. Han, S. Wang, S. Fang, Z. Zhang, S. Sun, *RSC Adv.* **2015**, *5*,

- 27290–27294.
- [140] C. R. Mulzer, L. Shen, R. P. Bisbey, J. R. McKone, N. Zhang, H. D. Abruña, W. R. Dichtel, *ACS Cent. Sci.* **2016**, *2*, 667–673.
- [141] L. Garzón-Tovar, J. Pérez-Carvajal, A. Yazdi, J. Hernández-Muñoz, P. Tarazona, I. Imaz, F. Zamora, D. MasPOCH, *Angew. Chem. Int. Ed.* **2019**, *58*, 9512–9516.
- [142] Q. Jiang, L. Sun, J. Bi, S. Liang, L. Li, Y. Yu, L. Wu, *ChemSusChem* **2018**, *11*, 1108–1113.
- [143] H. Furukawa, O. M. Yaghi, *J. Am. Chem. Soc.* **2009**, *131*, 8875–8883.
- [144] N. Huang, R. Krishna, D. Jiang, *J. Am. Chem. Soc.* **2015**, *137*, 7079–7082.
- [145] K. T. Tan, S. Tao, N. Huang, D. Jiang, *Nat. Commun.* **2021**, *12*, 6747.
- [146] J. L. Mendoza-Cortes, T. A. Pascal, W. A. Goddard, *J. Phys. Chem. A* **2011**, *115*, 13852–13857.
- [147] Y. Yang, M. Faheem, L. Wang, Q. Meng, H. Sha, N. Yang, Y. Yuan, G. Zhu, *ACS Cent. Sci.* **2018**, *4*, 748–754.
- [148] Z. Kang, Y. Peng, Y. Qian, D. Yuan, M. A. Addicoat, T. Heine, Z. Hu, L. Tee, Z. Guo, D. Zhao, *Chem. Mater.* **2016**, *28*, 1277–1285.
- [149] H. Fan, A. Mundstock, A. Feldhoff, A. Knebel, J. Gu, H. Meng, J. Caro, *J. Am. Chem. Soc.* **2018**, *140*, 10094–10098.
- [150] D. Jiang, J. Li, J. Wang, Z. Wu, S. Tao, *Angew. Chem. Int. Ed.* **2021**, anie.202101400.
- [151] S. Yuan, X. Li, J. Zhu, G. Zhang, P. Van Puyvelde, B. Van Der Bruggen, *Chem. Soc. Rev.* **2019**, *48*, 2665–2681.
- [152] C. Zhang, B. H. Wu, M. Q. Ma, Z. Wang, Z. K. Xu, *Chem. Soc. Rev.* **2019**, *48*, 3811–3841.
- [153] S. Zhao, C. Jiang, J. Fan, S. Hong, P. Mei, R. Yao, Y. Liu, S. Zhang, H. Li, H. Zhang, C. Sun, Z. Guo, P. Shao, Y. Zhu, J. Zhang, L. Guo, Y. Ma, J. Zhang, X. Feng, F. Wang, H. Wu, B. Wang, *Nat. Mater.* **2021**, *20*, 1551–1558.
- [154] X. Liu, D. Huang, C. Lai, G. Zeng, L. Qin, H. Wang, H. Yi, B. Li, S. Liu, M. Zhang, R. Deng, Y. Fu, L. Li, W. Xue, S. Chen, *Chem. Soc. Rev.* **2019**, *48*, 5266–5302.
- [155] G. Das, B. P. Biswal, S. Kandambeth, V. Venkatesh, G. Kaur, M. Addicoat, T. Heine, S. Verma, R. Banerjee, *Chem. Sci.* **2015**, *6*, 3931–3939.
- [156] Q. Gao, X. Li, G.-H. Ning, K. Leng, B. Tian, C. Liu, W. Tang, H.-S. Xu, K. P. Loh, *Chem. Commun.* **2018**, *54*, 2349–2352.
- [157] Y. Peng, Y. Huang, Y. Zhu, B. Chen, L. Wang, Z. Lai, Z. Zhang, M. Zhao, C. Tan, N. Yang, F. Shao, Y. Han, H. Zhang, *J. Am. Chem. Soc.* **2017**, *139*, 8698–8704.
- [158] S. Jhulki, A. M. Evans, X.-L. Hao, M. W. Cooper, C. H. Feriante, J. Leisen, H. Li, D. Lam, M. C. Hersam, S. Barlow, J.-L. Brédas, W. R. Dichtel, S. R. Marder, *J. Am. Chem. Soc.* **2020**, *142*, 783–791.
- [159] Y. Zhang, X. Shen, X. Feng, H. Xia, Y. Mu, X. Liu, *Chem. Commun.* **2016**, *52*, 11088–11091.
- [160] F. Niu, Z.-W. Shao, J.-L. Zhu, L.-M. Tao, Y. Ding, *J. Mater. Chem. C* **2021**, *9*, 8562–8569.
- [161] T. Zhang, C. Gao, W. Huang, Y. Chen, Y. Wang, J. Wang, *Talanta* **2018**, *188*, 578–583.
- [162] Z. Li, Y. Zhang, H. Xia, Y. Mu, X. Liu, *Chem. Commun.* **2016**, *52*, 6613–6616.
- [163] L. Ascherl, E. W. Evans, J. Gorman, S. Orsborne, D. Bessinger, T. Bein, R. H. Friend, F. Auras, *J. Am. Chem. Soc.* **2019**, *141*, 15693–15699.

- [164] J. Guo, D. Jiang, *ACS Cent. Sci.* **2020**, *6*, 869–879.
- [165] X. Chen, M. Addicoat, E. Jin, L. Zhai, H. Xu, N. Huang, Z. Guo, L. Liu, S. Irle, D. Jiang, *J. Am. Chem. Soc.* **2015**, *137*, 3241–3247.
- [166] V. S. Vyas, F. Haase, L. Stegbauer, G. Savasci, F. Podjaski, C. Ochsenfeld, B. V. Lotsch, *Nat. Commun.* **2015**, *6*, 8508.
- [167] D. Li, C. Li, L. Zhang, H. Li, L. Zhu, D. Yang, Q. Fang, S. Qiu, X. Yao, *J. Am. Chem. Soc.* **2020**, *142*, 8104–8108.
- [168] S. Nandi, S. K. Singh, D. Mullangi, R. Illathvalappil, L. George, C. P. Vinod, S. Kurungot, R. Vaidhyathan, *Adv. Energy Mater.* **2016**, *6*, 1–11.
- [169] N. Huang, K. H. Lee, Y. Yue, X. Xu, S. Irle, Q. Jiang, D. Jiang, *Angew. Chem. Int. Ed.* **2020**, *59*, 16587–16593.
- [170] P. Pachfule, M. K. Panda, S. Kandambeth, S. M. Shivaprasad, D. D. Díaz, R. Banerjee, *J Mater Chem A* **2014**, *2*, 7944–7952.
- [171] R. Gutzler, D. F. Perepichka, *J. Am. Chem. Soc.* **2013**, *135*, 16585–16594.
- [172] Y. Yang, K. Börjesson, *Trends Chem.* **2022**, *4*, 60–75.
- [173] T. Sick, A. G. Hufnagel, J. Kampmann, I. Kondofersky, M. Calik, J. M. Rotter, A. Evans, M. Döblinger, S. Herbert, K. Peters, D. Böhm, P. Knochel, D. D. Medina, D. Fattakhova-Rohlfing, T. Bein, *J. Am. Chem. Soc.* **2018**, *140*, 2085–2092.
- [174] E. Jin, K. Geng, S. Fu, S. Yang, N. Kanlayakan, M. A. Addicoat, N. Kungwan, J. Geurs, H. Xu, M. Bonn, H. I. Wang, J. Smet, T. Kowalczyk, D. Jiang, *Chem* **2021**, *7*, 3309–3324.
- [175] B. Sun, C. H. Zhu, Y. Liu, C. Wang, L. J. Wan, D. Wang, *Chem. Mater.* **2017**, *29*, 4367–4374.
- [176] C. Li, D. Li, W. Zhang, H. Li, G. Yu, *Angew. Chem. Int. Ed.* **2021**, *60*, 27135–27143.
- [177] R. Gutzler, *Phys. Chem. Chem. Phys.* **2016**, *18*, 29029–29100.
- [178] H. Zhang, Y. Geng, J. Huang, Z. Wang, K. Du, H. Li, *Energy Environ. Sci.* **2023**, *16*, 889–951.
- [179] N. Tessler, Y. Preezant, N. Rappaport, Y. Roichman, *Adv. Mater.* **2009**, *21*, 2741–2761.
- [180] M. K. Hota, S. Chandra, Y. Lei, X. Xu, M. N. Hedhili, A. Emwas, O. Shekhah, M. Eddaoudi, H. N. Alshareef, *Adv. Funct. Mater.* **2022**, 2201120.
- [181] H. Cheema, J. Watson, A. Peddapuram, J. H. Delcamp, *Chem. Commun.* **2020**, *56*, 1741–1744.
- [182] S. Yang, D. Streater, C. Fiankor, J. Zhang, J. Huang, *J. Am. Chem. Soc.* **2021**, DOI 10.1021/jacs.0c11719.
- [183] Z. Wang, C. Wang, Y. Chen, L. Wei, *Adv. Mater. Technol.* **2023**, 2201828.
- [184] S. Kandambeth, V. S. Kale, O. Shekhah, H. N. Alshareef, M. Eddaoudi, *Adv. Energy Mater.* **2022**, *12*, 2100177.
- [185] M. Wu, Y. Zhao, R. Zhao, J. Zhu, J. Liu, Y. Zhang, C. Li, Y. Ma, H. Zhang, Y. Chen, *Adv. Funct. Mater.* **2021**, 2107703.
- [186] Q. Jiang, Y. Li, X. Zhao, P. Xiong, X. Yu, Y. Xu, L. Chen, *J. Mater. Chem. A* **2018**, *6*, 17977–17981.
- [187] B. C. Patra, S. K. Das, A. Ghosh, A. Raj K, P. Moitra, M. Addicoat, S. Mitra, A. Bhaumik, S. Bhattacharya, A. Pradhan, *J. Mater. Chem. A* **2018**, *6*, 16655–16663.
- [188] X. Luo, W. Li, H. Liang, H. Zhang, K. Du, X. Wang, X. Liu, J. Zhang, X. Wu, *Angew.*

- Chem. Int. Ed.* **2022**, *61*, DOI 10.1002/anie.202117661.
- [189] W. Wang, V. S. Kale, Z. Cao, S. Kandambeth, W. Zhang, J. Ming, P. T. Parvatkar, E. Abou-Hamad, O. Shekhah, L. Cavallo, M. Eddaoudi, H. N. Alshareef, *ACS Energy Lett.* **2020**, *5*, 2256–2264.
- [190] R. Sun, S. Hou, C. Luo, X. Ji, L. Wang, L. Mai, C. Wang, *Nano Lett.* **2020**, *20*, 3880–3888.
- [191] H. Lu, F. Ning, R. Jin, C. Teng, Y. Wang, K. Xi, D. Zhou, G. Xue, *ChemSusChem* **2020**, *13*, 3447–3454.
- [192] R. M. Silverstein, F. X. Webster, D. J. Kiemle, D. L. Bryce, *Spectrometric Identification of Organic Compounds*, Wiley, Hoboken, NJ, **2015**.
- [193] R. Minnes, M. Nissinmann, Y. Maizels, G. Gerlitz, A. Katzir, Y. Raichlin, *Sci. Rep.* **2017**, *7*, 4381.
- [194] J. F. Watts, J. Wolstenholme, *An Introduction to Surface Analysis by XPS and AES*, J. Wiley, Chichester, West Sussex, England ; New York, **2003**.
- [195] M. A. Isaacs, J. Davies-Jones, P. R. Davies, S. Guan, R. Lee, D. J. Morgan, R. Palgrave, *Mater. Chem. Front.* **2021**, *5*, 7931–7963.
- [196] A. W. Coats, J. P. Redfern, *The Analyst* **1963**, *88*, 906.
- [197] L. S. K. Pang, J. D. Saxby, S. P. Chatfield, *J. Phys. Chem.* **1993**, *97*, 6941–6942.
- [198] G. Socrates, *Infrared and Raman Characteristic Group Frequencies: Tables and Charts*, Wiley, Chichester, **2010**.
- [199] J. A. Kaduk, S. J. L. Billinge, R. E. Dinnebier, N. Henderson, I. Madsen, R. Černý, M. Leoni, L. Lutterotti, S. Thakral, D. Chateigner, *Nat. Rev. Methods Primer* **2021**, *1*, 77.
- [200] D.-M. Smilgies, *J. Appl. Crystallogr.* **2009**, *42*, 1030–1034.
- [201] T. Runčevski, C. M. Brown, *Cryst. Growth Des.* **2021**, *21*, 4821–4822.
- [202] A. A. Coelho, *J. Appl. Crystallogr.* **2018**, *51*, 210–218.
- [203] J. C. Fischer, C. Li, S. Hamer, L. Heinke, R. Herges, B. S. Richards, I. A. Howard, *Adv. Mater. Interfaces* **2023**, *10*, 2202259.
- [204] S. Lowell, J. E. Shields, M. A. Thomas, M. Thommes, *Characterization of Porous Solids and Powders: Surface Area, Pore Size and Density*, Springer Netherlands, Dordrecht, **2004**.
- [205] M. Thommes, K. Kaneko, A. V. Neimark, J. P. Olivier, F. Rodriguez-Reinoso, J. Rouquerol, K. S. W. Sing, *Pure Appl. Chem.* **2015**, *87*, 1051–1069.
- [206] F. Ambroz, T. J. Macdonald, V. Martis, I. P. Parkin, *Small Methods* **2018**, *2*, 1800173.
- [207] J. W. M. Osterrieth, J. Rampersad, D. Madden, N. Rampal, L. Skoric, B. Connolly, M. D. Allendorf, V. Stavila, J. L. Snider, R. Ameloot, J. Marreiros, C. Ania, D. Azevedo, E. Vilarrasa-Garcia, B. F. Santos, X. Bu, Z. Chang, H. Bunzen, N. R. Champness, S. L. Griffin, B. Chen, R. Lin, B. Coasne, S. Cohen, J. C. Moreton, Y. J. Colón, L. Chen, R. Clowes, F. Coudert, Y. Cui, B. Hou, D. M. D'Alessandro, P. W. Doheny, M. Dincă, C. Sun, C. Doonan, M. T. Huxley, J. D. Evans, P. Falcaro, R. Ricco, O. Farha, K. B. Idrees, T. Islamoglu, P. Feng, H. Yang, R. S. Forgan, D. Bara, S. Furukawa, E. Sanchez, J. Gascon, S. Telalović, S. K. Ghosh, S. Mukherjee, M. R. Hill, M. M. Sadiq, P. Horcajada, P. Salcedo-Abraira, K. Kaneko, R. Kubat, J. Kevlin, S. Keskin, S. Kitagawa, K. Otake, R. P. Lively, S. J. A. DeWitt, P. Llewellyn, B. V. Lotsch, S. T. Emmerling, A. M. Pütz, C. Martí-Gastaldo, N. M. Padial, J. García-Martínez, N. Linares, D. Maspocho, J. A. Suárez Del Pino, P.

- Moghadam, R. Oktavian, R. E. Morris, P. S. Wheatley, J. Navarro, C. Petit, D. Danaci, M. J. Rosseinsky, A. P. Katsoulidis, M. Schröder, X. Han, S. Yang, C. Serre, G. Mouchaham, D. S. Sholl, R. Thyagarajan, D. Siderius, R. Q. Snurr, R. B. Goncalves, S. Telfer, S. J. Lee, V. P. Ting, J. L. Rowlandson, T. Uemura, T. Iiyuka, M. A. Van Der Veen, D. Rega, V. Van Speybroeck, S. M. J. Rogge, A. Lamaire, K. S. Walton, L. W. Bingel, S. Wuttke, J. Andreo, O. Yaghi, B. Zhang, C. T. Yavuz, T. S. Nguyen, F. Zamora, C. Montoro, H. Zhou, A. Kirchon, D. Fairen-Jimenez, *Adv. Mater.* **2022**, *34*, 2201502.
- [208] D. G. Brandon, W. D. Kaplan, *Microstructural Characterization of Materials*, Wiley, Chichester, **2010**.
- [209] V. Balzani, P. Ceroni, A. Juris, *Photochemistry and Photophysics: Concepts, Research, Applications*, Wiley-VCH Verlag GmbH & Co. KGaA, Weinheim, Germany, **2014**.
- [210] P. Makuła, M. Pacia, W. Macyk, *J. Phys. Chem. Lett.* **2018**, *9*, 6814–6817.
- [211] V. Vivier, M. E. Orazem, *Chem. Rev.* **2022**, *122*, 11131–11168.
- [212] N. Elgrishi, K. J. Rountree, B. D. McCarthy, E. S. Rountree, T. T. Eisenhart, J. L. Dempsey, *J. Chem. Educ.* **2018**, *95*, 197–206.
- [213] M. A. Springer, T.-J. Liu, A. Kuc, T. Heine, *Chem. Soc. Rev.* **2020**, *49*, 2007–2019.
- [214] A. Knebel, J. Caro, *Nat. Nanotechnol.* **2022**, *17*, 911–923.
- [215] H. Dou, M. Xu, B. Wang, Z. Zhang, G. Wen, Y. Zheng, D. Luo, L. Zhao, A. Yu, L. Zhang, Z. Jiang, Z. Chen, *Chem. Soc. Rev.* **2020**, DOI 10.1039/D0CS00552E.
- [216] J. L. Fenton, D. W. Burke, D. Qian, M. O. de la Cruz, W. R. Dichtel, *J. Am. Chem. Soc.* **2021**, DOI 10.1021/jacs.0c11159.
- [217] A. Kumar Mahato, S. Bag, H. S. Sasmal, K. Dey, I. Giri, M. Linares-Moreau, C. Carbonell, P. Falcaro, E. B. Gowd, R. K. Vijayaraghavan, R. Banerjee, *J. Am. Chem. Soc.* **2021**, jacs.1c09740.
- [218] J. I. Feldblyum, C. H. McCreery, S. C. Andrews, T. Kurosawa, E. J. G. Santos, V. Duong, L. Fang, A. L. Ayzner, Z. Bao, *Chem. Commun.* **2015**, *51*, 13894–13897.
- [219] H. S. Sasmal, A. Halder, S. Kunjattu H, K. Dey, A. Nadol, T. G. Ajithkumar, P. Ravindra Bedadur, R. Banerjee, *J. Am. Chem. Soc.* **2019**, *141*, 20371–20379.
- [220] R. D. Deegan, O. Bakajin, T. F. Dupont, G. Huber, S. R. Nagel, T. A. Witten, *Nature* **1997**, *389*, 827–829.
- [221] M. S. Tirumkudulu, V. S. Punati, *Langmuir* **2022**, *38*, 2409–2414.
- [222] R. A. Cox, K. Yates, *Can. J. Chem.* **1983**, *61*, 2225–2243.
- [223] C. J. Brinker, G. W. Scherer, *Sol-Gel Science: The Physics and Chemistry of Sol-Gel Processing*, Academic Press, Boston, **1990**.
- [224] S. J. Kowalski, *Thermomechanics of Drying Processes*, Springer Berlin Heidelberg, Berlin, Heidelberg, **2003**.
- [225] M. Naguib, O. Mashtalir, J. Carle, V. Presser, J. Lu, L. Hultman, Y. Gogotsi, M. W. Barsoum, *ACS Nano* **2012**, *6*, 1322–1331.
- [226] V. G. Makotchenko, E. D. Grayfer, A. S. Nazarov, S.-J. Kim, V. E. Fedorov, *Carbon* **2011**, *49*, 3233–3241.
- [227] H. Matsuoka, H. Nakamoto, Md. A. B. H. Susan, M. Watanabe, *Electrochimica Acta* **2005**, *50*, 4015–4021.
- [228] K. Nakanishi, T. Goto, M. Ohashi, *Bull. Chem. Soc. Jpn.* **1957**, *30*, 403–408.
- [229] L. E. Shmukler, M. S. Gruzdev, N. O. Kudryakova, Yu. A. Fadeeva, A. M. Kolker, L. P. Safonova, *RSC Adv.* **2016**, *6*, 109664–109671.

- [230] H. Xu, S. Tao, D. Jiang, *Nat. Mater.* **2016**, *15*, 722–726.
- [231] H. Kricheldorf, *Polycondensation*, Springer Berlin Heidelberg, Berlin, Heidelberg, **2014**.
- [232] G. De With, *Polymer Coatings: A Guide to Chemistry, Characterization, and Selected Applications*, Wiley-VCH, Weinheim, **2018**.
- [233] Y. Gu, J. Zhao, J. A. Johnson, *Angew. Chem. Int. Ed.* **2020**, *59*, 5022–5049.
- [234] Y. Zeng, P. Gordiichuk, T. Ichihara, G. Zhang, E. Sandoz-Rosado, E. D. Wetzel, J. Tresback, J. Yang, D. Kozawa, Z. Yang, M. Kuehne, M. Quien, Z. Yuan, X. Gong, G. He, D. J. Lundberg, P. Liu, A. T. Liu, J. F. Yang, H. J. Kulik, M. S. Strano, *Nature* **2022**, *602*, 91–95.
- [235] W. H. Stockmayer, *J. Chem. Phys.* **1944**, *12*, 125–131.
- [236] P. J. Flory, *Principles of Polymer Chemistry*, Cornell University Press, Ithaca (N.Y.) London, **1952**.
- [237] C. M. Fontana, *J. Polym. Sci. [A1]* **1968**, *6*, 2343–2358.
- [238] B. L. Deopura, R. Alagirusamy, Textile Institute, Eds. , *Polyesters and Polyamides*, CRC Press, Boca Raton, Fla., **2008**.
- [239] M. Parsa, S. Harmand, K. Sefiane, *Adv. Colloid Interface Sci.* **2018**, *254*, 22–47.
- [240] H. Hu, R. G. Larson, *Langmuir* **2005**, *21*, 3972–3980.
- [241] F. Giorgiutti-Dauphiné, L. Pauchard, *Colloids Surf. Physicochem. Eng. Asp.* **2015**, *466*, 203–209.
- [242] H. Lei, L. F. Francis, W. W. Gerberich, L. E. Scriven, *AIChE J.* **2002**, *48*, 437–451.
- [243] H. Hu, R. G. Larson, *Langmuir* **2005**, *21*, 3963–3971.
- [244] D. Yan, Z. Wang, P. Cheng, Y. Chen, Z. Zhang, *Angew. Chem. Int. Ed.* **2021**, *60*, 6055–6060.
- [245] M. Guo, S. Jayakumar, M. Luo, X. Kong, C. Li, H. Li, J. Chen, Q. Yang, *Nat. Commun.* **2022**, *13*, 1770.
- [246] J. Reynolds, T. A. Skotheim, B. C. Thompson, Eds. , *Conjugated Polymers: Properties, Processing, and Applications*, CRC Press, Taylor & Francis Group, Boca Raton, Fla. London New York, **2019**.
- [247] A. Pron, P. Gawrys, M. Zagorska, D. Djurado, R. Demadrille, *Chem. Soc. Rev.* **2010**, *39*, 2577.
- [248] M. Souto, D. F. Perepichka, *J. Mater. Chem. C* **2021**, *9*, 10668–10676.
- [249] L. Gong, X. Yang, Y. Gao, G. Yang, Z. Yu, X. Fu, Y. Wang, D. Qi, Y. Bian, K. Wang, J. Jiang, *J. Mater. Chem. A* **2022**, *10*, 16595–16601.
- [250] Q. Hao, Z.-J. Li, B. Bai, X. Zhang, Y.-W. Zhong, L.-J. Wan, D. Wang, *Angew. Chem. Int. Ed.* **2021**, anie.202100870.
- [251] L. He, B. Li, Z. Ma, L. Chen, S. Gong, M. Zhang, Y. Bai, Q. Guo, F. Wu, F. Zhao, J. Li, D. Zhang, D. Sheng, X. Dai, L. Chen, J. Shu, Z. Chai, S. Wang, *Sci. China Chem.* **2023**, DOI 10.1007/s11426-022-1484-0.
- [252] A. F. M. EL-Mahdy, M. G. Mohamed, T. H. Mansoure, H.-H. Yu, T. Chen, S.-W. Kuo, *Chem. Commun.* **2019**, *55*, 14890–14893.
- [253] H.-J. Yen, G.-S. Liou, *Prog. Polym. Sci.* **2019**, *89*, 250–287.
- [254] C. Lambert, G. Nöll, *Synth. Met.* **2003**, *139*, 57–62.
- [255] R. Caballero, B. Cohen, M. Gutiérrez, *Molecules* **2021**, *26*, 7666.
- [256] M. E. Cinar, T. Ozturk, *Chem. Rev.* **2015**, *115*, 3036–3140.
- [257] M. L. Petrus, R. K. M. Bouwer, U. Lafont, D. H. K. Murthy, R. J. P. Kist, M. L. Böhm, Y. Olivier, T. J. Savenije, L. D. A. Siebbeles, N. C. Greenham, T. J.

- Dingemans, *Polym. Chem.* **2013**, *4*, 4182.
- [258] L. D. Tran, K. F. Presley, J. K. Streit, J. Carpena-Núñez, L. K. Beagle, T. A. Grusenmeyer, M. J. Dalton, R. A. Vaia, L. F. Drummy, N. R. Glavin, L. A. Baldwin, *Chem. Mater.* **2022**, acs.chemmater.1c02565.
- [259] G. Galeotti, F. De Marchi, E. Hamzehpoor, O. MacLean, M. Rajeswara Rao, Y. Chen, L. V. Besteiro, D. Dettmann, L. Ferrari, F. Frezza, P. M. Sheverdyeva, R. Liu, A. K. Kundu, P. Moras, M. Ebrahimi, M. C. Gallagher, F. Rosei, D. F. Perepichka, G. Contini, *Nat. Mater.* **2020**, 1–7.
- [260] H. R. Tantawy, B.-A. F. Kengne, D. N. McIlroy, T. Nguyen, D. Heo, Y. Qiang, D. E. Aston, *J. Appl. Phys.* **2015**, *118*, 175501.
- [261] C. M. Cardona, W. Li, A. E. Kaifer, D. Stockdale, G. C. Bazan, *Adv. Mater.* **2011**, *23*, 2367–2371.
- [262] N. Turetta, F. Sedona, A. Liscio, M. Sambì, P. Samorì, *Adv. Mater. Interfaces* **2021**, *8*, 2100068.
- [263] M. Liu, Y. Liu, J. Dong, Y. Bai, W. Gao, S. Shang, X. Wang, J. Kuang, C. Du, Y. Zou, J. Chen, Y. Liu, *Nat. Commun.* **2022**, *13*, 1411.
- [264] H.-H. Liao, C.-M. Yang, C.-C. Liu, S.-F. Horng, H.-F. Meng, J.-T. Shy, *J. Appl. Phys.* **2008**, *103*, 104506.
- [265] C.-K. Lu, H.-F. Meng, *Phys. Rev. B* **2007**, *75*, 235206.
- [266] M. S. A. Abdou, F. P. Orfino, Y. Son, S. Holdcroft, *J. Am. Chem. Soc.* **1997**, *119*, 4518–4524.
- [267] S. Kim, M. A. M. Rashid, T. Ko, K. Ahn, Y. Shin, S. Nah, M. H. Kim, B. Kim, K. Kwak, M. Cho, *J. Phys. Chem. C* **2020**, *124*, 2762–2770.
- [268] L. Ma, P. Hu, H. Jiang, C. Kloc, H. Sun, C. Soci, A. A. Voityuk, M. E. Michel-Beyerle, G. G. Gurzadyan, *Sci. Rep.* **2016**, *6*, 28510.
- [269] L. Kergoat, L. Herlogsson, D. Braga, B. Piro, M.-C. Pham, X. Crispin, M. Berggren, G. Horowitz, *Adv. Mater.* **2010**, *22*, 2565–2569.
- [270] S. Ippolito, A. G. Kelly, R. Furlan De Oliveira, M.-A. Stoeckel, D. Iglesias, A. Roy, C. Downing, Z. Bian, L. Lombardi, Y. A. Samad, V. Nicolosi, A. C. Ferrari, J. N. Coleman, P. Samorì, *Nat. Nanotechnol.* **2021**, *16*, 592–598.
- [271] N. Turetta, W. Danowski, L. Cusin, P. A. Livio, R. Hallani, I. McCulloch, P. Samorì, *J. Mater. Chem. C* **2023**, 10.1039.D2TC05444B.
- [272] S. Ippolito, F. Urban, W. Zheng, O. Mazzarisi, C. Valentini, A. G. Kelly, S. M. Galli, M. Bonn, D. Beljonne, F. Corberi, J. N. Coleman, H. I. Wang, P. Samorì, *Adv. Mater.* **2023**, 2211157.
- [273] D. P. Chatterjee, A. K. Nandi, *J. Mater. Chem. A* **2021**, *9*, 15880–15918.
- [274] M. A. Scibioh, B. Viswanathan, in *Mater. Supercapacitor Appl.*, Elsevier, **2020**, pp. 315–372.
- [275] L. Li, F. Lu, R. Xue, B. Ma, Q. Li, N. Wu, H. Liu, W. Yao, H. Guo, W. Yang, *ACS Appl. Mater. Interfaces* **2019**, *11*, 26355–26363.
- [276] A. M. Bryan, L. M. Santino, Y. Lu, S. Acharya, J. M. D’Arcy, *Chem. Mater.* **2016**, *28*, 5989–5998.
- [277] C. R. DeBlase, K. E. Silberstein, T.-T. Truong, H. D. Abruña, W. R. Dichtel, *J. Am. Chem. Soc.* **2013**, *135*, 16821–16824.
- [278] A. F. M. EL-Mahdy, C.-H. Kuo, A. Alshehri, C. Young, Y. Yamauchi, J. Kim, S.-W. Kuo, *J. Mater. Chem. A* **2018**, *6*, 19532–19541.
- [279] M. Sobczyk, S. Wiesenhütter, J. R. Noennig, T. Wallmersperger, *J. Intell. Mater.*

- Syst. Struct.* **2022**, *33*, 379–399.
- [280] Y. Yin, J. A. Rogers, *Chem. Rev.* **2022**, *122*, 4885–4886.
- [281] A. Kumar, K. Sharma, A. R. Dixit, *Carbon Lett.* **2021**, *31*, 149–165.
- [282] Y. Shu, Z. Xiong, Y. Liu, Y. Zhou, M. Li, Y. Zheng, S. Chen, K. Sun, in *Flex. Thermoelectr. Polym. Syst.* (Ed.: J. Ouyang), Wiley, **2022**, pp. 163–207.
- [283] M. J. Allen, V. C. Tung, R. B. Kaner, *Chem. Rev.* **2010**, *110*, 132–145.
- [284] X. Huang, X. Qi, F. Boey, H. Zhang, *Chem Soc Rev* **2012**, *41*, 666–686.
- [285] N. Devi, R. Kumar, S. Singh, R. K. Singh, *Crit. Rev. Solid State Mater. Sci.* **2022**, 1–69.
- [286] X. Fu, J. Lin, Z. Liang, R. Yao, W. Wu, Z. Fang, W. Zou, Z. Wu, H. Ning, J. Peng, *Surf. Interfaces* **2023**, *37*, 102747.
- [287] J. Wu, H. Lin, D. J. Moss, K. P. Loh, B. Jia, *Nat. Rev. Chem.* **2023**, DOI 10.1038/s41570-022-00458-7.
- [288] D. Li, M. B. Müller, S. Gilje, R. B. Kaner, G. G. Wallace, *Nat. Nanotechnol.* **2008**, *3*, 101–105.
- [289] D. R. Dreyer, S. Park, C. W. Bielawski, R. S. Ruoff, *Chem Soc Rev* **2010**, *39*, 228–240.
- [290] R. Tarcan, O. Todor-Boer, I. Petrovai, C. Leordean, S. Astilean, I. Botiz, *J. Mater. Chem. C* **2020**, *8*, 1198–1224.
- [291] C. Valentini, V. Montes-García, P. A. Livio, T. Chudziak, J. Raya, A. Ciesielski, P. Samorì, *Nanoscale* **2023**, *15*, 5743–5755.
- [292] Brodie, Benjamin Collins, *Philos. Trans. R. Soc. Lond.* **1859**, *149*, 249–259.
- [293] X. Zhang, L. Hou, F. Richard, P. Samorì, *Chem. – Eur. J.* **2018**, *24*, 18518–18528.
- [294] C. Anichini, A. Aliprandi, S. M. Gali, F. Liscio, V. Morandi, A. Minoia, D. Beljonne, A. Ciesielski, P. Samorì, *ACS Appl. Mater. Interfaces* **2020**, *12*, 44017–44025.
- [295] D. Zhu, Z. Zhang, L. B. Alemany, Y. Li, N. Nnorom, M. Barnes, S. Khalil, M. M. Rahman, P. M. Ajayan, R. Verduzco, *Chem. Mater.* **2021**, acs.chemmater.1c00737.
- [296] H. Souri, H. Banerjee, A. Jusufi, N. Radacsi, A. A. Stokes, I. Park, M. Sitti, M. Amjadi, *Adv. Intell. Syst.* **2020**, *2*, 2000039.
- [297] M. Amjadi, K.-U. Kyung, I. Park, M. Sitti, *Adv. Funct. Mater.* **2016**, *26*, 1678–1698.
- [298] W. A. D. M. Jayathilaka, K. Qi, Y. Qin, A. Chinnappan, W. Serrano-García, C. Baskar, H. Wang, J. He, S. Cui, S. W. Thomas, S. Ramakrishna, *Adv. Mater.* **2019**, *31*, 1805921.
- [299] S. Chen, K. Jiang, Z. Lou, D. Chen, G. Shen, *Adv. Mater. Technol.* **2018**, *3*, 1700248.
- [300] W. Chiappim, M. A. Fraga, H. Furlan, D. C. Ardiles, R. S. Pessoa, *Microsyst. Technol.* **2022**, *28*, 1561–1580.
- [301] Q. Zheng, J. Lee, X. Shen, X. Chen, J.-K. Kim, *Mater. Today* **2020**, *36*, 158–179.
- [302] Y. Huang, Y. Zhao, Y. Wang, X. Guo, Y. Zhang, P. Liu, C. Liu, Y. Zhang, *Smart Mater. Struct.* **2018**, *27*, 035013.
- [303] C. Wang, K. Xia, H. Wang, X. Liang, Z. Yin, Y. Zhang, *Adv. Mater.* **2019**, *31*, 1801072.
- [304] D. Zhu, J.-J. Zhang, X. Wu, Q. Yan, F. Liu, Y. Zhu, X. Gao, M. M. Rahman, B. I. Yakobson, P. M. Ajayan, R. Verduzco, *Chem. Sci.* **2022**, 10.1039.D2SC03489A.

- [305] R. L. Li, A. Yang, N. C. Flanders, M. T. Yeung, D. T. Sheppard, W. R. Dichtel, *J. Am. Chem. Soc.* **2021**, *143*, 7081–7087.